

Structure-dissolution relationships of phosphate and bioactive glasses by liquid, solid-state and paramagnetic NMR

Structural role and coordination environment of cobalt in phosphate glasses & the role of cations on the mechanism of hydrolysis

DISSERTATION

zur Erlangung des akademischen Grades doctor rerum naturalium
doctor rerum naturalium (Dr. rer. nat.)



FRIEDRICH-SCHILLER-
UNIVERSITÄT
JENA

vorgelegt dem Rat der Chemisch-Geowissenschaftlichen Fakultät der
Friedrich-Schiller-Universität Jena

von M.Sc. Dahiana Andrea Avila Salazar
geboren am 27.12.1984 in Bogotá, Colombia

Gutachter:

1. Herr Prof. Dr. Buntkowsky, Technische Universität Darmstadt
2. Herr Prof. Dr. Robl, Friedrich-Schiller-Universität Jena
3. Herr Prof. Dr. Deubener, Technische Universität Clausthal

Tag der Verteidigung: Montag, den 23. Mai 2022

Selbständigkeitserklärung

Ich erkläre, dass ich die vorliegende Arbeit selbständig und unter Verwendung der angegebenen Hilfsmittel, persönlichen Mitteilungen und Quellen angefertigt habe.

Jena, Monday 8th August, 2022

Para Marlen, por supuesto.

"Craft must have clothes, but truth loves to go naked." Thomas Fuller

Table of contents

List of figures	xiii
List of schemes	xv
List of tables	xvi
Nomenclature	xviii
1 Introduction	1
1.1 Bioglasses	3
1.2 Phosphate glasses	4
1.2.1 Properties and applications	5
1.2.2 Structural characterization by solid state NMR	7
1.3 Dissolution of phosphate glasses	8
1.3.1 The two-stage dissolution model	9
1.3.2 Durability	10
1.3.3 Aqueous degradation	12
1.4 Cobalt	14
1.4.1 Cobalt sources and toxicity	14
1.5 Tissue engineering	20
1.5.1 Challenges	20
1.5.2 Angiogenesis	21
1.5.3 Hypoxia	21
1.5.4 Activation of the hypoxia-inducible pathway	22
1.5.5 Cobalt as hypoxia-mimicking agent	22
1.5.6 Cobalt in biomaterials	23
1.5.7 Cobalt-containing phosphate glasses	24
1.6 Paramagnetic NMR	24

2	Theoretical Framework	26
2.1	Diffusion	26
2.1.1	Fick's laws	26
2.1.2	Steady-state diffusion	27
2.1.3	Higuchi equation	27
2.1.4	Diffusion and a chemical reaction	28
2.2	Solubility	28
2.2.1	Lattice enthalpy	28
2.2.2	Hydration enthalpy	28
2.2.3	Congruent dissolution	28
2.3	NMR	29
2.3.1	The nuclear spin Hamiltonian operator	29
2.3.2	The paramagnetic shift	34
2.3.3	Homogeneity approach	35
2.3.4	Relaxation	35
2.3.5	Paramagnetic nuclear relaxation	36
2.4	EPR	38
2.4.1	EPR spin Hamiltonian operator	38
2.4.2	Electronic Zeeman interaction	39
2.4.3	Electronic spin-spin interaction	40
2.4.4	The hyperfine interaction	40
2.4.5	EPR effective spin Hamiltonian	41
2.4.6	ZFS	42
3	Experimental Section	43
3.1	Glass Preparation	43
3.2	Compositional Analysis	44
3.3	Buffer Preparation	44
3.4	Static dissolution Test	45
3.5	Liquid state ^{31}P NMR Spectroscopy	45
3.5.1	Sample Preparation	45
3.6	X-ray Powder Diffraction (XRD)	46
3.7	Solid-state ^{31}P MAS NMR	46
3.7.1	Borate-based 45S5 glasses	46
3.8	Solid-state ^1H MAS NMR	47
3.9	Solid-state ^{29}Si MAS NMR	48
3.10	Solid-state ^{11}B MAS NMR	48
3.11	Electron Paramagnetic Resonance (EPR)	48

3.12 Raman	48
3.13 UV–vis–NIR	49
3.14 DSC/TGA-MS	49
3.15 Hot Stage Microscopy (HSM)	49
4 Kinetics and mechanism of cation-catalyzed hydrolysis of P_2O_5–CaO–Na₂O glasses: the effect of ligand competition and reactivity of intermediate complexes on ³¹P NMR spectra	51
4.1 Abstract	51
4.2 Introduction	52
4.3 Glass System	53
4.4 Glass Structure	53
4.4.1 Water in the glasses	55
4.5 Dissolution Behavior	56
4.5.1 ICP-OES analysis	56
4.5.2 pH analysis	58
4.5.3 Liquid ³¹ P NMR Spectroscopy	59
4.6 Mechanism of hydrolysis	66
5 Structural role and coordination environment of cobalt in $45P_2O_5$–CaO–Na₂O phosphate glasses: Thermal properties, Raman, UV–vis–NIR and EPR spectroscopy	70
5.1 Abstract	70
5.2 Introduction	71
5.3 Glass System	72
5.4 Thermogravimetric analysis-mass spectrometry	73
5.5 Powder X-ray Diffraction (XRD)	74
5.6 Raman	74
5.7 UV–vis–NIR	77
5.8 EPR spectroscopy	81
5.9 Thermal Properties	83
6 Co²⁺ as an internal paramagnetic ³¹P NMR probe for structural analysis of cobalt-phosphate glasses in the solid-state and leachate solutions	87
6.1 Abstract	87
6.2 Introduction	88
6.3 Glass Structure	89
6.4 Paramagnetic effects on solid-state ³¹ P MAS NMR	91
6.4.1 Linewidth	91
6.4.2 Paramagnetic shift	94

6.4.3	Paramagnetic relaxation enhancement (PRE)	96
6.4.4	Homogeneity approach	97
6.5	Paramagnetic effects on liquid ^{31}P NMR	101
6.5.1	Linewidth	101
6.5.2	Paramagnetic shift	102
6.5.3	Paramagnetic relaxation enhancement (PRE)	102
6.6	Cobalt-phosphate complexes in solution	103
7	Structural characterization of bioactive glasses by solid-state NMR	107
7.1	Introduction	107
7.2	45S5-based glasses with variable borate content	108
7.2.1	Solid-state MAS NMR	109
7.3	Mg/Zn-based 45S5 bioactive glasses	112
7.3.1	Solid-state MAS NMR	113
7.4	Mg/Sr-based S53P4 bioactive glasses	118
7.4.1	^{31}P solid-state MAS NMR	119
8	Conclusions	122
	References	131

List of figures

1.1	Generations of biomaterials	4
1.2	Functionalization of phosphate glasses	5
1.3	Mechanism of dissolution of phosphate glasses	9
1.4	Systemic toxic effects of cobalt	14
1.5	Formation of vascularized networks triggered by cobalt	21
1.6	Paramagnetic effects on the NMR spectra	24
4.1	³¹ P MAS NMR of CNP45 phosphate glasses	54
4.2	Spin-echo ¹ H MAS NMR of L27.5 glass	55
4.3	ICP-OES vs. time for CNP45 glasses	56
4.4	pH vs. time for CNP45 glasses	59
4.5	Liquid ³¹ P NMR for standards and ³¹ P NMR vs. time in Tris at pH 7.4 for C30 glass	60
4.6	Liquid ³¹ P NMR vs. pH and ³¹ P NMR vs. time in deionized water for CNP45 glasses	62
4.7	Liquid ³¹ P NMR vs. time in deionized water and Tris at pH 7.9 for CNP45 glasses	64
4.8	Liquid ³¹ P NMR vs. time in EDTA for CNP45 glasses and COSY for C40 glass	65
5.1	XRD of cobalt-phosphate glasses	74
5.2	Raman of cobalt-phosphate glasses	76
5.3	Colour of cobalt-phosphate glasses	77
5.4	Normalized UV–vis–NIR.	79
5.5	X-band CW EPR of cobalt-phosphate glasses	81
5.6	EPR sup 1.	82
5.7	EPR-based number of Co(II) atoms per mg vs. CoO mol%	83
5.8	Thermal properties of cobalt-phosphate glasses	84
5.9	DSC and HSM of cobalt-phosphate glasses	86
6.1	³¹ P MAS NMR of the Co0 glass	91

6.2	^{31}P MAS NMR and fwhm of cobalt-phosphate glasses	93
6.3	f_{visible} from ^{31}P MAS NMR vs. x_{Co} for the glasses	98
6.4	Schematic of the radial spheres of influence of Co^{2+} in the glasses	100
6.5	Liquid ^{31}P NMR of the leachate solutions of the glasses in Tris	101
6.6	Liquid ^{31}P NMR vs. time of the leachate solutions of Co5 in EDTA	104
7.1	Schematic of the bioactive glass reaction in body fluid	107
7.2	^{31}P MAS NMR of 45S5-based glasses with variable borate content	110
7.3	^{29}Si MAS NMR of 45S5-based glasses with variable borate content	111
7.4	^{11}B MAS NMR of 45S5-based glasses with variable borate content	112
7.5	^{31}P MAS NMR of Mg/Zn-based 45S5 glasses	114
7.6	^{29}Si MAS NMR of Mg/Zn-based 45S5 glasses	116
7.7	^{31}P MAS NMR of Mg/Sr-based S53P4 glasses	119

List of Schemes

4.1	Hydration and rise of pH for CNP45 glasses	58
4.2	Formation of trimetaphosphate in solution	66
4.3	Mechanism of hydrolysis of trimetaphosphate	67
6.1	Equilibrium of formation of $M(\text{Tris})(\text{P}_{3m})$ and $M(\text{EDTA})(\text{P}_{3m})$	104
6.2	Displacement reaction of P_{3m} for EDTA in $\text{Co}(\text{EDTA})(\text{P}_{3m})$	105

List of tables

1.1	Glossary of common terms in tissue engineering	3
1.2	Composition of various bioactive glasses	4
1.3	Relevant applications of phosphate glasses	6
1.4	Physiological roles of therapeutic ions	8
1.5	Activation energies for dissolution of phosphate glasses	9
1.6	Activation energies for hydrolysis of phosphate glasses	12
1.7	Cobalt exposure sources	15
1.8	Cobalt sources related to systemic health effects	18
1.9	Partitioning of cobalt in blood plasma	19
1.10	Cobalt in biomaterials	23
2.1	NMR Hamiltonian operator	29
2.2	Standard reference substances in NMR	31
2.3	EPR Hamiltonian operator	38
3.1	Nominal glass composition of CNP45 glasses	43
3.2	Nominal glass composition of cobalt-phosphate glasses	44
3.3	³¹ P MAS NMR parameters of glasses	47
4.1	Analysed glass composition from ICP-OES, TGA and ³¹ P MAS NMR of CNP45 glasses	53
4.2	Liquid ³¹ P NMR of standards in Tris at pH 7.4	60
4.3	Liquid ³¹ P NMR of tri- and tetrametaphosphate	61
4.4	Activation energies of hydrolysis of phosphate species	68
5.1	Nominal and analysed composition of cobalt-phosphate glasses	73
5.2	Raman spectral bands of cobalt-phosphate glasses	75
5.3	Thermal properties of cobalt-phosphate glasses	83
6.1	ICP-OES of cobalt-phosphate glasses	90
6.2	³¹ P MAS NMR of cobalt-phosphate glasses	92

7.1	Nominal composition of 45S5-based glasses with variable borate content . . .	109
7.2	Solid-state MAS NMR of 45S5-based glasses with variable borate content . . .	110
7.3	Nominal composition of Mg/Zn-based 45S5 glasses	113
7.4	Solid-state MAS NMR of Mg/Zn-based 45S5 glasses	113
7.5	Nominal composition of Mg/Sr-based S53P4 glasses	118

Nomenclature

Chemical abbreviations

EDTA	ethylenediaminetetraacetate
L	a ligand
M	a metal
P _{3m}	trimetaphosphate anion
Q ⁰	orthophosphate anion
Q ¹	end-group of a polyphosphate anion, pyrophosphate
Q ²	middle-group of a polyphosphate anion, metaphosphate
TMS	tetramethylsilane
Tris	tris(hydroxymethyl)aminomethane

Greek Symbols

δ	chemical shift	ppm
δ^+	electrophilic centre	
δ_{iso}	isotropic chemical shift	ppm
δ_{max}	chemical shift at peak maximum	ppm
γ	gyromagnetic ratio	
μ	magnetic moment	
ω_0	nuclear Larmor frequency	
τ	evolution time	

Other Symbols

B_0	magnetic field	T
C	concentration	
ΔT	processing window, $\Delta T = T_{c,o} - T_g$	
E_a	activation energy	
I	nuclear spin	
L	orbital angular momentum	
m	mass	
\bar{n}	average phosphate chain length	
O/P	oxygen to phosphorus ratio	
r	cation radius	Å
r_0	wipe-out radius	Å
S	electron spin	
T_1	spin-lattice relaxation time	s
T_2	transverse relaxation time	s
$T_{c,o}$	onset point of the crystallisation curve	
T_{fusion}	fusion temperature	
T_g	glass transition temperature	
T_L	liquidus temperature	
$T_{m,i}$	absolute minimum of the melting curve	
T_{si}	sintering temperature	
T_{xf}	ending of the plateau of the glass crystallisation domain	
T_{xi}	starting of the plateau of the glass crystallisation domain	
x	mole fraction	

Z cation charge

Acronyms / Abbreviations

ABMS	anisotropic bulk magnetic susceptibility
BMS	bulk magnetic susceptibility
COSY	correlation spectroscopy
CPMG	Carr–Purcell–Meiboom–Gill pulse sequence
CW	continuous wave
DSC	differential scanning calorimetry
EPR	electron paramagnetic resonance
FID	free induction decay
fwhm	full width at half-maximum
HSM	hot stage microscopy
ICP-OES	inductively coupled plasma - optical emission spectrometry
LFSE	ligand-field stabilization energy
MAS	magic-angle spinning
MS	mass spectrometry
NMR	nuclear magnetic resonance
PCS	pseudo-contact shift
PRE	paramagnetic relaxation enhancement
SA	shift anisotropy
SD	standard deviation
SO	spin-orbit
TGA	thermogravimetric analysis
UV-vis-NIR	ultraviolet-visible-near infrared spectroscopy
ZFS	zero-field splitting

Zusammenfassung

Die Arbeit erfasst ein Studium der Zusammenhänge zwischen Struktur und Lösungsverhalten von Phosphat- und Bioaktivgläsern durch den Einsatz von analytische Techniken wie der Elektron- (engl. EPR), Kern- und paramagnetischen Kernspinresonanzspektroskopie (engl. NMR) in flüssiger und fester Phase.

Das Verstehen der Korrosionsprozesse von Phosphatgläsern ist für deren technologischen Anwendungen wie z.B. eine kontrollierte Abgabe von therapeutische Ionen, antibakterielle Mittel und Tissue Engineering von Bedeutung. Hierbei die Kernspinresonanzuntersuchungen liefern dabei Einblicke über die Rolle von Kationen in dem Mechanismus der Hydrolyse von Phosphatgläsern. Die Arbeit wurde bereits in einem Aufsatz mit dem Titel "*Unravelling the dissolution mechanism of polyphosphate glasses by ^{31}P NMR spectroscopy: ligand competition and reactivity of intermediate complexes*" veröffentlicht.

Der Einbau von Kobalt in Gläser ist ein neuer Ansatz zur Überwindung des bislang noch nicht gelösten Problems der Vaskularisierung im Tissue Engineering, bei dem die Bildung neuer Blutgefäße stimuliert wird. Derartige Gläser spielen auch unter anderem als Halbleiter, als optische Geräte und als Zustandslaser eine Rolle. In dieser Arbeit konnte gezeigt werden, dass die strukturellen Eigenschaften (wie z.B. die thermischen Eigenschaften) von kobalthaltigen Phosphatgläsern mit gleichbleibender Basizität von der Koordinationzahl von Co^{2+} bestimmt werden. Dies ist der erste Teil der Studie über das Glassystem und befindet sich unter dem Titel "*Structural role and coordination environment of cobalt in $45\text{P}_2\text{O}_5\text{--CaO--Na}_2\text{O}$ phosphate glasses: Thermal properties, Raman, UV-vis-NIR and EPR spectroscopy*" in der Veröffentlichungsphase.

Der zweite Teil der Studie zu kobalthaltigen Phosphatgläsern ist unter dem Titel " *Co^{2+} as an internal paramagnetic ^{31}P NMR probe for structural analysis of cobalt-phosphate glasses in the solid-state and leachate solutions*" ebenfalls in der Veröffentlichungsphase. In dieser Arbeit wird ein neuer Ansatz zur Untersuchung sowohl zur Glasstruktur als auch zum Löslichkeitsmechanismus von Phosphatgläsern basierend auf paramagnetischen Effekten vorgestellt. Dementsprechend korrelieren Eigenschaften wie die Spin-Bahn-Kopplung (engl.

SO coupling), die Nullfeldaufspaltung (engl. ZFS) und die Symmetrie der Co^{2+} -Umgebung mit der paramagnetischen Verschiebung, der paramagnetischen Relaxations-Verstärkung (engl. PRE) und der Verbreiterung der Resonanz. Das wiederum erlaubt die Einschätzung der Verteilung von Co^{2+} Ionen im Glasnetzwerk. Darüber hinaus ermöglicht es die Verfolgung der Struktur- und Konformationsdynamik von Phosphatkomplexen in Lösung, einschließlich Konformationsänderungen, nach der Charakterisierung von Ligandenbindung unter verschiedenen Bedingungen wie z.B. gepufferte wässrige Lösungen (Tris, EDTA).

Die Zusammensetzung von typischen Biogläsern weist Nachteile wie eine Tendenz zur Kristallisation und unvollständigen Abbau *in vivo* auf. Ein Lösungsansatz beider Probleme kann der Einbau von Ionen wie B^{3+} , Mg^{2+} , Zn^{2+} und Sr^{2+} in die Glasmatrix sein. Die vorliegende Studie präsentiert eine Ansammlung von ^{31}P , ^{29}Si und ^{11}B -Festkörper-MAS-NMR, die in Beziehung zu der potenziellen Koordinationszahl von verschiedener Metallkationen korreliert wurden, die Ca^{2+} auf bekannten Biogläsern ersetzen. Deshalb wurde im Rahmen einer gemeinsamen Arbeit eine Studie NMR-Analyse an Mg/Sr-basierten bioaktiven Gläsern S53P4 eingesetzt und unter dem Titel "*Structure and in vitro dissolution of Mg and Sr containing borosilicate bioactive glasses for bone tissue engineering*" veröffentlicht.

Zusammenfassend lässt sich sagen, dass diese Arbeit eine neue Methode zur Untersuchung der Struktur und des Lösungsverhaltens von Phosphatgläsern mit biomedizinischem Potential durch die Nutzung von paramagnetischen Effekten auf NMR vorstellt. Es konnte gezeigt werden, dass strukturelle Eigenschaften durch die symmetrische Umgebung der paramagnetischen Ionen in diesen Gläsern bestimmt werden. Zukünftige Forschungsvorhaben könnten sich mit der Entwicklung neuer fortschrittlicher paramagnetischer NMR-Techniken für die Strukturanalyse von Gläsern, wie z. B. ^{17}O -DNP auf Metallionenbasis, auseinandersetzen.

Abstract

The doctoral thesis comprises a study of the relationships between structure and dissolution behaviour of phosphate and bioactive glasses by employing analytical techniques such as electron paramagnetic resonance (EPR), liquid NMR, solid-state MAS NMR and paramagnetic NMR spectroscopy, among others.

The understanding of the corrosion processes of phosphate glasses is important for their technological applications, e.g. drug delivery, antibacterials and tissue engineering. In the present work, the NMR findings provided insights about the role of cations on the mechanism of hydrolysis of phosphate glasses. The work has already been published under the title: *"Unravelling the dissolution mechanism of polyphosphate glasses by ^{31}P NMR spectroscopy: ligand competition and reactivity of intermediate complexes"*.

The incorporation of cobalt into glasses is a new approach to overcome the vascularization limitation in tissue engineering by stimulating the production of blood vessels. These glasses are also interesting as semiconductors, optical devices and solid-state lasers, among others. This work shows that structural (i.e. thermal) properties of cobalt phosphate glasses with constant basicity are dictated by the coordination number of Co^{2+} sites. This is the first part of the study on the glass system and it is in publication process under the title: *"Structural role and coordination environment of cobalt in $45\text{P}_2\text{O}_5\text{--CaO--Na}_2\text{O}$ phosphate glasses: I, Thermal properties, Raman, UV-vis-NIR and EPR spectroscopy"*.

The second part of the study on cobalt phosphate glasses is in publication process under the title: *" Co^{2+} as an internal paramagnetic ^{31}P NMR probe for structural analysis of cobalt-phosphate glasses in the solid-state and leachate solutions"*. This work presents a new approach to investigate the mechanism of dissolution of phosphate glasses based on the paramagnetic effects. Accordingly, features such as the spin-orbit (SO) coupling, zero-field splitting (ZFS) and symmetry of Co^{2+} sites are correlated to the paramagnetic shift, paramagnetic relaxation enhancement (PRE) and broadening effects on the spectra. That allows the assessment of the distribution of Co^{2+} ions in the glass network. Additionally, it enables monitoring structural dynamics of phosphate complexes in solution, including conformational changes, upon

ligand binding recognition under different conditions, i.e. buffer aqueous solutions (Tris, EDTA).

The composition of typical bioglasses exhibits drawbacks such as crystallisation tendency and incomplete degradation *in vivo*. An approach to solve both problems may be the incorporation of ions such as B^{3+} , Mg^{2+} , Zn^{2+} and Sr^{2+} into the glass matrix. The present work gathers a collection of ^{31}P , ^{29}Si and ^{11}B solid-state MAS NMR correlated to the potential coordination number of different metal cations substituting Ca^{2+} on known bioglasses. Thereby, in the frame of a collaborative work, the NMR analysis on Mg/Sr-based S53P4 bioactive glasses has already been published under the title "*Structure and in vitro dissolution of Mg and Sr containing borosilicate bioactive glasses for bone tissue engineering*".

In summary, this work suggests a new method to study the structure and mechanism of dissolution of phosphate glasses with biomedical potential by exploiting the paramagnetic effects on NMR. It has been demonstrated that structural properties are dictated by the symmetry environment of the paramagnetic ions in these glasses. The outlook on future research would be the development of new advanced paramagnetic NMR techniques for structural analysis of glasses such as metal-ion-based ^{17}O DNP.

Chapter 1

Introduction

The doctoral thesis is divided into VIII chapters and comprises a structural study on the liquid and solid-state of phosphate and bioactive glasses by employing new analytical approaches such as paramagnetic NMR. The aim of the study is to find correlations between property and solubility trends on glasses for a variety of potential technological applications, including soft and hard tissue engineering.

Chapter I is the introduction which in turn is divided into six sections: (i) bioglasses, (ii) phosphate glasses, (iii) dissolution of phosphate glasses, (iv) cobalt, (v) tissue engineering and (vi) paramagnetic NMR. In each section a survey of the state-of-the-art of the field is performed in order to cover the interdisciplinary aspects that are involved in the research. Chapter II comprises the theoretical framework relevant to the discussion of the research problem. The concepts include: diffusion, solubility, hydration enthalpy, transition state and paramagnetic effects in NMR, among others. Chapter III corresponds to the experimental section in which a detailed description of the analytical procedures is presented.

Chapter IV comprises the first part of the results, the work has already been published under the title: *"Unravelling the dissolution mechanism of polyphosphate glasses by ^{31}P NMR spectroscopy: ligand competition and reactivity of intermediate complexes"* [1]. Herein, the NMR findings provided insights about the role of cations on the mechanism of hydrolysis of phosphate glasses.

Chapters V comprises the second part of the results, the work is in publication process under the title: *"Structural role and coordination environment of cobalt in $45\text{P}_2\text{O}_5\text{-CaO-Na}_2\text{O}$ phosphate glasses: Thermal properties, Raman, UV-vis-NIR and EPR spectroscopy"*. Herein the results showed that the structural properties of cobalt phosphate glasses with constant basicity are dictated by the coordination number of Co^{2+} .

Chapters VI comprises the third part of the results, the work is in publication process under the title: *Co²⁺ as an internal paramagnetic ³¹P NMR probe for structural analysis of cobalt-phosphate glasses in the solid-state and leachate solutions*. Herein the work presents a new approach to investigate the mechanism of dissolution of phosphate glasses based on the paramagnetic effects on the liquid and solid-state ³¹P NMR spectra.

Chapters VII comprises the fourth part of the results, some of the work has already been published under the title: *"Structure and in vitro dissolution of Mg and Sr containing borosilicate bioactive glasses for bone tissue engineering"* [2]. Herein a combination of ³¹P, ²⁹Si and ¹¹B solid-state MAS NMR spectra are correlated to the potential coordination number of different metal cations substituting Ca²⁺ on known bioactive glasses. Finally, the conclusions of the whole doctoral thesis are presented in chapter VIII.

Table 1.1: Glossary of common terms in tissue engineering.

Term	Definition
Bioactive	a material designed to induce specific biological activity [3]. A material that undergoes specific surface reactions, after immersion in a serum-like solution, leading to the formation of bone-like hydroxyapatite [4].
Biodegradation	transformation of a substance into new compounds through chemical or biochemical reactions or the action of microorganisms [5].
Osteogenesis	the process of bone growth and regeneration [6].
Angiogenesis	the process of developing new blood vessels. Newly formed blood vessels are involved in nutrient supply and transport of macromolecules during bone repair and regeneration [6].
Osteoconductivity	biomaterial's property to serve as template guiding bone growth onto or throughout [7].
Osteoinductivity	biomaterial's property to induce <i>de novo</i> bone formation [7].
Scaffold	a three-dimensional temporary structure with high porosity and pore interconnectivity that allows cells and extra cellular matrices to interact, and provides the mechanical support for growing and tissue forming cells [6, 8, 9].
TCP	tricalcium phosphate
HA	hydroxyapatite
HCA	carbonate substituted hydroxyapatite-like, similar to the mineral constituent of bone [9].
Osteoblast	mononuclear cells responsible for the production and mineralization of the bone matrix [6].
Osteoclast	multinucleated bone cells associated with the breakdown and resorption of bone tissue through enzymatic action. [6].
Hypoxia	low oxygen concentration
VEGF	vascular endothelial growth factor, induces angiogenesis [6].
TGF- β	transforming growth factor- β , a multifunctional cytokine that promotes angiogenesis. [10].
MGP	matrix GLA protein, calcification inhibitor in cartilage and vasculature [8].
HIF	hypoxia-inducible factor
RBC	red blood cell
MoM	metal-on-metal orthopedic prosthetics, i.e. CoCr alloy [11, 12].

1.1 Bioglasses

Specific compositions of borate, phosphate, silicate and borosilicate glasses (Table 1.2) have demonstrated to be suitable for hard and soft tissue engineering applications owing to their bioactive, resorbable and mechanical properties [8, 13]. The bioactive properties of such glasses are related to their dissolution behaviour. For instance, soluble silica and calcium ions released from 45S5 Bioglass[®] [14], have the ability to stimulate osteoblasts to produce

bone matrix [15]. Bioactive glasses can be classified as "third generation" biomaterials (Fig. 1.1), since their role is not only limited to provide temporary support, but to activate genes that stimulate regeneration of living tissues [15].

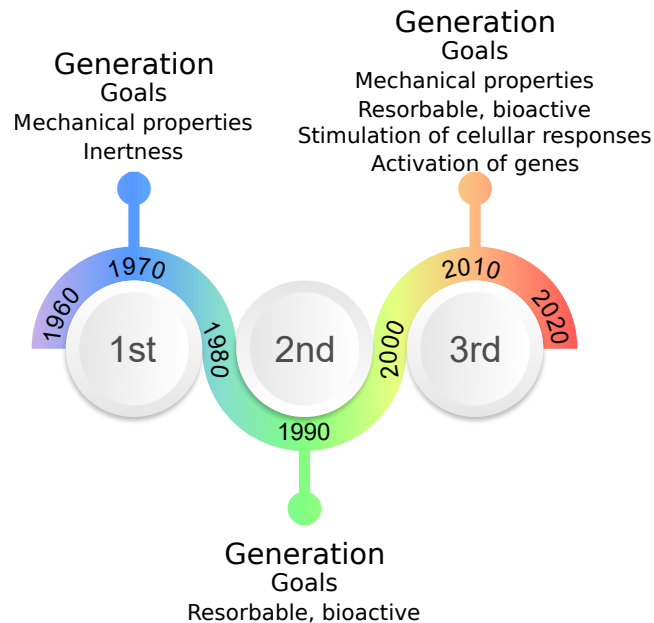


Fig. 1.1: Generations of biomaterials [15].

Table 1.2: Composition of various bioactive glasses (mol%).

Glass	P ₂ O ₅	B ₂ O ₃	SiO ₂	CaO	Na ₂ O	MgO	K ₂ O	SrO	Ref.
45S5	2.6		46.1	26.9	24.4				[14]
13-93	1.7		54.6	22.1	6.0	7.7	7.9		[16]
6P53B	2.5		51.9	19.0	9.8	15.0	1.8		[17]
58S	4		60	36					[18]
70S30C			70	30					[19]
B _{12.5} Mg ₅ Sr ₁₀	1.72	6.73	47.12	6.77	22.66	5		10	[2]
13-93B1	2	18	36	22	6	8	8		[20]
13-93B3	2	54		22	6	8	8		[20]
P ₅₀ C ₃₅ N ₁₅	50			35	15				[21]

1.2 Phosphate glasses

Phosphate glasses are able to form homogeneous systems with inorganic ions, which subsequently functionalize the glasses for different technological applications (Fig. 1.2). They are interesting matrices owing to physicochemical properties such as high thermal expansion coefficients, low transition and melting temperatures, and high UV transparency,

among others. Nevertheless, phosphate glasses have also drawbacks, i.e., low durability, hygroscopic nature and narrow processing windows, $\Delta T = T_{c,o} - T_g$, which are challenging for most applications [22, 23]. Despite it, the versatility of phosphate glasses to tailor properties as a function of composition, provide them a bright potential for a variety of applications (Table 1.3).

1.2.1 Properties and applications

Water softener, fertilizers and storage of wastes

In general, phosphate glasses have been known to have poorer durability as their silicate and borosilicate pairs. Yet, their solubility depends strongly upon composition, thus, phosphate glasses exhibit a wide spectrum of dissolution rates ($10^{-4} - 10^{-9} \text{ g}/(\text{cm}^2 \cdot \text{min})$) [24]. The most common use of phosphate glasses relates to the high solubility, i.e. NaPO_3 , as water softener [23]. For this application, the ability of phosphate species to prevent precipitation, and to redissolve precipitates of alkaline rare earth metals is exploited [25]. Solubility of

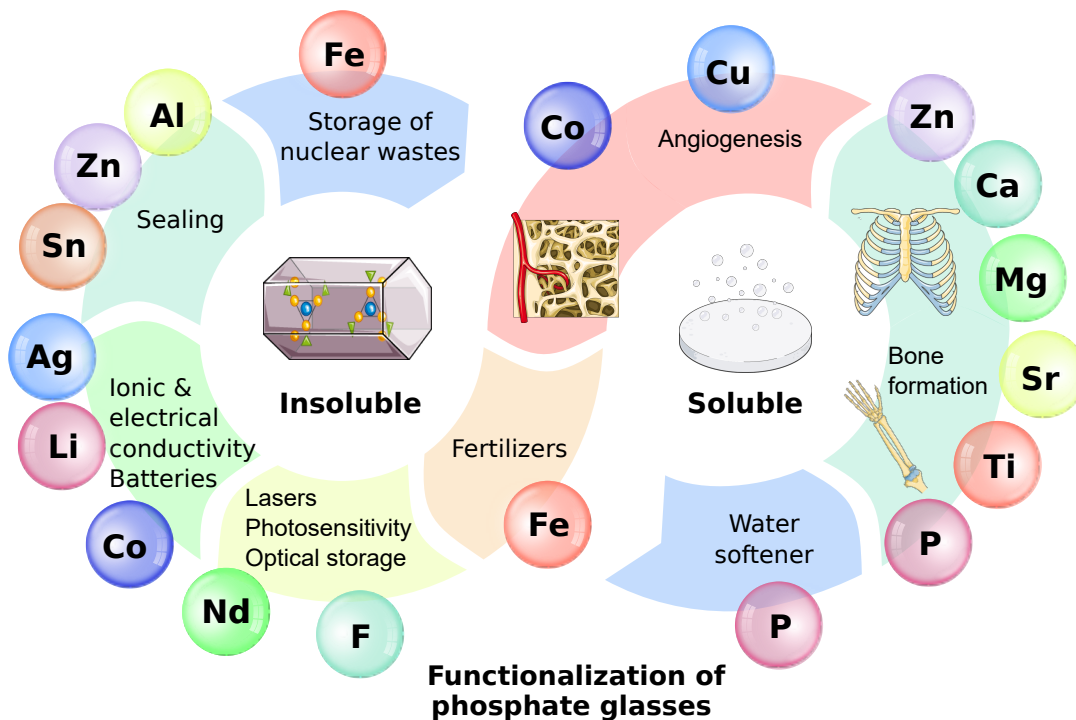


Fig. 1.2: Functionalization of phosphate glasses *via* relevant inorganic ions for soluble and insoluble materials applications.

phosphate glasses is also desired for controlled release of ions in applications such as eco-fertilizers [26, 27] and biomedicine, the latter being discussed in section 1.3 (Dissolution of phosphate glasses). Conversely, high durable glasses are required for nuclear waste entrapment. Thereby, iron phosphate glasses have excellent durability comparable and

Table 1.3: Relevant applications of phosphate glasses functionalized with inorganic ions.

Application	Ion	System / Role
Water softener	P	NaPO ₃ avoids deposits of calcium [31].
Fertilizers	P	K ₂ O–MgO–CaO–P ₂ O ₅ –SiO ₂ where macroelements such as P, Ca, Mg, K are released [26].
	Fe	SiO ₂ –P ₂ O ₅ –K ₂ O–MgO–CaO–Fe ₂ O ₃ where iron plays an important role as a microelement [27].
Sealing	Zn	SnO–ZnO–P ₂ O ₅ system for commercial sealing [31].
	Sn	Li ₂ O–SnO–P ₂ O ₅ for soldering electronic materials [31, 32].
	Al	Na ₂ O–Al ₂ O ₃ –P ₂ O ₅ for hermetically sealing aluminium alloys [33].
Photonics	Yb	Yb:fluoride phosphate glass femtosecond laser [34]
	Eu	Eu:fluoride phosphate glass exhibits photosensitivity [35].
	Nd	Nd-doped phosphate laser glasses in use on major multi-kilojoule lasers [36].
Solid electrolytes	Li	LiI–LiPO ₃ superionic glasses, ionic conductivity of about 10 ⁻⁶ S/cm [37] and LiPON electrolyte for microbatteries [23].
	Ag	AgI–AgPO ₃ superionic glasses, ionic conductivity of about 10 ⁻² S/cm [37].
	Na	Na ₂ O–Na ₂ SO ₄ –P ₂ O ₅ electrical conductivity ~ 100–fold higher than Na ₂ O–P ₂ O ₅ [38].
Semiconductors	Co	CoO–P ₂ O ₅ , DC and AC conductivities reported [39, 40].
Storage of wastes	Fe	FeO–Fe ₂ O ₃ –P ₂ O ₅ glassy wasteforms have a corrosion rate lower than that of comparable borosilicate glasses [28–30].

often superior to silicate and borosilicate glasses while conserving relative low melting points. Phosphate glasses can dissolve high concentrations of oxides and both Fe²⁺ and Fe³⁺ present in the structure contribute to the dielectric constant [28–30].

Photonics and sealing

Phosphate and fluoride phosphate glasses have been used for photonic applications such as lasers, photosensitivity, amplifiers, Faraday rotators and optical storage. As a consequence of their high UV transparency, low linear and non-linear refractive index, low melting temperature, low viscosity, low stress optic coefficient, including the high solubility of rare earth ions [35]. On the other hand, the criteria for a solder glass, for sealing of ordinary glasses, may be fulfilled by phosphate glasses which include: low viscosity, low softening temperature, delayed crystallization, high durability, high dielectric strength and thermal expansion close to the work-piece. The latter is particularly important since a wrong design is usually associated with mismatch in coefficient of thermal expansion, produces tensile stresses leading ultimately to cracks. High durability is required and for that purpose trivalent cations such as Al³⁺ have been added [31–33].

Solid electrolytes and semiconductors

Solid-state ionic materials are attractive alternatives to conventional liquid flammable electrolytes in batteries, which involve risk of leakage and combustion. Therefore, phosphate glasses as solid electrolytes have been investigated owing to the potentially simpler mechanism of conduction that a glassy phase may involve compared to polycrystalline materials. Furthermore, the conductivity of phosphate glasses may be tuned by compositional variations [23, 37]. On the other hand, phosphate glasses can form homogeneous systems with transition metals which exist in different valency states. It allows the movement of carriers between valency states to produce electrical conductivity, important for semiconductor devices [39, 40].

1.2.2 Structural characterization by solid state NMR

Phosphate glasses are comprised of a random network of phosphate tetrahedra, whose degree of polymerization is dictated by the composition [22, 41]. Their structural unit is PO_4^{3-} , which can attach to maximum three neighbouring groups [42]. The Lewis' description involves a localized double bond, leaving the P atom with more than eight electrons, hypervalent. Nevertheless, it has been demonstrated experimentally and theoretically that d-orbitals do not contribute to the bonding in these systems and hence hypervalent structures do not represent the bonding in phosphates. Actually, X-ray experiments on crystal structures have shown that delocalization of the "extra" electron pair occurs. Thereby, hyperconjugative interactions increase the valence of the phosphorus atom. However, this is compensated by P–O bond polarization [43].

The tetrahedral sites are characterized by the number of bridging oxygens (BO) in the phosphate group. The sites are defined in terms of Q^n where n is the number of BO per tetrahedron, thus, Q^3 (BO = 3), Q^2 (BO = 2), Q^1 (BO = 1) and Q^0 (BO = 0). ^{31}P MAS NMR is a sensitive short-range probe for the qualitative and quantitative analysis of Q^n distribution in phosphate glasses [44–49], since $Q^n \rightarrow Q^{n-1}$ increases the isotropic chemical shift by around 15–20 ppm [50]. The polymerization degree defines the type of network, thereby, ^{31}P MAS NMR has shown the Q^n distribution as follows: ultraphosphates (Q^3 and Q^2 tetrahedra), metaphosphates (Q^2 tetrahedra), polyphosphates (Q^2 and Q^1 tetrahedra) and orthophosphate (Q^0 tetrahedron). The polymerization degree of the glass network is inversely proportional to the content of modifiers (M^{n+}), i.e. Na^+ , Ca^{2+} , etc; whose role is to charge balance the phosphate anions [22]. Empirical relationships have correlated the ^{31}P chemical shift to the field strength of the next nearest-neighbours, cations, namely the ^{31}P shielding increases proportional to the average electron density on the P–O bonds [45, 51,

52]. Additionally, novel 2D ^{31}P MAS NMR experiments have been exploited in order to get insights into the medium-range structure of phosphate glasses [49, 50, 53].

1.3 Dissolution of phosphate glasses

Table 1.4: Physiological roles of therapeutic ions (see Glossary, Table 1.1).

Role	Ion	Physiological role
Angiogenesis	Cu	induces VEGF expression and wound healing [54, 55].
	Co	induces hypoxia on the cellular level by stabilizing HIF-1 α , which subsequently promotes VEGF expression [10, 56–58].
Osteogenesis	Li	activates the β -catenin signalling pathway, which positively regulate osteoblasts [59].
	Zn	contributes to bone formation by promoting osteoblast differentiation and suppressing osteoclastic resorption [55, 60, 61].
	Sr	promotes bone healing and bone fracture repair by stimulating osteoblasts and inhibiting osteoclasts [55, 62].
	Mn	promotes osteoblast differentiation and mineralization [63].
	Ti	its alloys are known to be supportive of osseointegration, the exact role remains unclear, it may elicit a favourable cell response [55].
Angiogenesis Osteogenesis	B	contributes to the upregulation of TGF- β and VEGF [64]. Dietary boron stimulates bone formation [8].
	Si	stimulates VEGF expression [65], may induce additional dose-dependent effects on bone and cartilage cells [66].
	P	stimulates pro-angiogenic VEGF [10]. Phosphate and matrix GLA protein (MGP) are key regulators of bone formation [67].
	Ca	stimulates pro-angiogenic VEGF [10]. Favours osteoblast proliferation, differentiation and extracellular matrix mineralization [8].
	Mg	enhances the mitogenic response to angiogenic factors [10, 68]. Stimulates new bone formation [8, 55].
Antibacterial	Ag	microbistatic effects against <i>Staphylococcus aureus</i> , <i>Escherichia coli</i> , <i>Bacillus cereus</i> , among others [69].
	Cu	antibacterial activity against <i>Staphylococcus aureus</i> and <i>Staphylococcus epidermidis</i> [70, 71].
	Co	antimicrobial activity against <i>Staphylococcus aureus</i> and <i>Candida albicans</i> when in direct contact [72].
	Sn	used in dentifrices because of its antimicrobial properties [73].
	F	fluorides are effective against dental caries [73].

Understanding the corrosion processes of phosphate glasses is important in general for their technological applications. Thereby, the durability should tailor the specific function of

a material. For instance, high durable glasses are required for nuclear waste entrapment [30, 74], while soluble glasses are desired as vehicles for controlled delivery of therapeutic ions in bioapplications [55], as seen in Table 1.4. Phosphate glasses are attractive matrices, since through compositional and structural modifications the solubility can vary orders of magnitude, offering a wide spectrum of tailored-solubility for specific applications [24].

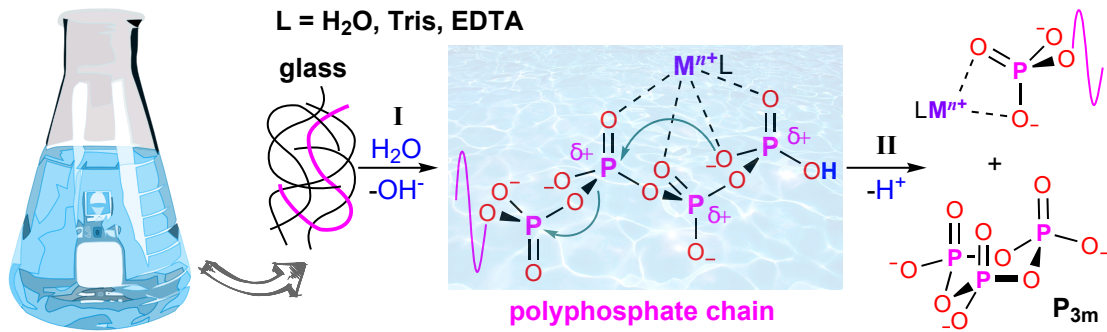


Fig. 1.3: Dissolution of polyphosphate glasses [1]: **I.** Hydration process associated to initial rise of pH owing to the basic character of Q¹ moieties of phosphate chains (highlighted in fuchsia) in aqueous solution. Congruent dissolution, concomitant release of phosphate chains and cations (Mⁿ⁺) from the glass into the aqueous solution. **II.** Degradation and hydrolysis processes associated to ring formation, i.e., trimetaphosphate (P_{3m}) [75–77], which is a strong acid [78–80]; and its breakage into tri-, pyro- and orthophosphate (weak acids), respectively. The reaction is catalysed by metal cations Mⁿ⁺ complexed in a polydentate manner with phosphate species and another ligand (L: H₂O, Tris, EDTA, etc) depending on the coordination number (CN) of Mⁿ⁺ and steric effects. (For the sake of simplicity hypervalent Lewis pictures are used, however, they do not aim to represent the bonding situation of P).

Table 1.5: A selection of activation energies of dissolution (E_a) of Na₂O–CaO–P₂O₅ glasses.

Glass	E_a (kJ/mol)	O/P	Av. chain length, \bar{n}	Ref.
26.2Na ₂ O–24CaO–0.1Al ₂ O ₃ –49.7P ₂ O ₅	83	3.01	~ 100	[81]
25Na ₂ O–25CaO–50P ₂ O ₅	79	3	meta	[82]
30Na ₂ O–20CaO–50P ₂ O ₅	67	3	meta	[24]
[M ₂ O+MO]–45P ₂ O ₅	39	3.1	9	[83]
31Na ₂ O–30CaO–3Al ₂ O ₃ –36P ₂ O ₅	24	3.46	~ 2	[81]

1.3.1 The two-stage dissolution model

The first step involved in the dissolution of phosphate glasses has been described as the detachment of ions from the solid surface to form hydrated species at the solid-liquid interface [24, 84]. The transport of water molecules into the glass structure may be rate determining,

a diffusion-controlled process. The hydration process occurs simultaneously with diffusion of water, leading to a reduced diffusion coefficient due to the reaction [85]. The second stage has been assigned as the transfer of hydrated ions from the solid-liquid interface to the bulk solution [24], which is also a mass transport process (Fig. 1.3I). Both the hydration and mass transport to the bulk solution can control the dissolution rates [85]. By correlating the E_a of dissolution (Table 1.5) with the rates of dissolution of phosphate glasses, it has been concluded that the kinetics at early periods are controlled by the first stage, namely the hydration process. Degradation processes taking place in solution after the second stage (Fig. 1.3II) do not control the kinetics at early periods, since the higher E_a values (Table 1.6) would lead to lower dissolution rates [24].

According to pH-stat titration data, the diffusion of water into the glass surface is diffusion controlled and corresponds to the first stage of glass dissolution [24]. In this process, the release of the cumulative amount of glass shows a direct proportionality with $t^{1/2}$ [24, 81, 86]. The description is based on a pseudo-steady state model in which the concentration gradient, $\Delta C = C_s - C_o$, remains relatively constant (with C_s and C_o as the saturation and bulk solution concentrations). It applies for highly diluted solutions and particles approximately log-normally distributed [87, 88]. The length of the first stage has been reported to be proportional to the durability of the glass [30, 81]. Therefore, for non-diluted solutions or longer periods, the dissolution rates do not follow $t^{1/2}$ dependency, but linear kinetics have been reported [24, 30, 81, 89]. Furthermore, penetration of water into the glass may not be affected by convection [82].

This two-stage dissolution model has been used to interpret that intact phosphate chains from the glass surface are hydrated and subsequently transported into the bulk solution leading to congruent dissolution [24, 30, 81]. Nevertheless, not only congruent dissolution, but also selective ion leaching has been reported for phosphate glass systems [30].

1.3.2 Durability

The hydration process involves the cleavage of bonds through water and the formation of hydrated species. Therefore, the process can be understood by considering the network and hydration enthalpies. The network enthalpy is analogous to the lattice enthalpy in crystals. Accordingly, it follows reasonably the empirical trend that states that compounds with ions with widely different radii are soluble in water. The hydration enthalpy is the sum of individual ion contributions and it is inversely proportional to the radius of the ion. Thus an exothermic process takes place when the hydration enthalpy is larger than the network enthalpy. However, both values depend on the radius of the ions in a more or less opposite

manner, making the outcome not obvious at a first glance. Additionally, the entropy change has to be taken into account since the solubility process is governed by the standard reaction Gibbs energy. Thereby, a decrease in entropy is expected owing to the ordering of water molecules involved by the hydrated ions [90].

The lattice enthalpy is inversely proportional to the distance between the centre of the corresponding ions, thus, a good orbital overlap leads to strong bonds. In this regard, high lattice enthalpies or networks enthalpies are partially associated with lower solubilities. Pearson introduced the concept of "hard" and "soft" acids and bases; which states that hard acids tend to bind hard bases and soft bases tend to bind soft bases [91]. The phosphate anion PO_4^{3-} is a hard base and the basicity of polyphosphates is inversely proportional to the chain length [81, 92]. The decrease in solubility for shorter phosphate glasses (higher O/P ratio) may be related to the higher hardness of shorter phosphate anions associated to larger network enthalpies [30, 74]. Interestingly, despite the lower solubility, a decrease in the activation energy for the dissolution of shorter polyphosphates has been reported (Table 1.5).

PO_4^{3-} binds stronger to hard acids, within the periodic table the hardness decreases vertically with increasing ionic radius, e.g. $\text{Li}^+ > \text{Na}^+ > \text{K}^+$; and horizontally from left to right owing to both decreasing radius and increasing charge, e.g. $\text{Al}^{3+} > \text{Mg}^{2+} > \text{Na}^+$ [90]. That accounts for the experimental evidence where the chemical durability of phosphate glasses is proportional to the field strength of the cations in the glass network [21, 89]. Likewise anions with high charge such as PO_4^{3-} lead also to high network enthalpies [90]. On the other hand, higher coordination numbers associated to the cation size, provide them the potential to cross-link to more phosphate tetrahedra. Such cross-links together with strong bonds have been correlated with higher durability [24]. For instance, Ca^{2+} binds together more fragments of the phosphate glass network than Na^+ [93].

The hydration enthalpy depends on the ion-dipole interaction between the cation and the polar water molecule. Such enthalpy is proportional to the charge density, namely cations with small size, e.g. $\text{Li}^+ > \text{Na}^+ > \text{K}^+$ and high charge, $\text{Al}^{3+} > \text{Mg}^{2+} > \text{Na}^+$. Thereby, the solubility follows the same trend as the lattice (network) enthalpy, as mentioned above. The solubility process depends on both the hydration and network enthalpies or in other words the enthalpy of the products minus the reagents. In general, for ions with high charge density such as Ca^{2+} and PO_4^{3-} , the network enthalpies outweigh the hydration enthalpy and become the deciding factor in the dissolution behaviour.

1.3.3 Aqueous degradation

Table 1.6: A selection of activation energies (E_a) of hydrolysis of phosphates (two-stage degradation: ring closure into trimetaphosphate^a and hydrolysis^b).

Glass	E_a (kJ/mol) / pH				O/P	Av. chain length, \bar{n}	Ref.
	1	4	7	10 – 12			
Pyrophosphate	95	114	125	167	3.5	2	[94]
Tripolyphosphate	96	104	109	127	3.33	3	[94]
Tetrapolyphosphate		115	106	106	3.25	4	[95]
Pentapolyphosphate		91	97	111	3.2	5	[95]
Hexapolyphosphate		85	84	115	3.17	6	[95]
Polyphosphate			98 ^a		3.02	~54	[96]
			86 ^b		3	3	[96]
Trimetaphosphate	87			115	3	3	[97]
Tetrametaphosphate	99			136	3	4	[97]

The degradation of phosphate glasses occurs after the second step of dissolution (Fig. 1.3II), thus the transport of entire hydrated phosphate species into the bulk solution [24]. It is known that only rings and chains (Q^1 and Q^2 moieties) can exist in aqueous solution, i.e. no branching units [42]. Long chain polyphosphates degrade in aqueous solution in two stages. The first stage consists of the formation of rings, mainly trimetaphosphate (P_{3m}) [1, 75–77]. While the second stage consists of the hydrolysis of rings (P_{3m}) into small polyphosphates which subsequently hydrolyze stepwise at the ends into ultimately orthophosphate [1, 96, 98]. The formation of trimetaphosphate suggests folding of the chain into a helix, where the three member phosphate tetrahedra seems to be favoured [96, 99].

Metal cations (M^{n+}) accelerate the degradation of phosphate glasses in solution, in the following order $K^+ < Na^+ < Li^+ < Ba^{2+} < Sr^{2+} < Ca^{2+} < Mg^{2+} < Al^{3+}$ [98]. The catalytic effect of metal cations is proportional to their field strength and is related to their capacity to complex with phosphate species [78]. Therefore, the mechanism of degradation may involve metal cations coordinating phosphate species (Fig. 1.3), whose role may be to increase the electrophilic character of the phosphorus atom for a subsequent nucleophilic attack [1]. The latter process produces ring closure in case the nucleophile is an intramolecular $P-O^-$ group, or hydrolysis in case the nucleophile is water [77]. Steric hindrance increases the barrier of the transition state which involves a 5-fold coordinated phosphorus atom [100, 101]. Accordingly, an ending group, $Q^{1''}$, is more favoured as nucleophile or electrophile than a more bulky middle group, $Q^{2''}$ [76, 100]. On the other hand, the catalytic effect may get greatly reduced in case stronger complexing agents such as EDTA are in the solution

[29, 30], since they compete for metal cations. The two processes related to the aqueous degradation of polyphosphates, namely ring formation and hydrolysis follow first order kinetics and depend on pH, temperature, concentration of reactant and ionic environment. [77, 94, 96, 102].

pH

Branched rings or chains of PO_4^{3-} (ultraphosphates) cannot exist in solution owing to the absence of stabilization by resonance [42]. Since taking into account that hydrogen and phosphorus exhibit the same electronegativity using the Pauling scale [103], protons corresponding to middle groups (Q^2) are strongly acidic. Therefore, the weak protons are provided exclusively by the ending groups (Q^1) [104, 105], where the basicity decreases from $4 \cdot 10^{-10}$ [106] to a value close to 10^{-8} as the polyphosphate chain is lengthened [42]. From the titration curve of trimetaphosphate is also evident the strong acidic character of its middle groups in aqueous solution. Potentiometric measurements have shown that only one hydrogen is partially associated in trimetaphosphate and corresponds to $pK_3 = 0.65 \pm 0.10$ at 25°C [79]. Thereby, computer simulations have provided a relatively higher value, $pK_3 = 2.05$ [107].

Published titration curves [42] show the increase in the ratio of weakly acid related to strongly acid hydrogens as the polymerization decreases, which is in agreement with the weak acidic character of the ending groups in polyphosphate chains. The protonation of Q^1 sites of polyphosphate anions is expected to cause a rise in the pH in static dissolution experiments at early periods of time [81]. Congruent dissolution may take place only when the protonation of Q^1 sites occurs after the second stage of dissolution, thus after transport of ions into the bulk solution (Fig. 1.3I) [1]. On the other hand, at prolonged time periods weak acidic phosphate species, i.g. orthophosphate, accumulate as a product of hydrolysis. Such weak acids, added to protons released as a result of ring formation decrease the pH monotonically until a buffer solution is achieved (Fig. 1.3II) [1].

The activation energies (E_a) of the dissolution processes depend on composition. They are noticeably lower (24 – 84 KJ/mol), Table 1.5, compared to the activation energies related to the degradation processes in aqueous solution (84 – 167 KJ/mol), Table 1.6, which depend also on composition and substantially on pH. The aqueous degradation of phosphate glasses is catalysed by acids, lower E_a values [94, 102, 108], owing to the improvement of the leaving group stability, involved in the transition state of a $\text{S}_{\text{N}}2$ -type reaction [1, 100]. For the same reason the degradation may not be catalysed in basic media, higher E_a values [24, 94]. The effect of cations depends on the pH, namely it retards the hydrolysis in acidic media and conversely accelerate it in neutral and basic media [109, 110].

1.4 Cobalt

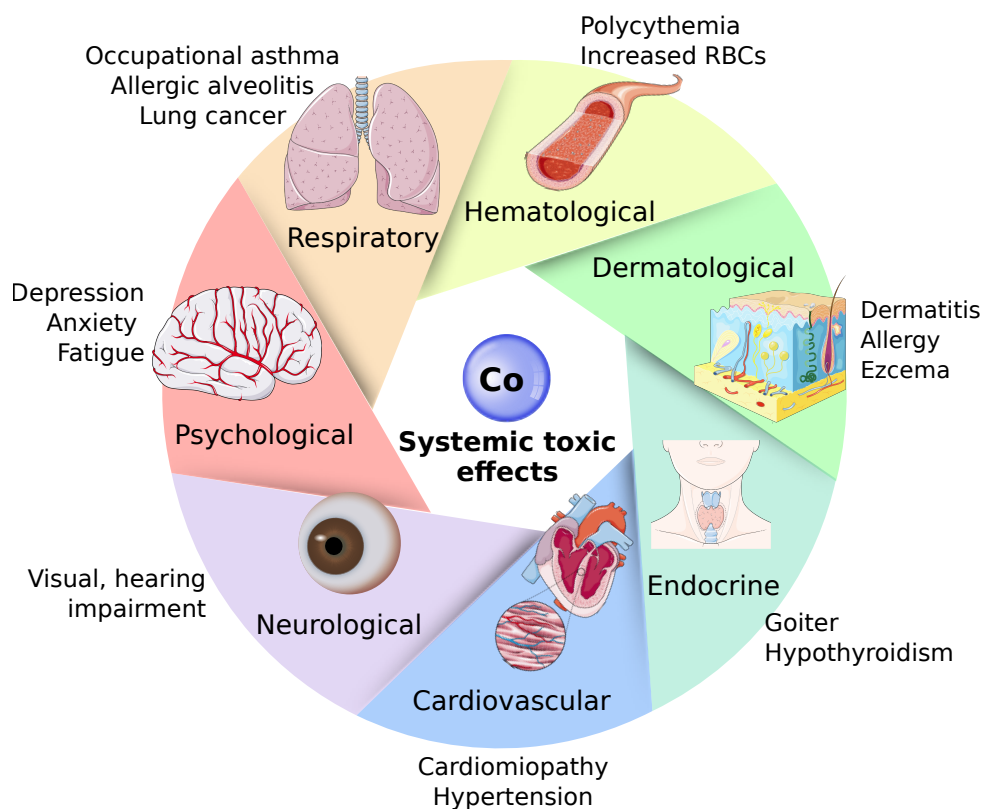


Fig. 1.4: Systemic toxic effects of cobalt [11].

1.4.1 Cobalt sources and toxicity

Cobalt metal and cobalt(II) compounds have a wide range of industrial applications such as: hard metal alloys, tungsten carbide (WC) and metallic cobalt (Co); diamond tools; catalysts in oil refining; drying agents in paints and lacquers; additives in fertilizers and animal feeds; and pigments for pottery, ceramics, glass, jewellery; among others (Tables 1.7 and 1.8). It is an essential element in our diet and thus this is the main source of exposure for the general population. Nevertheless, excessive exposure *via* inhalation, skin contact and oral ingestion through different settings (Table 1.7), may lead to adverse health effects involving the cardiovascular, neurological, endocrine, hematological, hematopoietic and respiratory systems (Table 1.8) [11, 111–113].

Cobalt exposure *via* inhalation

In the occupational setting the main exposure source is related to cobalt powders in the hard metal [114–116] and diamond polishing fields [117]. Which is associated with adverse

Table 1.7: Cobalt exposure sources.

Category	Industry / Source	Material	Intake route
Occupational	hard metal [114–116]	superalloys, Co-WC	inhalation
	construction [121]	cement	skin contact
	e-waste recycling	electric, electronic	inhalation, skin, oral
	diamond tools [111, 117]	polishing disks	inhalation
	pigments & paints [122]	dyes, glazes for pottery	inhalation, skin
Environmental	pollution [123]	air, water, soil	oral ingestion
	electronic devices	depleted batteries	skin contact
	cosmetics & jewellery [124]	lipstick, piercings	skin contact
	other [125, 126]	leather, tattoos	skin contact
Dietary	vitamin B ₁₂ [113]	beef liver, molluscs	oral ingestion
	beer (1960s) [111, 127–129]	foam stabilizer	oral ingestion
	supplements [113]	fortified food	oral ingestion
	drinking water	Co-rich rocks	oral ingestion
Medical	anemia [130–132]	CoCl ₂	oral ingestion
	estrogen hyperexcretion	CoCl ₂	oral ingestion
	blood doping [133]	CoCl ₂	oral ingestion
	MoM hip prostheses [12, 134–139]	CoCr alloys	internal

effects on the respiratory system when considering only the inhalation pathway [11, 111]. The hard metal toxicity has been correlated with activated oxygen species produced by the combination of cobalt metal and tungsten carbide particles (WC), but not by cobalt alone [115]. The inhalation of such hard metal particles may result in: asthma, interstitial pulmonary fibrosis, alveolitis and lung cancer [113–116, 118, 119]. Cardiac dysfunction was studied to find an early indicator for clinical examination of hard metal workers [120]. On the other hand, chronic exposure to cobalt dust from diamond polishing tools, microdiamonds cemented into ultrafine cobalt metal powder [111], been shown to cause respiratory impairment [117].

Cobalt exposure *via* oral ingestion

Traces of cobalt are essential in the diet as vitamin B₁₂ (cyanocobalamin), necessary for the production of red blood cells [112, 118]. Nevertheless, excessive intake of cobalt produces goiter and hypothyroidism. [111, 112, 140]. Toxic effects of cobalt in the terrestrial food chain has been suggested from soil-plant studies [123]. Cobalt intoxication related to beer consume was reported in the 1960s, which caused cardiomyopathy, polycythemia and thyroid lesions in heavy beer drinkers. The adverse effects were related to CoSO₄ and CoCl₂ added to beer as a foam stabilizer [111, 127–129]. Likewise, polycythemia, was reported in rats treated with cobalt [141]. Exposure to ~ 150 mg/d of CoCl₂ resulted in development of polycythemia with a substantial increase of hematocrit, hemoglobin and RBC volume [142, 143].

On this basis, it has been hypothesized that CoCl_2 oral intake may be an alternative blood doping technique, hardly detectable by current anti-doping testing policies [133]. CoCl_2 was used in the past in the treatment of anemia owing to its stimulant effect on the production of hemoglobin and RBCs [130–132]. Such as for the treatment of the type of anemia that is resistant to iron therapy [130]. CoCl_2 was also administered to a child presenting Fe-deficiency anemia, in order to suppress the sleeplessness and earth eating symptoms [131]. Additionally, CoCl_2 was successfully used for the treatment of patients with refractory anemia of chronic renal failure, where despite larger cobalt doses than the described for beer drinkers, no cases of cardiomyopathy were reported [132]. Cobalt neurotoxicity may cause peripheral as well as central deficits, which may be evidenced as hearing, visual, cognitive and motor performance problems. That occurs likely owing to the ability of cobalt to cross the very restrictive blood-brain barrier [11, 144].

Cobalt exposure *via* skin contact

Cobalt, independent from nickel, has been recognized as an allergen capable of causing contact dermatitis [125]. Among construction workers, contact dermatitis is the most common occupational disease [11]. Cobalt oxides in cement are insoluble, however, in the presence of amino acids the solubility increases to some extent. As a consequence of the capability of cobalt to form complexes with amino acids. Eczematous skin is caused by chromium in cement and has a high content of free amino acids. Thus, it is understandable that sensitivity by cobalt is secondary to chromium sensitivity [121]. Conversely, dermatitis owing to leather exposure is now associated to cobalt but not to chromate. Accordingly, 183 cases of patients with allergy from leather gave positive results only for cobalt [125].

Cobalt is used in pre-metallized dyes and may be released in high concentrations from leather items [126]. A rare case of allergic contact dermatitis from jewellery was reported. Patch testing and chemical analyses proved high concentrations of cobalt from a necklace in artificial sweat [124]. Cobalt blue underglaze colour was used in a Danish porcelain factory, where plate painters complained of itching skin [122]. Cobalt driers in paints have also been reported as producing allergic contact sensitivity. Likewise, azure blue and cobaltous aluminate are used as cobalt-containing tattoo pigments. Thereby, cases have been reported of allergic reaction confirmed by positive cobalt patch tests [125].

Cobalt exposure *via* MoM medical devices

Metal-on-metal (MoM) orthopedic prosthetics are predominantly comprised of cobalt (64%) and chromium (28%), CoCr alloy [11, 12]. Outside the occupational and dietary settings, patients with MoM implants undergo the most important Co exposure [11, 112]. The long-

term biological consequences remain a concern due to ion and particle release from the alloy implants [134]. Co^{2+} ions are released into the bloodstream from Co-containing prosthesis [112, 145]; as a result of both friction between the articulating surfaces and corrosion of the metal surfaces [135]. It has been observed that Co^{2+} ions migrate from the surface of CoCr implant materials and bind with synovial fluid proteins. They get trapped in serum deposits mainly as phosphates and hydroxides, which may contribute to osteolysis [136]. The release of corrosion products from MoM implants has been assessed on patients with hip replacements, where osteolysis and aseptic loosening was observed [137, 146]. Results suggest that metal ions elicited from corrosion affect proliferation and function of osteoblasts, contributing to the delay in mineralization of bone tissue [147]. Immune cells activate against infections caused by Co^{2+} released from the implants [138]. Oxidized cobalt together with Cr^{3+} from corroded CoCr metal-on-metal hip implants have been associated with mitochondrial damage [139]. Indications of possible carcinogenic effects of cobalt alloys for medical use have arisen [119]. However, toxicological weight of evidence suggested that CoCr-containing hip implants are unlikely to be associated with an increased risk of systemic cancers, owing to low Co/Cr particulate and ion concentration in blood [12].

Mechanism of cobalt toxicity

The dose-response of systemic toxicity of cobalt has been associated to the presence of free, namely unbound, Co^{2+} disseminated in different organs from the blood and lymphatic systems. It has the potential to interact with array of receptors, ion channels and proteins, owing to its higher bioavailability [152, 153] compared to bound Co-albumin in blood plasma [112, 154], as shown in Table 1.9. Disease states such as malnutrition, sepsis and alcoholism favours the equilibrium towards free Co^{2+} at expenses of bound Co-albumin. Thus, making such individuals susceptible to toxicity symptoms at lower doses than healthy ones [11]. For the latter population no adverse effects should be evidenced at concentrations of Co^{2+} in blood under $300 \mu\text{g/L}$ or $100 \mu\text{g/L}$ (taking into account a safety factor of 3) [112, 145]. Substantial high concentrations of Co^{2+} may cause: increased generation of reactive oxygen radicals [155], depression of mitochondrial oxygen uptake caused by Co^{2+} ions complexing with thiol groups of co-factors necessary for the citric acid cycle [156]. Among other factors, such mitochondrial dysfunction may potentially damage organs with high energy demand affecting, e.g. the cardiovascular system [157].

The toxicity of cobalt involves the following factors: (1) Solubility, since the bioavailability of cobalt is proportional to the solubility of cobalt compounds, thus, the amount of free Co^{2+} ions released [111, 113]. However, the toxicity does not only apply to highly soluble cobalt forms (e.g., CoCl_2), but also to less soluble ones (oxides) and even cobalt metal and

Table 1.8: Cobalt sources related to systemic health effects.

System	Symptom	Source	Refs.
Cardiovascular	cardiomyopathy	CoSO ₄ , CoCl ₂ , in beer	[128]
	hypertension	hard metal	[120]
	higher pulse rate	porcelain	[122]
Neurological	hearing impairment	CoCl ₂	[144]
	visual impairment		
	cognitive decline		
	motor axonopathy		
Endocrine	myocardial disease	CoSO ₄ , CoCl ₂ , in beer	[148]
	follicular distortion	CoSO ₄ , CoCl ₂ , in beer	[148]
	goiter, hypothyroidism	CoCl ₂	[111, 112, 140]
Hematological	polycythemia	CoCl ₂	[142]
	Increased RBCs, hemoglobin, hematocrit	CoCl ₂	[143]
Respiratory	occupational asthma	hard metal dust	[114–116]
	allergic alveolitis		
	interstitial pneumonia		
	chronic fibrosis		
	lung cancer		
Dermatological	dermatitis	hard metals	[111]
	Co allergy	cement	[121]
	eczema	jewellery	[124]
	acne	cosmetic products	[149]
		leather	[125, 126]
		CoSO ₄	[150]
Psychological	depression	MoM hip implants	[151]
	irritability		
	extreme fatigue		
	anxiety		

its alloys. Additionally, such bioavailability is constrained *in vivo* owing to both physiological concentrations of phosphates (i.e., Co₃(PO₄)₂, $K_{sp} = 2.5 \times 10^{-35}$ at 25 °C) and the high stability of complexes between cobalt and biomolecules such as albumin [113]. Although cobalt metal and its alloys are practically insoluble in water, the solubilization of these particles is possible owing to the ability of cobalt to reduce dissolved oxygen into reactive oxygen species through the oxidation of cobalt metal into Co ions. The reaction occurs at a non-significant rate, but it is catalysed on the surface of tungsten carbide, component of hard metals, releasing the products in large amounts [113, 115].

(2) Ligands, by binding various proteins and receptors in blood and tissues, free Co²⁺ have the ability to alter specific receptor activation, ion channel transport, among others [112]. CoCl₂ was reported to inhibit iodination by complexing with the enzyme tyrosine

iodinase causing hypothyroidism [140]. The bioavailability of cobalt is also influenced by nutritional factors owing to the reduced Co-albumin-binding capacity. Albumin is the main protein complexed with cobalt in serum, which offers a protective influence by reducing the cobalt-bioavailability [111, 112, 158]. Additionally, results showed the protective action of proteins rich in SH and NH₂ groups, acting as a reservoir to sequester Co²⁺ ions [157]. Conformational changes of proteins such as fibrinogen caused by the interaction of Co²⁺ [159], and binding competition of cobalt for enzymes or co-factors with i.e. iodine, iron, calcium, etc [112, 160, 161], among other factors may account as the mechanisms of action of Co²⁺ in the alteration of biological processes.

(3) Cation competition. The toxicity of cobalt occurs partially owing to its ability to compete for divalent binding sites with other other divalent metal species such as Zn²⁺, Fe²⁺, Mn²⁺, Mg²⁺ and Ca²⁺. For instance, competition between Co²⁺ and Fe²⁺ for binding in scaffolding proteins has been reported, which in turn hinders the biosynthesis of Fe–S clusters [112]. During long term cobalt exposure, Ca²⁺ hemoglobin-binding sites are irreversibly displaced by Co²⁺ [161].

Table 1.9: Partitioning of Co²⁺ binding proteins in blood plasma for healthy individuals and the mechanisms of action.

Co-ligand	Ligand	Co (%)	Effects
Strongly-bound	serum albumin	72	2 – 3 high-affinity Co-binding sites [154, 162]
	lipoic acid reduced glutathione		less bioavailable to cellular receptors
Weakly-bound	serum albumin	20	23 sites of lower affinity [162] less bioavailable to cellular receptors
Free Co ²⁺	none	8	high bioavailability, toxic [152, 153] fosters generation of oxygen radicals [155] alters mitochondrial function [156] inhibits thyroidal iodine uptake [160] alters Ca ²⁺ homeostasis [161]

Summary

In summary, the exposure to cobalt takes place mainly in the occupational, environmental, dietary and medical settings and at sufficient doses may lead to severe toxic effects [11, 111–113]. (1) Exposure *via* inhalation may affect the respiration system causing diseases such as: occupational asthma, allergic alveolitis, interstitial pneumonia, chronic fibrosis, likely lung cancer and associated cardiac dysfunctions [113–120]. (2) Exposure *via* oral ingestion may affect the cardiovascular, neurological, endocrine and hematological systems causing:

cardiomyopathy, hypertension, hearing and visual impairment, cognitive decline, goiter and hypothyroidism, polycythemia, among others [123, 127–133, 140–144]. (3) Exposure *via* skin contact may cause dermatological adverse reactions such as: dermatitis, allergy and eczema [121, 122, 124–126]. (4) Exposure *via* medical setting mainly through MoM implants, has been correlated with various of the mentioned systemic adverse effects, but involving additionally the psychological system. The overall reported symptoms include: high-frequency hearing loss, hand tremor, cognitive decline, depression, optic nerve atrophy, diastolic dysfunction, headaches, convulsions, fatigue, heart failure, hypothyroidism and metallosis, among others [112, 151].

The toxicity of cobalt is related to its bioavailability, or in other words the concentration of unbound Co^{2+} ions [152, 153]. Co^{2+} ions are small enough to penetrate cellular ion channels and also have the ability to interact with receptors and biomolecules [112]. Since the bioavailability of cobalt refers to the concentration of free Co^{2+} ions in serum, it is proportional to the solubility of cobalt compounds [111, 113]. Free Co^{2+} have the ability to alter specific receptor activation, ion channel transport, among others. That occurs owing to the potential of Co^{2+} ions to bind various ligands such as proteins and receptors in blood and tissues. Accordingly, the toxicity of cobalt occurs partially owing to its ability to compete for divalent binding sites with other divalent metal ions such as Zn^{2+} , Fe^{2+} , Mn^{2+} , Mg^{2+} and Ca^{2+} [112].

1.5 Tissue engineering

1.5.1 Challenges

The aim in tissue engineering (see Glossary, Table 1.1) is to restore, maintain, or enhance functional tissues and organs. For *in situ* regeneration, a scaffold implanted directly into the injured tissue stimulates the body's own cells to promote local tissue repair [10, 163, 164]. However, in absence of a functional vasculature, the assembling tissue is limited to oxygen diffusion ($\sim 200 \mu\text{m}$). Accordingly, the absence of capillaries linking the two systems remain the missing link [164, 165]. Hence, reduction in vascular supply at the site of injury is one of the principal reasons of impaired healing [163, 166]. As the matter of fact, a major challenge in tissue engineering is the development of scaffolds that promote tissue regeneration with concomitant formation of efficient vascularized networks, namely angiogenesis. Thus, the aim in tissue regeneration is the expansion of the conventional role of a scaffold from a simply template, into a delivery vehicle that additionally interact with specific adhesion and growth factor receptors [10, 163, 167].

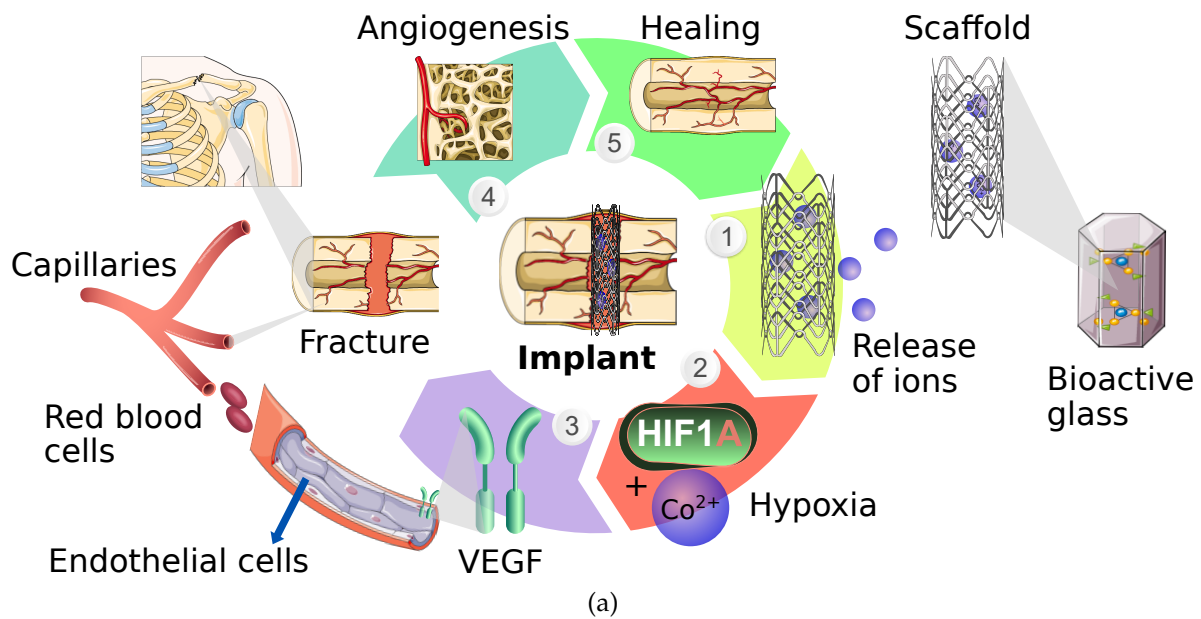


Fig. 1.5: Tissue regeneration with formation of vascularized networks triggered by cobalt-containing glass implants. 1. Controlled release of Co^{2+} ions from bioactive glass scaffolds. 2. Activation of the hypoxia-inducible HIF-1 α pathway by Co^{2+} ions. 3. Hypoxia as a stimulus of VEGF, vascular endothelial growth factor, production. 4. Angiogenesis, formation of new blood vessels. 5. Healing.

1.5.2 Angiogenesis

Angiogenesis is the formation, bridging and growth of new blood vessels from the pre-existing vasculature. Which is essential for the increased delivery of oxygen and nutrients required for tissue development and regeneration [10, 164, 168–170]. The walls of vessels are composed of endothelial cells, which are embedded in an extracellular matrix [169]. VEGF, vascular endothelial growth factor, is a potent mitogen for micro- and macrovascular endothelial cells derived from arteries, veins, and lymphatics. VEGF not only elicits a strong angiogenic response in a variety of *in vivo* systems [171], such as during endochondral ossification [172]. But also promotes angiogenesis *in vitro* such as the formation of a capillary-like network on collagen gels [170].

1.5.3 Hypoxia

The low oxygen pressure, hypoxia, in ischemic cells induces the production of VEGF and other angiogenic cytokines. Thus, hypoxia is an important stimulus for blood vessel growth by activating a broad range of homeostatic responses *via* induction of a transcriptional complex termed hypoxia-inducible factor (HIF) [167, 173–175]. It has been demonstrated that activation of HIF-1 pathway would increase vascularity and, subsequently, improve tissue

response to injury and regeneration. [166]. HIF-1 has an essential role in the maintenance of oxygen homeostasis. It is comprised of a heterodimer, HIF- α and HIF- β subunits, where O₂ regulates the former one. Subsequently, HIF- α is comprised of two isoforms (HIF-1 α and HIF-2 α), which are continuously synthesized and degraded under normoxic conditions. Whereas under hypoxic conditions, the degradation of HIF-1 α is inhibited and accumulates in the nucleus where it forms a dimer with the HIF- β subunit [166]. Thus, HIF-1 mediates developmental and physiological pathways that either promote O₂ delivery to cells or allow cells to survive O₂ deprivation [173, 175].

1.5.4 Activation of the hypoxia-inducible pathway

An attractive strategy to overcome the vascularization limitation in tissue engineering is to artificially stimulate the hypoxia-inducible HIF-1 α pathway. Which promotes the oxygen-regulated expression of angiogenic growth factors [167, 174]. Accordingly, it was reported that HIF-1 α is activated during bone repair and to improve skeletal healing [166]. Thus, materials capable to undertake controlled release of ions that activate the HIF-1 α pathway are of great interest. The incorporation of transition metals (e.g., Co²⁺, Cu²⁺) into biomaterials have been suggested as an approach to enhance the angiogenic properties. By taking into account that these ions promote the accumulation of HIF-1 α and HIF-2 α [10, 174, 176].

1.5.5 Cobalt as hypoxia-mimicking agent

Cobalt ions have been reported to bind HIF-2 α proteins at sites that alter their oxygen-regulated activity, thus mimicking hypoxia by inducing up-regulation of HIF- α protein expression and thereby, pro-vasculogenic genes such as VEGF [176]. Therefore, Co²⁺ ions have been used extensively to investigate *in vitro* and *in vivo* the hypoxic response as a trigger of angiogenesis (Table 1.10). Accordingly, CoCl₂ has been shown to promote rat bladder growth and angiogenesis [177]. The effect of CoCl₂ on human pulmonary and dermal microvascular endothelial cells was investigated in order to delineate the cellular signaling mechanism of hypoxia [56]. Likewise, CoCl₂ was added to granulosa cell culture to assess the VEGF production related to follicular angiogenesis [178]. Studies showed the potential of cobalt in healing bone, by regulating VEGF expression in osteoblasts [168].

Summary

The reduction in vascular supply, oxygen and nutrients, at the site of injury is one of the principal reasons of impaired healing and tissue regeneration. Thus, a major challenge in tissue engineering is the development of constructs that not only serve as a template for cell

growth, but also promote the formation of efficient vascularized networks. Angiogenesis refers to the process of developing new blood vessels. Thereby, the vascular endothelial growth factor (VEGF) is an important regulator of angiogenesis [10, 163, 167–171]. It has been demonstrated that induction of a transcriptional complex termed hypoxia-inducible factor (HIF) would increase vascularity. Since hypoxia stimulates the production of VEGF and other angiogenic cytokines [167, 173–175].

An attractive strategy to overcome the vascularization limitation in tissue engineering is the artificial stimulation of the hypoxia-inducible HIF–1 α pathway [166, 167, 174]. Cobalt ions are known to mimic hypoxia by binding HIF–2 α proteins at sites that alter their oxygen-regulated activity [176]. Therefore, Co²⁺ ions have been used extensively to investigate *in vitro* and *in vivo* the hypoxic response as a trigger of angiogenesis [56, 177, 178].

1.5.6 Cobalt in biomaterials

Table 1.10: Cobalt in biomaterials.

Co–Material	Test	Properties	Effects
TCP scaffolds [179]	<i>in vitro</i> <i>in vivo</i>	mechanical osteogenesis angiogenesis	positive for 2 and 5 wt% Co positive for 2 wt% Co and negative for Co > 5 wt% positive, increased VEGF, Co dose-dependently
β –TCP [180]	<i>in vitro</i> <i>in vivo</i>	osteogenesis immunological	positive <i>in vitro</i> , negative <i>in vivo</i> negative, release of pro-inflammatory cytokine
TCP coating on Ti [181]	<i>in vitro</i>	osteogenesis angiogenesis toxicity	positive, enhanced expression of the markers positive, enhanced expression of the markers negative, cytotoxicity for Co > 7 wt.%
HA nano-particles [182]	<i>in vitro</i> <i>in vivo</i>	osteogenesis angiogenesis biocompatibility	positive, up to 12 wt% of Co ²⁺ ions positive, up to 12 wt% of Co ²⁺ ions no negative for epithelial cells, negative for osteoblastic cells
Bioactive glasses [167]		bioactivity	positive, delayed HCA formation
Ti-phosphate glasses [182]	<i>in vitro</i>	biocompatibility toxicity	for osteoblastic cells positive, non cytotoxicity

An ideal biomaterial for a scaffold would selectively interact with the specific adhesion and growth factor receptors expressed by target cells in surrounding tissues required for wound healing [163]. Additionally, a controlled ion release system is vital for any tissue engineering strategy involving delivery of cobalt [167]. Inorganic therapeutic chemistry has a huge potential with approaches such as bioactive glasses as a vehicle for cobalt

delivery. Since they allow a tailorable and controlled release of ions at physiologically relevant concentrations, thus holding great potential as new hypoxia-mimicking materials for regenerative medicine [10]. Table 1.10 lists biomaterials doped with cobalt tested *in vitro* and/or *in vivo*.

1.5.7 Cobalt-containing phosphate glasses

Phosphate glasses are another class of bioactive glasses, highly attractive in hard and soft tissue engineering [10]. Since their chemical durability can be tailored through orders of magnitude, by modifying the chemical composition [24, 81]. This makes phosphate glasses suitable candidates for controlled release of therapeutic ions *in vivo*, such as cobalt, in low and sustained doses [55].

The effect of CoO doped into titanium phosphate glasses was studied, where the glasses were shown to be stable, biocompatible and VEGF secretion was significantly enhanced [57]. Additionally, static and dynamic cell tests on phosphate glass microspheres doped with TiO₂ and CoO, confirmed biocompatibility and VEGF upregulation by osteoblastic cells [58].

1.6 Paramagnetic NMR

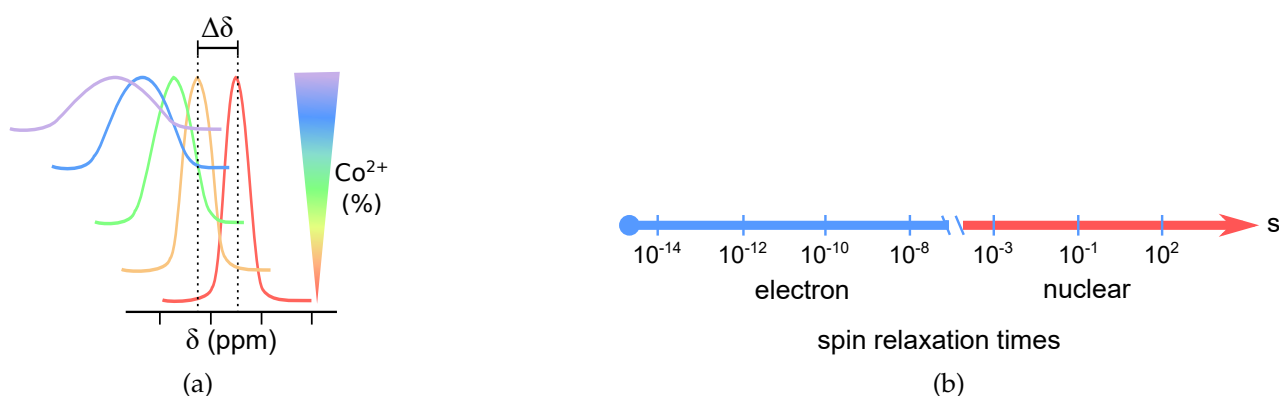


Fig. 1.6: (a) Paramagnetic effects on the NMR spectra: paramagnetic shifts and line broadening. (b) Range of electron relaxation times for metal ions compared with typical nuclear longitudinal relaxation times [183].

Paramagnetic systems are chemical moieties with positive magnetic susceptibility that contain one or more unpaired electrons. They produce a strong localized magnetic field as a consequence of the magnetic moment of the electron which is significantly bigger than that of the nucleus [184]. Therefore, NMR spectra are particularly sensitive to the presence of unpaired electron spins through the hyperfine interaction [183, 185, 186]. The paramagnetic

effects depend on the concentration of paramagnetic centres and refer to the paramagnetic shift, paramagnetic relaxation enhancement (PRE) and broadening sources [187]. In solids, the relaxation of nuclei can be achieved by strong dipolar coupling and motions, if the latter are significant enough [188]. Accordingly, in motionless solids the nuclear relaxation is very slow, however, it can be enhanced when paramagnetic impurities are present [189]. That is due to the spin diffusion, which consists in a mutual flipping of spins of dipolar-coupled nuclei. Another mechanism of relaxation influenced by the paramagnetic centres is through dipolar or direct contact electron-nucleus, which is orientation dependent and causes peak broadening [190]. On the other hand, the paramagnetic shift provides valuable structural information related to its dependency on the distance (r^{-3}) and orientation, allowing i.e. the determination of the location of the paramagnetic centre [183, 185].

Paramagnetic effects such as substantial broadening and peak-shifting outside the observed region may lead to low sensitivity or even non-observable NMR spectra (Fig. 1.6). Nevertheless, such interactions may be rather an opportunity instead of a shortcoming [191]. In fact, paramagnetic interactions yield important structural information, for instance regarding the bonding environment, spatial arrangement, delocalization of the unpaired electrons onto the coordinating ligands and dynamics, among others [186]. Hence, paramagnetic NMR provides the opportunity to further enhance the utility of structural NMR analysis. That may be achieved by approaches such as the systematic structure-based analysis of ligand-metal binding and molecule recognition. Accordingly, paramagnetic NMR has been extensively used as NMR probes over the past two decades for structural and mechanistic studies of biologically important macromolecules [185]. Nevertheless, it has not been widely applied to the study of other systems such as glasses and their dissolution products.

Chapter 2

Theoretical Framework

2.1 Diffusion

In the absence of convection, Brownian motion or the random transport of particles due to thermal motion, is the main mechanism of mass transport. This is an irreversible process and occurs from a region with high to one of lower concentration. The diffusion process is an example of the second law of thermodynamics, driven by the entropy change, $\Delta S > 0$. Even though no enthalpy is required in the process, heat may affect the diffusion rate [85].

2.1.1 Fick's laws

The basic equations that describe the diffusion process are Fick's first and second laws (Eqs. 2.1 and 2.2), where J is the flux or rate of diffusion, D is the diffusion coefficient, Q is the fraction dissolved, A is the area of the surface, C is the concentration of dissolved solid and t is time [85].

Fick's first law

Fick's first law (Eq. 2.1) states that the rate of transfer (dQ/dt) through the area (A) in the dimension (x) is proportional to the gradient of concentration. The negative sign indicates that the flow occurs from high to low concentration regions [85].

$$J = \frac{dQ}{A dt} = -D \frac{\partial C}{\partial x} \quad (2.1)$$

Fick's second law

Fick's second law (Eq. 2.2) is derived from Fick's first law (Eq. 2.1) and states that the rate of concentration change ($\partial C/\partial t$) in an element of volume (dV), or for a one-dimensional

system (dx), is proportional to the flux gradient ($\partial J/\partial x$) of the solute in the element [85].

$$\frac{\partial C}{\partial t} = -\frac{\partial J}{\partial x} = D \frac{\partial^2 C}{\partial x^2} \quad (2.2)$$

2.1.2 Steady-state diffusion

At the steady state there is no change of concentration with time (Eq. 2.3) in an element of volume, even though material still diffuses.

$$\frac{\partial C}{\partial t} = 0 \quad (2.3)$$

The concentration profile is linear with distance through the diffusional path, for a one-dimensional system (x) with constant surface area (Eq. 2.4) [85, 192].

$$\frac{\partial C}{\partial x} = \text{const.} \quad (2.4)$$

Pseudo-steady-state

The pseudo-steady state is established when during a finite time the concentration gradient becomes relatively constant (Eq. 2.5). In order to reach this state, the requirements are that the concentration change of dissolved solid in the bulk solution is negligible. Additionally, it requires that within the time for an average molecule to cross the diffusion layer, no change of particle surface area occurs [84, 85].

$$\frac{\partial C}{\partial t} \approx 0 \quad (2.5)$$

2.1.3 Higuchi equation

A rather simple equation was derived for the kinetics of dissolution [87], which relates the rate of release of a drug, as a solid of fine particles, that dissolves under perfect sink conditions (Eq. 2.6).

$$Q = \sqrt{ADC_s t} \quad (2.6)$$

Where Q is the amount of drug released, D is the diffusion constant, t is the time and A is the amount of non-dissolved drug per unit volume, which must be substantially bigger than its solubility C_s . Under these conditions ($A \gg C_s$) the concentration gradient remains constant and its linearity over the diffusion layer follows Fick's first law (Eq. 2.1).

2.1.4 Diffusion and a chemical reaction

In case a slow reaction takes place simultaneously with a diffusion process, the net effect of the reaction would be a reduction of the diffusant concentration. Therefore, the expression, i.e. first order reaction, is nothing but Fick's second law (Eq. 2.2) reduced by the reaction rate (R) as shown in (Eq. 2.7) [85].

$$\frac{\partial C}{\partial t} = D \frac{\partial^2 C}{\partial x^2} - R \quad (2.7)$$

2.2 Solubility

2.2.1 Lattice enthalpy

$$\Delta H_L^\ominus \propto \frac{1}{r_+ + r_-} \quad (2.8)$$

The lattice enthalpy is inversely proportional to the distance between the radii of the ions, where r_+ and r_- refer to the radii of the cation and anion respectively [90].

2.2.2 Hydration enthalpy

$$\Delta H_{\text{hyd}} \propto \frac{1}{r_+} + \frac{1}{r_-} \quad (2.9)$$

The hydration enthalpy is the sum of individual ion contributions, since each ion is hydrated individually, where r_+ and r_- refer to the radii of the cation and anion respectively [90].

2.2.3 Congruent dissolution

The concentrations of ions in solution can be normalized to the initial glass composition, which leads to the normalized mass release, $NL(i)$ (mg/cm²), and can be calculated by Eq. 2.10

$$NL(i) = \frac{C_i}{(f_i) \cdot (SA(t)/V)} \quad (2.10)$$

where C_i refers to the measured concentration (ppm) of ion (i), f_i is its mass fraction (wt%) in the glass and $SA(t)$ is a time-dependent ratio of the glass surface area (cm²) to leachate volume (L).

$$\frac{\partial NL(i)}{\partial t} = \text{const.} \quad (2.11)$$

Congruent dissolution takes place when the composition of ions in solution is equal to the ion composition in the glass structure. Thus, the ion release rate is equal for all ions (Eq.

2.11), which means that the normalized concentration of each ion in solution $NL(i)$ as a function of time (t) remains constant [30].

2.3 NMR

2.3.1 The nuclear spin Hamiltonian operator

The total NMR Hamiltonian, H_{NMR} , for any particular spin system is the sum of individual Hamiltonians that describe particular interactions, indicated by H_λ in Table 2.1. The main interactions involving single nuclei (i) and pairwise (ij) are described by (Eq. 2.12).

$$H_{NMR} = \sum_i (H_{IZ}^i + H_{CS}^i + H_Q^i + H_{RF}^i + \sum_{ij} (H_J^{ij} + H_{DD}^{ij})) \quad (2.12)$$

Table 2.1: Interactions of the NMR Hamiltonian operator [193].

H_λ	Interaction	Frequency	Description
H_{IZ}	Zeeman	10–1000 MHz	Magnetic interaction of nuclear spins with the static external field of the spectrometer.
H_{CS}	Chemical shift	0–100 kHz	The effect of the electron cloud surrounding the nuclear spins (modifications to the static field).
H_Q	Quadrupole	0–10 GHz	Nuclei with $I > 1/2$ are sensitive to the electric-field gradient generated by their surroundings.
H_{RF}	Radio frequency	0–300 kHz	Interaction of nuclear magnetic spins with a coherent, externally applied radio-frequency field.
H_J	J coupling	0–1000 Hz	Interaction of pairs of nuclear spins through bonding electrons.
H_{DD}	Dipole-dipole	0–40 kHz	Magnetic interaction of nuclear spin pairs through space.

Nuclear Zeeman interaction

The magnetic moment of the nucleus (μ_I) is proportional to the magnitude of the angular momentum $\mathbf{I}\hbar$ (Eq. 2.13).

$$\mu_I = \hbar\gamma_I\mathbf{I} = g_I\beta_I\mathbf{I} \quad (2.13)$$

where \mathbf{I} is the nuclear spin operator, γ_I is the gyromagnetic ratio, β_I is the nuclear magneton, g_I is the dimensionless nuclear g -factor and e and m_p are the charge and the rest mass of the proton (Eq. 2.14).

$$\beta_I = \frac{e\hbar}{2m_p} \quad (2.14)$$

The nuclear Zeeman Hamiltonian (H_{IZ}) represents the interaction between the nuclear magnetic moment (μ_I) and the magnetic field (B_0), Eq. 2.15. By convention the laboratory axis is defined so that B_0 lies along the z direction.

$$H_{IZ} = -\mu_I \cdot B_0 = -\hbar\gamma_I B_0 I_z = \hbar\omega_0 I_z \quad (2.15)$$

where $\omega_0 = -\gamma_I B_0$ is the nuclear Larmor frequency. A nucleus of spin quantum number I has $2I + 1$ states, thus, values from $-I$ to I .

Chemical shift

The Hamiltonian given in Eq. 2.16 describes the chemical shift interaction, where δ is the chemical shift tensor which is explained further below.

$$H_{CS} = -\hbar\gamma_I \mathbf{B}_0 \cdot \delta \cdot \mathbf{I} \quad (2.16)$$

The magnetic field caused by the electrons makes the overall magnetic field B experienced by a particular nucleus lower than the applied B_0 (Eq. 2.17). This is the result of additional magnetic fields (B') produced by the electronic environment around the nucleus [193–195].

$$B = B_0 - B' \quad (2.17)$$

The chemical shift (δ) is defined by Eq. 2.18, where ν and ν_{ref} are the frequencies of the nucleus of interest and the reference substance (Table 2.2), respectively [193, 196].

$$\delta/\text{ppm} = \frac{(\nu - \nu_{ref})/\text{Hz}}{\nu_{ref}/\text{MHz}} \quad (2.18)$$

The chemical shift varies with the orientation of the moiety with respect to the external magnetic field. Such orientation dependence is known as the chemical shift anisotropy (CSA) and it is a second-rank tensor (3 by 3 matrix). By using the principal axis system, the three diagonal elements ($\delta_{xx}, \delta_{yy}, \delta_{zz}$) and the three Euler angles (α, β, γ) fully define the tensor [193]. The isotropic chemical shift (δ_{iso}) corresponds to the average of the three

Table 2.2: Primary (1) and secondary (2) standard references for common nuclei [197].

Nucleus	Reference substance	Natural abundance (%)	Chemical shift (ppm)
^1H $\frac{1}{2}$	TMS (1)		0.00
	Adamantane site 1, 4H (2)	99.985	1.873
	Adamantane site 2, 12H (2)		1.756
^{13}C $\frac{1}{2}$	TMS (1)	1.108	0.00
	Adamantane (2)		38.4
^{19}F $\frac{1}{2}$	CFCl_3 (1)	100	0.00
	NaF(aq) 1 M (2)		- 120
^{31}P $\frac{1}{2}$	H_3PO_4 85 % (1)	100	0.00
	$\text{NH}_4\text{H}_2\text{PO}_4$ (2)		0.9
^{29}Si $\frac{1}{2}$	TMS (1)	4.70	0.00
	TTMS (2)		-9.9
^{11}B $\frac{3}{2}$	$\text{BF}_3 \cdot \text{Et}_2\text{O}$ (1)	80.1	0.00
	NaBH_4 (2)		3.2
^{27}Al $\frac{5}{2}$	$\text{Al}(\text{H}_2\text{O})_6^{3+}$ (1)	100	0.00
	$\text{Y}_3\text{Al}_5\text{O}_{12}$ (2)		0.7
^7Li $\frac{3}{2}$	LiCl(aq)	92.5	0.00
^{23}Na $\frac{3}{2}$	NaCl(aq)	100	0.00

diagonal elements of the matrix (Eq. 2.19) and it is the center of gravity of the lineshape.

$$\delta_{iso} = \frac{1}{3} (\delta_{xx} + \delta_{yy} + \delta_{zz}) \quad (2.19)$$

The chemical shift tensor have been described by different conventions such as the Haeberlen-Mehring-Spiess [198–200] used by the software SIMPSON [201]. Thereby the principal components of the CS tensor are sorted with respect to the isotropic chemical shift as shown by Eq. 2.20.

$$|\delta_{zz} - \delta_{iso}| \geq |\delta_{xx} - \delta_{iso}| \geq |\delta_{yy} - \delta_{iso}| \quad (2.20)$$

The anisotropy (δ_{aniso}) is defined as the largest separation from the center of gravity (Eq. 2.21). The asymmetry parameter (η) refers to the deviation of the lineshape from an axially symmetric tensor (Eq. 2.22). For an isotropic CSA tensor $\delta_{aniso} = 0$, for an uniaxial CSA tensor $\delta_{aniso} \neq 0$ and $\eta = 0$, and for a biaxial tensor $\delta_{aniso} \neq 0$ and $\eta \neq 0$ [193].

$$\delta_{aniso} = \delta_{zz} - \delta_{iso} \quad (2.21)$$

$$\eta = \frac{(\delta_{yy} - \delta_{xx})}{\delta_{aniso}}; (0 \leq \eta \leq 1) \quad (2.22)$$

Nuclear quadrupole interaction

The nuclear quadrupolar Hamiltonian shown in Eq. 2.23 refers to the interaction between the quadrupolar moment of the nucleus ($I > 1/2$) and the electric-field gradient owing to the surrounding electrons.

$$H_Q = \frac{eQ}{2I(2I-1)} \mathbf{I} \cdot \mathbf{V} \cdot \mathbf{I} \quad (2.23)$$

where Q is the electric quadrupolar moment of the nucleus, e is the charge of the electron, \mathbf{V} is the electric-field gradient tensor and \mathbf{I} is the nuclear spin.

The Hamiltonian shown in Eq. 2.24 is defined in terms of the quadrupolar coupling constant C_Q (Hz) and the quadrupolar splitting frequency ω_Q , which are defined in Eq. 2.25.

$$H_Q = \frac{2\hbar\omega_Q}{3eq} \mathbf{I} \cdot \mathbf{V} \cdot \mathbf{I} \quad (2.24)$$

where eq is the electric-field gradient anisotropy defined as $V_{zz} = eq$ for $|V_{zz}| \geq |V_{yy}| \geq |V_{xx}|$.

$$C_Q = \frac{e^2qQ}{h}, \quad \omega_Q = \frac{3\pi C_Q}{2I(2I-1)} \quad (2.25)$$

J-coupling

The *J*-coupling, indirect spin-spin coupling or indirect dipole-dipole coupling provides a direct evidence of chemical bonding. The nuclear spins are coupled together through the bonding of electrons, therefore, the *J*-coupling is exclusively intramolecular. The Hamiltonian (H_J^{ij}) given in Eq. 2.26 represents the heteronuclear *J*-coupling interaction.

$$H_J^{ij} = 2\pi \mathbf{I}_i \mathbf{J}_{ij} \mathbf{I}_j \quad (2.26)$$

where \mathbf{I}_i and \mathbf{I}_j are the nuclear spins, \mathbf{J}_{ij} is the J -coupling tensor and the factor 2π makes reference to the Hz units in which the J -coupling is invariably expressed.

Dipole-dipole interaction

The through-space dipole-dipole coupling or direct dipole-dipole coupling takes place when the spin fields propagate through space without involving the electron clouds. The dipole-dipole interaction may be intermolecular or intramolecular. The NOESY (Nuclear Overhauser Effect Spectroscopy) pulse sequence makes use of magnetization transfer through dipole-dipole interactions, cross-relaxation [193]. The secular part of the Hamiltonian of the dipolar interaction [202] for two spin-1/2 particles separated by a vector forming an angle θ with an external magnetic field is described by Eq. 2.27.

$$H_{DD} = -\frac{1}{2}b[I^i I^j - I_z^i I_z^j](1 - 3\cos^2\theta) \quad (2.27)$$

where b is the dipole-dipole coupling constant. The factor $1 - 3\cos^2\theta$ vanishes when θ is equal to 54.7356° [203]. The effect of the “magic angle spinning” (MAS) is similar to the tumbling of a molecule in a liquid so it has the potential to remove the dipolar interactions and to average out the anisotropy of the chemical shift to the isotropic value δ_{iso} [203, 204]. The speed of the rotation is an important factor, when the frequency (Hz) is smaller than the spectral width of the respective static spectrum, sidebands at integer multiples of the rotation frequency show up. The intensity depends on the speed, such sidebands have been used to extract the chemical shift anisotropy [205, 206].

Nutation frequency

The amplitude of a pulse is specified through the nutation frequency (ω_{nut}). Thereby, β_p and τ_p refer to the flip angle and duration of the pulse, respectively (Eq. 2.28).

$$\beta_p = \omega_{nut}\tau_p \quad (2.28)$$

For a flip angle $\beta_p = \pi/2$, the nutation frequency in (Hz) can be calculated as follows as shown by Eq. 2.29 [193].

$$\pi/2 = \omega_{nut}\tau_p = 2\pi\nu_{nut}\tau_p; \quad \nu_{nut} = \frac{1}{4\tau_p} \quad (2.29)$$

2.3.2 The paramagnetic shift

The shift, rather than a splitting of the NMR resonance, is a result of the electronic relaxation occurring at orders of magnitude faster than the nuclear one (10^{-14} – 10^{-8} vs. 10^{-3} – 10^2 s). Which does not lead to a coupling between the spins of the nucleus to the electron but rather to the average of the electronic magnetic moment. Thus, the rapid electron relaxation effectively “decouples” the NMR spectrum, resulting in a singlet appearing at a frequency that corresponds to the weighted average of the two peaks ($\bar{\omega}$) [183]. Hence, this interaction is partially alike to the chemical shift [183], as shown by Eq. 2.30,

$$\bar{\omega} = -\omega_{0,I} + \frac{g_e \beta_e A B_0}{4\hbar kT} = -\omega_{0,I}(1 + \delta_{iso}^S) \quad (2.30)$$

where A is the hyperfine coupling constant and δ_{iso}^S is the isotropic paramagnetic shift (Eq. 2.31), which is proportional to the magnetic field B_0 as shown in Eq. 2.30.

$$\delta_{iso}^S = \frac{g_e \beta_e A}{4\hbar \gamma_I kT} \quad (2.31)$$

There are three important contributions to the paramagnetic shift according to the susceptibility formalism: the through-bond Fermi-contact, the through-space spin-dipolar coupling which leads to the pseudo-contact shift (PCS) and the antisymmetric hyperfine interaction.

Contact shift

The contact shift arises from the through-bond spin-spin interaction. As can be seen in Eq. 2.32, the contact shift ($\delta_{iso}^{con,\chi}$) is proportional to the isotropic magnetic susceptibility (χ^{iso}), which means that ions with higher magnetic moments lead to larger contact shifts. The magnitude of the unpaired electron density ($\rho^{\alpha-\beta}(0)$) at the nuclear site is also proportional to $\delta_{iso}^{con,\chi}$. Thus, a good overlap between the orbitals of the metal ion and the s-orbital of the nucleus favors larger shifts. The sign of the contact shift corresponds to the sign of $\rho^{\alpha-\beta}(0)$.

$$\delta_{iso}^{con,\chi} = \frac{\chi^{iso}}{3S} \rho^{\alpha-\beta}(0) \quad (2.32)$$

Pseudo-contact shift

The PCS is a shift that arises from the through-space spin-dipolar interaction. Thus, it is a long range effect compared to the contact shift and it depends on the relative spatial position between the nucleus and the paramagnetic ion. Owing to the dependency of PCS on the anisotropic but not on the isotropic susceptibility, PCS only takes place for ions that

undertake SO interaction.

$$\delta_{iso}^{pcs} = \frac{1}{12\pi R^5} \left[\Delta\chi_{ax}(2z^2 - x^2 - y^2) + \frac{3}{2}\Delta\chi_{rh}(x^2 - y^2) \right] \quad (2.33)$$

where x , y and z are the Cartesian coordinates, while $\Delta\chi_{ax}$ and $\Delta\chi_{rh}$ are the susceptibility anisotropy parameters. As can be seen in Eq. 2.33, the PCS depends only on the susceptibility anisotropy and not on the isotropic susceptibility.

2.3.3 Homogeneity approach

The homogeneity of the doping of a paramagnetic species into a diamagnetic host can be assessed through quantitative NMR according to a model function [207] that correlates the molar fraction of the paramagnetic dopant x_{para} with the respective fraction of target "visible" nuclei $f_{visible}$ as follows:

$$f_{visible} = \exp(-k_1 r_0^3 x_{para}) \quad (2.34)$$

where the constant k_1 is a fitting parameter, r_0 is the wipe-out radius and $f_{visible}$ is defined by

$$f_{visible} = \frac{A_{doped}/n_{doped}}{A_{non-doped}/n_{non-doped}} \quad (2.35)$$

where A and n are the peak area and the number of moles of the respective doped and non-doped samples. This is nothing else than the relative area normalized by using the non-doped sample as reference. The model assumes that the target nuclei inside the wipe-out radius r_0 will not contribute to the NMR signal due to the broadening and shift caused by paramagnetic effects. Thus, A_{doped} corresponds to the area under the peak that remains at the same position as the non-doped sample. In case of uniform distribution of the paramagnetic dopant in the system, the decay of the NMR signal should follow Eq. 2.34 and at certain concentration, $f_{visible}$ should vanish completely meaning that all target nuclei are under the influence of paramagnetic centres.

2.3.4 Relaxation

Spin-lattice relaxation time

Also known as relaxation in the z -direction or longitudinal relaxation, this process corresponds to the return of the macroscopic magnetization to the Boltzmann equilibrium. The transfer of the energy given by the RF pulse to the lattice is achieved through lattice vibrations and rotations at the Larmor frequency. The relation between the time t that takes

the recovery of the equilibrium magnetization M_z^0 and $M_z(t)$ is given by

$$M_z(t) = M_z^0(1 - e^{-t/T_1}) \quad (2.36)$$

from this expression is evident that T_1 is the time that takes to recover about 63 % of M_z^0 , it is also obvious that the time to reach the equilibrium follows an exponential law [193, 208]. Saturation recovery is an experimental method to determine T_1 , where initially a loop of $(\frac{\pi}{2})$ pulses is applied to cause saturation, afterwards the magnetization is allowed to recover during a τ delay and finally a $(\frac{\pi}{2})$ is applied to measure the signal. A rule of thumb states that when $\tau = 5T_1$ the equilibrium magnetization is practically reached [209].

Correlation function

The reduced correlation function (Eq. 2.37) contains all the information about the dynamics, chemical exchange, and electronic relaxation properties.

$$g(\tau_c; \tau) = \exp(-|\tau|/\tau_c) \quad (2.37)$$

where $g(\tau_c; \tau)$ is the correlation function and τ_c is the correlation time.

Spectral density

The reduced spectral density $j(\tau_c; \omega)$ which is the Fourier transform of the correlation function $g(\tau_c; \tau)$ is shown in Eq. 2.38.

$$j(\tau_c; \omega) = \int_{-\infty}^{\infty} \exp(-|\tau|/\tau_c) d\tau = \frac{2\tau_c}{1 + \omega^2\tau_c^2} \quad (2.38)$$

where the spectral density $j(\tau_c; \omega)$ is a Lorentzian function and ω is the frequency.

In the extreme-narrowing limit τ_c is short enough (up to 10 ps) that $|\omega\tau_c| \ll 1$, and $j(\tau_c; \omega) \approx 2\tau_c$ and independent of ω . This applies for situations in which unrestricted tumbling takes place, such as small species in solution. Conversely, in the spin-diffusion limit τ_c is long enough (> 1 ns) that $|\omega\tau_c| \gg 1$ and $j(\tau_c; \omega) \approx 2/\omega^2\tau_c$ [183].

2.3.5 Paramagnetic nuclear relaxation

The paramagnetic relaxation enhancement (PRE) is the result of the random variation of the electron–nuclear spin interactions, which opens new pathways for spin relaxation (T_1 and T_2), as well as for some other phenomena (such as cross-correlated relaxation) [186]. For large paramagnetic systems with slow rotational dynamics, the transverse relaxation time

(T_2) is dominated by the Curie relaxation, whereas the longitudinal relaxation time (T_1) is dominated by the Solomon–Bloembergen–Morgan relaxation.

For rigid solids neither tumbling nor internal motional dynamics are relevant for relaxation. Therefore, vibrations are the only motional source which are not an efficient way for the nuclear relaxation, leading to significant long T_1 values in diamagnetic systems (from minutes to hours). Even though, it seems obvious that the Curie relaxation would apply for rigid solids, the model is not valid. Instead, the Solomon relaxation takes place for rigid solids. Regarding paramagnetic systems with slow rotational dynamics, short relaxation times take still place, since vibrations still cause electronic relaxation which subsequently cause nuclei relaxation [183].

Solomon–Bloembergen–Morgan relaxation

In this theory only the first-order Fermi-contact and spin-dipolar parts from the hyperfine tensor are used for calculating T_1 and T_2 . It is useful to describe the PRE in systems undertaking fast rotational diffusion (τ_R), which are comparable to the electronic relaxation times (T_{1e}, T_{2e}). Therefore, it works well for small complexes in solution in which the nuclear relaxation is dominated by the electron relaxation rather than any molecular dynamics.

The Solomon mechanism refers to the relaxation by the point-dipole part of the hyperfine interaction. This model applies for nuclei fairly far away from the paramagnetic center ($> 4 \text{ \AA}$), in which the unpaired electrons can be thought as localized at the paramagnetic ion. This allows to treat the unpaired electrons as point dipole moments. On the other hand, in this theory the relaxation mediated by the isotropic Fermi-contact interaction was proposed by Bloembergen. In this mechanism the nuclear relaxation is induced by chemical exchange and electronic relaxation [183].

Curie-spin relaxation

This mechanism of relaxation is suitable when the electronic relaxation occurs on significant shorter scales than the rotational processes. The effect of the Curie-spin relaxation is proportional to the magnetic field B_0 , thus becoming more important at high magnetic fields. It is useful to describe the PRE in systems undertaking slow rotational diffusion (τ_R), order of magnitude slower than the electronic relaxation times ($T_{1e}, T_{2e} \ll \tau_R$). Therefore, it works well for large species in solution, such as proteins, in which the nuclear relaxation is dominated by the electron relaxation rather than any molecular dynamics [183].

2.4 EPR

2.4.1 EPR spin Hamiltonian operator

The EPR spin Hamiltonian (H_{EPR}) shown in Eq. 2.39 accounts for transition metal ions, where each interaction (H_λ) is described in Table 2.3.

$$H_{EPR} = H_{LF} + H_{SO} + H_{SZ} + H_{SS} + H_{HF} \quad (2.39)$$

Ligand field interaction

The crystal or ligand field interaction takes place between the metal ion and the ligands in a coordination complex. For the transition elements the crystal field interaction is large enough ($\sim 10^4 \text{ cm}^{-1}$), that only the ground state is thermally populated and it is the biggest interaction in the EPR Hamiltonian.

Table 2.3: EPR spin Hamiltonian interactions for transition metals [183].

H_λ	Interaction	Frequency	Description
H_{LF}	Ligand field	$10^3 - 10^4 \text{ cm}^{-1}$	Interaction between the metal ion and the ligands.
H_{SO}	Spin-orbit coupling	$10^2 - 10^3 \text{ cm}^{-1}$	Transition metal ions with $S > 1/2$ undertake SO coupling.
H_{SZ}	Zeeman	$10^{-1} - 10^1 \text{ cm}^{-1}$	Magnetic interaction of nuclear spins with the static external field of the spectrometer.
H_{SS}	Electronic spin-spin	$10^{-1} - 1 \text{ cm}^{-1}$	Magnetic coupling between individual electrons.
H_{HF}	Hyperfine	$10^{-1} - 1 \text{ cm}^{-1}$	Magnetic coupling between the nucleus and the unpaired electron.

Spin-orbit coupling

The spin-orbit coupling (Eq. 2.40) is the second largest interaction ($10^2 - 10^3 \text{ cm}^{-1}$) after the crystal field splitting.

$$H_{SO} = \lambda \mathbf{L} \mathbf{S} \quad (2.40)$$

where H_{SO} is the Hamiltonian representing the spin-orbit coupling by assuming LS coupling and Hund's rules. The many-electron SO coupling parameter λ is given by Eq. 2.41.

$$\lambda = \pm \frac{\zeta}{2S} \quad (2.41)$$

where ζ is the single electron coupling parameter, which takes positive values for shells less than half filled, and correspondingly negative values for shells more than half filled (Eq. 2.41).

2.4.2 Electronic Zeeman interaction

The electronic Zeeman interaction (H_{SZ}) that combines the orbital and the spin Zeeman terms is shown in Eq. 2.42, which are described below.

$$H_{SZ} = -\beta_e \cdot \mathbf{B}_0 = (\mathbf{L} + g_e \mathbf{S}) \quad (2.42)$$

In the limit of LS coupling, the total angular momentum operator is $\mathbf{J} = \mathbf{L} + \mathbf{S}$. Thus, the total magnetic moment operator (m) is defined by Eq. 2.43.

$$m = -\beta_e(\mathbf{L} + g_e \mathbf{S}) \quad (2.43)$$

The orbital angular momentum is quantized and denoted by the quantum number L where each level comprises $2L + 2$ states. An electron of spin quantum number S has $2S + 1$ states, thus, values from $-S$ to S . The gyromagnetic ratio between the free electron and ^1H ($|\gamma_S/\gamma_I|$) is 658.23.

Spin Zeeman term

The magnetic moment of the electron (μ_S) is proportional to its spin angular momentum $\hbar \mathbf{S}$ (Eq. 2.44).

$$\mu_S = \hbar \gamma_S \mathbf{S} = -g_e \beta_e \mathbf{S} \quad (2.44)$$

where \mathbf{S} is the electron spin operator, γ_S is the electron gyromagnetic ratio, g_e is the free-electron g -factor ($g = 2.002322$) and β_e is the Bohr magneton, which can be calculated from the charge (e) and the rest mass (m_e) of the electron (Eq. 2.45).

$$\beta_e = \frac{e\hbar}{2m_e} \quad (2.45)$$

The electron Zeeman Hamiltonian (H_{SZ}) represents the interaction between the electron magnetic moment (μ_S) and the magnetic field (B_0). By convention the laboratory axis is defined so that B_0 lies along the z direction (Eq. 2.46).

$$H_{SZ} = -\mu_S \cdot B_0 = g_e \beta_e B_0 S_z \quad (2.46)$$

Orbit Zeeman term

3d transition-metal ions with spin $S > 1/2$ undertake SO coupling. In turn this affects the paramagnetic shift.

$$\mu_L = -\beta_e \mathbf{L} \quad (2.47)$$

where μ_L is the orbital contribution to the magnetic moment and \mathbf{L} is the total orbital angular momentum operator, which is orientation dependent.

2.4.3 Electronic spin-spin interaction

The electronic spin-spin interaction H_{SS} refers to the magnetic coupling of individual electrons (Eq. 2.48).

$$H_{SS} = -\rho \left[(\mathbf{L} \cdot \mathbf{S})^2 + \frac{1}{2}(\mathbf{L} \cdot \mathbf{S}) - \frac{1}{3}L(L+1)S(S+1)\mathbf{1} \right] \quad (2.48)$$

where ρ is an energy coefficient that for transition metal ions takes values up to 1 cm^{-1} .

2.4.4 The hyperfine interaction

The nuclear and electronic magnetic moments couple to each other resulting in the hyperfine interaction. Thus, the Hamiltonian can be written in terms of the electron (\mathbf{S}) and nuclear (\mathbf{I}) spin operators (Eq. 2.49). The hyperfine interaction consists of two important contributions namely, the Fermi contact (through-bond, scalar interaction) and the pseudocontact shift (through-space) interactions, which couple the unpaired electron and the nucleus at the side and outside the nucleus, respectively [183, 186].

$$H_{SI} = \mathbf{S} \cdot \mathbf{A} \cdot \mathbf{I} \quad (2.49)$$

where \mathbf{A} is the hyperfine coupling tensor (Eq. 2.50), which comprises a 'through-bond' isotropic Fermi-contact term (A^{FC}), analogous to the J -coupling, and a 'through-space'

anisotropic spin-dipolar term (\mathbf{A}^{SD}).

$$\mathbf{A} = A^{\text{FC}}\mathbf{1} + \mathbf{A}^{\text{SD}} \quad (2.50)$$

The Fermi-contact interaction

The Fermi-contact coupling constant associated to electrons delocalized onto the ligands is shown by Eq. 2.51. The Fermi contact shift is analogous to the J -coupling interaction between nuclei. This situation refers to an electron in immediate vicinity of the nucleus and it is proportional to the total unpaired electron spin density transferred to the nucleus. Thus, the sum of the contributions from the individual electrons. This contribution is different for each unpaired electron, since each one sits on orbitals with different spatial distribution of electron density. Therefore, the magnitude and the sign of the shift depend on the bond nature, orbital overlap, bond distances, and angles [183, 185].

$$A^{\text{FC}} = \frac{\mu_0 \beta_e g_e \hbar \gamma_I}{3S} \rho^{\alpha-\beta}(0) \quad (2.51)$$

where $\rho^{\alpha-\beta}(r)$ is the total spin-unpaired electron density at the position r , $2S$ is the number of unpaired electrons and μ_0 is the permeability of free space.

The spin-dipolar interaction

The spin-dipolar interaction is analogous to the classical interaction between two magnetic dipoles. The Cartesian components of the spin-dipolar tensor are given by Eq. 2.52.

$$A_{ij}^{\text{FC}} = \frac{\mu_0 \beta_e g_e \hbar \gamma_I}{8\pi S} \int \frac{3r_i r_j - \delta_{ij} r^2}{r^5} \rho^{\alpha-\beta}(r) d^3r \quad (2.52)$$

where i and j are equal to x , y , or z , e_i is the unit vector along axis i , and δ_{ij} is the Kronecker delta.

2.4.5 EPR effective spin Hamiltonian

The Hamiltonian formulated in Eq. 2.53 includes the coupling between the electronic spin and orbital angular momentum. It is comprised by three terms and it is referred as the EPR effective spin Hamiltonian.

$$H_{\text{EPR}} = \beta_e \mathbf{B}_0 \cdot \mathbf{g}_e \cdot \mathbf{S} + \mathbf{S} \cdot \mathbf{A} \cdot \mathbf{I} + \mathbf{S} \cdot \mathbf{D} \cdot \mathbf{S} \quad (2.53)$$

where the first term refers to the electronic Zeeman interaction, which is spatially anisotropic owing to the SO coupling and the \mathbf{g} shift is analogous to the chemical shielding of the nucleus. The second term is the hyperfine interaction and the third term is the zero-field splitting, described below.

EPR and NMR tensors

The Hamiltonian shown in Eq. 2.54 includes the nuclear Zeeman and chemical shielding (σ^{orb}) interactions, besides the terms shown in Eq. 2.53.

$$H_{EPR} = -\hbar\gamma_I \mathbf{B}_0 \cdot (\mathbf{1} - \sigma^{orb}) \cdot \mathbf{I} + \beta_e \mathbf{B}_0 \cdot \mathbf{g}_e \cdot \mathbf{S} + \mathbf{S} \cdot \mathbf{A} \cdot \mathbf{I} + \mathbf{S} \cdot \mathbf{D} \cdot \mathbf{S} \quad (2.54)$$

2.4.6 ZFS

The zero-field splitting (ZFS) is equivalent to the nuclear quadrupole interaction, $(\mathbf{I} \cdot \mathbf{Q} \cdot \mathbf{I})$, where \mathbf{Q} is the tensor related to the orientation dependence of the quadrupolar coupling. Likewise, it is zero for both $S < 1$ and perfect cubic symmetry (Eq. 2.55).

$$H = \mathbf{S} \cdot \mathbf{D} \cdot \mathbf{S} \quad (2.55)$$

where H is the Hamiltonian in absence of the external magnetic field and nuclear magnetic moments, \mathbf{S} is the electron spin operator and \mathbf{D} is the ZFS tensor (Eq. 2.56).

$$\mathbf{D} = \mathbf{D}_{NR} + \mathbf{D}_{SO} \quad (2.56)$$

where the ZFS tensor (\mathbf{D}) is comprised by the electron spin-spin interaction (\mathbf{D}_{NR}) and a term involving the SO interaction (\mathbf{D}_{SO}), the latter taking place only for $S > 1/2$ and non perfect cubic symmetries.

Chapter 3

Experimental Section

3.1 Glass Preparation

Glasses in the system $45\text{P}_2\text{O}_5 - x\text{CaO} - (55 - x)\text{Na}_2\text{O}$ (CNP45, $25 \leq x \leq 40$ mol%, O/P = 3.1), where the CaO/Na₂O ratio was varied while the phosphate content was maintained constant, were prepared by a melt-quench route in platinum crucibles as described previously [210]. Nominal glass compositions are given in Table 3.1; batch size was 25 g. Glass powders were prepared by crushing the glass in a steel mortar and sieving to different particle size ranges. Glasses in the system $45\text{P}_2\text{O}_5 - (30 - x)\text{CaO} - 25\text{Na}_2\text{O} - x\text{CoO}$ with $0 \leq x \leq 10$ mol%,

Table 3.1: Nominal glass composition in mol% of CNP45 glasses.

Glass	P ₂ O ₅	CaO	Na ₂ O	Li ₂ O
C25	45.0	25.0	30.0	
C27.5	45.0	27.5	27.5	
C30	45.0	30.0	25.0	
C35	45.0	35.0	20.0	
C40	45.0	40.0	15.0	
L27.5	45.0	27.5		27.5

O/P = 3.11 given in Table 3.2. The glasses were produced, in the frame of a collaborative work [211], by a melt-quench route. Batches of 60 g were prepared by thoroughly mixing stoichiometric amounts of (NaPO₃)_n (Carl Roth, 96.5 – 99.5%), Ca(H₂PO₄)₂·H₂O (Chemische Fabrik Budenheim KG), CaCO₃ (Carl Roth, ≥ 99%) and CoCO₃ (Alfa Aesar, 99.5%). The mixtures were calcined at 600 °C for 30 min in quartz crucibles (AdValue Technology, High Form) and subsequently melted in a preheated oven at 1050 °C for 1 h. The melts

Table 3.2: Nominal glass composition in mol% of cobalt-phosphate glasses.

Glass	P ₂ O ₅	CaO	Na ₂ O	CoO
Co0	45.0	30.0	25.0	–
Co0.01	45.0	29.99	25.0	0.01
Co0.05	45.0	29.95	25.0	0.05
Co0.5	45.0	29.5	25.0	0.5
Co1	45.0	29.0	25.0	1
Co2	45.0	28.0	25.0	2
Co5	45.0	25.0	25.0	5
Co10	45.0	20.0	25.0	10

were rapidly quenched between brass plates, annealed at the respective glass transition temperatures, $T_g \pm 5$ °C, for 2 h, and let to cool down overnight. Glasses were crushed in a steel mortar, sieved into different size ranges, and stored in desiccators prior to analysis.

3.2 Compositional Analysis

Glass samples (100 mg, $x \leq 38$ μm) for compositional analysis were digested in volumetric flasks (50 mL), with a mixture of 10 mL of HNO₃ (Merk, Suprapur[®], 65%) and 10 mL deionized water, placed inside an ultrasonic bath for periods of 10 min, to avoid heating, until complete dissolution and filled up to the mark with deionized water. Quantification was carried out with ICP-OES (Optima 5300 DV, Perkin Elmer) using external calibration with matrix-matched (HNO₃ + deionized water) multi-element standard solutions. Glass solutions were diluted with the solvent (deionized water) to obtain analyte concentrations interpolated from the calibration curve. Experiments were performed in triplicates, and results are presented (Table 5.1) as the mean \pm standard deviation (SD).

3.3 Buffer Preparation

Respective masses of tris(hydroxymethyl)amino methane (Sigma-Aldrich, $\geq 99.8\%$) and EDTA tetrasodium salt dihydrate (Roth, $\geq 99\%$) were weighted to obtain 2 L of Tris (0.0250 M) and EDTA (0.0500 M) buffer solutions, transferred quantitatively into 2 L PE beakers and dissolved in about 1800 mL of deionized water + 80% of the corresponding volume of HCl (Roth, 1 M). Solutions were kept in a shaking incubator (37 °C) over night and afterwards the

remaining HCl was added slowly while stirring, to the solution placed inside a water bath (37 °C) until the respective pH for Tris (pH 7.4) and EDTA (pH 10.0) buffers was adjusted. The pH was monitored with a calibrated pH electrode (HI 8314 with pH electrode HI 1217 D, HANNA Instruments). Finally, each solution was transferred quantitatively into a 2 L volumetric flask and filled up to the mark with deionized water.

3.4 Static dissolution Test

Glass samples (50 mg, $125 \leq x \leq 315 \mu\text{m}$) were immersed in 50 mL of Tris buffer solution 0.0250 M (pH 7.4, 37 °C) and maintained in a shaking incubator at 37 °C from 0.25 up to 14 days. After the respective periods of time, samples were filtered (5 μm particle retention, VWR International) and pH measurements of solutions (HI 8314 with pH electrode HI 1217 D, HANNA Instruments) were performed inside a water bath (37 °C). Solutions (30 mL) were acidified using 750 μL of HNO_3 (Merk, Suprapur®, 65%) for ICP-OES analysis, carried out following the procedure described in the compositional analysis, where matrix-matched standards, blanks and dilutions were prepared using the corresponding solvent, Tris buffer 0.0250 M.

3.5 Liquid state ^{31}P NMR Spectroscopy

Quantitative ^{31}P NMR experiments were recorded at 37 ± 1 °C on a Bruker AVANCE III spectrometer, with magnetic field $B_0 = 9.4$ T and equipped with a 5 mm broad band probe (BBFO). ^{31}P spin-lattice relaxation times were determined by inversion-recovery ($180-\tau-90$). The spectra were acquired using a 30° single-pulse of 8 μm , 60 s delay time (D_1) and collecting 64 scans. FID's were exponentially multiplied with a line broadening factor of 1.0 Hz before Fourier transform. D_2O was used as an internal heteronuclear lock on ^2H and chemical shifts were referenced to 85% H_3PO_4 resonating at 0 ppm.

3.5.1 Sample Preparation

The samples were prepared by immersing about 250 mg of glass powder with grain size smaller than 38 μm into 50 mL of the respective buffer solution 0.0250 M. After specific periods of time (7, 10 and 14 days) the pH was measured with a portable pH-meter (Mettler-Toledo AG) at 37 °C. $\text{NaH}_2\text{PO}_4 \cdot 2\text{H}_2\text{O}$ (Carl Roth, $\geq 99\%$), $\text{Na}_4\text{P}_2\text{O}_7 \cdot 10\text{H}_2\text{O}$ (Carl Roth, $\geq 98\%$), $\text{Na}_5\text{P}_3\text{O}_{10} \cdot 6\text{H}_2\text{O}$ (Sigma-Aldrich, $\sim 98\%$) and $\text{Na}_3\text{P}_3\text{O}_9$ (Sigma-Aldrich, $\geq 95\%$) were used to prepare the standard solutions (Tris buffer solution 0.0250 M, pH 7.4, 37 °C) used for peak assignment. Afterwards 495 μL of the solution were transferred into a 5

mm diameter NMR-tube (Type 5HP, Armar Chemicals) and 55 μL D_2O (Sigma-Aldrich, 99,9 atom% D) were added to obtain 4.0 cm height of solution inside the tube. Finally, the samples were stored in a freezer ($-20\text{ }^\circ\text{C}$) previous to the NMR analysis to prevent further reactions in solution. The ^{31}P spin-lattice relaxation times were measured on samples in Tris buffer solution 0.0250 M set at pH₀ 7.4. By taking into account that T_1 of the identified trimetaphosphate [212], as slowest relaxing species.

3.6 X-ray Powder Diffraction (XRD)

XRD patterns were recorded on a Rigaku Miniflex 600 X-ray diffractometer using $\text{Cu K}\alpha$ radiation at a wavelength of 1.5418 \AA (30 kV, 10 mA). Data were collected at room temperature in the 2θ range between 10° and 60° .

3.7 Solid-state ^{31}P MAS NMR

^{31}P single pulse solid-state MAS NMR spectra were recorded at room temperature on a Bruker AVANCE III HD NMR spectrometer with magnetic field $B_0 = 9.4\text{ T}$. Magic angle spinning (MAS) was performed with a commercial 4 mm rotor. All chemical shift values (δ_{iso}) were quoted to 85% H_3PO_4 . Quantitative spectra with 16 accumulations were taken at a spinning frequency of 12.5 kHz and nutation frequency of 62–71 kHz after adjusting the delay time (D_1) to minimum five times the spin-lattice relaxation time (T_1), Table 3.3. The latter was calculated after the measurement of a 2-scan (T_1) saturation recovery experiment followed by further processing such as the fitting of the line-shape of the pseudo 2D spectrum with the Bruker NMR software [213].

3.7.1 Borate-based 45S5 glasses

^{31}P single pulse solid-state MAS NMR spectra were recorded at room temperature on a Bruker AVANCE III HD NMR spectrometer with magnetic field $B_0 = 7.0\text{ T}$. Magic angle spinning (MAS) was performed with a commercial 4 mm rotor. All chemical shift values (δ_{iso}) were quoted with respect to 85% H_3PO_4 . Quantitative spectra with 16 accumulations were taken at a spinning frequency of 10 kHz and nutation frequency of 62.5 kHz after adjusting the delay time ($D_1 \sim 350\text{ s}$) to five times the spin-lattice relaxation time (T_1) of the slowest relaxing species. Signal deconvolutions into Gaussian components were done with the DMFIT software [216].

Table 3.3: ^{31}P MAS NMR parameters: spin-lattice relaxation time (T_1) for Q^0 , Q^1 and Q^2 sites, delay time (D_1) and duration of the pulse (τ_p); used to record quantitative spectra. 45S5-based glasses were analysed in the frame of collaborative works [214, 215].

Glass	Q^0		Q^1		Q^2		D_1 (s)	τ_p (μs)
	T_1 (s)	$5 \times T_1$ (s)	T_1 (s)	$5 \times T_1$ (s)	T_1 (s)	$5 \times T_1$ (s)		
C25			391.3	1956.5	376.4	1882.1	3000	3.845
C27.5			445.1	2225.4	412.2	2061.0	3000	3.780
C30			488.5	2442.6	474.4	2371.9	4000	3.966
C35			627.1	3135.5	615.9	3079.4	4000	4.044
C40			791.7	3958.4	705.8	3529.1	4000	4.000
Co0					25.80	129.00	1000	3.685
Co0.01					24.58	122.90	1000	3.597
Co0.05					18.48	92.425	1000	3.665
Co0.5					5.306	26.530	1000	3.560
Co1					5.305	26.525	1000	3.611
Co2					1.617	8.085	1000	3.611
Co5					0.674	3.370	1000	3.611
45S5		1365.5					5000	
45S5-Mg100	273.1	1365.5					3000	
45S5-Zn25	132.7	663.5					3000	3.500
45S5-Zn50	115.9	579.5					5000	3.600
45S5-Zn75	104.4	522.0					3000	3.580
45S5-Zn100	92.19	460.95					3000	3.680

3.8 Solid-state ^1H MAS NMR

^1H MAS NMR spin-echo solid-state MAS NMR spectra were recorded at room temperature on a Bruker AVANCE III HD NMR spectrometer with magnetic field $B_0 = 7.0$ T. Magic angle spinning (MAS) was performed at 30 kHz. All chemical shift values (δ_{iso}) were quoted to TMS. Spectra with 4096 accumulations were collected using the rotor-synchronized spin-

echo pulse sequence ($\pi/2 - \tau - \pi - \tau$ -acquisition) with $\pi/2$ of 1.5 μs , evolution period (τ) of 98.5 μs and delay time (D_1) of 2 s.

3.9 Solid-state ^{29}Si MAS NMR

^{29}Si single pulse solid-state MAS NMR spectra were recorded at room temperature on a Bruker AVANCE III HD NMR spectrometer with magnetic field $B_0 = 9.4$ T. Magic angle spinning (MAS) was performed with a commercial 4 mm rotor. All chemical shift values (δ_{iso}) were quoted with respect to TMS. Quantitative spectra with 64 accumulations were taken at a spinning frequency of 12.5 kHz with 30° pulses, after full destruction of longitudinal magnetization using a train of 90° pulses; a nutation frequency of 52.6 kHz and a delay time (D_1) of 4000 s. Line broadening of 200 Hz was applied prior Fourier transform. Signal deconvolutions into Gaussian components were done with the DMFIT software [216].

3.10 Solid-state ^{11}B MAS NMR

^{11}B single pulse solid-state MAS NMR spectra were recorded at room temperature on Varian VNMRs 500 spectrometer with magnetic field $B_0 = 11.7$ T. Magic angle spinning (MAS) was performed with a commercial 2.5 mm rotor. All chemical shift values (δ_{iso}) were quoted with respect to $\text{BF}_3 \cdot \text{Et}_2\text{O}$. Quantitative spectra with 128 – 1024 accumulations depending on the B content were taken at a spinning frequency of 30 kHz and nutation frequency of 500 kHz after adjusting the delay time ($D_1 = 50$ s) to five times the spin-lattice relaxation time (T_1).

3.11 Electron Paramagnetic Resonance (EPR)

All EPR measurements were done using a commercial Bruker Elexsys E580 spectrometer at X-band. Oxford Instruments temperature control system was used to maintain cryogenic temperature (7 and 20 K). The weighted powdered samples (typically 11 – 13 mg) were placed into quartz sample tubes (OD 2.8 mm) and investigated. The number of Co^{2+} spins was calculated using a reference Co^{2+} sample with known weight and amount of Co^{2+} nuclei. Modelling of the EPR spectra was done using EasySpin [217].

3.12 Raman

Raman spectra were collected at room temperature using a Renishaw inViaTM Raman spectrometer (Renishaw, Gloucestershire, UK) equipped with a Peltier cooled CCD array

detector, a 2400 lines/mm visible grating and a confocal system. The spectrometer was calibrated using the 520.7 cm^{-1} line of mono-crystalline Silicon (reference sample). Samples were excited with an Argon-Ion laser emitting at 514.5 nm. The light was focused into the polished sample through a Leica microscope equipped with 50x long working distance objective and the back scattered signal was collected through the same objective. All spectra were recorded in the range from 200 to 1400 cm^{-1} with a spectral resolution of $\sim 2\text{ cm}^{-1}$. The Raman spectra were first baseline corrected then the data were corrected for temperature and excitation line effects following Neuville and Mysen (1996) [218]. Finally, Raman spectra were normalized to the intensity of the most intensive band, positioned around 1167 cm^{-1} .

3.13 UV–vis–NIR

UV–vis–NIR absorption spectra were obtained from 200 to 1500 nm using a double-beam spectrophotometer (Cary 5000, Agilent Technologies). Polished samples with 1 mm thickness were measured at a scan speed of 600 nm/min.

3.14 DSC/TGA-MS

Differential scanning calorimetry coupled with thermogravimetric analysis-mass spectrometry (DSC/TGA-MS, Netzsch STA 449 F1 Jupiter TG instrument coupled with a Netzsch QMS 403 C Aëolos MS detector) was carried under N_2 atmosphere (50 mL/min purge and 20 mL/min protective flow) at a heating rate of 10 K/min. About 40 mg of each sample (particle size $< 38\text{ }\mu\text{m}$), was measured in a Pt-Rh pan from 40 to 900 °C. Mass scanning was carried out over the m/Z range of 2 to 200.

The glass transition temperature (T_g) was defined as the onset of the glass transition peak. The melting point was characterised by both the liquidus temperature (T_L) defined as the offset temperature of the melting peak, and the absolute minimum of the melting curve ($T_{m,i}$). The latter was used for comparison with HSM measurements. The crystallisation temperature was taken at the onset point of the crystallisation curve ($T_{c,o}$), while the difference between the crystallisation and glass transition temperatures is referred as the processing window ($\Delta T = T_{c,o} - T_g$).

3.15 Hot Stage Microscopy (HSM)

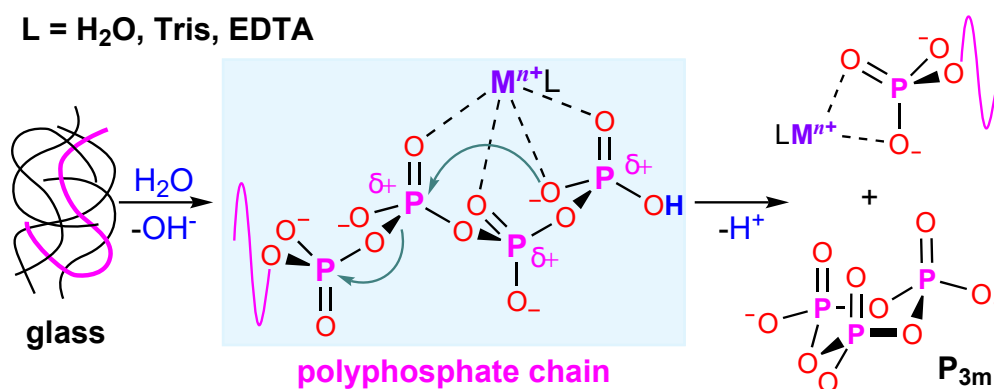
The sintering behaviour of the glass series (size fraction $< 45\text{ }\mu\text{m}$) was studied using hot stage microscopy (HSM, Misura 3.0, Expert System). The heating rate was 40 °C/min to 350 °C and then 5 °C/min to 800 °C. A cylindrical sample (height 3 mm, diameter 2 mm)

pressed from the powdered glass was imaged after every 5 °C increase in temperature. The sintering curve given by the sample height as a function of temperature was used to define the sintering temperature (T_{si}), the starting and ending of the plateau (T_{xi} and T_{xf}), corresponding to the glass crystallisation domain and fusion temperature (T_{fusion}).

Chapter 4

Kinetics and mechanism of cation-catalysed hydrolysis of $P_2O_5-CaO-Na_2O$ glasses: the effect of ligand competition and reactivity of intermediate complexes on ^{31}P NMR spectra

4.1 Abstract



Structural changes in phosphate glasses tailor degradation, which is of interest for biomedical applications such as therapeutic ion delivery. Here, ^{31}P MAS NMR of $45P_2O_5 - xCaO - (55 - x)Na_2O$ glasses was correlated with dissolution kinetics. Glasses dissolved congruently, the first dissolution stage was attributed to the hydration of chains (8 – 9 groups), identified in EDTA via liquid ^{31}P NMR. The mild initial rise in pH was ascribed as protonation of the two terminal groups of chains. Trimeta- and orthophosphate were the predominant species in solution, indicating fast degradation of chains. Hydrolysis was proportional to phosphate complex stability, being the complexes with chains stronger than with rings. Competition between solvent and phosphates for metal ions occurred in the order: EDTA > Tris > H_2O . Coordination of phosphate species with metal ions may play a catalytic role in the hydrolysis mechanism which consist in turning phosphorus into a suitable electrophile, for a subsequent nucleophilic attack by water.

4.2 Introduction

Chemical durability of phosphate glasses can be tailored through compositional modifications, within orders of magnitude [24]. In this regard, different ions have been added, which in turn functionalize glasses for potential biomedical applications, e.g., Ca^{2+} for reinforcement of biodegradable implants [219], bone cell growth [220] and dental cements [221]; Zn^{2+} for bone formation [222] and osteoblast cell adhesion [61]. Co^{2+} and Cu^{2+} have been investigated for tissue regeneration and wound healing owing to their ability to stimulate blood vessel formation [10, 57, 58, 223]. Solubility has been correlated with the cellular reaction *in vitro* [224], and biological response [220]. On the other hand, highly durable glasses such as iron phosphates for vitrifying nuclear wastes are of interest [29, 30, 225].

Various studies have been undertaken on the dissolution behaviour of phosphate glasses. Yet, divergent interpretations have been reported and crucial questions remain unanswered, i.e., regarding the mechanism of hydrolysis of phosphate species [24, 81–83, 86, 226, 227]. On the other hand, previous investigations on condensed phosphates provide unexploited physicochemical foundations to be extrapolated to their glass pairs. Thereby, it is well known that only simple rings and straight chains can exist in aqueous solution [78]. The rate of degradation of phosphate species via hydrolysis follows linear first-order dependence [94]. It increases considerably in acid medium, in contrast with the mild increase in basic conditions [24]. Rate constants are directly proportional to temperature [228]. Rings (primarily trimetaphosphate, $\text{P}_{3\text{m}}$) have been suggested to be the principal degradation product of long chains [75, 76, 95].

Nucleophilic attack by water molecules, via $\text{S}_{\text{N}}2$ reaction, seems to be the most likely mechanism of scission of P–O bonds [97, 109, 229–231]. The catalytic effect of metal complexes on the hydrolytic degradation have been studied [25, 98, 105, 109, 110, 232]. ^{31}P NMR have been used to assess the stability of phosphate-metal complexes, as well as ligand competition for cations between phosphate species and the solvent [233–235]. ^{31}P chemical shifts as a function of pH have been reported [236, 237]. In general, the dissolution behaviour of condensed phosphates has been addressed by performing structural analysis via, e.g., chromatography [75, 76, 81, 89, 95, 238, 239] or ^{31}P NMR [99, 212, 240–242].

The major differences in the current research compared with previous work comprise: (i) The study of the dissolution behaviour of the system, $45\text{P}_2\text{O}_5 - x\text{CaO} - (55 - x)\text{Na}_2\text{O}$ (CNP45, $25 \leq x \leq 40$ mol%, O/P = 3.1), with biomedical potential, under physiological conditions, namely pH 7.4 and 37 °C. (ii) The use of liquid ^{31}P NMR as a sensitive tool to

assess interactions such as: metal-induced shifts, i.e., Na^{1+} and Ca^{2+} ; and ligand-induced shifts, i.e., H_2O , Tris, EDTA and phosphate species. The relationship between the structure of complexes and hydrolysis is discussed. (iii) An attempt to formulate a mechanism of dissolution by combining glass structure by ^{31}P MAS NMR and kinetics, i.e., pH, ICP-OES and liquid ^{31}P NMR.

4.3 Glass System

Table 4.1: Nominal and analysed glass composition (mol%) from ICP-OES, including water content (%) from TGA. Experimental O/P ratio and average chain length \bar{n} from deconvolution of quantitative ^{31}P MAS NMR.

Glass	P_2O_5	CaO	Na_2O	Li_2O	H_2O %	Exp. O/P	\bar{n}
					(± 0.02)	(± 0.07)	(± 0.2)
C25	45.0 (44.0 \pm 0.4)	25.0 (25.1 \pm 0.1)	30.0 (30.8 \pm 0.1)		0.16	3.12	8.5
C27.5	45.0 (44.0 \pm 0.3)	27.5 (27.8 \pm 0.2)	27.5 (28.2 \pm 0.2)		0.16	3.12	8.7
C30	45.0 (43.9 \pm 0.2)	30.0 (30.2 \pm 0.2)	25.0 (25.8 \pm 0.2)		0.11	3.11	8.8
C35	45.0 (43.8 \pm 0.1)	35.0 (35.6 \pm 0.2)	20.0 (20.5 \pm 0.2)		0.12	3.11	8.8
C40	45.0 (44.0 \pm 0.4)	40.0 (40.5 \pm 0.2)	15.0 (15.5 \pm 0.1)		0.47	3.11	9.0
L27.5	45.0 (43.8 \pm 0.4)	27.5 (27.8 \pm 0.2)		27.5 (28.4 \pm 0.2)	0.06	3.11	9.0

4.4 Glass Structure

As can be seen in Fig. 4.1a, the isotropic chemical shifts (δ_{iso}) are typical for P with Q^1 and Q^2 topology. It is evident from the stacked spectra, that a systematic increase in shielding of both resonances occurs with increasing CaO content. Such trend can be addressed as a cation effect related to the higher field strength (Z/r^2) of Ca^{2+} in comparison with Na^+ [45, 51], which subsequently reflects an increase in the covalent character of the M–O bonds [48, 243]. $45\text{P}_2\text{O}_5 - x\text{CaO} - (55 - x)\text{Na}_2\text{O}$ glasses should be comprised by chains, based

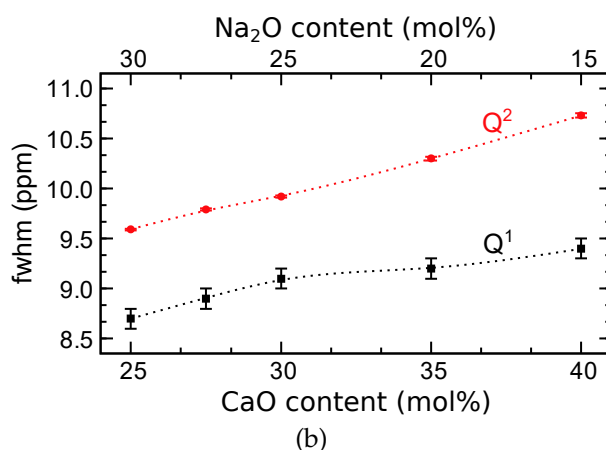
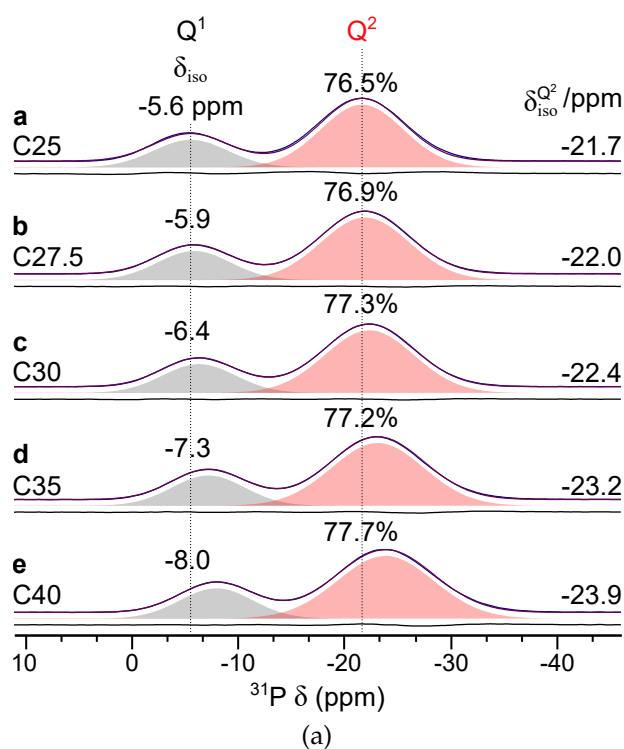


Fig. 4.1: Quantitative solid-state ^{31}P MAS NMR for the series of glasses. (a) Experimental spectra (fuchsia), best-fit (blue) and the difference curve (gray) beneath each NMR spectrum. For the deconvolution [216] into two Gaussian lines corresponding to Q^1 (black) and Q^2 (red, fractional population in %) groups, the spinning sidebands were taken into account. (b) Full width at half maximum (fwhm) of the ^{31}P δ_{iso} peaks ascribed as Q^1 and Q^2 moieties (\pm SD from deconvolution [213]), as a function of nominal composition (lines are guides for the eye).

on composition [22, 41], being the theoretical chain-length equal to 9 phosphate groups. Which is in good agreement with the experimental average chain length, $\bar{n} = 8 - 9$ phosphate groups (Table 4.1), obtained from deconvolution of ^{31}P MAS NMR quantitative spectra. It also confirms constant polymerization $\text{O}/\text{P} \sim 3.11$, as expected for the glass system.

As can be seen in Fig. 4.1b, the full width at half-maximum (fwhm) of δ_{iso} for Q^1 and Q^2 peaks increases with CaO content. Thus, a wider range of P environments, namely bond lengths and angles [45]. The fwhm for Q^1 and Q^2 peaks show a non-linear behaviour as a function of CaO content. Interestingly, below 30 mol% CaO, the fwhm trend lines for both sites remain fairly parallel. It indicates non-preferential distribution of Ca^{2+}/Na^+ in Q^1 and Q^2 sites. Whereas, above 30 mol% CaO, the slope of the fwhm trend line increases for Q^2 , as it resembles a plateau for Q^1 sites. It suggests saturation of Q^1 sites with Ca^{2+} , since the theoretical Q^1/Q^2 ratio is $\sim 2/7$, in the glass system.

4.4.1 Water in the glasses

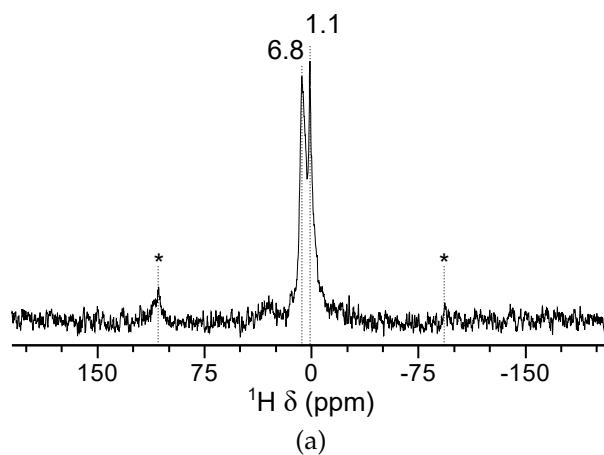


Fig. 4.2: Spin-echo 1H MAS NMR spectrum for the glass L27.5. The MAS spectrum was measured at 30 kHz and quoted to TMS.

Phosphate glasses are known for their potential hygroscopic nature [22], whereby water may act as an additional network modifier in the glass structure [44]. Thus, the water content was assessed via TGA and the maximum amount obtained was equal to 0.47% (Table 4.1). Such relatively low value is in accordance with the good agreement between the theoretical and experimental polymerizations.

1H MAS NMR allows the determination of distinct proton environments, accordingly, studies on silicate and phosphate glasses have shown two main chemical shift ranges. The first 1H environment is related to molecular water (0 – 10 ppm), thus, weak intermolecular hydrogen bonds. Whereas the second one involves structural water (11 – 16 ppm), thus, intramolecular hydrogen bonds such as P–OH groups [244–246].

As can be seen in Fig. 4.2, the 1H MAS NMR spectrum exhibits only two resonances at 1.1 and 6.8 ppm. In this regard, the nature of water in the glass system (Table 4.1) is

assumed to be molecular adsorbed water, which is weakly bound to the phosphate glass network. The fact that two different chemical shifts occur has been associated to adsorption on sites with different acidities [246]. Accordingly, since the glass structure consists of chains comprised of middle (Q^2) and end (Q^1) sites, it may be suggested that the two peaks correspond to adsorbed water in the nearby of each site.

These findings are in good agreement with the low content of water in the glasses, and the good correspondence between the experimental and theoretical polymerizations, as mentioned above. The corrosion process of phosphate glasses involves as initial step the adsorption of water, followed by hydration and hydrolysis [245, 246]. Hence, the glass system seemingly has a relatively high resistance to corrosion under the non-dry experimental conditions, since the nature of the water detected is related to the first step exclusively.

4.5 Dissolution Behavior

4.5.1 ICP-OES analysis

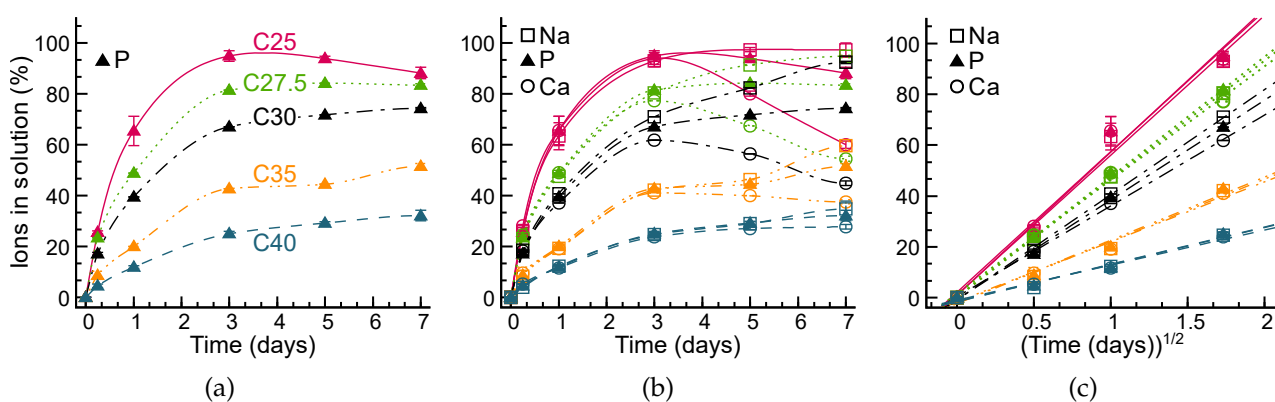


Fig. 4.3: Percentage of glass dissolved in Tris buffer 0.0250 M ($\text{pH}_0 7.4 \pm 0.1$) at 37°C . (a) Percentage of phosphorus, (b) sodium, phosphorus and calcium ($\alpha \pm \text{SD}$) as a function of time (lines are guides for the eye) and (c) as a function of the square root of time (lines are fits, $R^2 > 0.99$, by using the square-root time model [24, 81, 88], $\alpha (\%) = k \times t^{1/2}$) for the glass series.

As discussed above, the glasses are comprised of phosphate chain anions (8 – 9 phosphate groups), connected to one another through Ca^{2+} and Na^+ cations. Since in order to detach the polyphosphate anions from the glass network, $\text{M}-\text{O}$ bonds must be broken. It is expected that the durability increases proportionally to the CaO content [24, 227, 247] as shown in Fig. 4.3a, owing to the higher field strength of Ca^{2+} compared to Na^+ . In addition

to the stronger M–O bonds, molecular dynamics simulations have suggested that calcium ions connect more phosphate fragments and P–O₄ tetrahedra than sodium ions, leading to higher durability [93].

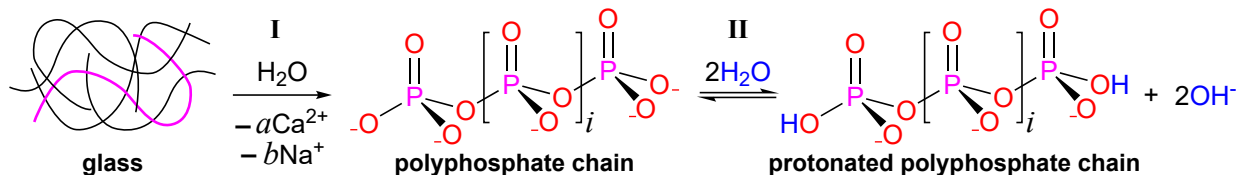
The relative concentrations of Na, P or Ca in solution (Fig. 4.3b) remained fairly equal (within the error limits) up to day 3 and 5 for C25 and C40, respectively. This indicates congruent dissolution [24, 82, 248] and hence no selective leaching of Ca²⁺ or Na⁺ ions occurred. Since only the two Q¹ sites of polyphosphate anions behave as weak bases, thus being able to produce an alkaline reaction [24, 78, 104, 105] through an exchange of Na⁺ or Ca²⁺ for H⁺ from H₂O. It can be inferred that such ion exchange occurs exclusively after complete hydration of a given polyphosphate chain from the glass structure, as shown in Scheme 4.1II, otherwise congruent dissolution would not take place. As shown in Fig. 4.3b, after 3 – 5 days, the concentration of Ca and P decreased in comparison to Na, which suggests saturation of the solution and, subsequently, precipitation of calcium phosphate (CaP) species.

The dissolution kinetics under static conditions have been described as a two-stage process [24]. In the first stage, the process is controlled by water diffusion into the bulk glass (Scheme 4.1I) [24, 249]. The hydration process may be considered as a chemical reaction, and in order to hydrate the chains, existing intermolecular interactions in the solid and solvent should be broken i.e., M–O bonds and water-water hydrogen bonds (19 kJ/mol) to form the hydrated ions. However, the formation of water-polyphosphate interactions (hydration) requires in the first place mass transfer of water molecules into the bulk glass, to allow the encountering between the reaction pair [250]. Thus, the reaction occurs simultaneously with diffusion and causes a reduction of the free diffusant concentration, leading to a diffusion coefficient reduced by the reaction rate [85]. In this regard, the increase in durability of the glass system may be addressed as the effect of a progressively slower reaction, with increasing content of Ca²⁺ ions, occurring simultaneously with the diffusion of water into the glass. Such diffusion-controlled reaction, determines the kinetics of the dissolution process at early time periods [24].

During the first stage of dissolution the release of the cumulative amount of glass shows a direct proportionality to $t^{1/2}$ [24, 81]. The description is based on a pseudo-steady state model, in which the concentration gradient remains relatively constant, thus, it applies for very diluted solutions and particles approximately log-normally distributed [88]. The length of the first stage has been reported to be proportional to the durability of the glass [30, 81]. The square root dependency on time gave satisfactory fits to the experimental dissolution profiles (Fig. 4.3c), at the early stages of glass dissolution, thus concentrations

well below saturation. Condition that seems fairly fulfilled by the glass system before 3 – 5 days. Penetration of water into the glass may not be affected by convection, therefore, a dissolution process controlled by the first step should be independent of the stirring speed in diluted solutions, as observed by [82].

During the second stage of the dissolution process fully hydrated chains (8 – 9 PO₄ groups) together with Na⁺ and Ca²⁺ ions are released congruently from the solid matrix (4.1I). This process undertakes linear reaction kinetics and it dominates at later time periods [24, 81, 86, 248]. The second step corresponds to the mass transport of the extracted ions from the solid-liquid interface to the bulk solution [85]. At early stages the rate of diffusion of hydrated ions from the glass interface across the diffusion layer to the bulk solution [251–253], is much faster than the diffusion of water into the glass surface. Nevertheless, excluding natural convection, e.g., density and thermal gradients, under static conditions the diffusion layer is growing in thickness with concomitant decrease of the concentration gradient. The second step becomes important and rate-determining at later time stages. As can be seen in Fig. 4.3a, for the glass system, the dissolution profile of P reaches a plateau or even decreases in the glass system after 3 – 5 days, as the concentration gradient decreases until it becomes zero, saturation [254, 255].



Scheme 4.1: I. Hydration of 45P₂O₅ – xCaO – (55 – x)Na₂O glass series. Congruent dissolution: concomitant release of a phosphate chain (highlighted in fuchsia) and cations from the glass into aqueous solution; with $i = Q^2$ moieties (from MAS NMR, theoretical value = 7), $a = [x(i + 2)] / (45 \cdot Z_{Ca})$ and $b = [(55 - x)(i + 2)] / (45 \cdot Z_{Na})$, with $Z = \text{charge}$. II. Rise of pH: basic character of Q¹ moieties of phosphate chains in aqueous solution [78, 105] (For the sake of simplicity hypervalent Lewis pictures are used, however, they do not aim to represent the bonding situation of P) [43].

4.5.2 pH analysis

A pH rise occurred at early time points (Fig. 4.4) of dissolution tests in Tris buffer solutions (pH₀: 7.4 and 7.9) or deionised water (pH₀ 5.5), which was also observed for related glasses in the literature [81, 247]. This effect was more prominent in the unbuffered medium (Fig. 4.4c). As discussed above, the glass system is comprised of polyphosphate chains ($\bar{n} \sim 9$). Since the Q² groups in such chains are expected to be strongly acidic [24, 78, 104, 105], only the Q¹ groups are capable of affecting the pH. Phosphate Q¹ anions behave as weak bases,

whose basicity decreases, K_{a4} from $\sim 10^{-10}$ for pyrophosphate [106, 256] to $\sim 10^{-8}$, as the chain is lengthened [78]. Protonation of the two Q^1 groups of a polyphosphate chain, Scheme 4.1II, should occur only until the polyphosphate chain is completely hydrated, Scheme 4.1I, to be consistent with congruent dissolution [24].

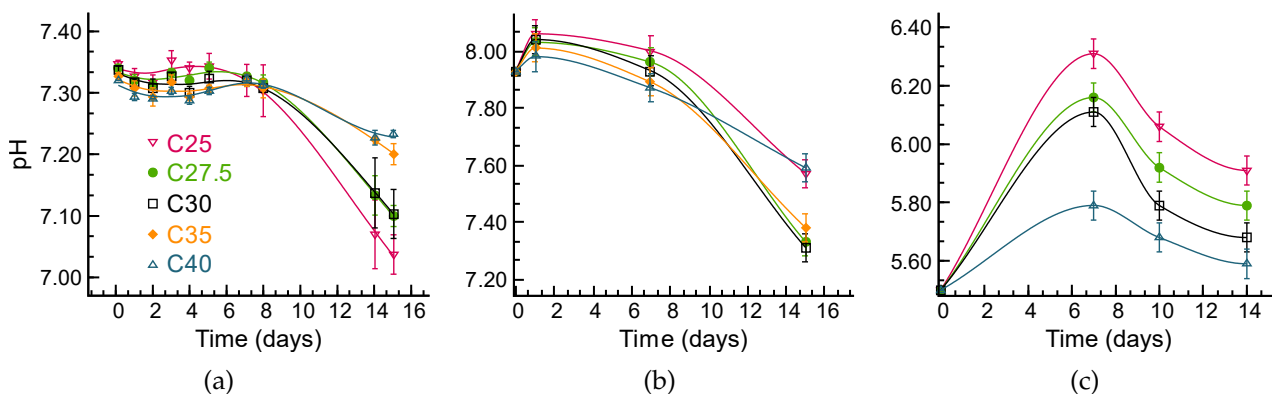


Fig. 4.4: pH (\pm SD) of the leachate solutions at 37 °C in Tris buffer 0.0250 M at (a) pH_0 7.4 ± 0.1 , (b) pH_0 7.9 ± 0.1 and in (c) deionized water at pH_0 5.5 ± 0.1 (lines are guides for the eye) for the glass series.

The fact that the average chain length in solution has been found to correspond to the calculated one in the glass [24, 81], suggest that scission of P–O–P bonds does not occur on the glass surface but rather on the bulk solution. As discussed above, the glass system is exclusively comprised of chains. Hence, the predominant presence of the trimetaphosphate ring P_{3m} (as will be discussed below), is a consequence of a cleavage of P–O–P bonds from the chain [75, 76, 95, 230] in the bulk solution, rather than a hydration product from the glass. The strong acidity of cyclic phosphates, i.e., tri- (P_{3m}) and tetrametaphosphate (P_{4m}) [79, 80, 107], implies the full release of the two protons gained by the Q^1 groups, Scheme 4.1II, providing that the ring-formation involves the endings of the chain [76, 257], Scheme 4.2. Thus, summing up the effect of protonation of Q^1 groups and ring closing, the net effect on the pH should be zero after a given time. However, accumulation of weak acidic species produced during scission of P–O–P bonds by hydrolysis, Scheme 4.3, account for the monotone decrease on the pH at late time periods.

4.5.3 Liquid ^{31}P NMR Spectroscopy

Tris buffer solution, pH 7.4

The species in solution were identified by dissolving commercial grade reagents in Tris buffer set at pH 7.4 (Fig. 4.5a and Table 4.2). However, the assignment of chemical shifts of larger cyclic metaphosphates than P_{3m} , i.e., tetra- P_{4m} , penta- P_{5m} and hexametaphosphate P_{6m}

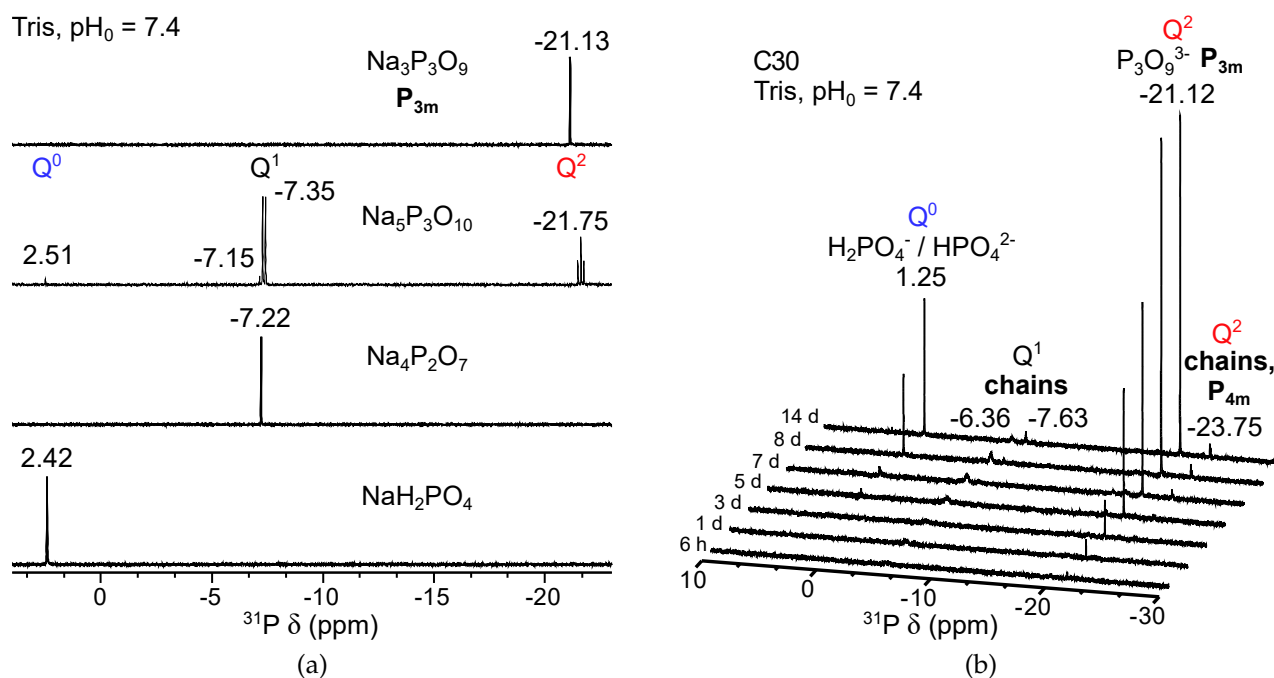


Fig. 4.5: Liquid ^{31}P NMR at $37\text{ }^\circ\text{C}$ in Tris buffer 0.0250 M ($\text{pH}_0\ 7.4 \pm 0.1$). (a) Spectra of standard solutions used for peak assignment with polymerization groups highlighted: Q^0 (blue), Q^1 (black) and Q^2 (red). NaH_2PO_4 : 2.42 (s, Q^0); $\text{Na}_4\text{P}_2\text{O}_7$: -7.22 (s, Q^1); $\text{Na}_5\text{P}_3\text{O}_{10}$: 2.51 (s, Q^0 , hydrolysis product), -7.15 (s, Q^1 , hydrolysis product), -7.35 (d, $J_{\text{PP}} = 21.65\text{ Hz}$, Q^1), -21.62 (t, $J_{\text{PP}} = 21.65\text{ Hz}$, Q^2); and $\text{Na}_3\text{P}_3\text{O}_9$ ($\text{P}_{3\text{m}}$): -21.13 (s, Q^2). (b) Spectra of the leachate solutions of glass C30 as a function of time (from 6 h to 14 d), with peaks assigned: polyphosphate chains, tri- $\text{P}_{3\text{m}}$ and tetrametaphosphate $\text{P}_{4\text{m}}$.

(Fig. 4.6a and Table 4.3), was based on literature [99, 238, 258]. In Fig. 4.5b can be seen the

Table 4.2: ^{31}P NMR at $37\text{ }^\circ\text{C}$. Chemical shifts ($\delta \pm 0.01\text{ ppm}$) of $\text{Q}^{(n)}$ groups, multiplicity (s: singlet, d: doublet and t: triplet) and $\text{P}-\text{O}-\text{P}$ spin coupling ($^3J_{\text{PP}}$) of standard substances in Tris buffer 0.0250 M ($\text{pH}_0\ 7.4 \pm 0.1$, $37\text{ }^\circ\text{C}$) used for peak assignment; with respect to $85\% \text{H}_3\text{PO}_4$.

Glass	pH_0 (Tris)	δ (ppm)			$^3J_{\text{PP}}$ (Hz)
		Q^0	Q^1	Q^2	
$\text{Na}_3\text{P}_3\text{O}_9$	7.4			-21.13 (s)	
$\text{Na}_5\text{P}_3\text{O}_{10}$	7.4	2.50 (s)	-7.15 (s), -7.35 (d)	-21.62 (t)	21.65
$\text{Na}_4\text{P}_2\text{O}_7$	7.4		-7.22 (s)		
NaH_2PO_4	7.4	2.42 (s)			

^{31}P NMR spectra of C30 in Tris buffer ($\text{pH}_0\ 7.4$) as a function of time. The trimetaphosphate ring ($\text{P}_{3\text{m}}$, Q^2) is steadily the predominant species, being noticeable already at 6 h leaching time. It seems that two factors combine simultaneously in its predominance. Namely, a

Table 4.3: ^{31}P NMR at 37 °C. Chemical shifts of Q^2 groups of trimetaphosphate ($\text{P}_{3\text{m}}$) and tetrametaphosphate ($\text{P}_{4\text{m}}$) complexes with respect to 85% H_3PO_4 .

Solvent (L)	pH_0	Q^2 / δ (ppm)		
		$\text{P}_{3\text{m}}$	$\text{M}^{n+}(\text{L})(\text{P}_{3\text{m}})$	$\text{M}^{n+}(\text{L})(\text{P}_{4\text{m}})$
H_2O	5.5		-21.10 (± 0.01)	-23.70 (± 0.01)
Tris	7.4		-21.12 (± 0.01)	-23.71 (± 0.01)
Tris	7.9		-21.14 (± 0.01)	-23.71 (± 0.01)
EDTA	10.0	-21.02 (± 0.02)	-21.22 (± 0.02)	

very favorable formation from polyphosphate chains [76, 95, 97, 105, 230] together with a high stability in aqueous solution at around neutral pH [97, 108, 259]. Hence, the hydrolytic degradation path may involve an initial scission of chains ($\bar{n} \sim 9$) in solution into mainly the $\text{P}_{3\text{m}}$ ring (Scheme 4.2).

Larger rings were also identified, i.e., tetra- $\text{P}_{4\text{m}}$, penta- $\text{P}_{5\text{m}}$ and hexametaphosphate $\text{P}_{6\text{m}}$. However, at significant much lesser proportions than $\text{P}_{3\text{m}}$. Helical conformation of polyphosphates in solution may account for probability of ring formation, being $\text{P}_{3\text{m}}$ particularly favorable [99, 105]. In general cyclic metaphosphate are resistant to hydrolysis [97, 257, 258]. However, the stability of a ring decreases as its structure flexibility increases [79, 97, 258, 260], which is related to the catalytic effect of metal complexes on the hydrolytic degradation, as will be discussed below. Cleavage of $\text{O}-\text{P}-\text{O}$ bonds of condensed phosphates lead ultimately to accumulation of orthophosphate [76, 94, 257]. Nevertheless, the concentration of orthophosphate (Q^0) becomes ostensible only after 5 d leaching time. Such delayed build-up of orthophosphate suggests a stable intermediary source, namely rings such as $\text{P}_{3\text{m}}$ (Scheme 4.3). The low intensity of resonances corresponding to end- Q^1 and middle Q^2 groups of chains throughout time, points out the lability of chains compared with rings [95, 257]. Which is another fact supporting a favored degradation path through rings. Since an alternative path involving successive cleavage of polyphosphate chains ($\bar{n} \sim 9$) into shorter chains, instead of $\text{P}_{3\text{m}}$ rings, would mean a much rapid build-up of orthophosphate. For the same reasons, scission of polyphosphates into $\text{P}_{3\text{m}}$ rings may take place preferably at the end of the chains [76, 257], supporting a decrease of pH owing to the strong acidity of rings (Scheme 4.2) as discussed above.

^{31}P chemical shifts as a function of pH

Cyclic metaphosphates were identified owing to their strong acidity (Fig. 4.6a), which meant that their ^{31}P chemical shift was not affected by pH as long as the pH remained above 2 [79, 236, 258, 259] as well as its single sharp ^{31}P resonance [258, 260, 261]. Thereby,

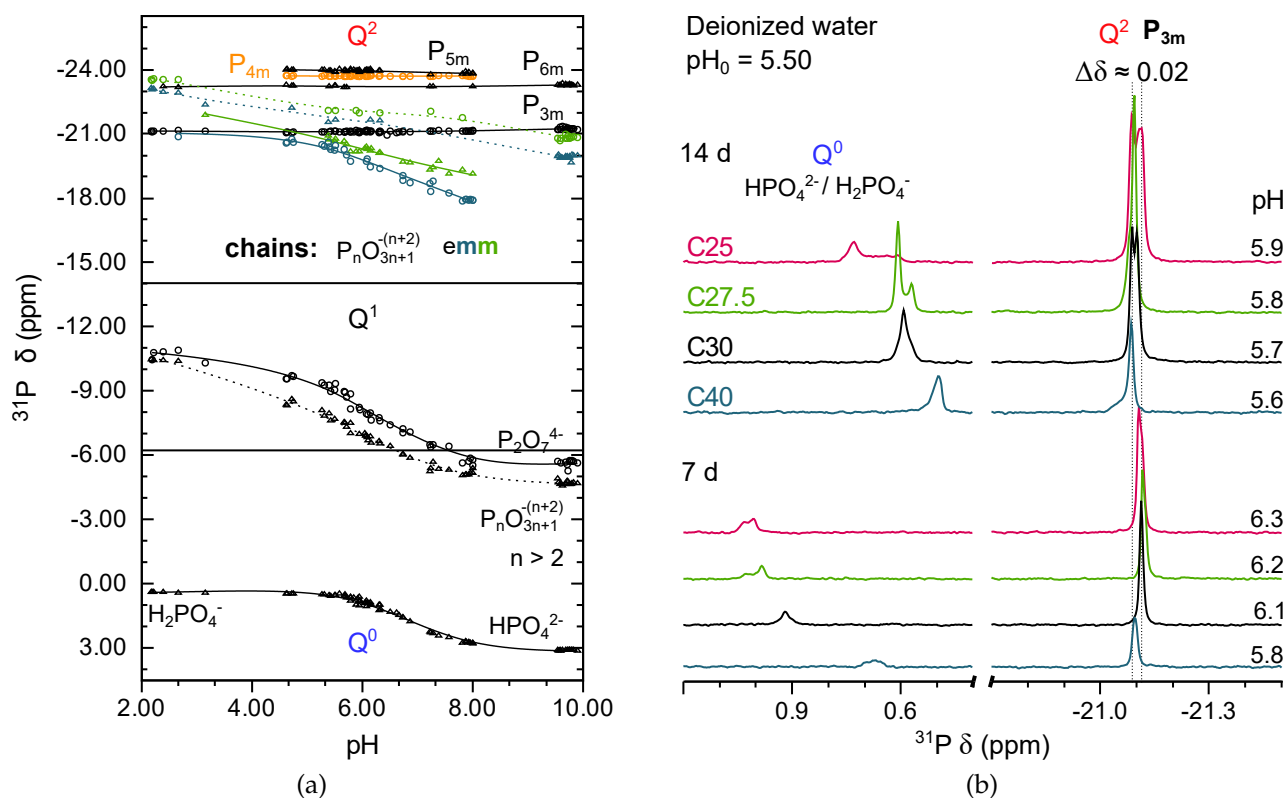


Fig. 4.6: (a) ^{31}P chemical shifts δ as a function of pH at 37 °C, with cyclic metaphosphates as: tri- P_{3m} , tetra- P_{4m} , penta- P_{5m} and hexametaphosphate P_{6m} ; end- (e) and middle (m) groups of chains ($\text{P}_n\text{O}_{3n+1}^{-(n+2)}$). (b) Liquid ^{31}P NMR at 37 °C of the leachate solutions for the glass series in deionized water ($\text{pH}_0 = 5.5 \pm 0.1$) after: 7 d ("early" time), P_{3m} single peak and 14 d ("late" time), P_{3m} peak splitting ($\Delta\delta \approx 0.02$). pH-dependence for the Q^0 peak is also evident.

P_{3m} : -21.15 ± 0.07 ppm, P_{4m} : -23.70 ± 0.02 ppm, P_{5m} : -23.93 ± 0.07 ppm; and P_{6m} : -23.26 ± 0.05 ppm. It can be noticed that the ^{31}P chemical shift of ring structures do not vary correspondingly with the number of phosphorus atoms. Such behaviour has been ascribed as a result of preferential average conformations [99, 105]. The standard deviation associated to the respective ^{31}P chemical shifts and signal line-width reflects, among other aspects, the influence of cations in solution [241, 262]. Regarding polyphosphates, the resonances corresponding to Q^1 and Q^2 groups are pH sensitive [236] (Fig. 4.6a) and exhibit multiplet structure owing to ^{31}P spin coupling, whose spin coupling constants J_{PP} are affected by cations [263]. The Q^1 signals of end groups from chains ($\text{P}_n\text{O}_{3n+1}^{-(n+2)}$, $n > 2$) were not resolved and less shielded than the single peak of pyrophosphate ($\text{P}_2\text{O}_7^{4-}$), throughout the pH range [236, 240]. In contrast, four different Q^2 signals of middle groups from chains ($\text{P}_n\text{O}_{3n+1}^{-(n+2)}$) were identified. In general the further the middle- (m) from the end (e) group, the more shielded the Q^2 resonance, but no regular trend between such Q^2 shifts and the length of the

chain has been found [240]. Nevertheless, by taking into account the discussion above, the Q^2 groups might be ascribed as hydrolysis products of the identified cyclic metaphosphates [238, 257–259], thus, chains most probably with sizes up to 6 phosphorus atoms.

Effect of Na^+ and Ca^{2+} on ^{31}P peak splitting

In Fig. 4.6b can be seen, that at 7 d leaching time, the glass series exhibits a P_{3m} single resonance line, corresponding to three phosphorus atoms chemically and magnetically equivalent [212]. Nevertheless, after 14 d leaching time, a splitting of the P_{3m} resonance occurs ($\Delta\delta \approx 0.02$ ppm) for the less durable glass, C25. Simultaneously, the full width at half-maximum (fwhm) for such split-peak becomes more than twice as for P_{3m} single peaks, thus 6.60 ± 0.05 Hz and 3.00 ± 0.05 Hz, respectively. As cations form complexes with phosphates, they withdraw electron density from P–O bonds [262, 263]. The appearance of the more shielded bifurcation of the P_{3m} resonance, is evidence of Na^+ replacing Ca^{2+} in the complex [241, 263], since the former by having lower field strength (Z/r^2), draw less electron density from P–O bonds. This indicates a favourable equilibrium towards the formation of binary complexes between P_{3m} and Ca^{2+} , compared with Na^+ , as expected [25, 259, 264]. Hence, P_{3m} peak splitting occurs at "late" time periods, when the concentration of Ca^{2+} ions in solution becomes scarce owing to precipitation of Ca/P species. This also evidences the rapid exchange between metal cations bound to phosphate anions [263]. Unlike P_{3m} , the ^{31}P δ for orthophosphate species Q^0 is sensitive to pH changes, specially in the 5 – 8 range (Fig. 4.6a). As observed in Fig. 4.6b, the ^{31}P resonance for Q^0 splits 7 d earlier than for P_{3m} , which occurs at 14 d for C25. Since such peak splitting is attributed to Na^+ replacing Ca^{2+} in the complex. Even though, Na^+ forms weak complexes, stability constants with Q^0 have been reported, being as expected higher for Na^+ [235]. The earlier splitting is an indication of the poorer complexing ability of orthophosphate species compared to P_{3m} [25, 265, 266]. Since the stability of a complex is proportional to the charge of the ligand and to the number of donor groups [235, 267], being in both cases higher for P_{3m} ($P_3O_9^{3-}$) as compared with Q^0 ($HPO_4^{2-}/H_2PO_4^-$). Hereby, it is necessary to point out that owing to the fast hydrolysis of polyphosphates, as discussed above, competition for complexation with cations takes place mainly between P_{3m} and orthophosphate anions [234].

Effect of Tris on the hydrolysis

Figs. 4.5b, 4.7a and 4.7b, correspond to time-dependended spectra of the glass system leaching in Tris pH 7.4, deionized water and Tris pH 7.9, respectively. The conjugated base of Tris (tris(hydroxymethyl)amino methane) is a stronger Lewis base than H_2O , thus it forms stronger complexes, $M(\text{Tris})$. Tris has a $pK_a = 7.71$ at $37^\circ C$, calculated taken into account the pK_w value for liquid water at $37^\circ C$ [268]. At $pH = 7.4$ (0.0250 M) the alpha value

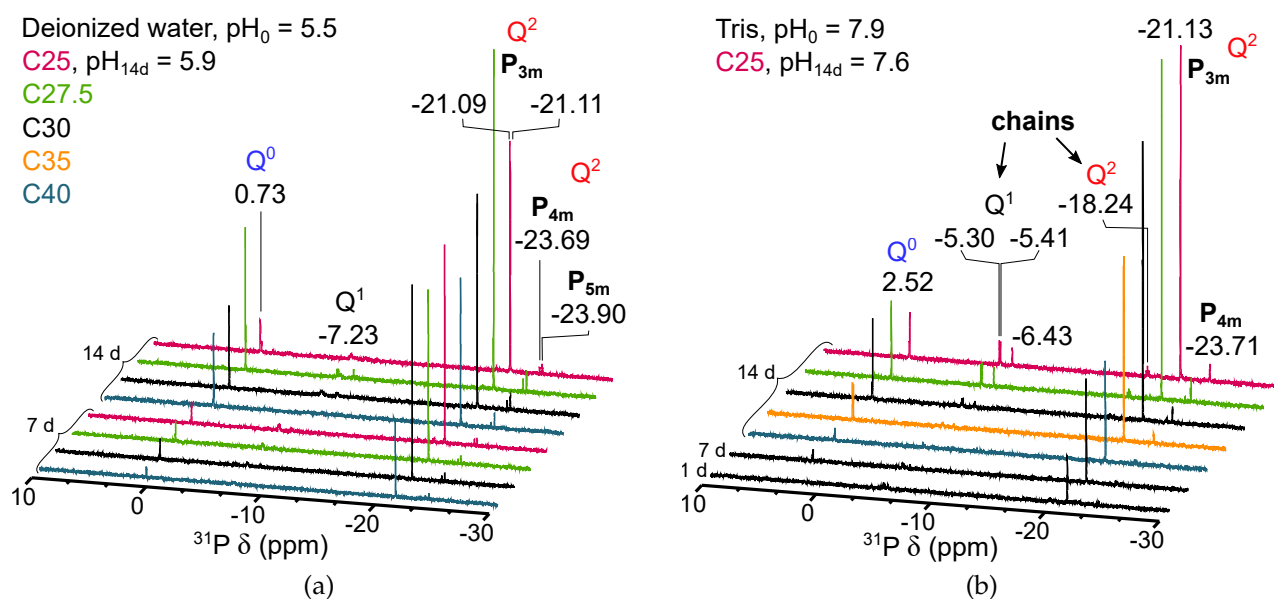


Fig. 4.7: Liquid ^{31}P NMR at 37°C of the leachate solutions for the glass series, with cyclic metaphosphates as: tri- P_{3m} , tetra- P_{4m} and pentametaphosphate P_{5m} . (a) In deionized water at $\text{pH}_0 5.5 \pm 0.1$ and (b) in 0.0250 M Tris buffer at $\text{pH}_0 7.9 \pm 0.1$ as a function of time (from 1 to 14 d).

($\alpha = [\text{A}^-]/[\text{AH}]$) is equal to 0.52, which means that the concentration of the conjugated base $[\text{A}^-]$ is about half of its conjugated acid $[\text{AH}]$. While Tris at pH 7.9 has an alpha value equal to 1.6, thus a concentration of $[\text{A}^-]$ of about 62%. Since the scission of $\text{O}-\text{P}-\text{O}$ is catalyzed by cations, as will be discussed below (Schemes 4.2 and 4.3). It is expected that the degradation of phosphates is less effectively catalyzed by $\text{M}(\text{Tris})$ as by $\text{M}(\text{H}_2\text{O})$. As Tris undergoes the highest competition for Na^+ and Ca^{2+} with phosphate species. In that sense, it can be rationalized that the concentration of phosphate chains increases as the strength and proportion of Lewis bases $[\text{A}^-]$ competing for cations increases. Therefore, the relative intensity of resonances corresponding to end- Q^1 and middle Q^2 groups of chains vary as follows: $\text{H}_2\text{O} < \text{Tris pH } 7.4 < \text{Tris pH } 7.9$, being more notorious for the weaker glasses (C25 and C27.5) at 14 d.

Effect of EDTA on the hydrolysis

Fig. 4.8a shows liquid ^{31}P NMR spectra of the glass system in EDTA set at $\text{pH}_0 10.0$. Even though, the peak corresponding to P_{3m} is still predominant throughout time, the intensity pattern between $\text{Q}^{(n)}$ resonances evidences a significant contrast, as compared with the patterns obtained in Tris (pH: 7.4, 7.9) and deionized water, Figs. 4.5b, 4.7b and 4.7a, respectively. Namely: (i) the proportion of end- Q^1 and middle Q^2 groups of chains was greatly increased, which is in accordance with long polyphosphate chains in EDTA solution identified through

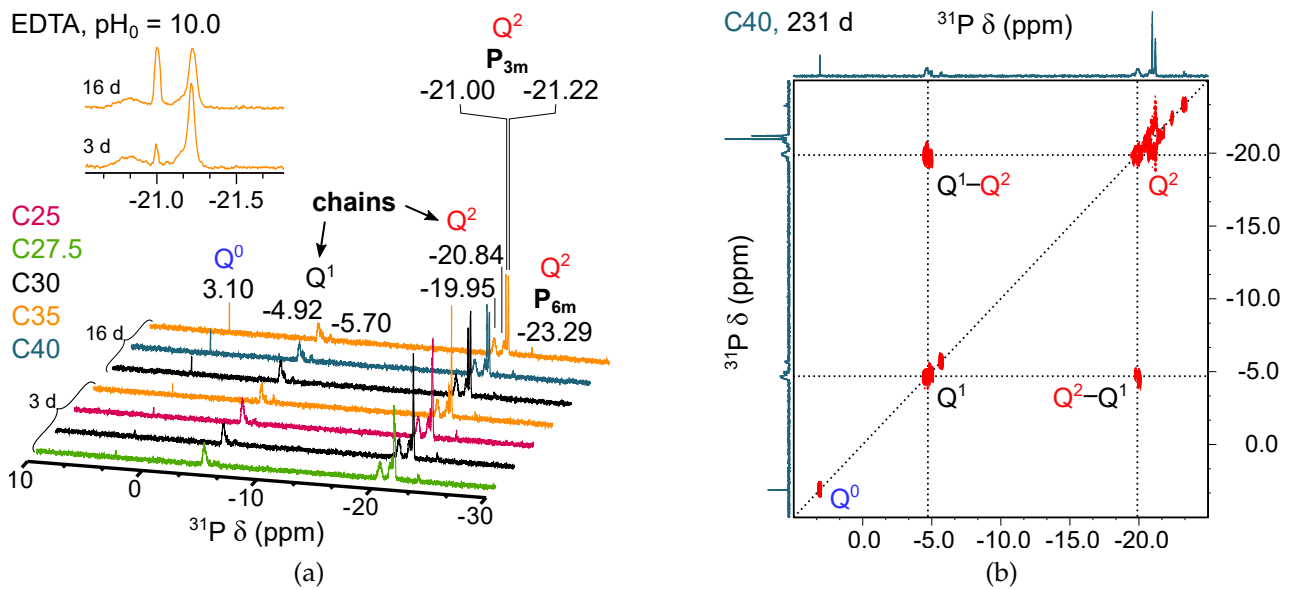


Fig. 4.8: Liquid ^{31}P NMR at 37°C in EDTA pH_0 10.0 ± 0.1 , with cyclic metaphosphates as: tri- $\text{P}_{3\text{m}}$ and hexametaphosphate $\text{P}_{6\text{m}}$. (a) Spectra of the leachate solutions of the glass series, from 3 to 16 d. (b) ^{31}P COSY of the leachate solution of C40 glass after 231 d.

chromatography [29]. (ii) The intensity pattern remains relatively constant throughout the glass series and time. (iii) Orthophosphate builds up mildly (Q^0), even at later time points (16 d). Altogether, these facts indicate a substantial reduction in the rate of hydrolysis under the current experimental conditions. This is further supported by ^{31}P COSY of a leachate solution of glass C40 (Fig. 4.8b), which clearly shows the cross peaks corresponding to the J-coupling between end- Q^1 and middle Q^2 groups of chains, even after a leaching time of 231 d. Time in which no signs of precipitation of Ca/P species are observable either.

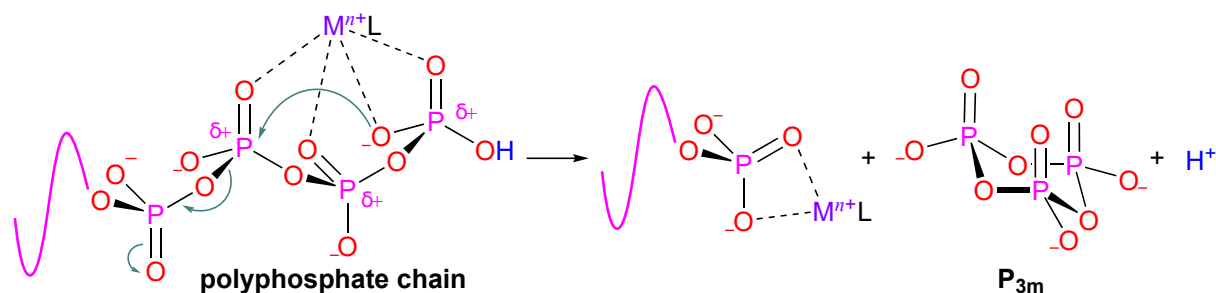
EDTA (ethylenediaminetetraacetate) is a hexadentate ligand, with $\text{p}K_6 = 10.37$ (NH^+) and at pH_0 10.0, the alpha value $\alpha = [\text{Y}^{4-}]/[\text{HY}^{3-}] = 0.3$ (20°C) [269]. The buffer capacity allowed the pH to remain fairly constant upon time. The formation constant, K_f , of the complex $\text{Ca}(\text{EDTA})$ is orders of magnitude higher, as compared with the rigid $\text{Ca}(\text{P}_{3\text{m}})$ complex [25, 269]. In general, K_f increases with the number of the charges of the ligand [235]. In spite, the substantial increase of K_f for complexes between Ca^{2+} and polyphosphates ($\text{P}_n\text{O}_{3n+1}^{-(n+2)}$) [25, 234, 235], owing to the charge, the stability of the $\text{Ca}(\text{EDTA})$ complex is still higher. Hence, it can be safely assumed that Ca^{2+} ions are quantitatively complexed with EDTA and that dissociation of $\text{Ca}(\text{EDTA})$ is negligible. Nevertheless, Ca^{2+} is large enough to accommodate more than six ligand atoms, ternary eight-coordinate complexes such as the $\text{Ca}(\text{EDTA})(\text{H}_2\text{O})_2^{2-}$ have been reported [270, 271].

Phosphate species, as stronger Lewis bases, have the potential to replace water as addi-

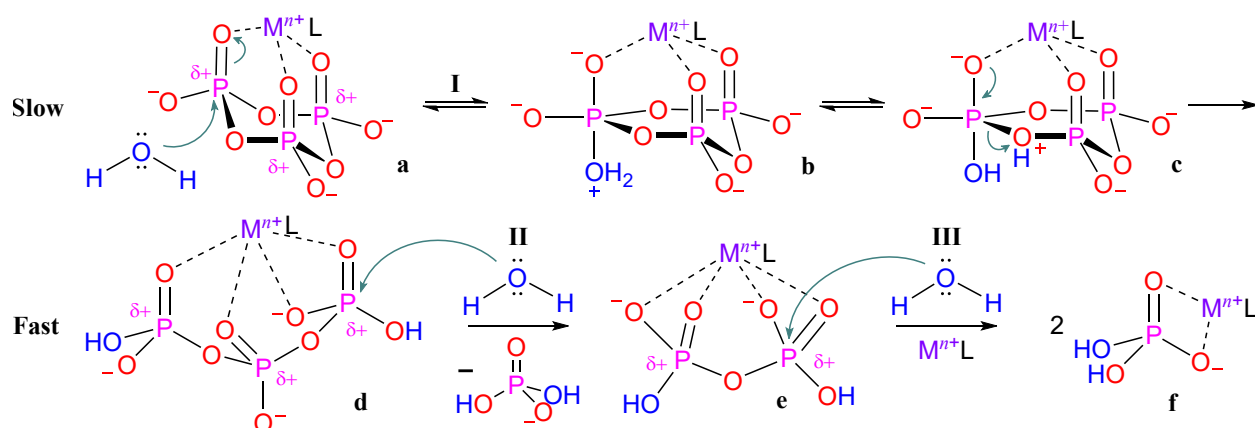
tional ligand, e.g, P_{3m} forms weak ternary complexes with lanthanides and EDTA such as $La(EDTA)(P_{3m})$ [233, 234]. Taking into account that Ca^{2+} exhibits a pronounced preference for eightfold coordination [270], and also considering the electronic repulsion and steric hindrance that occur between ligands in the complex [234]. It may be expected that P_{3m} adopts the boat conformation, as a bidentate ligand [233, 272], to form $Ca(EDTA)(P_{3m})$. Hence, causing an appreciable upfield shift ($\Delta\delta \approx 0.1$) of the P_{3m} resonance (-21.20 ± 0.02 ppm), as compared with the P_{3m} shift in Tris and water, where P_{3m} coordinates most probably in a tridentate fashion [233, 234]. In contrast with Ca^{2+} , no more than six ligands can be inserted in the coordination sphere of Na^+ [267].

The weak constants of formation of the $Na(EDTA)$ and $Na(P_{3m})$ complexes are comparable in magnitude [25, 267], hence, ligand competition is expected. The dissociation into the free P_{3m} from complexes with Ca^{2+} and/or Na^+ seems to be slow on the NMR time scale, which resulted in separated signals. The bifurcation appears at lower field ($\Delta\delta \approx 0.2$) and its intensity increases gradually upon time. The high stability of $Ca(EDTA)$ and the weak nature of Na^+ complexes lead to a poor catalytic effect of such on the O–P–O scission. In spite of the remarkable decrease of the hydrolysis in EDTA, it still takes place even on the stable P_{3m} ring, since the build-up of chains and rings of different sizes, including orthophosphate, is associated to cleavage of polyphosphates from the glass. Thus, the weak but existing interaction between cations and phosphate species may still catalyse the degradation process in EDTA [234] (Schemes 4.2 and 4.3).

4.6 Mechanism of hydrolysis



Scheme 4.2: Formation of trimetaphosphate (P_{3m}) from a hydrated polyphosphate chain [75–77] (chain tail as a line in fuchsia), reaction catalyzed by a metal cation M^{n+} complexed in a polydentate manner with phosphate species and another ligand (L: H_2O , Tris, EDTA, etc) depending on the coordination number (CN) of M^{n+} and steric effects. Decrease of pH during P_{3m} formation owing to its strong acidity [78–80] (For the sake of simplicity hypervalent Lewis pictures are used, however, they do not aim to represent the bonding situation of P) [43].



Scheme 4.3: Mechanism of hydrolysis of trimetaphosphate, P_{3m} . The metal cation M^{n+} acts as a catalyst, which by complexing with phosphate groups increases its electrophilic character δ^+ , favoring nucleophilic attack by water [229]. **I**. Addition of water to a rigid complex $M^{n+}(L)(P_{3m})$, L: H_2O , Tris, EDTA, etc; may lead to a higher E_a for the formation a five-coordinated phosphorus in the transition state [77, 100]. **II**. Hydrolysis of tripolyphosphate and **III**. pyrophosphate is faster, owing to the more flexible nature of chain-complexes, which may lead to a comparatively lower E_a . (For the sake of simplicity hypervalent Lewis pictures are used, however, they do not aim to represent the bonding situation of P) [43].

The hydrolysis of condensed phosphates is reminiscent of a bimolecular nucleophilic substitution, S_N2 [97, 229, 231]. Where the solvent in this reaction, water, works also as a nucleophile. Hence, the reaction follows first-order kinetics [94, 97, 102, 229–231, 257], instead of the expected second-order law characteristic of a concerted process [273].

The relative facility of S_N2 -type reactions depends on several factors: (i) The leaving group, an electron pair of the π bond of $P=O$, gets displaced by water as nucleophile (Scheme 4.3a). Since weak bases are good leaving groups, the conjugated acids of phosphates, $[P-O-H]^+$, are better leaving groups (Scheme 4.3c). That may address the dramatic rate increase of hydrolysis rate in acid medium [24, 94, 102].

(ii) The reactivity of the nucleophile, where the basicity correlates with its strength, thus, HO^- is more nucleophilic than H_2O . Therefore, it would be expected a considerable increase of the hydrolysis rate with pH. However, protic solvation weakens substantially the nucleophile strength by hydrogen bonding [110, 229, 230]. That may account for the mild increase of hydrolysis rate in aqueous basic solution [24, 94, 230].

(iii) The electrophilic nature of the substrate. Since nucleophilic attack takes place on an electrophilic centre, the polarization (δ^+) of the $P=O$ bond [109, 110], is as a necessary initial step. As can be seen in Scheme 4.3, such polarization can be achieved by cations in

general $[P-O-M]^{n+}$, including protons. The catalytic effect of cations is proportional to Z/r^2 ratio [25, 98, 105, 109, 110, 232, 274]. Cations interact simultaneously with different ligands (L) in solution depending on their CN and other factors [233, 234], as discussed above. The suggested mechanism corresponds to an electrophilic cation-addition, which is suited for reactions of relatively weak nucleophiles such as water [273].

(iv) The structure of the substrate. Cyclo metaphosphates are comprised exclusively of middle Q^2 groups, thus the reactive center is a middle group surrounded by equals. That creates a substantial higher steric repulsion with the incoming nucleophile (Scheme 4.3a), as compared with the less crowded chain (Scheme 4.3d). That also implies that in the latter, nucleophilic attack may be more favorable through end- Q^1 instead of middle Q^2 groups [76, 257] (Scheme 4.3II). Folding into conformations in order to unblock the backside for nucleophilic attack, may be an additional role of the cations. Effect more efficient in flexible structures such as chains in comparison with the rigid rings. Altogether, such factors account for the slow hydrolysis (Scheme 4.3I) of cyclo metaphosphates [97, 257, 258] related to the fast hydrolysis of chains (Schemes 4.3II and 4.3III) [233, 234]. (v) Regarding the transition state, a five-coordinated phosphorus atom, formed by addition of a water molecule has been suggested [77, 100]. Which seems likely owing to the capacity of phosphorus of expanding its valence shell. As can be seen in Schemes 4.3b and 4.3c, a substantial steric hindrance in the P_{3m} ring structure is obvious, hence a high energy transition-state for the $O-P-O$ cleavage is expected, activation energies for hydrolysis 84 – 170 kJ/mol (Table 4.4). The

Table 4.4: A selection of activation energies for hydrolysis (E_a) of phosphate glasses (Two-stage degradation of polyphosphates: ring closure into trimetaphosphate^a and hydrolysis^b).

Glass	E_a (kJ/mol) / pH				O/P	Av. chain length, \bar{n}	Ref.
	1	4	7	10 – 12			
Pyrophosphate	95	114	125	167	3.5	2	[94]
Tripolyphosphate	96	104	109	127	3.33	3	[94]
Tetrapolyphosphate		115	106	106	3.25	4	[95]
Pentapolyphosphate		91	97	111	3.2	5	[95]
Hexapolyphosphate		85	84	115	3.17	6	[95]
Polyphosphate			98 ^a		3.02	~54	[96]
			86 ^b		3	3	[96]
Trimetaphosphate	87			115	3	3	[97]
Tetrametaphosphate	99			136	3	4	[97]

$P-O^-$ group is a stronger nucleophile than water, owing to the negative charge. In the case of ring formation from polyphosphate chains (Scheme 4.2), the reaction still does not follow second-order kinetics of S_N2 reactions, since the substrate and the nucleophile are belonging to the same species [77]. Phosphate groups in chains are more bulky than water, which also

causes steric hindrance. Therefore, it is expected that end- Q^1 instead of middle Q^2 groups behave preferentially as the nucleophiles [76, 257]. Where cations may contribute to twist the chain into a proper conformation, probably helical [99, 105], for nucleophilic attack.

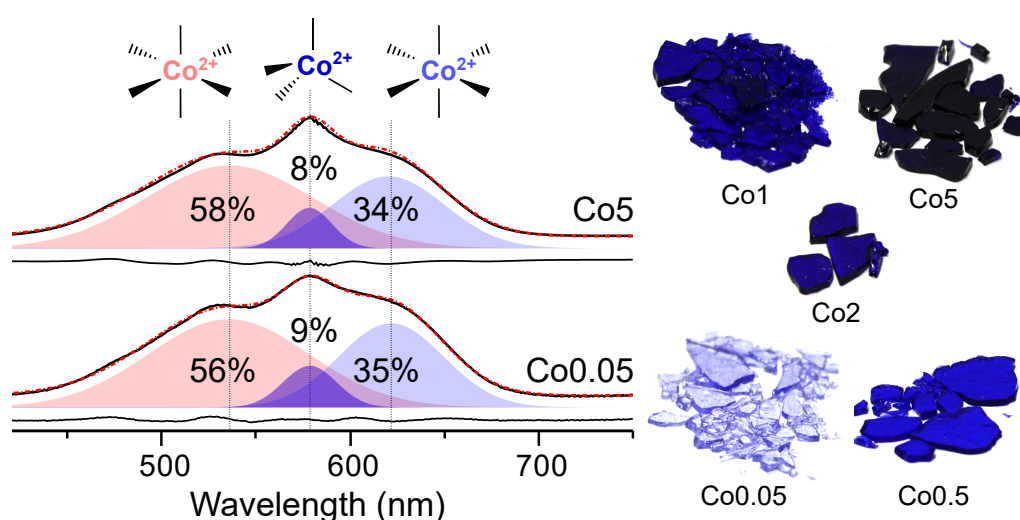
As can be seen in Table 4.4, the activation energies related to the degradation processes in aqueous solution (84 – 167 KJ/mol) depend on composition and substantially on pH. The aqueous degradation of phosphate glasses is catalyzed by acids, lower E_a (Table 4.4) [94, 102, 108], owing to the improvement of the leaving group stability, involved in the transition state of a S_N2 -type reaction [1, 100]. For the same reason the degradation may not be catalyzed in basic media, higher E_a (Table 4.4) [24, 94]. The effect of cations depends on the pH, namely it retards the hydrolysis in acidic media and conversely accelerate it in neutral and basic media [109, 110].

On the other hand, as can be seen in Table 4.4, at pH 7 the E_a of hydrolysis decreases from pyrophosphate to hexapolyphosphate, in agreement with the hypothesis of higher lability of longer chains in solution. Despite the higher E_a for ring closure into trimetaphosphate (98 kJ/mol) compared with the E_a of hydrolysis (86 kJ/mol) of longer chains, referred as polyphosphate on the Table. The ring closure is favoured as discussed thorough the chapter and hence, the ring formation may be kinetically instead of thermodynamically controlled. Regarding, the higher stability of rings compared with chains, no data (E_a) was found at neutral pH. Nevertheless, according to the NMR findings discussed in the present chapter, the ring closure of polyphosphates should more favoured than the hydrolysis of such.

Chapter 5

Structural role and coordination environment of cobalt in $45\text{P}_2\text{O}_5\text{--CaO--Na}_2\text{O}$ phosphate glasses: Thermal properties, Raman, UV-vis-NIR and EPR spectroscopy

5.1 Abstract



Cobalt-containing materials are of interest for a wide range of applications, from biomaterials to solid-state lasers in optics. For instance, Co^{2+} is known to trigger the formation of new blood vessels, i.e. angiogenesis. Thereby, phosphate glasses are an attractive strategy to overcome the vascularisation limitation in tissue engineering, as a vehicle for local release of Co^{2+} ions. This study aimed to establish structure-property correlations as a function of the coordination environment of cobalt, on $45\text{P}_2\text{O}_5\text{--}(30-x)\text{CaO--}25\text{Na}_2\text{O--}x\text{CoO}$ (x : 0.01 to 10 mol%) glasses. The constant polymerization, O/P ratio, and ultimately constant basicity were proved by ICP-OES and Raman spectroscopy. The latter, combined with EPR analysis, indicated that the presence of Co^{3+} might be excluded, Co^{2+} being the predominant

oxidation state. The expected cation-dependent shifts on the Raman spectra are discussed. UV–vis–NIR absorption spectra accounted for the characterization of the coordination number of Co^{2+} , which showed that the ratio between $^{[\text{IV}]}\text{Co}^{2+}$ and $^{[\text{VI}]}\text{Co}^{2+}$ remained constant throughout the glass series. Owing to the higher field strength of Co^{2+} compared to Ca^{2+} , $^{[\text{VI}]}\text{Co}^{2+}$ is expected to strengthen the glass network. Conversely, despite the higher field strength, $^{[\text{IV}]}\text{Co}^{2+}$ would weaken the network by binding together less fragments of the phosphate glass network. Hence, a compensation between the opposite effects takes place leading to a levelling off of the thermal properties measured by DSC and HSM, i.e. constant T_g values. These results indicate that the structural properties of the glasses with constant basicity are dictated by the coordination number of Co^{2+} .

5.2 Introduction

An attractive strategy to overcome the vascularization limitation in tissue engineering is to artificially stimulate the hypoxia-inducible HIF– 1α pathway, which is correlated with the production of new blood vessels, i.e., angiogenesis. Cobalt (II) is known to mimic hypoxia by binding HIF– 2α proteins at sites that alter their oxygen-regulated activity [166, 167, 173–176]. Nevertheless, excessive exposure to cobalt may lead to adverse health effects involving the cardiovascular, neurological, endocrine, haematological, haemopoietic and respiratory systems [11, 111–113]. Therefore, a controlled ion release system is vital for any tissue engineering strategy involving delivery of cobalt [167]. Phosphate glasses are a highly attractive vehicle for cobalt delivery *in vivo* [55, 57, 58]. Their chemical durability can be tailored through orders of magnitude by modifying the chemical composition [24, 81]. Therefore, phosphate glasses have the potential to release Co^{2+} ions at low and sustained doses [55].

On the other hand, cobalt-doped materials are also considered as potential candidates for tunable solid-state lasers [275–277], nonlinear optical devices [278, 279], plasma display panels [280], new inorganic pigments with large colour scale [281], over-heat temperature indicators [282], DC electrical conductivity [39, 40], among others. For this reason, there is a large number of studies of cobalt in both crystalline [277, 281–284] and amorphous matrices, i.e., glass ceramics [278, 285], silicate [279], borate [280, 286, 287], borosilicate [276, 288] and phosphate glasses [39, 40, 92, 289, 290]. These materials have been characterised by various methods such as: XRD, SEM, DSC, density, EDS, EXAFS, XANES, Diffuse reflectance, UV–vis–IR absorption, Raman, luminescence, EPR, solid state NMR spectra, gamma rays, DC and AC conductivity [39, 40, 92, 276–280, 282–293]. Particularly, optical spectroscopy has been extensively used for structural analysis, since the colour provided by Co^{2+} is related

to its coordination number [292, 294]. The latter varies as a function of the optical basicity, a concept that is useful to explain the electron density distribution in glass networks [288, 295]. Co^{2+} in octahedral coordination exhibits a pink colour in contrast with its tetrahedral counterpart, which is blue with a substantially higher extinction coefficient [294]. Other less common intermediate Co-species with 5-fold [281, 284, 287] and 8-fold coordination [92] have been reported.

Despite the fact that the relationship between optical basicity and coordination number of Co^{2+} has been known for a long time [291–295], most of the studies on glasses have varied both the basicity of the glass network and CoO content simultaneously. Thus, the variation of more than one parameter at the time has led to biased correlations, such as the ratio of tetrahedral coordination being necessarily proportional to the CoO content [279, 280, 289]. Moreover, relatively little information is available about the structural role of cobalt in phosphate glasses [92, 289, 296].

The present study aimed to explain the structural properties induced by CoO as a function of the coordination environment of cobalt, in a phosphate glass network with constant basicity, $45\text{P}_2\text{O}_5-(30-x)\text{CaO}-25\text{Na}_2\text{O}-x\text{CoO}$ (x : 0.01 to 10 mol%). The glasses were characterised by UV–vis–NIR absorption, Raman and EPR spectroscopy and thermal properties. In contrast with previous studies, we report a constant ratio tetrahedral to octahedral coordination independent of CoO content. This study accounts for also constant thermal properties throughout the glass series. The paramagnetic effects of Co^{2+} on NMR spectra is exploited in part II of this research, to explain the dissolution behaviour of the glass system.

5.3 Glass System

Table 5.1 gives the nominal and analysed compositions of the glasses, which were produced in the frame of a collaborative work [211]. The small differences between the values are explained by phosphate losses during melting. Thereby, minor SiO_2 amounts in the analysed compositions has dissolved from the quartz crucibles.

The durability of phosphate glasses varies with phosphate content [22, 81], and polyphosphate glasses generally tend to be more durable compared to their phosphate-richer counterparts, namely metaphosphate ($\text{O}/\text{P} = 3$) and ultraphosphate ($\text{O}/\text{P} = 2.5$) glasses [22, 42]. The composition of $45\text{P}_2\text{O}_5-(30-x)\text{CaO}-25\text{Na}_2\text{O}-x\text{CoO}$ glasses (Table 5.1), $\text{O}/\text{P} = 3.11$, lies in the polyphosphate region ($3 < \text{O}/\text{P} < 3.5$) [22, 41]. By using ^{31}P MAS NMR, we have recently shown this glass to consist of middle (Q^2) and end (Q^1) tetrahedra, corresponding

Table 5.1: Nominal and (analysed) glass composition in mol% as mean \pm standard deviation (SD), experimental O/P ratio and experimental average phosphate chain length (\bar{n}) obtained from ICP-OES analysis.

Glass	P ₂ O ₅	CaO	Na ₂ O	CoO	SiO ₂	Exp. O/P	\bar{n}
Co0	45.0 (44.6 \pm 0.5)	30.0 (30.4 \pm 0.3)	25.0 (24.6 \pm 0.3)	– –	– (0.35 \pm 0.01)	3.12	8.9
Co0.01	45.0 (43.0 \pm 0.2)	29.99 (30.9 \pm 0.1)	25.0 (25.4 \pm 0.1)	0.01 (0.010 \pm 0.001)	– (0.59 \pm 0.04)	3.16	8.6
Co0.05	45.0 (43.0 \pm 0.4)	29.95 (31.0 \pm 0.3)	25.0 (25.4 \pm 0.3)	0.05 (0.050 \pm 0.001)	– (0.52 \pm 0.01)	3.16	8.6
Co0.5	45.0 (44.6 \pm 0.5)	29.5 (30.2 \pm 0.3)	25.0 (24.5 \pm 0.2)	0.5 (0.44 \pm 0.01)	– (0.32 \pm 0.01)	3.12	8.9
Co1	45.0 (44.8 \pm 0.5)	29.0 (29.1 \pm 0.3)	25.0 (25.0 \pm 0.3)	1 (0.90 \pm 0.01)	– (0.23 \pm 0.01)	3.12	9.0
Co2	45.0 (44.6 \pm 0.5)	28.0 (28.4 \pm 0.3)	25.0 (24.6 \pm 0.3)	2 (1.80 \pm 0.02)	– (0.67 \pm 0.01)	3.12	8.9
Co5	45.0 (44.5 \pm 0.5)	25.0 (25.7 \pm 0.3)	25.0 (24.5 \pm 0.2)	5 (4.51 \pm 0.05)	– (0.79 \pm 0.02)	3.12	8.9
Co10	45.0 (43.0 \pm 0.1)	20.0 (20.9 \pm 0.1)	25.0 (25.7 \pm 0.1)	10 (9.98 \pm 0.01)	– (0.50 \pm 0.01)	3.16	8.6

to chains of about 9 phosphate tetrahedra in length on average. We expect the other glasses to show a similar chain length as discussed below [1].

5.4 Thermogravimetric analysis-mass spectrometry

Phosphate glasses are known for their potential hygroscopic nature [22]. Therefore, the evolution of water was followed in situ by the coupled TGA-MS system. The respective TGA curves of the glasses fluctuated around the quantification limits ($\pm 0.08\%$) over the entire range of temperature (40 to 900 °C). Hence, no significant mass-loss corresponding to dehydration processes was determined by TGA. Additionally, the characterization of water release by means of mass spectra was possible through the ions: H₂O⁺ ($m/Z = 18$), OH⁺ ($m/Z = 17$) and O⁺ ($m/Z = 16$). Thereby, the evolution curves of such ions did not show any appreciable peak over the entire range of temperature. Thus, the presence of both absorbed and structural water in the glass system may be neglected [44, 297].

Water may act as an additional network modifier in the glass structure [44], therefore,

a significant water content would be expected to cause depolymerization of the phosphate chains. Nevertheless, ICP-OES and Raman analyses (Table 5.1 and Fig. 5.2), showed the experimental and theoretical composition and polymerization of the glasses to be in good agreement, as discussed below. On the other hand, we have recently reported a non-significant water content for P_2O_5 –CaO–Na₂O glasses of the same polymerization ($O/P = 3.11$)[1].

5.5 Powder X-ray Diffraction (XRD)

X-ray diffraction patterns of the glasses, Fig. 5.1, reveal no presence of crystalline phases, hence pointing out the amorphous nature of all prepared glasses.

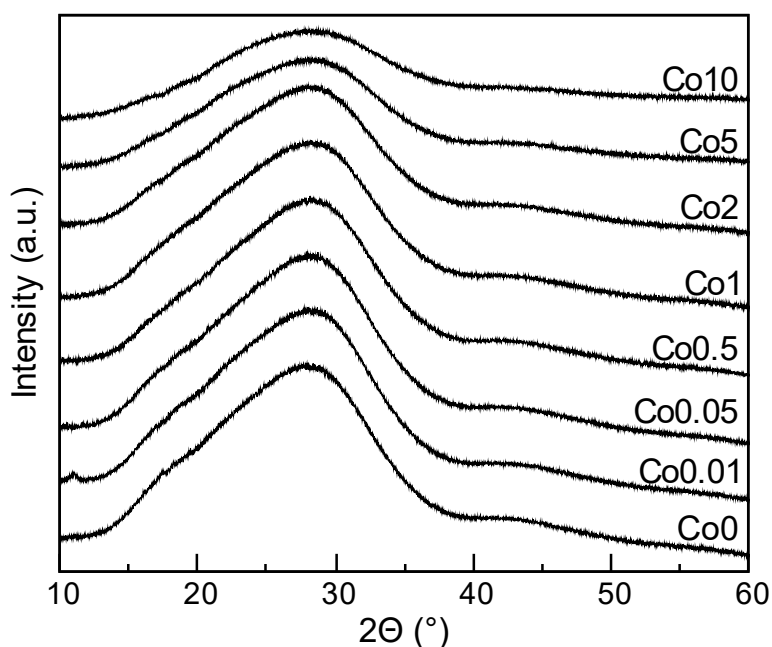


Fig. 5.1: Powder XRD patterns of $45P_2O_5-(30-x)CaO-25Na_2O-xCoO$ glasses, with $0 \leq x \leq 10$ mol%.

5.6 Raman

The analysis of Raman spectra in the frequency region between 200 and 1400 $1/cm$ is summarized in Table 5.2. Based on the P_2O_5 content, the glass system comprises chains with constant polymerization degree and theoretical average length equal to 9 phosphate groups [22, 41]. This is in good agreement with the ICP-OES analysis, which provided the experimental average phosphate chain length (\bar{n}) ~ 9 and O/P 3.1 – 3.2 (Table 5.1).

Table 5.2 shows the typical bands associated with chains as follows: terminal $\nu_s(PO_3)$ for

Q^1 , and $\nu_s(\text{PO}_2)$ and $\nu_{as}(\text{PO}_2)$ for Q^2 tetrahedra; besides the bands associated with P–O–P vibrations of linear polymers in the region between ca. 600 and 850 cm^{-1} . Qualitative evalu-

Table 5.2: Raman spectral bands (cm^{-1}) and assignments for $45\text{P}_2\text{O}_5-(30-x)\text{CaO}-25\text{Na}_2\text{O}-x\text{CoO}$ glasses

Assignment	Wavenumber (cm^{-1})	Ref.
$\delta(\text{P}-\text{O}-\text{P})$, network bending	340	[47, 298–300]
$\nu_s(\text{P}-\text{O}-\text{P})$, stretch, BO	690	[299–302]
$\nu_s(\text{PO}_3)$, stretch, NBO, Q^1	1021	[47, 299, 302, 303]
$\nu_s(\text{PO}_2)$, stretch, NBO, Q^2	1167	[299–302]
$\nu_{as}(\text{PO}_2)$, stretch, NBO, Q^2	1258	[47, 299, 300, 302]

ation of the spectra (Fig. 5.2) does not show any appreciable change neither in position nor in intensity of the vibrations sensitive to the length of the phosphate chains, i.e., $\nu_s(\text{P}-\text{O}-\text{P})$, $\nu_s(\text{PO}_2)$ and $\nu_{as}(\text{PO}_2)$ [299, 300, 302]. In case of depolymerization, the former band (690 cm^{-1}) would be expected to increase in peak frequency owing to a decrease in the P–O–P bond angle. While, a decrease in intensity and the full width at half-maximum (fwhm) would be expected. On the other hand, for the band $\nu_s(\text{PO}_2)$ at 1167 cm^{-1} an opposite effect in position and fwhm, compared with $\nu_s(\text{P}-\text{O}-\text{P})$, would be observed [302]. However, the negligible changes in the Raman spectral features (Fig. 5.2) indicate constant polymerization (\bar{n}) throughout the glass series, which is in agreement with ^{31}P MAS NMR reported for an analogous glass system [1]. The relative constant \bar{n} implies that depolymerization caused by water as an additional network modifier may be discarded, as discussed above. Additionally, it also suggests that a non-significant amount of Co^{3+} exists in the glasses, since it would lead to depolymerization of the glass network especially at high CoO content. Thereby, Co^{3+} ($3d^6$) in octahedral coordination has been reported to be a potential oxidation product resulting from melting and annealing processes [276, 278–280, 289].

Regarding the cation effect, namely the substitution of CaO for CoO, the strong and sharp band $\nu_s(\text{PO}_2)$ occurring at 1167 $1/\text{cm}$ and the weaker band $\nu_s(\text{P}-\text{O}-\text{P})$ observed at 690 $1/\text{cm}$ (Fig. 5.2) are expected to be cation-dependent. In reported binary and mixed-modifier metaphosphate glasses, the series $\text{Li}^+ \rightarrow \text{Cs}^+$ and $\text{Mg}^{2+} \rightarrow \text{Ba}^{2+}$ show a clear trend of frequency decreasing in both bands as the ionic radius increases [301, 304, 305].

According to a reported vibration model, the cation-dependent shifts are caused by changes in network bond angles and variation in metal-oxygen bonding force constants ($F_{\text{M-O}}$). Thus, as the angle increases and $F_{\text{M-O}}$ decreases through the series of alkali and alkali earth metals, the frequency of $\nu_s(\text{PO}_2)$ and $\nu_s(\text{P}-\text{O}-\text{P})$ bands decrease by both parameters [304]. How-

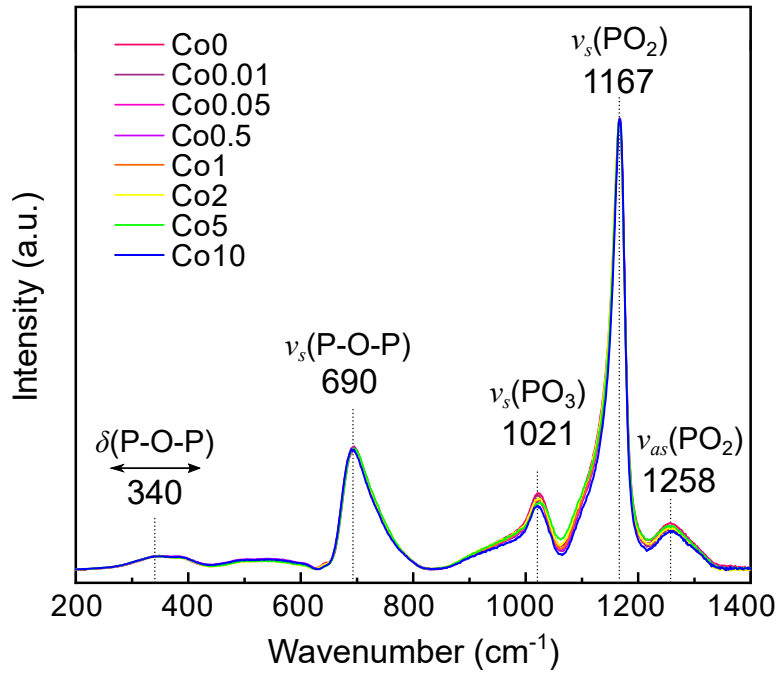


Fig. 5.2: Normalized Raman spectra of $45\text{P}_2\text{O}_5-(30-x)\text{CaO}-25\text{Na}_2\text{O}-x\text{CoO}$ glasses, with $0 \leq x \leq 10$ mol%.

ever, discrepancies between the observed and predicted vibrational frequencies have been associated to more covalent interactions between the metal cation and the glass network [301]. Accordingly, for reported binary metaphosphate glasses of Mn^{2+} , Fe^{2+} , Zn^{2+} and Hg^{2+} no clear trend was observed despite the similar ionic radii [301, 306]. Therefore, there is no a reliable basis to predict the magnitude of the frequency shift caused by the substitution of Ca^{2+} for Co^{2+} .

Cobalt ions exist predominately as Co^{2+} in glass networks [279, 280, 289, 294], as an admixture of tetrahedral and octahedral symmetries depending glass composition [294, 307]. Whereas Ca^{2+} ions preferentially undertake coordination numbers from 6 to 8 [308]. Thereby, the coordination number of Ca^{2+} in $50\text{P}_2\text{O}_5-\text{CaO}-\text{Na}_2\text{O}$ glasses has been reported to correspond to 6 [309]. By assuming that Ca^{2+} exists predominantly as 6-fold coordinated in the glass system, the ionic radius of Ca^{2+} would be 25% and 42% bigger than $^{[\text{VI}]}\text{Co}^{2+}$ and $^{[\text{IV}]}\text{Co}^{2+}$, respectively (Ionic radii: $^{[\text{VI}]}\text{Ca}^{2+} = 1 \text{ \AA}$, high-spin $^{[\text{VI}]}\text{Co}^{2+} = 0.745 \text{ \AA}$, high-spin $^{[\text{IV}]}\text{Co}^{2+} = 0.58 \text{ \AA}$) [306], thus, $r_{\text{Co}} < r_{\text{Ca}}$.

An increase in the frequency of $\nu_s(\text{PO}_2)$ and $\nu_s(\text{P-O-P})$ vibrations proportional to CoO content would be expected, owing to the higher field strength, calculated from the respective ionic radii [306], of Co^{2+} compared with Ca^{2+} ions (Z/r^2 : $^{[\text{VI}]}\text{Ca}^{2+} = 2.1/\text{\AA}^2$, $^{[\text{VI}]}\text{Co}^{2+} = 3.60/\text{\AA}^2$, $^{[\text{IV}]}\text{Co}^{2+} = 5.9/\text{\AA}^2$). Nevertheless, no distinguishable cation effect on the Raman

spectra was observed, Fig. 5.2. On the other hand, for $50\text{P}_2\text{O}_5-(50-x)\text{SrO}-x\text{CoO}$ glasses, a slight shift to higher frequencies has been reported. Namely, 11 and 14 $1/\text{cm}$ for the $\nu_s(\text{P}-\text{O}-\text{P})$ and $\nu_s(\text{PO}_2)$ bands, respectively, for complete CoO substitution [296]. Regarding the $45\text{P}_2\text{O}_5-(30-x)\text{CaO}-25\text{Na}_2\text{O}-x\text{CoO}$ glasses, the Co^{2+} content is always a minority compared to Na^+ and Ca^{2+} . For example, in the Co10 glass any shift due to Co^{2+} would be diluted by a factor of ~ 8 compared to having exclusively Co^{2+} as a network modifier. By doing a rough correlation between the reported slight shifts [296] with the dilution factor calculated for Co10, the resulted blue shifts for Co10 would be 1 and 2 $1/\text{cm}$ for the $\nu_s(\text{P}-\text{O}-\text{P})$ and $\nu_s(\text{PO}_2)$ bands, respectively. Therefore, the expected cation-dependent shifts in $45\text{P}_2\text{O}_5-(30-x)\text{CaO}-25\text{Na}_2\text{O}-x\text{CoO}$ glasses may not be noticeable not even for the highest CoO content, 10 mol%. This is in agreement with the reported data on $50\text{P}_2\text{O}_5-(50-x)\text{SrO}-x\text{CoO}$ glasses, where the expected blue shifts are only observable up to 25 mol% CoO substitution [296].

Despite this, it is interesting to notice that the size difference in the case of octahedral Co^{2+} would be expected to be less abrupt than for tetrahedral Co^{2+} symmetries. Hence, the observed independence of the intensity and shift of $\nu_s(\text{PO}_2)$ and $\nu_s(\text{P}-\text{O}-\text{P})$ vibrations thorough the series, may suggest a major proportion of octahedral Co^{2+} in the glass network, as discussed below.

5.7 UV–vis–NIR

As shown in Fig. 5.3, synthesized glasses are transparent up to Co2. The colour changes from blue-violet (Co0.01, Co0.05), turns into an intense blue (Co0.5), and reaches finally an opaque dark blue colour (Co5). The analysis of UV–vis–NIR absorption spectra (200–1250



Fig. 5.3: Colour of $45\text{P}_2\text{O}_5-(30-x)\text{CaO}-25\text{Na}_2\text{O}-x\text{CoO}$ glasses, with $0.01 \leq x \leq 5$ mol%.

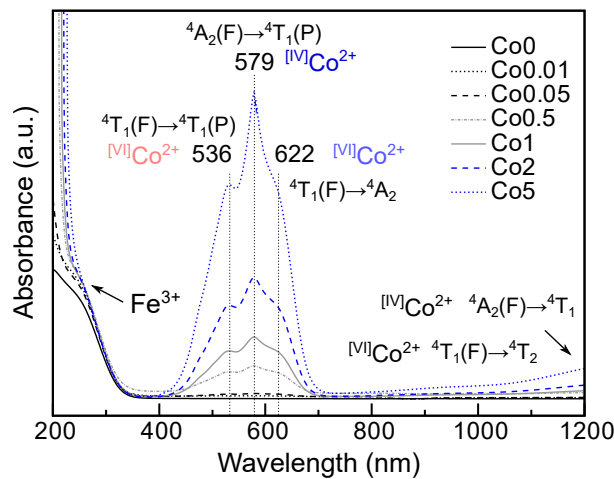
nm) for the glass series is summarized in Fig. 5.4a. The strong UV absorption was ascribed as an $\text{O} \rightarrow \text{M}$ charge-transfer band owing to Fe^{3+} traces, which have been associated with impurities in starting materials for glass preparation [281, 286, 289]. It is well known that Co^{2+} ($3d^7$) exhibits octahedral and tetrahedral symmetries in glasses [276, 278–280, 289, 294], and indeed both coexist also in the $45\text{P}_2\text{O}_5-(30-x)\text{CaO}-25\text{Na}_2\text{O}-x\text{CoO}$ system.

The d–d electronic transitions corresponding to Co^{2+} in octahedral symmetry were assigned for low crystal field splitting ($\Delta_0/B < 15$, with Δ_0 being the crystal field splitting and B being the Racah parameter) *via* the Tanabe–Sugano diagrams [310, 311], as has been already reported for Co^{2+} in phosphate matrices [281, 282, 296]. Thus, the visible bands with maxima at 533 and 622 nm were ascribed as ${}^4\text{T}_{1g}({}^4\text{F}) \rightarrow {}^4\text{T}_{1g}({}^4\text{P})$ and ${}^4\text{T}_{1g}({}^4\text{F}) \rightarrow {}^4\text{A}_{2g}({}^4\text{F})$ transitions respectively; while in the IR region the ${}^4\text{T}_{1g}({}^4\text{F}) \rightarrow {}^4\text{T}_{2g}({}^4\text{F})$ transition is expected to lie in the mid-IR [281], out of the measured range.

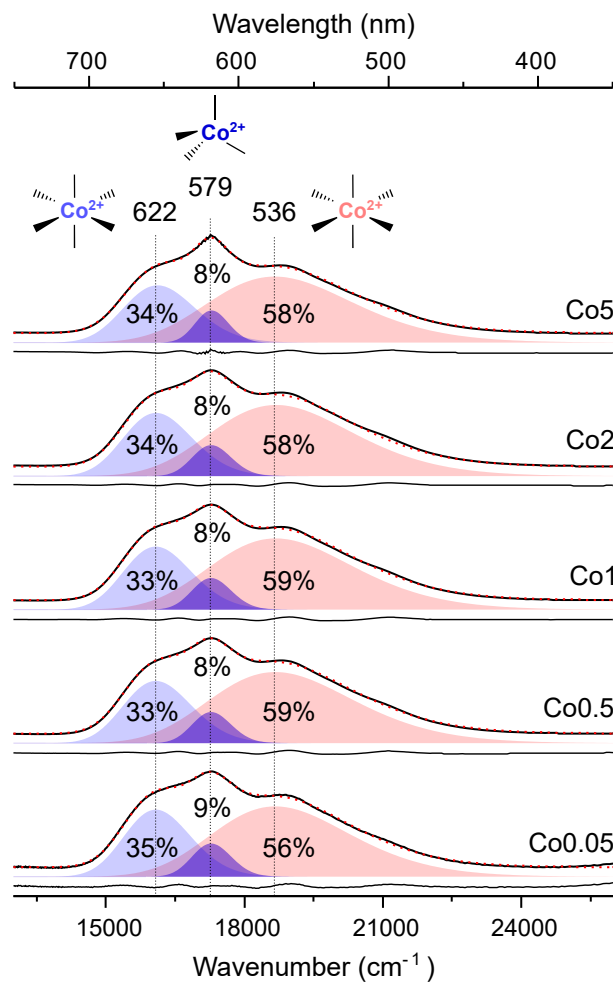
The d–d electronic transitions associated with Co^{2+} ions in a tetrahedral field were also observed [284, 285, 289, 294]. Thus, the absorption centred at 579 nm was assigned as the ${}^4\text{A}_2({}^4\text{F}) \rightarrow {}^4\text{T}_1({}^4\text{P})$ transition. In the IR range, an additional lower intensity band is expected owing to the ${}^4\text{A}_2({}^4\text{F}) \rightarrow {}^4\text{T}_1({}^4\text{F})$ transition [296]. Even though the maxima of the IR bands are out of the measured range, they can still be noticed to emerge from ~ 1000 nm.

The proportion of cobalt octahedral relative to tetrahedral symmetry depends upon the basicity of the glass. Thus the tetrahedral coordination requires a threshold of basicity to appear, where the basicity is proportional to the content of metal oxides [92, 292, 294]. Even though the ligand field stabilization energy LFSE for octahedral coordination is higher than for tetrahedral coordination, the preference for the former is less pronounced for weak-field ligands [293]. π –donor ligands or Lewis bases such as phosphate matrices belong to this group, since they decrease the crystal field splitting [90, 291]. Indeed, phosphates may provide crystal-field splittings among the smallest for transition metals, such as Co^{2+} in octahedral symmetry [281, 282]. However, the Lewis base character on terminal groups of polyphosphates is inversely proportional to the average chain length (\bar{n}), where the middle groups behave as strong acids [24, 78, 104, 105]. Thus, the residual negative charge on NBOs and subsequently, the crystal field splitting varies to a certain extent as a function of the polyphosphate chain length [92, 281, 312].

According to the Oxygen Bonding Model, the first coordination sphere around oxygen atoms must satisfy a total formal charge of +2 bond donation [46]. In order to balance NBOs with a high residual negative charge, an increase in the bond donation through a rise in the covalent character of Co–O bonds would be necessary. This may explain the reduction in the coordination number of Co^{2+} proportional to the basicity of the glass network [92, 295]. In contrast, highly covalent P–O bonds would force M–O bonds to be more ionic, increasing the coordination number [282].



(a)



(b)

Fig. 5.4: (a) Normalized UV–vis–NIR absorption spectra and (b) deconvolution in the visible range (400–700 nm) of experimental spectra (black), best-fit (red) and the difference curve (gray) beneath each spectrum; the Gaussian lines correspond to transitions for octahedral symmetry at 536 nm (pink) and 622 nm (blue); and tetrahedral symmetry at 579 nm (dark blue, fractional population in %) of $45\text{P}_2\text{O}_5-(30-x)\text{CaO}-25\text{Na}_2\text{O}-x\text{CoO}$ glasses, with $0 \leq x \leq 5$ mol%.

In $45\text{P}_2\text{O}_5 - (30 - x)\text{CaO} - 25\text{Na}_2\text{O} - x\text{CoO}$ glasses, the polymerization remains constant as discussed above, owing to the constant metal oxide content, hence kept constant to 55 mol% ($25\text{Na}_2\text{O} + (30 - x)\text{CaO} + x\text{CoO}$). Alkali cations such as Na^+ ions would have a more pronounced effect on the basicity [294], hereby Na_2O was maintained constant to 25 mol%. Therefore, it would be expected that the basicity remains invariant for the glass system, which implies that the ratio between octahedral and tetrahedral symmetries remains likewise constant. Indeed, it was confirmed by deconvolution in the visible range (400–700 nm) of the spectra using the minimum number of component Gaussian lines. As shown in Fig. 5.4b, the constant ratio between symmetries, independent of the CoO content, is appreciable even at concentrations as low as 0.05 mol% CoO.

On the other hand, there is no appreciable change in the position of the bands as the CoO content increases. Changes in the absorption spectra (400–1200 nm) are only related to the intensity (5.4a and 5.4b). This is in agreement with a relatively constant Lewis base character. Hence, a constant average chain length (\bar{n}) of phosphate ligands provides a steady crystal field throughout the glass series.

The characteristic colour of Co^{2+} ions with octahedral symmetry is pink or violet [281, 282, 291], being the corresponding bands 536 and 622 nm (Fig. 5.4b). The former band corresponds to green absorption and red emission, while the latter corresponds to orange absorption and blue emission. As a result, the colour emitted would be violet. The absorption band at 579 nm was assigned as Co^{2+} with tetrahedral symmetry, which corresponds to yellow absorption and, accordingly, blue emission.

Transitions between d orbitals are forbidden in octahedral complexes owing to the Laporte selection rule which applies for centrosymmetric geometries. Nevertheless, d-d ligand-field transitions in octahedral complexes may still occur because the selection rule gets relaxed as a result of symmetry distortions, which are expected on the glasses. That accounts in general for the weakness of the transitions in octahedral compared with those in tetrahedral complexes [90]. Accordingly, the extinction coefficient of Co^{2+} in tetrahedral coordination is about two orders of magnitude larger than for its octahedral counterpart [288, 294, 296]. Hence, instead of violet, the glasses develop an intense blue colour abruptly, from low Co^{2+} concentrations (0.5 mol%, Fig. 5.3), characteristic of tetrahedral symmetry. This means that the colour emission is dominated by Co^{2+} in tetrahedral coordination regardless of the minor proportion, 8–9%.

For cobalt pyrophosphate and orthophosphate salts a five-fold coordination has been reported [284]. Taking into account that the basicity is inversely proportional to the chain

length, a high proportion of tetrahedral symmetry may be expected for such salts [294]. Therefore, a five-fold coordination may account as an intermediate between tetrahedral and octahedral symmetries owing to the high basicity of short phosphates. Nevertheless, for metaphosphate glasses, an absorption (~ 480 nm) owing to a possible five-fold transition of Co^{2+} ions was not excluded [296]. On the other hand, a Jahn-Teller effect is possible for octahedral high-spin d^7 electron configurations. However, as the t_{2g} orbitals do not point directly at the ligands, the effect may be insignificant to induce a measurable distortion in the structure [90]. Accordingly, no assignments in this regard were performed in the current work, yet Jahn-Teller effects on Co^{2+} ions have been correlated to band-shoulders elsewhere [296].

5.8 EPR spectroscopy

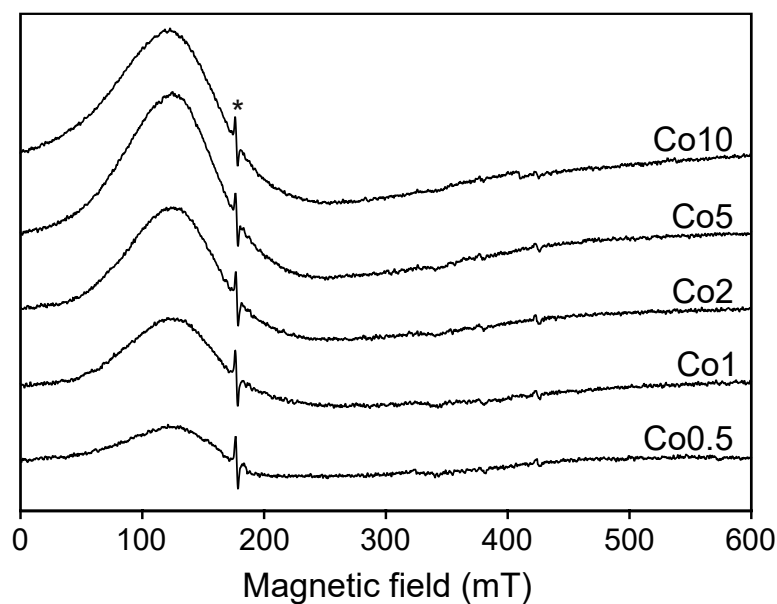


Fig. 5.5: X-band (9.78 GHz) CW EPR spectra of $45\text{P}_2\text{O}_5-(30-x)\text{CaO}-25\text{Na}_2\text{O}-x\text{CoO}$ glasses, with $0.5 \leq x \leq 10$ mol%, measured at 20 K. The spectra are obtained in the same conditions, shown on the same scale and normalized to their weight. Asterisk indicates a signal of resonator, useful for calibration.

Fig. 5.5 shows the EPR spectra of the glass system measured at 20 K. Lower concentrated samples had insufficient sensitivity at 20 K. At the same time, measurement at lower temperatures (7 K) was challenging since samples Co1 and below began to experience microwave saturation, and therefore could not be reliably measured. The spectra of all samples shown in Fig. 5.5 are typical of high-spin Co^{2+} ($S = 3/2$) with significant zero-field splitting (D value larger than the microwave quantum at X-band $\sim 0.3 \text{ cm}^{-1}$). As an

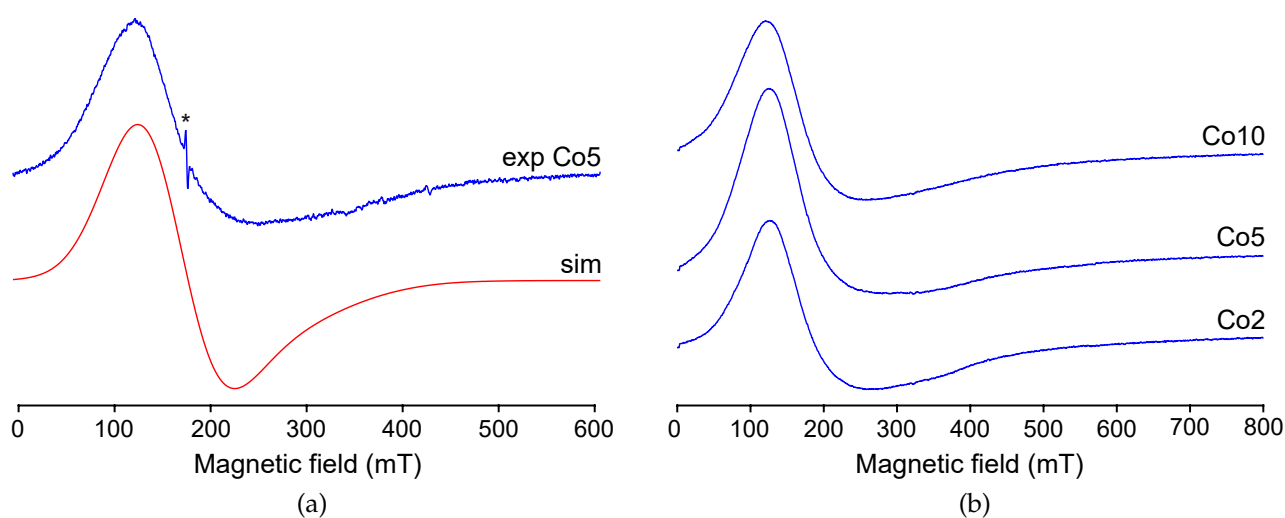


Fig. 5.6: (a) Experimental EPR spectrum of Co5 at 20 K and theoretical modelling ($S = 3/2$, $g = [2.2 \ 2.2 \ 2.4]$, $\nu_{mw} = 9.78$ GHz, $D \gg 0.3$ cm $^{-1}$, $E = 0$). Asterisk indicates a signal of resonator, useful for calibration. (b) Experimental EPR spectra of Co2, Co5 and Co10 glasses measured at 7 K in the same conditions.

illustration, Fig. 5.6a shows the theoretical modelling of the Co $^{2+}$ spectrum using reasonable spectroscopic parameters. It is noteworthy that all detected spectra are extremely broad, and they do not become narrower even at 7 K temperature (Fig. 5.6b). Thus, such broad lineshapes are most likely determined by a distribution of spectroscopic parameters in cobalt centres due to the corresponding geometrical distributions. This situation is not surprising for glassy states, whereas narrower Co $^{2+}$ signals are typically observed in crystals. An estimation of the number of high-spin Co $^{2+}$ ions was done for the series of spectra shown in Fig. 5.5. Due to the broad lineshapes, the accuracy of such measurements does not exceed 20 – 30% (see Fig. 5.7). Nevertheless, from the absolute numbers, it is clear that the observed Co $^{2+}$ signals correspond to the main fraction of cobalt nuclei, which, according to the UV–vis–NIR results, has to be assigned to a mixture of high-spin Co $^{2+}$ ions in octahedral and tetrahedral environments.

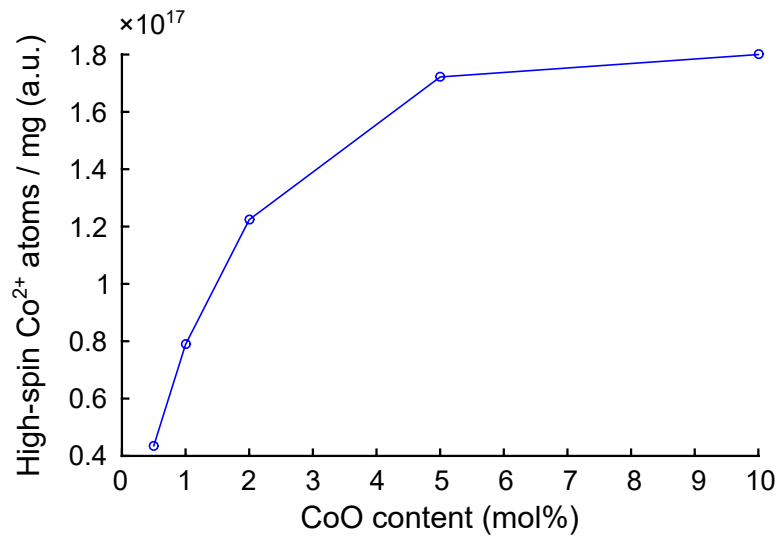


Fig. 5.7: The calculated EPR-based number of high-spin Co(II) atoms per mg vs. CoO mol%.

5.9 Thermal Properties

The thermal properties of $45\text{P}_2\text{O}_5-(30-x)\text{CaO}-25\text{Na}_2\text{O}-x\text{CoO}$ glasses recorded by DSC and HSM are summarized in Fig. 5.8 and Table 5.3. All glasses were prepared in fused silica crucibles. Therefore, a change in the polymerization degree of the phosphate network may not be excluded owing to the potential intake SiO_2 [313]. Nevertheless, the SiO_2 content (0.2 – 0.8 mol%, Table 5.1) was seemingly low enough not to produce any significant change in the polymerization of the glass series, as shown by Raman (Fig. 5.2) and ICP-OES (Table 5.1) analyses. As shown in Fig. 5.8a, T_g values obtained from DSC remained comparatively

Table 5.3: Thermal properties of selected glasses. DSC ($\pm 5^\circ\text{C}$): glass transition temperature (T_g), crystallisation onset ($T_{c,o}$), melting point characterised by both the liquidus (T_L) and the absolute minimum ($T_{m,i}$) temperatures and the processing window ($\Delta T = T_{c,o} - T_g$). HSM ($\pm 5^\circ\text{C}$): sintering (T_{si}), starting and ending of the plateau (T_{xi} and T_{xf}), corresponding to the crystallisation domain and fusion (T_{fusion}) temperatures.

Glass	DSC ($\pm 5^\circ\text{C}$)					HSM ($\pm 5^\circ\text{C}$)				
	T_g	$T_{c,o}$	$T_{m,i}$	T_L	$\Delta T = T_{c,o} - T_g$	T_{si}	T_{xi}	$T_{xi} - T_{si}$	T_{xf}	T_{fusion}
Co0	377	485	736	740	107	395	459	64	721	736
Co0.01	379	496	734	738	117	400	465	65	721	733
Co0.05	378	494	733	737	116	404	459	55	722	730
Co1	372	481	731	741	109	390	451	61	718	732
Co5	371	491	714	722	119	390	461	71	699	713
Co10	368	481	708	712	113	381	449	68	692	706

constant ($374 \pm 4^\circ\text{C}$) throughout the glass series. Such a constant trend in the T_g values was

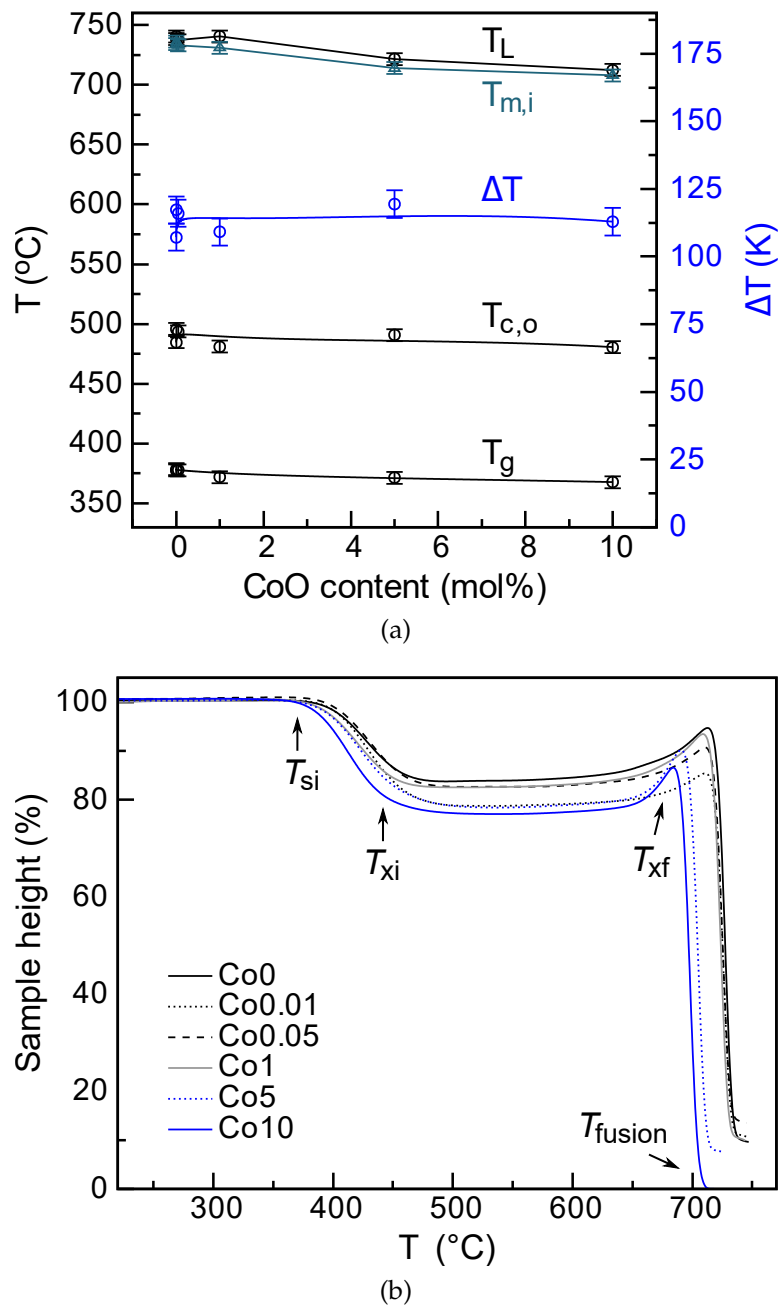


Fig. 5.8: Thermal properties of $45\text{P}_2\text{O}_5-(30-x)\text{CaO}-25\text{Na}_2\text{O}-x\text{CoO}$ glasses, with $0 \leq x \leq 10$ mol%. (a) DSC (± 5 $^{\circ}\text{C}$): glass transition (T_g), crystallisation ($T_{c,o}$), liquidus (T_L), melting at the absolute minimum ($T_{m,i}$) temperatures and processing window ($\Delta T = T_{c,o} - T_g$) as a function of the nominal CoO content. (b) HSM (± 5 $^{\circ}\text{C}$), sample height as a function of temperature: sintering (T_{si}), starting and ending of the glass crystallisation plateau (T_{xi} and T_{xf}) and fusion (T_{fusion}) temperatures.

further confirmed by HSM measurements, since the offset of T_g would approximately correspond to the sintering temperature (T_{si}), Fig. 5.9. Accordingly, T_{si} remained approximately constant over the glass series, 393 ± 8 $^{\circ}\text{C}$ (Fig. 5.8b and Table 5.3).

Taking into account exclusively the field strength (Z/r^2 , calculated from the respective ionic radii), it is expected that introducing CoO at expenses of CaO would strengthen the glass network (Z/r^2 : $^{[VI]}Ca^{2+} = 2 \text{ 1/\AA}^2$, $^{[VI]}Co^{2+} = 3.60 \text{ 1/\AA}^2$, $^{[IV]}Co^{2+} = 5.9 \text{ 1/\AA}^2$) [306]. However, that would be the case only for $^{[VI]}Co^{2+}$, which would keep the cross-linking of PO_4 tetrahedra as in the Co-free glass network, assuming that calcium exists exclusively as $^{[VI]}Ca^{2+}$ in the glasses [309]. In this case an increase of T_g proportional to the cobalt content would be expected. Analogously, $^{[IV]}Co^{2+}$ would decrease the cross-linking of PO_4 tetrahedra compared with $^{[VI]}Ca^{2+}$ and ultimately cause a decrease in T_g [312].

According to the UV–vis–NIR results, both octahedral and tetrahedral symmetries co-exist and its ratio remains constant throughout the glass series. Hence, a levelling off of both effects may explain the relatively constant T_g as a function of the CoO content. Such a constant trend in the T_g values ($512 \pm 5 \text{ }^\circ\text{C}$) has been further confirmed by reported data on $50P_2O_5-(50-x)SrO-xCoO$ glasses [296].

As shown in Fig. 5.8a and Table 5.3, the crystallisation temperatures $T_{c,o}$ (DSC) remained also relatively constant ($488 \pm 7 \text{ }^\circ\text{C}$) over the glass series. Altogether, the relative constant T_g and $T_{c,o}$ temperatures lead to a steady processing window $\Delta T = T_{c,o} - T_g = 114 \pm 5 \text{ }^\circ\text{C}$ over the glass series. Likewise such trend was confirmed by HSM, where the difference between the starting of crystallisation and sintering temperatures, $T_{xi} - T_{si} = 64 \pm 6 \text{ }^\circ\text{C}$ analogous to ΔT (Fig. 5.9), remained steady. The relatively constant $T_{c,o}$ and T_{xi} values may be explained in terms of bond enthalpies which increase as the bond length M–O decreases [90]. The bond enthalpies are expected to change in the following order: $^{[VI]}Ca^{2+} < ^{[VI]}Co^{2+} < ^{[IV]}Co^{2+}$, thus $T_{c,o}$ and T_{xi} should increase with CoO content. Nevertheless, a levelling off occurs as a result of the constant $^{[IV]}Co^{2+}$ and $^{[VI]}Co^{2+}$ ratio. Namely, the rise in energy cost that is involved in breaking more covalent M–O bonds in the glass network, and the energy gain involved in the formation of more stable M–O bonds in the crystal phases.

As shown in Table 5.3 and Fig. 5.9, the melting $T_{m,i}$ (DSC) and fusion T_{fusion} (HSM) temperatures are in good agreement with each other. The liquidus temperature (T_L) follows the same trend as $T_{m,i}$, but with an offset of about $\sim 6 \text{ }^\circ\text{C}$ in average, as shown in Fig. 5.8a and Table 5.3. $T_{m,i}$ values remained relatively steady for glasses from 0 to 1 mol% CoO content, namely 736 and 731 $^\circ\text{C}$, respectively. A decrease trend in $T_{m,i}$ occurs for the glasses with substantially higher content of cobalt, thus 714 and 708 $^\circ\text{C}$ for 5 and 10 mol% CoO, respectively. Thus, a decrease of about 30 $^\circ\text{C}$ between the Co-free glass (Co0) and Co10 (10 mol% CoO) occurs. On the other hand, T_{xi} and $T_{c,o}$ were relatively unaffected by the CoO substitution for CaO. Unlike the end temperature of crystallisation T_{xf} , which decreases

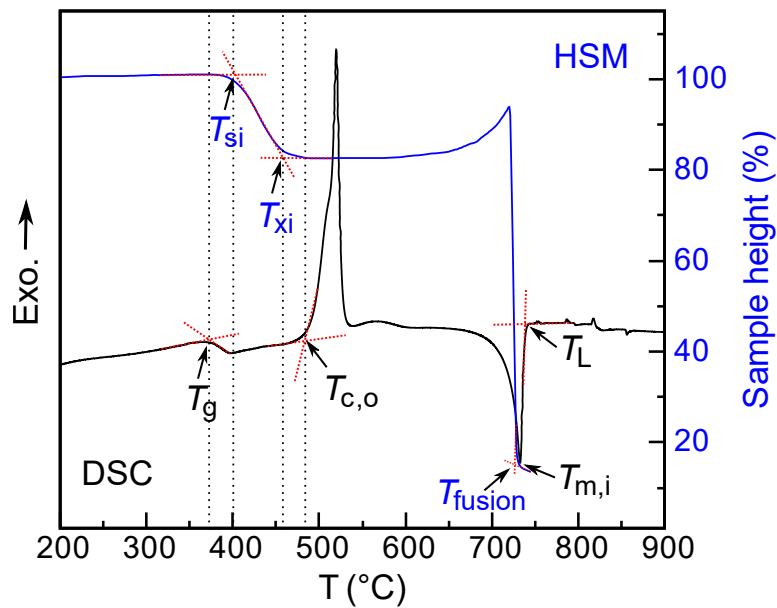


Fig. 5.9: DSC and HSM curves for glass Co_{0.05}, $x = 0.05$ mol% CoO. Thermal properties: glass transition inflection point (T_g), crystallisation onset ($T_{c,o}$), melting point at the absolute minimum ($T_{m,i}$), the liquidus (T_L), sintering (T_{si}), starting of crystallisation domain (T_{xi}) and fusion (T_{fusion}) temperatures.

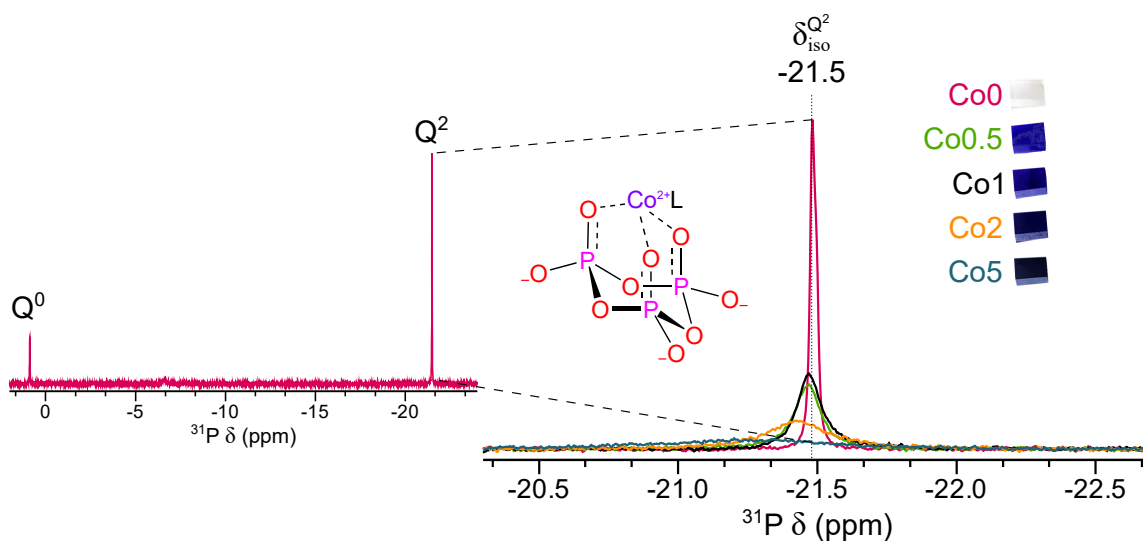
proportionally to T_{fusion} , thus reducing the crystallisation domain range (Fig. 5.8b, Table 5.3).

According to the Pauling scale [103], the electronegativity of calcium is significantly lower than that of cobalt. Therefore, the higher ionic bonding nature of calcium-rich crystal phases may lead to higher melting points. Analogous trends regarding T_c , T_m , T_{xi} , T_{xf} and T_{fusion} have been observed in a glass system where MgO was substituted for CaO. The former oxide is well known to undertake tetrahedral and octahedral symmetries such as CoO [314].

Chapter 6

Co²⁺ as an internal paramagnetic ³¹P NMR probe for structural analysis of cobalt-phosphate glasses in the solid-state and leachate solutions

6.1 Abstract



The incorporation of CoO into phosphate glasses is of interest for therapeutic applications where cobalt could be released locally such as in wound healing or as bactericide. Herein Co²⁺ was used as an internal paramagnetic ³¹P NMR probe for the study of the structure of 45P₂O₅–(30–*x*)CaO–25Na₂O–*x*CoO (*x*: 0 to 10 mol%) glasses, both in the liquid and solid-state, seeking for insights regarding the mechanism of dissolution. According to ³¹P solid-state MAS NMR, all glasses were composed of pyrophosphate Q¹ and metaphosphate Q² species with chains from 8 to 9 phosphate groups in length. Owing to paramagnetic effects, namely the paramagnetic shift and inhomogeneous broadening, the intensity of both resonances decreased concomitantly with increasing CoO content. The

paramagnetic relaxation enhancement (PRE) also increased with CoO content, since Co^{2+} may undertake strong zero-field splitting (ZFS) proportional to the expected site asymmetry in glasses, opening new spin relaxation pathways. The assessment of the homogeneity of Co^{2+} ion distribution in the diamagnetic host glass suggested a cluster scenario at high CoO content. Additionally, paramagnetic liquid ^{31}P NMR offers a new approach to investigate the mechanism of dissolution of phosphate glasses. Thereby, Co^{2+} ions allowed the tracking of the structure and dynamics of phosphate complexes, including conformational changes, upon ligand binding recognition under different conditions, i.e. Tris and EDTA set at pH 7.4 and 10.0 at 37 °C, respectively.

6.2 Introduction

Phosphate glasses are able to form homogeneous systems with inorganic ions, which subsequently functionalize the glasses for a variety of technological applications. Among them, it can be highlighted: water softeners [31], fertilizers [26, 27], sealings [31–33], in photonics [34–36], solid electrolytes [23, 37, 38], semiconductors [39, 40] and storage of wastes [28–30]. The versatility of phosphate glasses lie on their potential to tailor properties as a function of composition. For example, phosphate glasses exhibit a wide spectrum of durability ($10^{-4} - 10^{-9}$ g/(cm² · min)) [23, 24]. Moreover, phosphate glasses dissolve in aqueous media congruently without any preferential leaching of ions [1, 24, 81]. Accordingly, the glasses have the capability to release ions at low and sustained doses [55]. For this reason, inorganic therapeutic chemistry has a huge potential with approaches such as bioactive glasses as a vehicle for ion delivery *in vivo* [55, 57, 58].

The reduction in vascular supply at the site of injury is one of the principal reasons of impaired healing [163, 166]. Therefore, a major challenge in tissue engineering is to promote the formation of efficient vascularized networks, angiogenesis [164, 165]. Co^{2+} ions have been used extensively to investigate *in vitro* and *in vivo* the hypoxic response as a trigger of angiogenesis [56, 166, 167, 173–178]. However, the excessive exposure to Co^{2+} may lead to adverse health effects [11, 111–113]. Thus, a controlled ion release system such as a phosphate-glass matrix is of acute interest in bioinorganic chemistry. [167]. On the other hand, studies of cobalt–phosphate compounds are also interesting because of their optical [92, 289, 290, 296, 315] and electrical properties [39, 40]. For this reason, they also find potential applications in solar collectors [316], cathode materials in Li-ion batteries [183] and solid-state lasers [317], among others.

Paramagnetic systems are materials that contain unpaired electrons and have positive

magnetic susceptibility [183, 186, 318]. The unpaired electron–nucleus interaction causes the paramagnetic shift and the PRE of the nuclear spin [318], such effects provide atomic-level and long-range information [183, 185, 186, 319]. Therefore, paramagnetic NMR may offer a valuable source of structural, thermodynamic, and dynamic insights for a wide variety of materials including both solids and liquids [186, 320]. Nevertheless, paramagnetic NMR has been generally restricted to medicinal chemistry and drug discovery [185, 186, 321]. Thus, it has been mostly used to elucidate the structure of metalloproteins [183, 319]. In that sense, it has been rarely applied to the study of minerals and glasses, mainly owing to severe line broadening and signal loss [320, 322]. In crystalline materials, models based on peak positions and areas have been developed as a criterion of doping homogeneity [207, 320, 323]. Another interesting approach related to paramagnetic NMR is dynamic nuclear polarization (DNP), which involves the electron to nuclear spin polarization transfer [318].

This work presents a new approach to investigate the mechanism of dissolution of phosphate glasses for different applications, i.e. local delivery of Co^{2+} as a therapeutic ion. Herein the paramagnetic nature of Co^{2+} was exploited as an internal ^{31}P NMR probe to undertake structural analysis in both the liquid and solid-state. The paramagnetic effects were investigated on $45\text{P}_2\text{O}_5 - (30-x)\text{CaO} - 25\text{Na}_2\text{O} - x\text{CoO}$ (x : 0 to 10 mol%) glasses *via* ^{31}P solid-state MAS NMR and liquid ^{31}P NMR. Accordingly, features such as the spin-orbit (SO) coupling, ZFS and symmetry of Co^{2+} sites are correlated to the paramagnetic shift, PRE and broadening effects on the spectra. That allowed the assessment of the distribution of Co^{2+} ions in the glass network and the tracking of the hydrolysis process of phosphate fragments associated to the structure and dynamics of cobalt-complexes in aqueous solutions, i.e. Tris and EDTA.

6.3 Glass Structure

Table 6.1 gives the nominal and analysed compositions (ICP-OES) of the glasses, which were produced in the frame of a collaborative work [211]. The small differences between the values are explained by phosphate losses during melting. Thereby, minor SiO_2 amounts in the analysed compositions has dissolved from the quartz crucibles.

As can be seen in Fig. 6.1, the isotropic chemical shifts (δ_{iso}) are typical for ^{31}P with Q^1 and Q^2 topology (-6.2 and -22.1 ppm). $45\text{P}_2\text{O}_5 - (30-x)\text{CaO} - 25\text{Na}_2\text{O} - x\text{CoO}$ (x : 0 to 10 mol%) glasses should be comprised by chains, based on composition [22, 41], being the theoretical chain-length equal to 9 phosphate groups. This is in good agreement with the experimental average chain length ($\bar{n} \sim 8.8$) and O/P ratios (~ 3.14) obtained from ICP-OES

Table 6.1: Nominal and (analysed) glass composition in mol% as mean \pm standard deviation (SD), experimental O/P ratio and experimental average phosphate chain length (\bar{n}) obtained from ICP-OES analysis.

Glass	P ₂ O ₅	CaO	Na ₂ O	CoO	SiO ₂	Exp. O/P	\bar{n}
Co0	45.0 (44.6 \pm 0.5)	30.0 (30.4 \pm 0.3)	25.0 (24.6 \pm 0.3)	– –	– (0.35 \pm 0.01)	3.12	8.9
Co0.01	45.0 (43.0 \pm 0.2)	29.99 (30.9 \pm 0.1)	25.0 (25.4 \pm 0.1)	0.01 (0.010 \pm 0.001)	– (0.59 \pm 0.04)	3.16	8.6
Co0.05	45.0 (43.0 \pm 0.4)	29.95 (31.0 \pm 0.3)	25.0 (25.4 \pm 0.3)	0.05 (0.050 \pm 0.001)	– (0.52 \pm 0.01)	3.16	8.6
Co0.5	45.0 (44.6 \pm 0.5)	29.5 (30.2 \pm 0.3)	25.0 (24.5 \pm 0.2)	0.5 (0.44 \pm 0.01)	– (0.32 \pm 0.01)	3.12	8.9
Co1	45.0 (44.8 \pm 0.5)	29.0 (29.1 \pm 0.3)	25.0 (25.0 \pm 0.3)	1 (0.90 \pm 0.01)	– (0.23 \pm 0.01)	3.12	9.0
Co2	45.0 (44.6 \pm 0.5)	28.0 (28.4 \pm 0.3)	25.0 (24.6 \pm 0.3)	2 (1.80 \pm 0.02)	– (0.67 \pm 0.01)	3.12	8.9
Co5	45.0 (44.5 \pm 0.5)	25.0 (25.7 \pm 0.3)	25.0 (24.5 \pm 0.2)	5 (4.51 \pm 0.05)	– (0.79 \pm 0.02)	3.12	8.9
Co10	45.0 (43.0 \pm 0.1)	20.0 (20.9 \pm 0.1)	25.0 (25.7 \pm 0.1)	10 (9.98 \pm 0.01)	– (0.50 \pm 0.01)	3.16	8.6

analysis (Table 6.1). As can be seen in Table 6.2, this is also in good agreement with the values ($\bar{n} \sim 8.5$, O/P ~ 3.12) obtained from deconvolution of quantitative solid-state ³¹P MAS NMR spectra. Even though, the values are slightly smaller as the ones obtained by ICP-OES analysis, that may be associated to the decrease in sensitivity and resolution owing to the systematic line broadening of the solid-state NMR spectra.

The relative constant experimental \bar{n} and O/P values throughout the glass series confirm constant polymerization, as expected for the glass system with constant P₂O₅ content (45 mol%). As discussed in the last chapter, as a consequence of the constant polymerization, the glass network has constant basicity consistent with invariant metal oxide content, 55 mol%. The constant basicity is subsequently related to a constant proportion between the tetrahedral and octahedral symmetries of Co²⁺ ions, independently of the CoO content. EPR showed the typical spectra of high-spin Co²⁺ (d⁷), the electronic ground state therefore has spin $S = 3/2$, and excluded the presence of Co³⁺ ions in the glasses.

It is evident from Fig. 6.2a and Table 6.2, that no increase in shielding of the Q¹ and

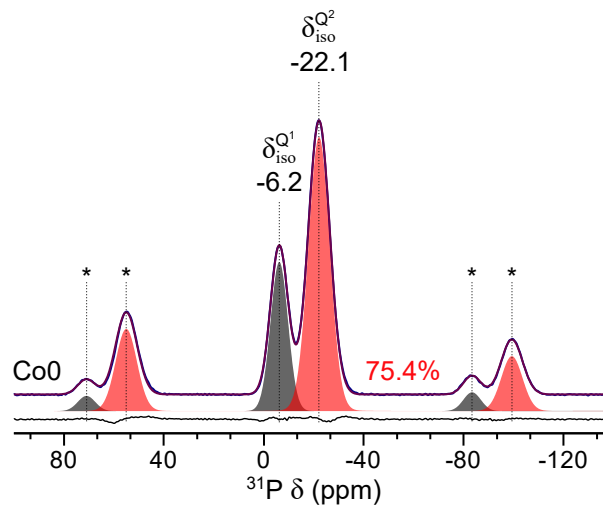


Fig. 6.1: Quantitative ^{31}P solid-state MAS NMR for the cobalt-free glass, Co0. (a) Experimental spectra (fuchsia), best-fit (blue) and the difference curve (gray) beneath each NMR spectrum. For the deconvolution [216] into two Gaussian lines corresponding to Q^1 (black) and Q^2 (red, fractional population in %) groups, the spinning sidebands (*) were taken into account.

Q^2 groups occurs with increasing CoO content. Overlooking by now the paramagnetic effects caused by the Co^{2+} ions, an increase in shielding of Q^1 and Q^2 resonances proportional to CoO content would be expected [45, 51]. Since the field strength of Co^{2+} is higher compared with Ca^{2+} ions, herein calculated from the respective ionic radii (Z/r^2 : $^{VI}\text{Ca}^{2+} = 2 \text{ 1/\AA}^2$, $^{VI}\text{Co}^{2+} = 3.60 \text{ 1/\AA}^2$, $^{IV}\text{Co}^{2+} = 5.9 \text{ 1/\AA}^2$) [306]. Accordingly, an increase in the covalent character of the M–O bonds for the former ions is expected [48, 243]. Nevertheless, direct relationships between the ^{31}P solid-state MAS NMR parameters such as the field strength (Z/r^2) and structure are complicated. That is related to the fact that the chemical shifts in phosphates are dictated predominantly caused by the paramagnetic rather than the diamagnetic contribution of the shielding tensor. Thereby, the paramagnetic term may not be directly related to the bonding electron distribution. Hence, ^{31}P solid-state MAS NMR is limited to empirical correlations regarding the bonding environment of phosphate tetrahedra [197]. Additionally as will be discussed below, the paramagnetic shifts may be large enough to shift the resonances outside the recorded spectral window.

6.4 Paramagnetic effects on solid-state ^{31}P MAS NMR

6.4.1 Linewidth

The dispersion of the spinning sidebands involves the chemical shift and paramagnetic shift anisotropies (SA), both proportional to the gyromagnetic ratio (γ_I). Given that in the glass

Table 6.2: Isotropic chemical shifts ($\delta_{\text{iso}} \pm 0.2$ ppm), full width at half-maximum (fwhm ± 0.2 ppm) and ^{31}P spin-lattice relaxation time (T_1) of Q^i_{P} phosphate species determined from fitting of quantitative single-pulse ^{31}P MAS NMR spectra [213, 216].

Glass	$Q^1 (\pm 0.2 \text{ ppm})$		$Q^2 (\pm 0.2 \text{ ppm})$			Exp. O/P	\bar{n}
	δ_{iso}	fwhm	δ_{iso}	fwhm	T_1 (s)		
Co0	-6.2	8.2	-22.1	10.0	25.80	3.12	8.1
Co0.01	-6.3	8.2	-22.2	10.1	24.58	3.12	8.2
Co0.05	-6.2	8.3	-22.1	10.2	18.48	3.12	8.1
Co0.5	-6.3	9.6	-22.2	11.5	5.306	3.12	8.2
Co1	-6.3	11.1	-22.3	13.1	3.05	3.11	9.2
Co2	-6.2	14.1	-22.4	16.0	1.617	3.11	9.0
Co5	–	–	–	–	0.6743	–	–

system neither ^1H nor ^{19}F are present, ^{31}P is the best nucleus to perform the NMR study. Even though the anisotropy was not determined, an initial inspection of the SA, within the spectral window, indicates that it covers the range between 220 and -270 ppm for all glasses (Fig. 6.2a). Both the SA and inhomogeneous broadening are proportional to the magnitude of the external magnetic field. Thus, low magnetic fields may be more convenient ($B_0 \leq 200$ MHz) to acquire the spectra of paramagnetic samples. However, another approach would be to achieve broadband excitation pulse sequences applicable to high fields [183]. The fwhm peak widths are reported in Table 6.2 and Fig. 6.2b, indicating a systematic trend of severe increasing for Q^1 and Q^2 peaks width with CoO content in the glasses, as also observed in spectra 6.2a. The resolution of the spectra allowed only the determination of the fwhm peak widths up to 2 mol% CoO.

The incorporation of an additional metal ion, cobalt, in the glass network is expected to lead to a wider range of P environments, namely bond lengths and angles [45]. As can be seen in Fig. 6.2b, below 0.5 mol% CoO, the fwhm trend lines for both sites remain fairly parallel. It may indicate non-preferential distribution of $\text{Ca}^{2+}/\text{Co}^{2+}$ in Q^1 and Q^2 sites at low CoO content. The fwhm of Q^2 related to the Q^1 peak is about 2 ppm higher for the former with increasing CoO content, up to 0.5 mol%, which may attributed to the ratio Q^1/Q^2 ratio is $\sim 2/7$, in the glass system. In other words, there are 3.5 more Q^2 sites per 1 Q^1 site, making the former peak 2 ppm broader along the glass series.

The paramagnetic nature of Co^{2+} ions in the glass network causes also severe broadening

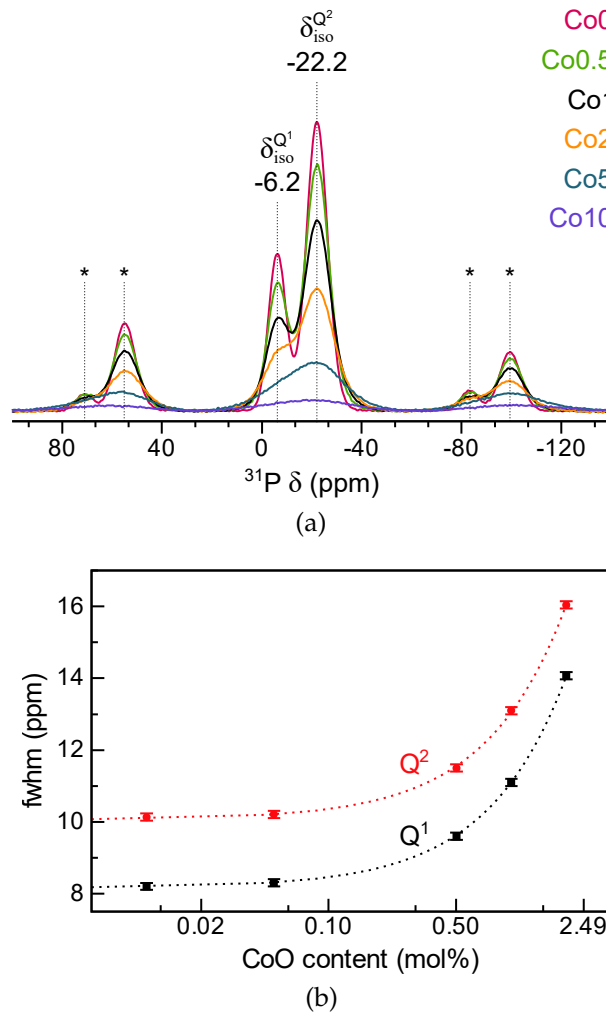


Fig. 6.2: (a) Quantitative ^{31}P solid-state MAS NMR spectra of the glass series $45\text{P}_2\text{O}_5-(30-x)\text{CaO}-25\text{Na}_2\text{O}-x\text{CoO}$ (x : 0 to 10 mol%), where the δ_{iso} are assigned for the Q^1 and Q^2 moieties, the spinning sidebands are marked with asterisks (*). (b) Full width at half maximum (fwhm) of the Q^1 and Q^2 peaks (\pm SD from deconvolution [213]), as a function of nominal composition in the log scale for the glasses with x : 0.01 to 2 mol% CoO (lines are guides for the eye).

due to the potential combination of the anisotropic bulk magnetic susceptibility (ABMS), PRE and the extended network of dipolar couplings [183]. Co^{2+} belongs to the paramagnetic ions that undertake rapid electronic relaxation (1 – 10 ps) and strong SO coupling, for which is generally found that BMS, and not the transverse PRE, dominates the linewidth [183]. The broadening contribution of the former is about one order of magnitude larger than the latter. The fast FID decay of such systems causes significant phase dispersion owing to the dead time. Thereby, the rotor-synchronised spin-echo pulse sequence helps by refocussing both the inhomogeneous decay and the isotropic shift [183]. Moreover, sensitivity enhancement can be obtained by applying a series of spin-echoes rotor period synchronized pulses called

Carr–Purcell–Meiboom–Gill sequence. In the present work the CPMG sequence was not used to record the spectra, however it may be considered in a future complementary work. For instance, it could be incorporated into a more sophisticated experiment to enhance sensitivity, such as the SHAP-CPMG (short high-power adiabatic pulse) sequence for broadband excitation [183].

The spectra were recorded at an external field corresponding to a ^{31}P Larmor frequency of 162 MHz and 12.5 kHz MAS. The MAS speed used in the present work is clearly below the ultra fast MAS (60 – 100 kHz) used to enhance spectral resolution and sensitivity in paramagnetic systems. In this regard, higher rotation frequencies reduce signal overlap and number of spinning sidebands and dipolar couplings [318, 324]. Nevertheless, the ABMS broadening is not removed by MAS and may dominate the lineshapes and linewidths due to the magnetic anisotropy of ions such as Co^{2+} . Despite the enhancement in sensitivity and resolution associated to high magnetic field, fields lower than 200 MHz are advantageous in paramagnetic NMR, since shifts, SA and inhomogeneous broadening scale up with the external magnetic field [183, 197].

6.4.2 Paramagnetic shift

The presence or absence of paramagnetic shifts may provide structural information such as clustering or random distribution of paramagnetic species in solid systems [207, 320, 323]. The "paramagnetic shift" instead of a splitting is the result of the coupling between the nucleus and the unpaired electron spins, known as the hyperfine interaction [183]. This interaction is comprised by the Fermi-contact due to a through-bond transfer and the pseudo-contact shift (PCS) due to a through-space spin-dipolar transfer of the unpaired electron spin onto the nucleus [183]. The magnitude and sign of paramagnetic shifts are highly dependent on different factors such as: the distance, bonding geometry and dihedral angle between the observed NMR nucleus and the paramagnetic centre [185, 320]. Accordingly, the shorter distances of more covalent M–O bonds may be related to larger paramagnetic shifts owing to the Fermi-contact interaction [183]. In fact, oxygens directly bonded to paramagnetic cations have displayed paramagnetic shifts as large as 3000-7500 ppm [320]. Regarding ^{31}P spectra of paramagnetic samples, they may be challenging owing to large paramagnetic shifts (100-1000 ppm) [191].

The isotropic paramagnetic shift is the sum between the contact (through-bond) and pseudo-contact (through-space) interactions. However, PCS only appears on metal ions with electronic configurations that are subject to SO coupling, since it depends on the susceptibility anisotropy but not on the isotropic susceptibility. Therefore, transition metal ions that

do not undertake SO coupling or in coordination environments with cubic symmetry, the isotropic paramagnetic shift is defined entirely by the Fermi-contact interaction [183, 320]. Accordingly, for such systems the zero-field splitting (ZFS) interaction is non zero and it is proportional to SO coupling effects [183]. In $45\text{P}_2\text{O}_5-(30-x)\text{CaO}-25\text{Na}_2\text{O}-x\text{CoO}$ (x : 0.01 to 10 mol%) glasses, Co^{2+} ions are a $3d^7$ high spin system with $S = 3/2$, as shown by EPR. Hence, large SO coupling effects related to Co^{2+} ions are expected, which may contribute significantly to the total paramagnetic shift, especially the PCS due to the likely large ZFS interaction. Even though UV-vis-NIR showed that the glass system is comprised by Co^{2+} ions with about 8% tetrahedral and 92% octahedral symmetries, non cubic environment can be assumed owing to the expected lower symmetry of glasses compared to crystals [320]. Hence, this also supports the fact that both the Fermi-contact and PCS contributions are important in the overall paramagnetic shift of the glasses [320].

The ^{31}P paramagnetic shifts on the glasses are expected to have most likely an important contribution from the Fermi-contact. This may be the case for nuclei located within the first and second coordination spheres of the Co^{2+} ion, it means relative short-range pathways [320]. However, this depends on a favourable orbital overlap and accordingly an appreciable transfer of electronic spin density from the Co^{2+} ion to phosphorus. That is confirmed by the large ^{31}P paramagnetic shifts reported for LiCoPO_4 , indicating a strong orbital overlap, thus, the Fermi-contact interaction along the $\text{Co}-\text{O}-\text{P}$ pathways [183]. The magnitude and number of the individual short-range $\text{Co}-\text{O}-\text{P}$ pathway contributions depend on the symmetry of the P sites and coordination angles. The sign of the pathway contribution is correlated to the latter and therefore difficult to predict. A positive contribution indicates a dominance of the delocalization spin-transfer mechanism, whereas, a negative one indicates a dominance of the polarization mechanism. Generally, it is likely that both mechanisms are active, being the case for LiCoPO_4 [183].

As can be seen in Fig. 6.2a and Table 6.2, the δ_{iso} from the Q^2 and Q^1 moieties remain invariant within the experimental errors. Owing to the low symmetry nature of the glasses, it is expected that the number of $\text{Co}-\text{O}-\text{P}$ pathways is substantially larger than for LiCoPO_4 and proportional to the broad range of P sites (Fig. 6.2b). Even though, it may be likely to have positive and negative signs of the electron-spin transfer for each pathway contribution; it may be rather unlikely to have a levelling off of the sign for all pathways contributions thorough the glass series. Accordingly, the overall paramagnetic shifts involving the Fermi-contact interaction may be sufficiently large to lie outside the spectral window, making them not observable. In fact the reported δ_{iso} of the Q^0 group for LiCoPO_4 is 2756 ppm [183], whereas the experimental spectral window used herein was from 300 to -300 ppm.

Both the non perfect cubic symmetry expected in a glass system and the large magnetic anisotropy of the Co^{2+} ion may lead to a non negligible PCS contribution. Thus, PCS or spin-dipolar interactions are expected from both intermolecular and intramolecular long-range pathways. Such long-range pathway contributions are counted further away than the five nearest-neighbour interactions, thus Co^{2+} ions at larger distances than the second coordination sphere [320]. As discussed above, the P sites (Q^1 and Q^2) are non equivalent in the glasses but rather split into a broad range of distinct sub-sites, which subsequently involve broad peaks associated to the paramagnetic shifts. Hence, a broad range of PCS contributions proportional to the corresponding range of P sites, would be expected for the glasses. That may be extrapolated to the larger linewidth of the Q^2 compared to the Q^1 peaks (Fig. 6.2b). For LiCoPO_4 , a non negligible PCS contribution on the overall ^7Li and ^{31}P paramagnetic shift was reported [183]. Accordingly, herein the overall paramagnetic shifts involving the PCS interaction most likely lie outside the spectral window, as discussed for the Fermi-contact interaction.

Regarding the effect of the temperature on the paramagnetic shift, it is related to a coupled cluster of paramagnetic ions. Accordingly, the shifts may increase or decrease with temperature in correspondence with antiferromagnetic and ferromagnetic coupling, respectively. Both effects are due to ordering of the electronic spin states at low temperatures, which may lead subsequently to an increase or decrease of the magnetic moment [183]. In general, as the temperature increases it is expected that the paramagnetic shifts converge to the main peak [320]. The temperature dependence of the paramagnetic shifts on the glass system was not investigated. Nevertheless, it may be unlikely that all magnetic exchange interactions between the paramagnetic centres may not persist up to room temperature, at which the spectra were recorded.

6.4.3 Paramagnetic relaxation enhancement (PRE)

The motions associated to the phosphate polymers that comprise the glasses are expected to start at their glass transition temperature. However, the spectra of the glass system were measured at room temperature, way below their glass transition temperatures. Therefore, neither overall tumbling nor internal motional dynamics on the relevant timescale can account for the mechanism of electronic relaxation, as it is the case for liquids. In solids such as glasses, phonons have been suggested as a likely mechanism for electronic against nuclear relaxation. For metal ions with non-zero SO coupling such as Co^{2+} , the interaction of such metal with the lattice may be mediated phonons. In fact, three main mechanisms have been suggested for the electronic relaxation. (1) Phonons matching the electronic Zeeman interaction, only important at low temperatures (~ 10 K). (2) The Raman effect, where the

energy difference between two phonons should match the electronic spin transition energy and (3) the Orbach process [183].

T_1 values of glasses depend strongly on their preparation technique, i.e. solid or liquid-state syntheses, casting, etc [325]. As can be seen in Table 6.2, the diamagnetic glass (Co0) exhibits a relatively long T_1 value, 25.80 s. Nevertheless in the present thesis, significantly larger T_1 values (~ 800 s) have been measured for other alike diamagnetic glass systems, discussed on other chapters, as can be seen in Table 3.3. One reason may lie on the more restricted motions of rigid diamagnetic systems, such as vibrations, which are a less efficient source of nuclear relaxation as compared to more mobile systems [183]. Conversely, in paramagnetic glasses there is a substantial reduction of T_1 values, which is proportional to the concentration of paramagnetic centres, i.e. $T_1 = 0.6743$ s for Co5 (Table 6.2). For instance, owing to signal loss it was not possible to determine the T_1 value for Co10. Hence, the paramagnetic relaxation enhancement (PRE) was efficient. Despite the rigid nature of the glasses, the vibration motion is still an efficient source of electronic relaxation related to the paramagnetic centres, which subsequently induces nuclei relaxation [183]. Hence, Co^{2+} ions open new pathways for nuclear spin relaxation, which allows rapid acquisition by reducing the recycle time [183, 186].

The Solomon–Bloembergen–Morgan relaxation mechanism is expected to work in rigid systems, such as glasses, in an analogous way as in solution. It is the principal mechanisms of nuclear relaxation and includes: (1) the spin-dipolar hyperfine interaction called the Solomon mechanism, and (2) the Fermi-contact interaction called Bloembergen mechanism [183]. On the other hand, d-block transition metal ions with large SO couplings result in fast electronic relaxation, i.e. Co^{2+} ($S = 3/2$, 1 – 10 ps) [183]. The Curie mechanism dominates for such systems, namely for paramagnetic centres with fast correlation and electronic fluctuation times ($< 10^{-11}$ s) [183]. Nevertheless, the Curie mechanism may only take place in solids, providing that slow internal motions still take place. That is not the case for glasses owing to their motionless nature below the transition temperature, as discussed above. Hence, the contribution of the Curie relaxation to the linewidths and their coherence lifetimes may be negligible in glasses. Accordingly, PRE caused by Co^{2+} in the glasses is not expected to decrease the magnetization transfers, conversely as for solutions [185].

6.4.4 Homogeneity approach

An empirical function to assess the homogeneity of paramagnetic ion distribution in a diamagnetic host was used, $f_{\text{visible}} = \exp(-k_1 r_0^3 x_{\text{Co}})$ [207]. The model assumes that the perturbed nuclei by the paramagnetic effects are located inside a radial sphere (r_0) of influence

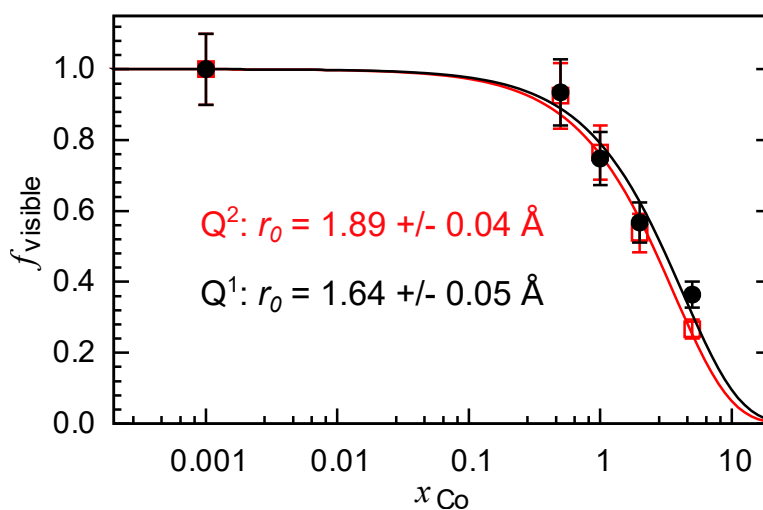


Fig. 6.3: The visible fraction of ^{31}P nuclei (f_{visible}) from quantitative single pulse ^{31}P solid-state MAS NMR for $45\text{P}_2\text{O}_5-(30-x)\text{CaO}-25\text{Na}_2\text{O}-x\text{CoO}$ (x : 0 to 10 mol%) glasses, calculated according to the statistical distribution model based on the fitted function $f_{\text{visible}} = \exp(-k_1 r_0^3 x_{\text{Co}})$ plotted against the Co^{2+} doping mole fraction x_{Co} in the log scale [207]. Two functions were used by fitting with the peaks Q² (red) and Q¹ (black) with $k_1 = 0.0405 \pm 0.0009$ and $k_1 = 0.0537 \pm 0.0018$, respectively. The determined wipe-out radii r_0 are 1.89 ± 0.04 and 1.64 ± 0.05 Å for Q² and Q¹, respectively.

of the paramagnetic ion, in this case Co^{2+} (Fig. 6.4). Such nuclei are non-observable by assuming that the paramagnetic shift is large enough to shift the resonance outside the spectral window. The approach involves quantitative single-pulse ^{31}P MAS-NMR to obtain the distribution of Co^{2+} in the diamagnetic glass, $45\text{P}_2\text{O}_5-30\text{CaO}-25\text{Na}_2\text{O}$. The expected peak areas of the ^{31}P nuclei that are outside the sphere of Co^{2+} ions were obtained by simulating the spectra, where the position and width of the peaks were constrained to the values of the diamagnetic glass [320]. Thus, the relative areas of the unshifted resonances, relative to the diamagnetic glass, as a function of the Co^{2+} content are used to assess its random distribution [207].

As can be seen in Figs. 6.2a and 6.2b, the ^{31}P solid-state MAS NMR spectra of the glass series show a monotonous decay of the signal intensity with concomitant broadening of the resonance as a function of the Co^{2+} content. In the present work, the fraction of unperturbed ^{31}P nuclei determined from the NMR signal followed the curve correlating the empirical fitting function (f_{visible}) and the mole fraction of the paramagnetic centre (x_{Co}) in the log scale [207]. That relationship shows a simple behaviour following a monotonous decay, as can be seen in Fig. 6.3. Two functions were used by fitting with the peaks Q² and Q¹, whose fitting parameters are $k_1 = 0.0405 \pm 0.0009$ and 0.0537 ± 0.0018 , respectively. Accordingly as can be seen in Fig. 6.4, the determined wipe-out radii r_0 are 1.89 ± 0.04 and 1.64 ± 0.05 Å

for Q^2 and Q^1 , respectively.

Interestingly, in the last chapter it has been suggested that $^{[\text{IV}]}\text{Co}^{2+}$ may link preferentially to Q^1 sites in the glasses, owing to the higher basicity of Q^1 compared with Q^2 sites. That may be correlated with the slightly smaller wipe-out radius (r_0) for Q^1 sites, by taking into account the ionic radii of high spin Co^{2+} , namely $^{[\text{IV}]}\text{Co}^{2+} < ^{[\text{VI}]}\text{Co}^{2+}$ [306]. Additionally, the theoretical effective magnetic moment for high spin Co^{2+} is 5.2, $\mu_{S+L} = \sqrt{4S(S+1) + L(L+1)}$, with $S = 3/2$ and $L = 3$. However, owing to significant quenching of orbital angular momentum in tetrahedral compared to octahedral complexes, μ_{eff} may be lower for the former ones [319]. Hence, herein the wipe-out radii (r_0) obtained by fitting the peaks Q^1 and Q^2 are associated with $^{[\text{VI}]}\text{Co}^{2+}$ and $^{[\text{IV}]}\text{Co}^{2+}$, respectively.

The wipe-out radii (r_0) for $^{[\text{VI}]}\text{Co}^{2+}$ and $^{[\text{IV}]}\text{Co}^{2+}$ are rather small compared to the reported one for Eu^{2+} ions, 17 Å [207]. Lanthanide ions are in the "weak crystal-field limit", where the SO coupling is much stronger than the crystal-field interaction. Thus, in non-cubic systems the ZFS is generally expected to dominate [183]. Owing to the half-filled f shell of Eu^{2+} ($4f^7$) with spin $S = 7/2$, the SO coupling is effectively zero and subsequently the PCS contribution is likewise zero. Conversely, the Fermi-contact shifts are expected to be large for Eu^{2+} ions [183]. On the other hand, high spin Co^{2+} with $S = 3/2$ is expected to undertake substantially smaller Fermi-contact shifts in comparison with Eu^{2+} ions. Additionally, PCSs are also expected for Co^{2+} owing to the and large SO couplings despite the tetrahedral and octahedral symmetries of Co^{2+} in the glasses. That is related to the non perfect cubic symmetries expected in glasses owing to their amorphous nature.

As mentioned above, the calculated r_0 values for the tetrahedral and octahedral symmetries may be too small (Figs. 6.3 and 6.4). By taking into account the potential magnitude of the Co–O–P pathway distances, the threshold of the calculated r_0 values may not reach even the short-range pathways. Thereby, the ionic radii, high-spin $^{[\text{VI}]}\text{Co}^{2+} = 0.745$ Å and $^{[\text{IV}]}\text{Co}^{2+} = 0.58$ Å [306], are a hint about the potential pathway distances. On the other hand, the model assumes that at extremely low paramagnetic concentration, the spheres would not overlap with each other [207]. Thus clustering is a matter of statistical probability which may be noticeable on the NMR spectra at relatively high content of paramagnetic centres. In that sense, multiple interactions caused either by clustering or saturation with paramagnetic centres may cancel each other. Unpaired electrons from clusters exchange magnetic interactions via coupling, which may result in temperature-dependent ferromagnetic or antiferromagnetic behaviour [183].

A levelling off between Co^{2+} interactions owing to clustering may be a reason for the

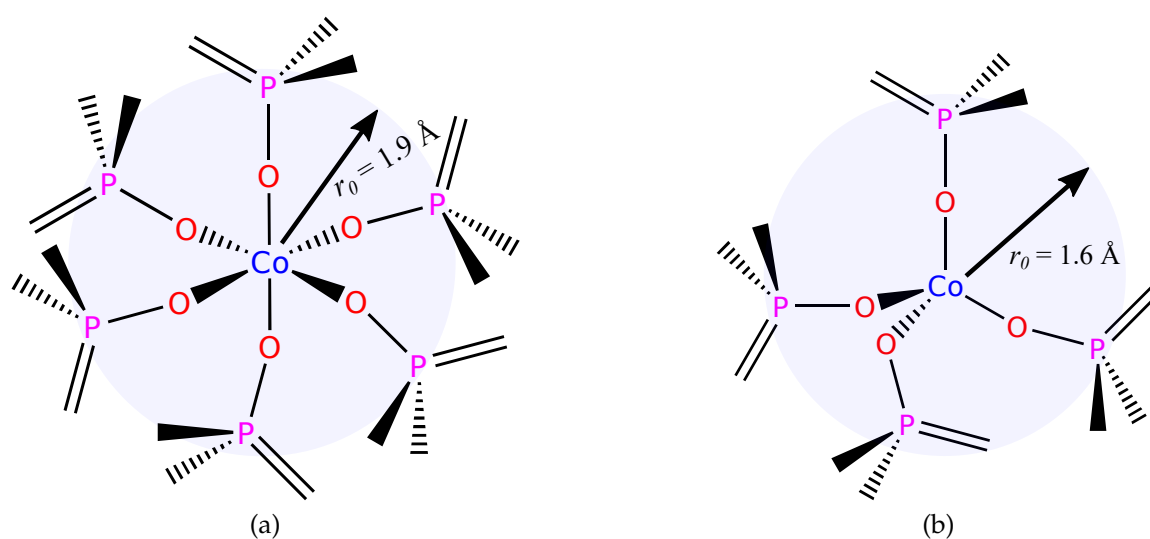


Fig. 6.4: Schematic of the calculated radial spheres of influence r_0 of the paramagnetic ion Co^{2+} with (a) octahedral and (b) tetrahedral symmetries in the glass series. According to the model, the NMR resonances are assumed to become non observable for the ^{31}P nuclei located inside the wipe-out radius r_0 [207].

small wipe-out radii r_0 of the two symmetries of Co^{2+} in the glasses (Fig. 6.4). A strong indication of clustering may be the non disappearance of the NMR signal even for concentrations of Co^{2+} as high as 10 mol% , Co_{10} , as can be seen in Fig. 6.2a. That may be further confirmed by Fig. 6.3, which shows a mild decay of the curve relating the empirical function f_{visible} against x_{Co} in comparison with the curve published for Eu^{2+} [207]. Hence, it is a good indication that the Co^{2+} ions are not randomly distributed in the angstrom scale but rather heterogeneity may occur as a result of clustering in the glasses.

On the other hand, Co^{2+} in non-cubic environments may undertake a ZFS interaction which is proportional to the spin-spin and SO interactions. The ZFS is analogous to the nuclear quadrupole interaction and hence presents a radial dependence [183]. Accordingly, the radial sphere model [207] may not apply for Co^{2+} ions even in tetrahedral and octahedral symmetries owing to the distortion of such environments in non-crystalline solids. Nevertheless, it may still provide a hint about the distribution of Co^{2+} ions in the diamagnetic host glass, $45\text{P}_2\text{O}_5 - 30\text{CaO} - 25\text{Na}_2\text{O}$. In this case, clustering instead of random distribution has been suggested at high concentrations of Co^{2+} ions.

An open question still remains regarding the constant nature of the wipe-out radius. It has been published that the wipe-out radius of Eu^{2+} may be a constant value independently of the lattice. Accordingly, the cation distribution may be potentially assessed from interpolation on the published curve involving the empirical fitting function [207]. However, by

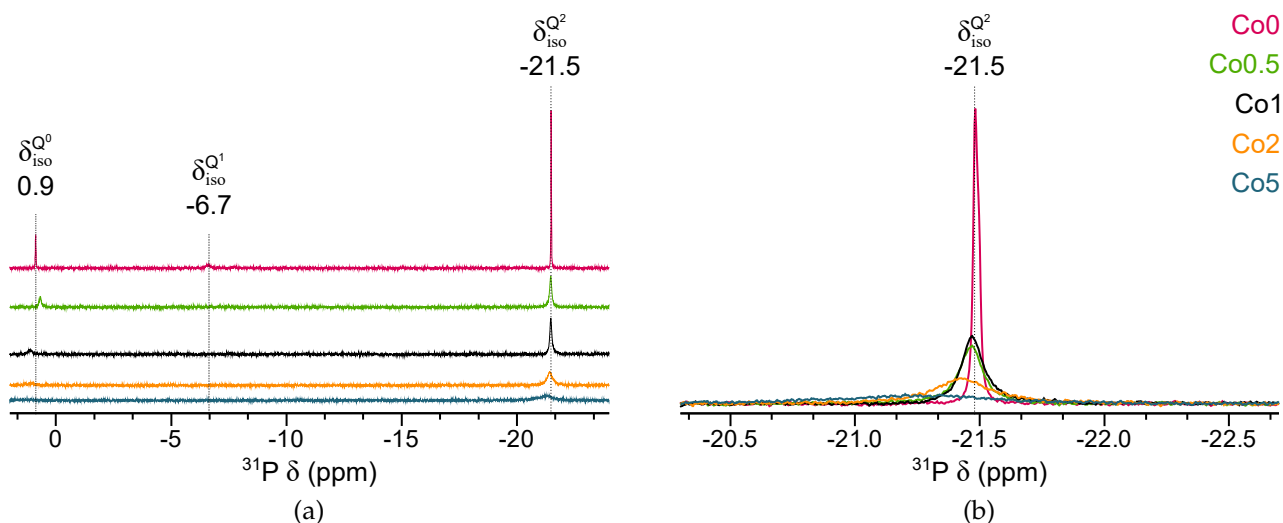


Fig. 6.5: Liquid ^{31}P NMR spectra of the leachate solutions for the glass series $45\text{P}_2\text{O}_5-(30-x)\text{CaO}-25\text{Na}_2\text{O}-x\text{CoO}$ (x : 0 to 5 mol%), recorded at 37°C in Tris buffer 0.0250 M ($\text{pH}_0 7.4 \pm 0.1$). (a) The $^{31}\text{P} \delta_{\text{iso}}$ are assigned for all phosphate species in solution, thus Q^0 , Q^1 and Q^2 moieties. (b) Spectra shown only on the $^{31}\text{P} \delta_{\text{iso}}$ range of the Q^2 moieties.

taking into account the discussion regarding the paramagnetic shifts, through-bond and through space. The invariance of the wipe-out radius (r_0) seems quite unlikely since the shifts depend strongly on the pathway geometries, which are particular of the lattice [183].

6.5 Paramagnetic effects on liquid ^{31}P NMR

6.5.1 Linewidth

The linewidth of the liquid NMR spectra involves both fluctuations of the local field and the distribution of Larmor frequencies. Thereby, the linewidth is given by a combination of PRE and the inhomogeneous broadening owing to the non-spherical shape of the sample container [183]. For paramagnetic ions with rapid electronic relaxation such as Co^{2+} , the transverse PRE contributes to the broadening. As can be seen in Figs. 6.5a and 6.5b, the Co^{2+} causes severe broadening of all peaks (Q^2 , Q^1 and Q^0) of the spectra. From the spectra is obvious that the broadening of the resonances is proportional to the CoO content, as expected. Accordingly, it indicates that the ^{31}P nuclei are located in the immediate environment of the Co^{2+} ions. As a result, at high concentration of paramagnetic centres the NMR signal may turn non observable. That is in fact the case for the Q^1 and Q^0 peaks of the glass with 5 mol% of Co^{2+} (Co5). Thereby, the Q^2 peak is still slightly observable as shown in Figs. 6.5a and 6.5b.

6.5.2 Paramagnetic shift

The hyperfine coupling constant related to the Fermi-contact interaction is proportional to the electron density transferred to the nucleus of the ligands [183]. The contact shift is expected to attenuate after five bonds, thus the second coordination sphere, $\text{Co}^{2+}-\text{O}-\text{P}$. Therefore, this contribution is restricted to ^{31}P nuclei coordinated around the Co^{2+} ions. The Fermi-contact interactions should be important, even though the PCS contributions may be predominant in Co^{2+} complexes [319]. Hence, for long phosphate chains in solution it would be expected that the paramagnetic shift is composed significantly by the the dipolar interaction, PCS (5 – 30 Å) [183, 319]. This would imply that electron delocalization around the ^{31}P nuclei may not be extensive, but rather the electrons reside substantially as point dipoles at the metal centre [319]. That is the reason for the utility of high spin Co^{2+} complexes associated to the PCS interaction, which depends strongly on the geometry and thus provides a long-range structural information [319]. However, independently of the origin of the paramagnetic shifts, they are expected in the glasses to be sufficiently large to shift the peaks outside of the spectral window, rendering them non-observable. Hence, the slight shifts observed in Fig 6.5b of the Q^2 species for Co2 and Co5 are related to potential variations of the field during spectra acquisition, rather than paramagnetic shifts.

6.5.3 Paramagnetic relaxation enhancement (PRE)

The presence of paramagnetic ions, such as Co^{2+} , attached to a phosphate fragment influences T_1 and T_2 values of the ^{31}P NMR signal. Such effects is expected to be substantially larger than that caused by diamagnetic sodium and calcium ions. Thereby, T_2 is always shorter than T_1 , either because the former time reflects the Fermi-contact contribution in the limit of fast exchange or because it is influenced by the ligand residence time [326]. Hence, the binding of phosphate fragments to the paramagnetic Co^{2+} to form the corresponding Co-phosphate complexes can be monitored by the enhancement in ^{31}P NMR relaxation rates. The PRE can be obtained by subtracting the relaxation times between the paramagnetic Co-phosphate and the diamagnetic phosphate complexes in solution [327]. In the present work the PREs were not determined but this will be the subject of a future study.

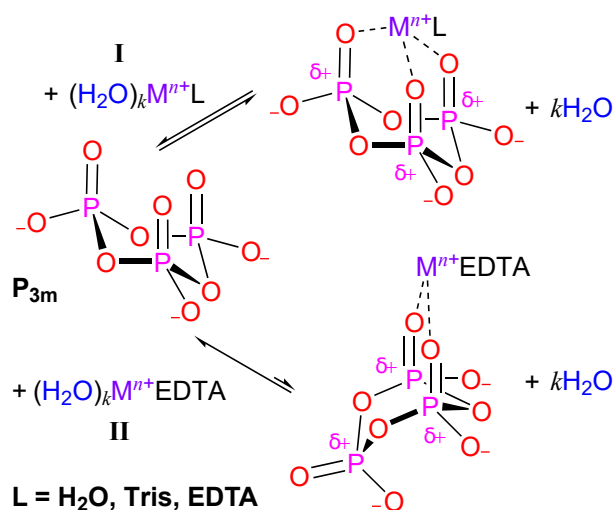
The Curie contribution dominates for paramagnetic metals with relaxation times substantially shorter than the reorientation times [183]. Therefore, the PREs dominated by Curie mechanism is useful to obtain structural information of macromolecules such as metalloproteins [319, 326]. The Curie relaxation may be interpreted as a consequence of hyperfine interaction associated to stochastic modulation, it affects T_2 and leads to severe line broadening [183]. Therefore, for Co^{2+} the Curie relaxation is important in the range 3 – 10 Å [185]. On the other hand, the Solomon-Bloembergen-Morgan mechanism involves

the spin-dipolar hyperfine and the Fermi-contact interactions known as the Solomon and Bloembergen mechanisms, respectively [183]. This mechanism becomes important for high external magnetic fields and fast molecular dynamics. Herein both conditions apply for the relaxation of the ^{31}P nuclei, thus the high magnetic field $B_0 = 9.4$ T and the fast motion owing to the relative small size of the phosphate fragments in solution.

The principal mechanisms of electronic relaxation are modulation of the transient, ZFS and phonons [183]. For metal ions such as Co^{2+} with spin $S > 1/2$, the electronic relaxation is mainly due to its considerable ZFS and corresponding strong SO couplings, being both inversely proportional to the symmetry [183, 319]. Hence, rapid relaxation times are an indication of low symmetry. Owing to the presence of different potential ligands in solution (H_2O , Tris, EDTA), high-spin Co^{2+} ions are expected to undertake different distorted octahedral symmetries [319]. As can be seen in scheme 6.1, the complexes between a metal ion ($\text{M}^{n+} = \text{Co}^{2+}$) and a phosphate fragment ($\text{P}_{3\text{m}}$) may undertake different denticities (bi-, tri-, tetradentate), and accordingly different conformations. Therefore, the examination of paramagnetic effects such as PREs on the ^{31}P nuclei offers a logical alternative to probe the conformational structures and dynamics of Co^{2+} –phosphate complexes in solution.

6.6 Cobalt-phosphate complexes in solution

In aqueous solutions phosphate fragments and other potential ligands (L: Tris) bind to metal cations such as Co^{2+} , replacing a given number of water molecules, $k\text{H}_2\text{O}$ (Scheme 6.1). In this case an appreciable change in the ^1H NMR relaxation of the bulk water is expected, since coordinated water molecules are exchangeable with Co^{2+} [326]. Complexes that react quickly are known as labile such as $[\text{Co}(\text{OH}_2)_6]^{2+}$, and their lifetimes are of the order of ns which is the time for diffusion of a molecular diameter [90]. Hence it may be worth it to explore PREs on ^1H nuclei in a future work. Regarding the nature of the cations, they are less labile as the radius decreases, namely $\text{Co}^{2+} < \text{Ca}^{2+} < \text{Na}^+$, owing to the larger M–L bond strengths. Additionally, for the same reason it is sterically difficult for incoming ligands to approach the metal cation (M) closely. Therefore, the aqua complexes of the s-block ions i.e. Na^+ and Ca^{2+} ions are very labile. It means that in non-saturated solutions all leachate cations from the glass system (Co^{2+} , Ca^{2+} , Na^+), are complexed to ligands with higher basicity than water, i.e. Tris < phosphate species < EDTA [1]. As can be seen in Scheme 6.1I, it would be expected that in the leachate solutions buffered with Tris, the equilibrium would be favoured towards the formation of complexes between M^{n+} and phosphate fragments in a polydentate fashion [234]. That is also related to the additional stability from the ligands i.e. LFSE and chelate effects [90].



Scheme 6.1: Formation of a complex between a metal cation (M^{n+} : Na^+ , Ca^{2+} , Co^{2+}) and trimetaphosphate (P_{3m}), and an additional ligand (L: H_2O , Tris, EDTA) depending on the coordination number of M^{n+} and steric effects. The metal cation (M^{n+}) acts as a catalyst of hydrolysis, which by complexing with phosphate groups increases the electrophilic character of P, δ^+ , favouring nucleophilic attack by water [1]. (I) Favoured formation of $\text{M}(\text{L})(\text{P}_{3m})$ with L: H_2O , Tris and P_{3m} coordinated in a tridentate manner as a chair conformation. (II) Non-favoured formation of $\text{M}(\text{L})(\text{P}_{3m})$ with L: H_2O , EDTA and P_{3m} coordinated in a bidentate manner as a boat conformation.

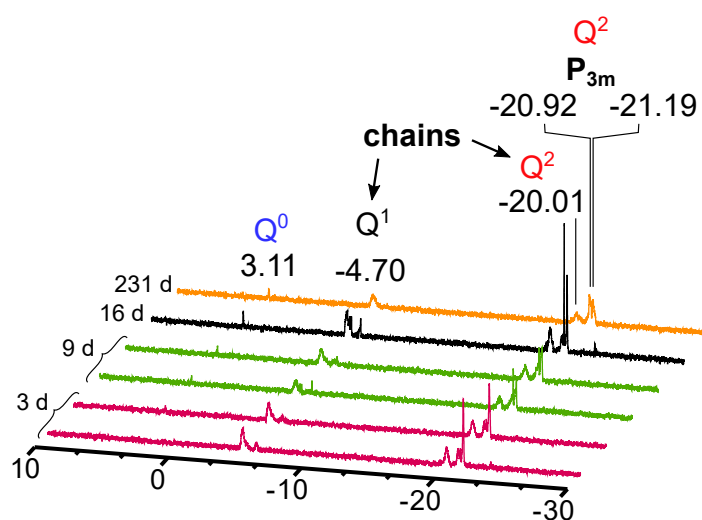
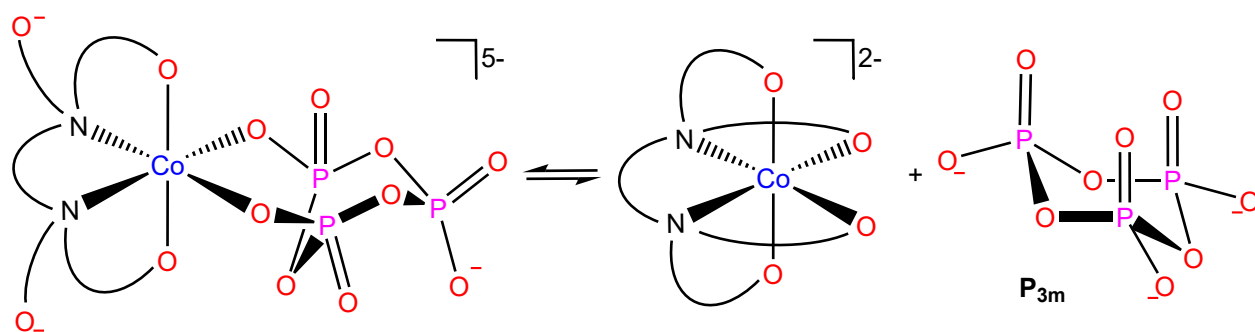


Fig. 6.6: Liquid ^{31}P NMR at 37°C of the leachate solutions for Co5 in EDTA at $\text{pH}_0 10.0 \pm 0.1$, from 3 to 231 days. The polymerization of the phosphate species in solution, namely Q^0 , Q^1 and Q^2 from chains and rings (P_{3m}) is highlighted on the spectra.

In Scheme 6.1I, the formation of the $\text{M}(\text{Tris})(\text{P}_{3m})$ complex is depicted and aims to explain the ^{31}P NMR spectra of leachate solutions for the glass series in Tris buffer (Fig. 6.5). From Fig. 6.5b is evident the decrease of the P_{3m} peak intensity as a function of the Co^{2+}



Scheme 6.2: Displacement reaction in which the trimetaphosphate (P_{3m}) ligand is driven out of the $\text{Co}(\text{EDTA})(P_{3m})$ complex leaving P_{3m} as a free anion and the stable $\text{Co}(\text{EDTA})$ complex.

owing to the PRE and paramagnetic shift. It confirms the direct binding of Co^{2+} to the P_{3m} ring, most likely in chair conformation. As shown in Fig. 6.5a, the peak broadening, as an indication of the direct coordination of the phosphate fragments to the paramagnetic Co^{2+} , is observed for all the resonances, namely Q^0 , Q^1 and Q^2 moieties.

The results confirm the ones reached indirectly through the analysis of the time-dependent ^{31}P NMR spectra of leachate solutions in Tris buffer in analogous diamagnetic glasses [1]. Thereby, the catalytic role of the metal cations in the hydrolysis were proved by the increase of the Q^0 resonance at expenses of the Q^1 and Q^2 ones. Owing to the high stabilization by chelate effects, it is expected that the equilibrium would be non-favoured towards the formation of complexes between $\text{M}(\text{EDTA})(\text{H}_2\text{O})_k$ and phosphate fragments. Accordingly, the formation of the $\text{M}(\text{EDTA})(P_{3m})$ complex is depicted in Scheme 6.1III, which explains the ^{31}P NMR spectra (Fig. 6.6) of leachate solutions for the glass series in EDTA buffer. From Fig. 6.6 is evident that the intensities of the Q^1 and Q^2 peaks remain steady even after 231 days, no precipitation took place in EDTA solution along time. Even though this is an indication of substantially low rates of hydrolysis, it still takes place as it is obvious from the appearance and evolution of the Q^0 peak. The suggested mechanism of hydrolysis is catalysed by metal cations [1], thus, the paramagnetic effects of Co^{2+} on the ^{31}P peaks may be expected. Nevertheless that is not the case in EDTA solutions, which is expected owing to the high stabilities of $\text{M}(\text{EDTA})$ complexes, associated to LFSE and chelate effects. The only remarkable difference of the spectra in EDTA, related to the ones in Tris, is the splitting of the P_{3m} resonance ($\Delta\delta \approx 0.2$ ppm) to lower field into a sharper peak with stable position ($\delta = -21.00 \pm 0.02$ ppm), whose intensity tends to increase with time (Fig. 6.6).

Scheme 6.2 shows a reaction that intends to explain the P_{3m} peak splitting, in which both EDTA and P_{3m} are initially coordinated to Co^{2+} in a tetra- and bidentate fashion, respectively.

That corresponds to the second bifurcation at high field of the P_{3m} resonance (-21.22 ± 0.02 ppm) of the $\text{Co(EDTA)}(P_{3m})$ complex, assignment based on the broadening correlated to the paramagnetic effects. Additionally, the boat conformation is suggested owing to the slight shift of the broad bifurcation to higher field (-21.08 ± 0.02 ppm), of the P_{3m} in EDTA compared to Tris. Even though it may be expected that from the beginning the most stable complex Co(EDTA) may exist in solution, seemingly the coordination of the phosphate fragments to Co^{2+} occurs, potentially nearby the glass surface and at early time periods.

On the other hand, the slow increase in intensity of the sharp bifurcation of the P_{3m} peak implies a high activation energy of ligand displacement of EDTA for P_{3m} , owing to the steric repulsion associated to bulky ligands such as P_{3m} [90]. Hence, the $\text{Co(EDTA)}(P_{3m})$ complex may be non labile, which is translated into low rates of reaction. The existence of the free P_{3m} anion in EDTA solution, as dissociation product of the $\text{Co(EDTA)}(P_{3m})$ complex, is supported by the sharp resonance with fixed position, independently of time and glass composition. Additionally, the sharp feature of the resonance may indicate that the free P_{3m} anion undergoes fast dynamic conformational changes in the NMR timescale.

Chapter 7

Structural characterization of bioactive glasses by solid-state NMR

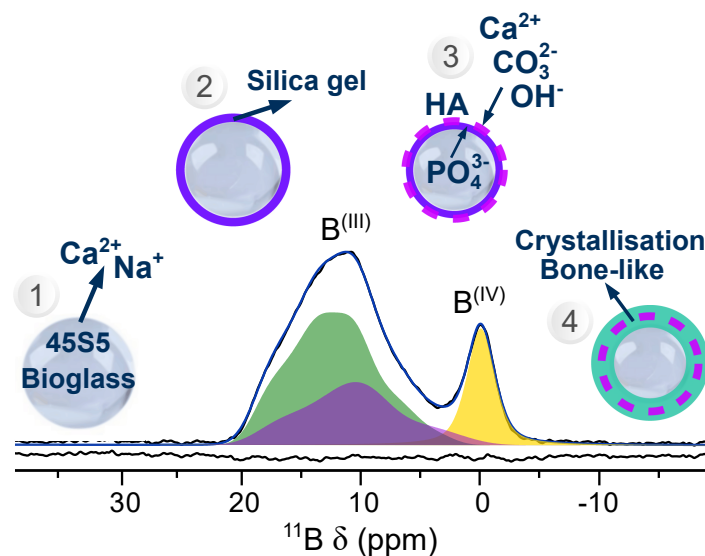


Fig. 7.1: ^{11}B solid-state MAS NMR spectrum of a Borate-based 45S5 bioactive glass, 45S5-25B. Schematic of the bioactive glass reaction in body fluid: (1) Selective leaching of Na^+ and Ca^{2+} ions at early stages. (2) Break-up of the silicate network and subsequent condensation of silanols to form a silica gel layer. (3) Migration of Ca^{2+} and PO_4^{3-} to the interface to form amorphous HA. (4) Crystallisation of HA to form new bone [15, 328].

7.1 Introduction

The current state of the art of solid-state MAS NMR involves increasingly sophisticated computational methods and has provided invaluable structural information about bioactive glasses. 45S5-based glasses are predominantly comprised of Q_{Si}^2 species with eventual presence of Q_{Si}^1 , Q_{Si}^3 and Q_{Si}^4 unresolved fractions, not accessible by deconvolution of ^{29}Si MAS

NMR spectra [329]. P_2O_5 in 45S5 attracts network modifiers, as shown by ^{31}P MAS NMR, where a single resonance assigned as orthophosphate species Q_p^0 appears, whose asymmetric features did not exclude minor amounts of Q_p^1 in the form of $P-O-P$ or $P-O-Si$ species [329], which were not detected by ^{17}O MQMAS NMR [330]. Conversely, in a sodium-free 45S5-based glass, $P-O-P$ species were excluded by using a J -based experiment (^{31}P refocused INADEQUATE), whereas the presence of $P-O-Si$ species in ^{29}Si -enriched samples was proved by ^{31}P $\{^{29}Si\}$ REDOR [331].

Nearly statistical intermixing of spatial distribution of phosphate species was concluded from DQ ^{31}P MAS NMR and MD simulations on bioactive phosphosilicate glasses with $NC \sim 2.11$ [332]. Conversely, aggregates of 5 – 6 phosphate units were deduced from ^{31}P MQ NMR experiments on a sodium free bioglass [331]. Regarding preferential bonding, a set of bioactive glasses including 45S5, where the Ca/Na ratio was varied, was probed by MD simulations together with ^{23}Na $\{S\}$ REDOR and $\{S\}$ ^{23}Na REAPDOR, with $S = \{^{29}Si, ^{31}P\}$. This indicated a random distribution with either phosphate or silicate species. However, an eventual preference of Ca^{2+} for the most negative Q_p^0 , Q_{Si}^1 and Q_{Si}^2 species, was not excluded [333]. On the other hand, some degree of selectivity between Na^{1+}/Q_p^1 and Ca^{2+}/Q_p^0 for particular P_2O_5 contents was suggested from ^{31}P MAS NMR analysis [334]. However, it seems the subject has not been unambiguously explained yet.

Since until now there are still open questions regarding the interlinking between (a) $Si-O-B^{(IV)}/B^{(III)}$ (b) $B-O-B^{(IV)}/B^{(III)}$ (c) $P-O-B^{(IV)}/B^{(III)}$, $P-O-Si$ ($B^{(III)}$ as ring and non ring) (d) the spacial distribution of phosphate species and (e) Ca/Na in the ternary-former system at compositions relevant for bioactive glasses; and this type of information concerns connectivity, which can be addressed by NMR through REDOR and REAPDOR as self verifiable experiments, homonuclear dipole–dipole interactions, DQ-NMR, and J -based experiments [329]. The aim of the present chapter was to undertake a preliminary structural investigation by solid-state NMR, in order to perform future advance solid-state NMR studies on selected 45S5-based systems to establish structural relationships with solubility and bioactivity trends.

7.2 45S5-based glasses with variable borate content

45S5 is the standard Bioglass[®] [14], however it has critical drawbacks such as a narrow processing window, which restrains the manufacturing of porous scaffolds by sintering. As a consequence the material poorly meets the mechanical properties of the original tissue. Boron-containing bioglasses have drawn attention recently, since by introducing B_2O_3 at ex-

penses of SiO₂, the mentioned drawbacks smooth out to a big extent, while holding or even increasing bioactivity [9]. In this regard, the boron content increases both the processing window and the degradation rate, which leads to a fully transformation into HA [335–337]. Thereby, the rates of the dissolution processes are tunable by adjusting the B₂O₃/SiO₂ ratio [20]. Currently, scientific work has also addressed biological responses of borate-based bioactive glasses such as: inhibition of cell proliferation at high concentrations of B₂O₃ [335], biocompatibility and enhancement of bone formation in rats [338], healing capacity of soft tissue wounds by ionic dissolution products [337] and stimulation of angiogenesis *in vivo* [339], among others.

Structural approaches concerning degradable borate-based 45S5 glasses are highly desirable to enable the design of bioactive glasses with an improved high-temperature processing window. In the frame of a collaborative work [215], ³¹P, ²⁹Si and ¹¹B solid-state MAS NMR were combined to investigate the system 24.4Na₂O–26.9CaO–*x*B₂O₃–(46.1–*x*)SiO₂–2.6P₂O₅ with 0 ≤ *x* ≤ 6.1 mol% (Table 7.1) in an attempt to get insights into the structure of such glasses.

Table 7.1: Nominal composition of 45S5-based glasses with variable borate content (mol%).

Glass	B ₂ O ₃	Na ₂ O	CaO	P ₂ O ₅	SiO ₂
45S5-25B	6.1	25.8	28.6	2.8	36.7
45S5-20B	4.8	25.5	28.2	2.7	38.7
45S5-15B	3.6	25.2	27.9	2.7	40.6
45S5-10B	2.4	24.9	27.6	2.7	42.5
45S5-1B	0.2	24.4	27.0	2.6	45.8
45S5	0	24.4	26.9	2.6	46.1

7.2.1 Solid-state MAS NMR

³¹P MAS NMR

According to solid-state ³¹P MAS NMR, the system containing 2.6 mol% of P₂O₅ was composed mainly by orthophosphate Q_P⁰ with a minor presence of pyrophosphate Q_P¹ tetrahedra (Fig. 7.2), corresponding the latter either to P–O–Si or P–O–B species [331, 340, 341]. The isotropic chemical shift for 45S5 was $\delta_{iso}^{Q^0} = 8.7$ ppm, the slight shift to higher frequencies with increasing boron content (~ 0.4 ppm) can be accounted as a deshielding effect of sodium relative to calcium (Table 7.2). That would be expected, owing to the higher field strength (Z/r^2) of calcium compared with sodium.

Table 7.2: Isotropic (δ_{iso}), at peak maximum (δ_{max}) chemical shifts (± 0.2 ppm) and relative areas of Q_p^n phosphate, Si^{IV} silicate (tetrahedral) and B^{III} , B^{IV} borate (trigonal, tetrahedral coordinations) species; determined from deconvolution [216] of quantitative single-pulse MAS NMR spectra.

B_2O_3 mol%	Q_p^0		Q_p^1		Si^{IV}		B^{III}		B^{IV}	
	δ_{iso} (ppm)	δ_{iso} (ppm)	A (%)	δ_{max} (ppm)	δ_{iso}^1 (ppm)	δ_{iso}^2 (ppm)	δ_{iso} (ppm)	A (%)		
6.1	8.7	0.4	1.6	-78.5	18.8	19.3	-0.1	17.8		
4.8	8.5	0.4	3.6	-	18.9	19.1	-0.3	13.6		
3.6	8.5	0.4	2.8	-	19.0	18.8	-0.5	13.3		
2.4	8.5	0.4	3.2	-79.1	18.7	19.0	-0.8	11.7		
0.2	8.5	0.4	4.0	-79.6	14.7	18.6	-1.2	7.7		
0	8.4	0.4	5.6	-79.7	-	-	-	-		

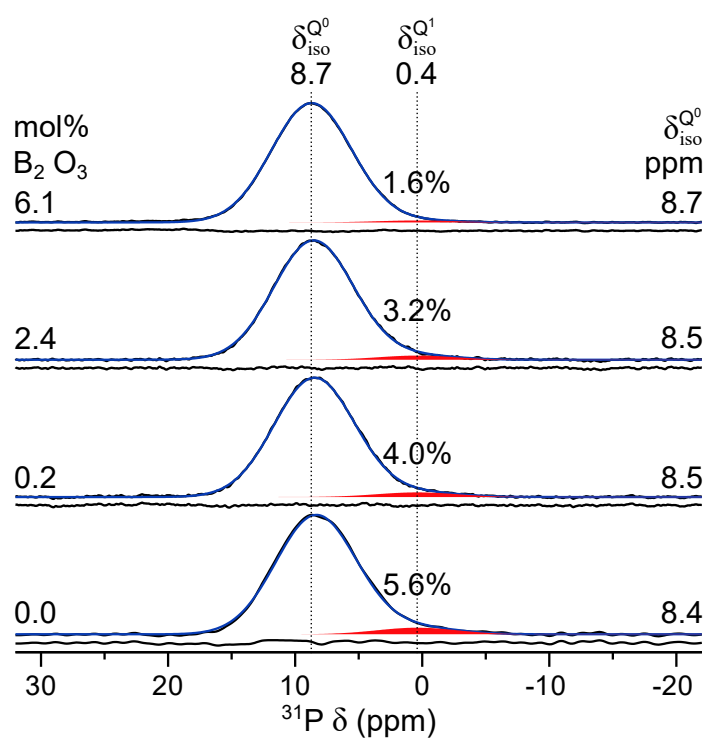


Fig. 7.2: Quantitative solid-state ^{31}P MAS NMR spectra of the glass series $24.4\text{Na}_2\text{O}-26.9\text{CaO}-x\text{B}_2\text{O}_3-(46.1-x)\text{SiO}_2-2.6\text{P}_2\text{O}_5$ with $0 \leq x \leq 6.1$ mol% in (black), best-fit (blue) and the difference curve (black) beneath each NMR spectrum. For the deconvolution [216] into two Gaussian lines corresponding to Q^0 and Q^1 (red, relative areas in %) groups, the spinning sidebands were taken into account.

^{29}Si MAS NMR

As can be seen in Fig. 7.3, solid-state ^{29}Si MAS NMR spectra showed only one broad resonance ranging from -65 to -100 ppm which corresponds to four-coordinated Si-O sites. The ^{29}Si lineshape was fitted into three Gaussian peaks consisting of a dominant Q_{Si}^2 merged

with Q_{Si}^1 and Q_{Si}^3 groups [340, 342]. Only a weak but clear decrease in shielding (~ 1.2 ppm) from $x=0$ to $x=6.1$ mol% was observed (Table 7.2), which can be explained by Si–O–B replacing Si–O–Si species.

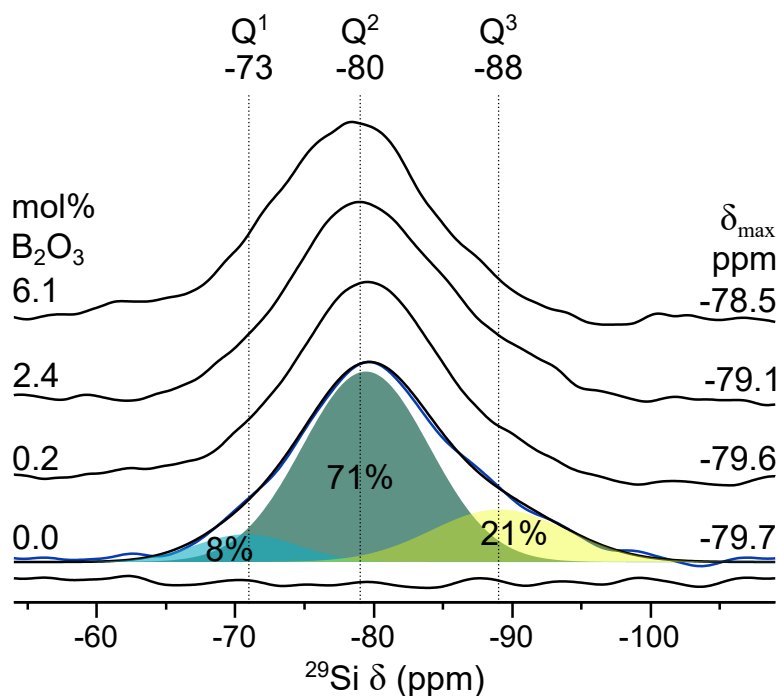


Fig. 7.3: Quantitative solid-state ^{29}Si MAS NMR spectra of the glass series $24.4\text{Na}_2\text{O}-26.9\text{CaO}-x\text{B}_2\text{O}_3-(46.1-x)\text{SiO}_2-2.6\text{P}_2\text{O}_5$ with $0 \leq x \leq 6.1$ mol% in (black), best-fit (blue) and the difference curve (black) beneath each NMR spectrum. The experimental spectra are comprised of a single resonance corresponding to tetrahedral Si–O sites. 45S5 (B_2O_3 : 0.0 mol%) was deconvoluted [216] into three Gaussian lines: Q_{Si}^1 , Q_{Si}^2 and Q_{Si}^3 ; where the positions and relative areas were constrained based on [342].

^{11}B MAS NMR

As can be seen in Fig. 7.4, solid-state ^{11}B MAS NMR revealed that the glasses are comprised by BO_3 and BO_4 moieties. The peak assigned as B^{III} was deconvoluted into two 2nd order quadrupolar lines corresponding to ring and non-ring trigonal borate species. The spectra exhibited progressive decrease of the BO_3/BO_4 ratio at growing boron-content with concomitant deshielding of both resonances (Table 7.2). This suggests two coexistent environments, a B-rich and a Si-rich one formed by a network of BO_3 entities and a network of $\text{B}^{\text{IV}}-\text{O}-\text{Si}$ species, respectively. Therefore, at increasing content of boron a depolymerization of BO_3 into BO_4 may occur as well as a reduction of the number of Si–neighbours in the $\text{B}^{\text{IV}}-\text{O}-\text{Si}$ species.

Connectivity between BO_3-SiO_4 preferred at expenses of BO_4-SiO_4 on a borosilicate

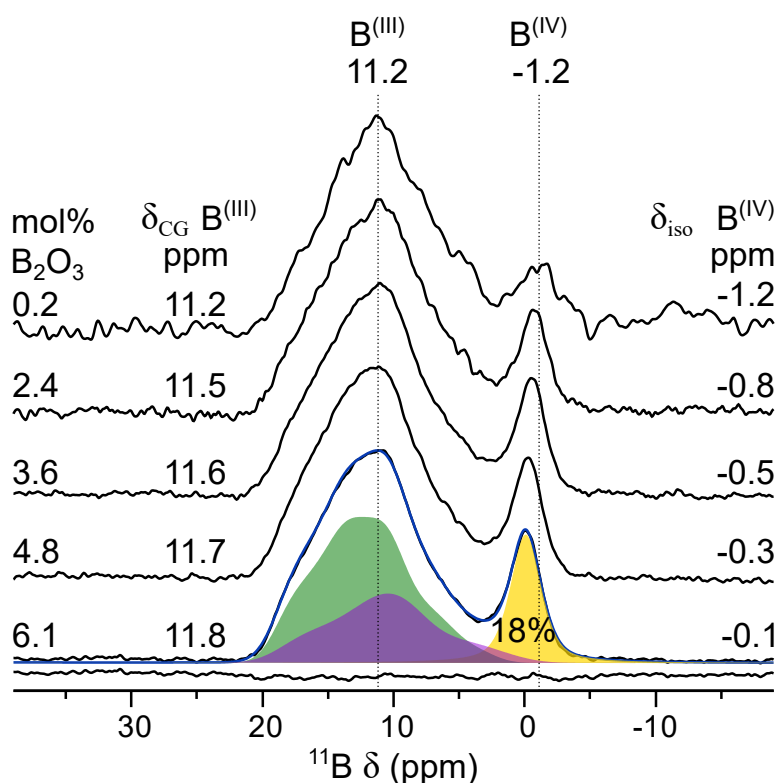


Fig. 7.4: Quantitative solid-state ^{11}B MAS NMR spectra (black). The spectrum with B_2O_3 : 6.1 mol% was deconvoluted [216] into one Gaussian line for tetrahedral borate B^{IV} (relative area in %) and into two 2nd order quadrupolar lines for the resonance (δ_{CG} , centre of gravity shifts) corresponding to trigonal borate B^{III} (ring and non-ring); best-fit (blue) and the difference curve (black) beneath the spectrum.

system has been controversial [325] and opposite to results on bosilicate-bioactive glasses [340]. On the other hand, ^{29}Si $\{^{11}\text{B}\}$ double-resonance REAPDOR and CP heteronuclear correlation (HETCOR) showed clear Si–O–B linkages, although no indication for the presence of direct bonds between boroxol rings and the silicate network was found [343].

7.3 Mg/Zn-based 45S5 bioactive glasses

45S5 Bioglass[®] [14] has a high trend to crystallisation which restricts the manufacture range of the glass into fibres and porous scaffolds [9]. An strategy to overcome the small processing window limitation is the incorporation of different ions into the 45S5 matrix, including Mg^{2+} and Zn^{2+} ions [344, 345]. These ions in turn may additionally play an active role in the human bone by stimulating osteoblast proliferation [8, 55, 60, 61].

The aim of this preliminary study was to combine ^{31}P and solid-state ^{29}Si MAS NMR to get insights concerning the structural role of Mg^{2+} and Zn^{2+} ions substituting Ca^{2+} in the

45S5 glass network. The glasses were analysed in the frame of a collaborative work [214], thus, $24.4\text{Na}_2\text{O} - (26.9 - x)\text{CaO} - x\text{XO} - 46.1\text{SiO}_2 - 2.6\text{P}_2\text{O}_5$ with $0 \leq x \leq 26.9$ mol% and X: Zn and Mg (Table 7.3).

Table 7.3: Nominal glass composition of Mg/Zn-based 45S5 glasses (mol%).

Glass	Na ₂ O	CaO	P ₂ O ₅	SiO ₂	MgO	ZnO
45S5	24.4	26.9	2.6	46.1	–	–
45S5-Mg100	24.4	–	2.6	46.1	26.9	–
45S5-Zn25	24.4	20.2	2.6	46.1	–	6.7
45S5-Zn50	24.4	13.5	2.6	46.1	–	13.5
45S5-Zn75	24.4	6.7	2.6	46.1	–	20.2
45S5-Zn100	24.4	–	2.6	46.1	–	26.9

7.3.1 Solid-state MAS NMR

Table 7.4: Chemical shifts (± 0.2 ppm) at peak maximum (δ_{max}) and the full width at half-maximum (fwhm) of Q_pⁿ phosphate and Si^{IV} silicate (tetrahedral) species; determined from deconvolution [216] of quantitative single-pulse MAS NMR spectra.

Glass	Q _p ⁰		Si ^{IV}	
	δ_{max} (ppm)	fwhm (ppm)	δ_{max} (ppm)	fwhm (ppm)
45S5	8.2	7.52 ± 0.04	-79.7	13.6 ± 0.1
45S5-Mg100	8.4	7.94 ± 0.04	-80.4	14.31 ± 0.07
45S5-Zn25	8.7	7.47 ± 0.04	–	–
45S5-Zn50	9.3	7.36 ± 0.05	–	–
45S5-Zn75	10.2	7.10 ± 0.06	–	–
45S5-Zn100	11.3	6.40 ± 0.07	-80.3	16.8 ± 0.1

³¹P MAS NMR of Zn-based 45S5 glasses

According to solid-state ³¹P MAS NMR, Zn-based 45S5 glasses are comprised mainly by orthophosphate Q_p⁰ with a minor presence of pyrophosphate Q_p¹ tetrahedra (Fig. 7.5), the latter corresponding most likely to P–O–Si species [331, 340]. The Q_p⁰ chemical shift at peak maximum for 45S5 was $\delta_{\text{max}} = 8.2$ ppm. A shielding effect of zinc relative to calcium would be expected owing to the higher field strength (Z/r^2) of the former (Ionic radii: [VI]Ca²⁺ = 1 Å, [IV]Zn²⁺ = 0.6 Å, [VI]Zn²⁺ = 0.68 Å, [IV]Zn²⁺ = 0.74 Å) [306]. Nevertheless as can be seen in Table 7.4, a steady shift of the Q_p⁰ peak to higher frequencies with increasing zinc content occurs, ~ 3.1 ppm between the complete zinc-substituted (45S5-Zn100) and 45S5 glasses. This may be accounted as a deshielding effect of sodium relative to calcium owing to the higher field strength (Z/r^2) of the latter, since the Ca-content decreases within the

series. Hence, preferential bonding of Na^+ into the phosphate network and accordingly preferential bonding of Zn^{2+} into the silicate network may occur with increasing content of Zn^{2+} substituting Ca^{2+} ions. The hypothesis of enrichment of Na^+ ions into the phosphate network is further confirmed by the fwhm values (Table 7.4). The fwhm for the Q_p^0 peaks decreases with ZnO content, which translates into a narrower range of P environments, i.e. bond lengths and angles, caused by the exclusion of Ca^{2+} ions around the phosphate network.

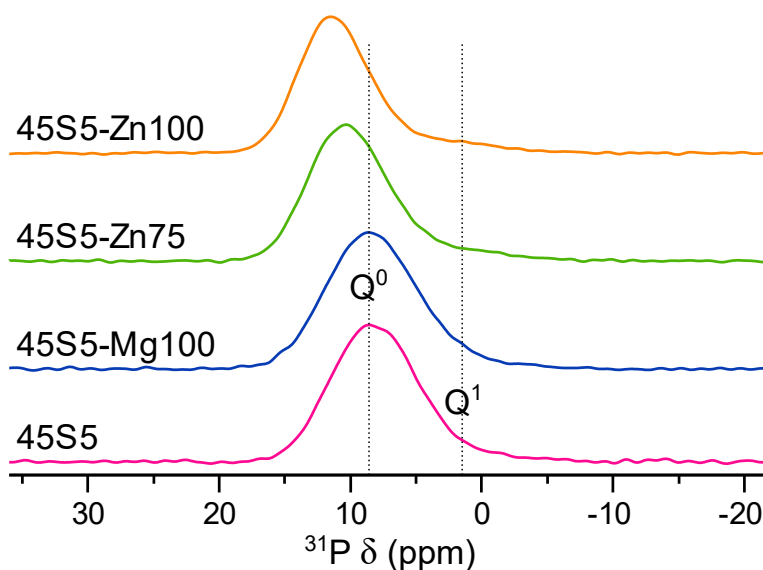


Fig. 7.5: Quantitative solid-state ^{31}P MAS NMR spectra of the glass series $24.4\text{Na}_2\text{O}-(26.9-x)\text{CaO}-x\text{XO}-46.1\text{SiO}_2-2.6\text{P}_2\text{O}_5$ with $0 \leq x \leq 26.9$ mol% and X: Zn and Mg.

^{31}P MAS NMR of Mg-based 45S5 glasses

According to solid-state ^{31}P MAS NMR, Mg-based 45S5 glasses are comprised mainly by orthophosphate Q_p^0 with a minor presence of pyrophosphate Q_p^1 tetrahedra (Fig. 7.5), the latter corresponding most likely to $\text{P}-\text{O}-\text{Si}$ species [331, 340]. As can be seen in Table 7.4, a negligible change in the Q_p^0 shift (~ 0.2 ppm) between 45S5 and 45S5-Mg100 was observed (Fig. 7.5). Nevertheless, a shielding effect of magnesium relative to calcium would be expected owing to the higher field strength (Z/r^2) of the former (Ionic radii: $^{[\text{VI}]}\text{Ca}^{2+} = 1 \text{ \AA}$, $^{[\text{IV}]}\text{Mg}^{2+} = 0.57 \text{ \AA}$, $^{[\text{VI}]}\text{Mg}^{2+} = 0.66 \text{ \AA}$, $^{[\text{VI}]}\text{Mg}^{2+} = 0.72 \text{ \AA}$) [306].

MD simulations and NMR on 45S5-based glasses have suggested that Na^+ and Ca^{2+} ions coordinate preferentially with Q_p^0 species [340, 346]. In case of preferential bonding of Mg^{2+} on the silicate network, a similar effect as observed for Zn-based 45S5 glasses would be expected. Thus, an enrichment of Na^+ coordinated to the orthophosphate species, leading

to deshielding and narrowing of the Q_p^0 peak, as described above. Conversely, only at low substitution of Mg^{2+} for Ca^{2+} ions, a steady chemical shift and fwhm of the Q_p^0 resonance would be expected, owing to its small concentration (2.6 mol%). Nevertheless, as can be seen in Table 7.4, even after complete substitution of Mg^{2+} for Ca^{2+} (45S5-Mg100) a negligible shift and fwhm increase (~ 0.42 ppm) of Q_p^0 occurs.

Interestingly, similar results regarding the negligible shift and fwhm change of the Q_p^0 peak have been observed on an analogous bioactive glass system. In which no statement was made regarding the Ca/Mg distribution in the vicinity of the orthophosphate species [344]. Contrarily to a different study on the substituting Mg^{2+} for Ca^{2+} on bioactive glasses, which reported a substantial deshielding of the Q_p^0 resonance, similar to the Zn-based 45S5 glasses [345]. By taking into account that PO_4^{3-} is a hard base, it binds preferentially and stronger to hard acids, following the Pearson's series [91]. Thus, within the periodic table the hardness decreases vertically with increasing ionic radius, i.e. $Mg^{2+} > Ca^{2+}$; and horizontally from left to right owing to both decreasing radius and increasing charge e.g. $Mg^{2+} > Na^+$ [90]. Hence, it is obvious that the orthophosphate species should coordinate as well with Mg^{2+} ions.

According to the Oxygen Bonding Model, the first coordination sphere around oxygen atoms must satisfy a total formal charge of +2 bond donation [46]. In order to balance NBOs with a high residual negative charge, an increase in the bond donation through a rise in the covalent character of M–O bonds would be necessary. This may explain the reduction in the coordination number of M proportional to the basicity of the glass network [92, 295]. In contrast, highly covalent P–O bonds would force M–O bonds to be more ionic, increasing the coordination number [282]. Taking into account that the basicity is inversely proportional to the chain length, a high proportion of Mg^{2+} in tetrahedral symmetry may be expected for pyrophosphate and orthophosphate species. Thereby, Mg^{2+} in a 5-fold coordination may account as an intermediate between tetrahedral and octahedral symmetries owing to the high basicity of short phosphates.

This is confirmed by MD simulations in which the local environment of phosphate tetrahedra of 45S5 based glasses is reported to be coordinated preferentially by 5-fold coordinated Mg^{2+} ions with a non negligible amount of 4-fold coordination. The polymerization of phosphate species on Mg-based 45S5 glasses, where Mg^{2+} substitutes Ca^{2+} , is assumed to remain constant. Hence the basicity of such should remain invariant within the series and the ratio Mg^{2+} 5-fold to 4-fold coordination around the phosphate species may likewise remain constant. A hypothesis to explain the negligible shift of the Q_p^0 resonance even after complete substitution of Mg^{2+} for Ca^{2+} , may be the compensation between opposite

effects. Thus, on one hand the deshielding caused by enrichment of Q_P^0 with Na^+ ions and on the other hand, the shielding expected by Mg^{2+} likely in 5-fold and 4-fold symmetries coordinated to the phosphate species.

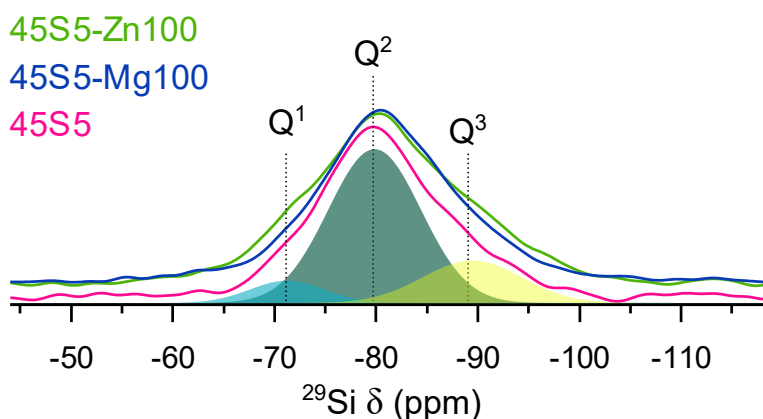


Fig. 7.6: Quantitative solid-state ^{29}Si MAS NMR spectra of the glass series $24.4Na_2O-(26.9-x)CaO-xXO-46.1SiO_2-2.6P_2O_5$ with $0 \leq x \leq 26.9$ mol% and X: Zn and Mg. The experimental spectra are comprised of a single resonance corresponding to tetrahedral Si–O sites. 45S5 was deconvoluted [216] into three Gaussian lines: Q_{Si}^1 , Q_{Si}^2 and Q_{Si}^3 ; where the positions and relative areas were constrained based on [342].

^{29}Si MAS NMR of Zn-based 45S5 glasses

As can be seen in Fig. 7.6, solid-state ^{29}Si MAS NMR spectra of Zn-based 45S5 glasses showed only one broad resonance ranging from -65 to -100 ppm which corresponds to four-coordinated Si–O sites. The ^{29}Si lineshape of 45S5 was fitted into three Gaussian peaks consisting of a dominant Q_{Si}^2 merged with Q_{Si}^1 and Q_{Si}^3 groups [340, 342]. Taking into account the solid-state ^{31}P MAS NMR findings, in which it was concluded that Zn^{2+} exhibits preferential bonding with the silicate rather than the phosphate network. A shielding effect of zinc relative to calcium would be expected owing to the higher field strength (Z/r^2) of the former (Ionic radii: $[VI]Ca^{2+} = 1 \text{ \AA}$, $[IV]Zn^{2+} = 0.6 \text{ \AA}$, $[VI]Zn^{2+} = 0.68 \text{ \AA}$, $[VII]Zn^{2+} = 0.74 \text{ \AA}$) [306]. Nevertheless as can be seen in Table 7.4, only a negligible change in shielding (~ 0.6 ppm) from 45S5 to 45S5-Zn100 was observed. In contrast with the significant increase in the fwhm of the ^{29}Si lineshape (~ 3.2 ppm) between the same glasses.

The basicity depends on the glass network polymerization and ultimately it determines the coordination number of the cations, as mentioned above. The polymerization of the silicate network on Zn-based 45S5 glasses, is assumed to remain constant by substituting Ca^{2+} for Zn^{2+} ions. Hence, the basicity of such should remain invariant within the series and the ratio between the potential symmetries of Zn^{2+} (4, 5 and 6-fold) around the silicate species

may likewise remain constant.

In order to balance NBOs with a high residual negative charge, an increase in the bond donation through a rise in the covalent character of M–O bonds would be necessary. This may explain the reduction in the coordination number of M proportional to the basicity of the glass network [92, 295]. Thus, Q_{Si}^1 species may be coordinated to 4-fold coordinated Zn^{2+} ions. In contrast, highly covalent Si–O bonds such as Q_{Si}^3 species would force M–O bonds to be more ionic, increasing the symmetry into Zn^{2+} 6-fold coordinated [282]. Regarding the Q_{Si}^2 species, the most likely symmetries may correspond to 5 and 6-fold coordinations. This corresponds well with the fwhm of the 45S5-Zn100 glass relative to 45S5 of the ^{29}Si resonance (Table 7.4), in which the increase in the chemical environments should be proportional for each Q_{Si}^n site, assuming constant polymerization. Hence, by introducing Zn^{2+} into the glasses the Q_{Si}^n distribution should remain equal as for 45S5, as can be seen in Fig. 7.6.

^{29}Si MAS NMR of Mg-based 45S5 glasses

As can be seen in Fig. 7.6, solid-state ^{29}Si MAS NMR spectra of Mg-based 45S5 glasses showed only one broad resonance ranging from -65 to -100 ppm which corresponds to four-coordinated Si–O sites. The ^{29}Si lineshape of 45S5 was fitted into three Gaussian peaks consisting of a dominant Q_{Si}^2 merged with Q_{Si}^1 and Q_{Si}^3 groups [340, 342]. Taking into account the solid-state ^{31}P MAS NMR findings, in which it was concluded that Mg^{2+} does not exhibit preferential bonding. Thus, it most probably binds to both the phosphate and the silicate network. As mentioned above, a shielding effect of magnesium relative to calcium would be expected owing to the higher field strength (Z/r^2) of the former (Ionic radii: $^{VI}Ca^{2+} = 1 \text{ \AA}$, $^{IV}Mg^{2+} = 0.57 \text{ \AA}$, $^{VI}Mg^{2+} = 0.66 \text{ \AA}$, $^{VII}Mg^{2+} = 0.72 \text{ \AA}$) [306]. Nevertheless as can be seen in Table 7.4, only a negligible change in shielding (~ 0.7 ppm) from 45S5 to 45S5-Mg100 was observed.

The basicity depends on the glass network polymerization and ultimately it determines the coordination number of the cations, as mentioned above. The polymerization of the silicate network on Mg-based 45S5 glasses is assumed to remain constant by substituting Ca^{2+} for Mg^{2+} ions. The silicate network connectivity ($NC_{Si} \approx 2.1$) has been found to remain similar to that of the 45S5 Bioglass[®] on Mg-45S5 glasses, which results from the unchanged number of NBOs [347]. Hence, by introducing Mg^{2+} into the glasses the Q_{Si}^n distribution should remain equal as for 45S5, as can be seen in Fig. 7.6. Accordingly, the basicity of such should remain invariant within the series and the ratio between the potential symmetries of Mg^{2+} ions (4, 5 and 6-fold) around the silicate species may likewise remain constant.

In order to balance NBOs with a high residual negative charge, an increase in the bond donation through a rise in the covalent character of M–O bonds would be necessary. This

may explain the reduction in the coordination number of M proportional to the basicity of the glass network [92, 295]. Highly covalent Si–O bonds would force M–O bonds to be more ionic, thus increasing the symmetry into Mg^{2+} 6-fold coordinated [282]. This is confirmed by MD simulations in which it was concluded that the majority of the Mg-silicate crystal phases exhibited a 6-fold coordinated Mg^{2+} ion [347].

45S5-Zn100 showed a substantial increase in the ^{29}Si fwhm (3.2 ppm), in contrast with the slight increase in fwhm (~ 0.7 ppm) that displayed 45S5-Mg100 relative to 45S5 (Table 7.4). This is in agreement with a silicate network rich in a single symmetry of Mg^{2+} ions, namely 6-fold, rather than the whole potential symmetries (4, 5 and 6-fold). Conversely, the significant increase in the chemical environments on the silicate network for 45S5-Zn100, may lie on the presence of multiple symmetries of Zn^{2+} (4, 5 and 6-fold). These results are in agreement with solid-state ^{31}P MAS NMR of Mg-based 45S5 glasses, in which it was suggested that Q_p^0 may be coordinated preferentially to Mg^{2+} with 5-fold and 4-fold symmetries.

7.4 Mg/Sr-based S53P4 bioactive glasses

BonAlive[®] S53P4 is a clinically used glass, however the composition has still some drawbacks such as an adverse crystallization and incomplete degradation *in vivo* [9]. An alternative to enhance the hot forming domain is the incorporation of ions such as Mg^{2+} and Sr^{2+} into the S53P4 matrix [2, 314]. Regarding the dissolution behaviour, the substitution of SiO_2 with B_2O_3 has been reported to improve the degradation rate and the transformation of bioglasses into hydroxyapatite (HA) [335–337].

The aim of this study was to perform solid-state ^{31}P MAS NMR to get insights concerning the structural role of Mg^{2+} and Zn^{2+} ions substituting Ca^{2+} in the S53P4 glass network. Thus, $47.12\text{SiO}_2 - 6.73\text{B}_2\text{O}_3 - (21.77 - x - y)\text{CaO} - 22.65\text{Na}_2\text{O} - 1.72\text{P}_2\text{O}_5 - x\text{MgO} - y\text{SrO}$ with $x, y = 0, 5, 10$ mol% (Table 7.5). The glasses were analysed in the frame of a collaborative work already published about the development of new bioactive glasses [2].

Table 7.5: Nominal glass composition of Mg/Sr-based S53P4 glasses (mol%).

Glass	B_2O_3	Na_2O	CaO	P_2O_5	SiO_2	MgO	SrO
B12.5	6.73	22.66	21.77	1.72	47.12	–	–
B12.5-Mg10	6.73	22.66	11.77	1.72	47.12	10	–
B12.5-Sr10	6.73	22.66	11.77	1.72	47.12	–	10
B12.5-Mg5-Sr10	6.73	22.66	6.77	1.72	47.12	5	10

7.4.1 ^{31}P solid-state MAS NMR

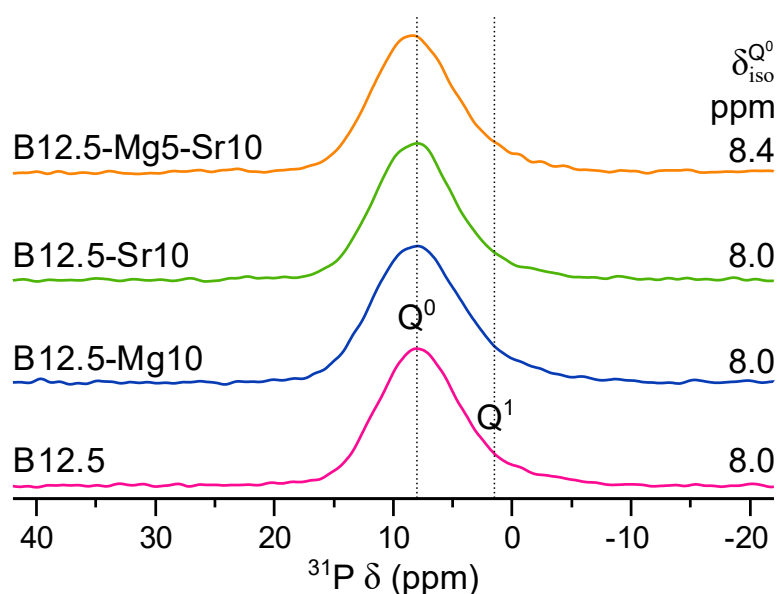


Fig. 7.7: Quantitative solid-state ^{31}P MAS NMR spectra of the glass series $47.12\text{SiO}_2 - 6.73\text{B}_2\text{O}_3 - (21.77 - x - y)\text{CaO} - 22.65\text{Na}_2\text{O} - 1.72\text{P}_2\text{O}_5 - x\text{MgO} - y\text{SrO}$ with $x, y = 0, 5, 10$ mol%.

According to solid-state ^{31}P MAS NMR, Mg/Sr-based S53P4 glasses containing 1.72 mol% of P_2O_5 are comprised mainly by orthophosphate Q_P^0 with a minor presence of pyrophosphate Q_P^1 tetrahedra (Fig. 7.7), the latter corresponding most likely to $\text{P}-\text{O}-\text{Si}$ species [331, 340]. As can be seen in Fig. 7.7, the isotropic chemical shift for B12.5 was $\delta_{\text{iso}}^{\text{Q}^0} = 8.0$ ppm and no change in the Q_P^0 shift between B12.5, B12.5-Mg10 and B12.5-Sr10 was observed. While only a slight shift to higher frequencies for B12.5-Mg5-Sr10 (~ 0.4 ppm) occurred. Nevertheless, a shielding effect of magnesium relative to calcium would be expected owing to the higher field strength (Z/r^2) of the former, whereas strontium would cause the opposite effect (Ionic radii: $^{[\text{VI}]}\text{Ca}^{2+} = 1 \text{ \AA}$, $^{[\text{IV}]}\text{Mg}^{2+} = 0.57 \text{ \AA}$, $^{[\text{VI}]}\text{Mg}^{2+} = 0.66 \text{ \AA}$, $^{[\text{VI}]}\text{Mg}^{2+} = 0.72 \text{ \AA}$, $^{[\text{VI}]}\text{Sr}^{2+} = 1.18 \text{ \AA}$, $^{[\text{VII}]}\text{Sr}^{2+} = 1.21 \text{ \AA}$, $^{[\text{VIII}]}\text{Sr}^{2+} = 1.26 \text{ \AA}$) [306].

MD simulations and NMR on 45S5-based glasses have suggested that Na^+ and Ca^{2+} ions coordinate preferentially with Q_P^0 species [340, 346]. That was the hypothesis used to explain the no shift of the Q_P^0 resonance in the B12.5, B12.5-Mg10 and B12.5-Sr10 glasses [2]. Nevertheless as discussed above, for 45S5-based glasses containing 2.6 mol% of P_2O_5 , a negligible shift of Q_P^0 occurred even after complete substitution of Mg^{2+} for Ca^{2+} (Table 7.4). Such results were also observed on an analogous bioactive glass system [344]. Contrarily to a different study on the substitution of Mg^{2+} for Ca^{2+} on bioactive glasses (P_2O_5 : 1.07 mol%), which reported a substantial deshielding of the Q_P^0 resonance, similar to the Zn-based 45S5

glasses [345].

By taking into account that PO_4^{3-} is a hard base, it binds preferentially and stronger to hard acids, following the Pearson's series [91]. Thus, within the periodic table the hardness decreases vertically with increasing ionic radius, i.e. $\text{Mg}^{2+} > \text{Ca}^{2+} > \text{Sr}^{2+}$; and horizontally from left to right owing to both decreasing radius and increasing charge e.g. $\text{Mg}^{2+} > \text{Na}^+$ [90]. Hence, it is obvious that the orthophosphate species should coordinate as well with Mg^{2+} ions. Whereas, that may not be necessarily the case for Sr^{2+} ions. Hence, the preferential bonding of Na^+ and Ca^{2+} with phosphate species to explain the no shift related to B12.5 of the Q_p^0 resonance may apply only for the B12.5-Sr10 glass (Table 7.5).

The basicity depends on the glass network polymerization and ultimately it determines the coordination number of the cations, as mentioned above. The polymerization of the glass network on Mg/Sr-based S53P4 glasses is assumed to remain constant by substituting Ca^{2+} for Mg^{2+} and Sr^{2+} ions, which results from the unchanged number of NBOs. The silicate network connectivity ($\text{NC}_{\text{Si}} \approx 2.1$) has been found to remain similar to that of the 45S5 Bioglass[®] on Mg-45S5 glasses, which results from the unchanged number of NBOs [347]. Accordingly, the basicity of such should remain invariant within the series and the ratio between the potential symmetries of Mg^{2+} ions (4, 5 and 6-fold) around the phosphate species may likewise remain constant.

According to the Oxygen Bonding Model, the first coordination sphere around oxygen atoms must satisfy a total formal charge of +2 bond donation [46]. In order to balance NBOs with a high residual negative charge, an increase in the bond donation through a rise in the covalent character of M–O bonds would be necessary. This may explain the reduction in the coordination number of M proportional to the basicity of the glass network [92, 295]. In contrast, highly covalent P–O bonds would force M–O bonds to be more ionic, increasing the coordination number [282].

Taking into account that the basicity is inversely proportional to the chain length, a high proportion of Mg^{2+} in tetrahedral symmetry may be expected for pyrophosphate and orthophosphate species. Thereby, Mg^{2+} in 5-fold coordination may account as an intermediate between tetrahedral and octahedral symmetries owing to the high basicity of short phosphates. As discussed above for the Mg-based 45S5 glasses, the no shift of the Q_p^0 resonance of B12.5-Mg10 related to B12.5 may be addressed as the compensation between opposite effects. Thus, on one hand the deshielding caused by enrichment of Na^+ and on the other hand, the shielding expected by Mg^{2+} 5-fold to 4-fold coordinated to the phosphate species. This under the assumption that the Sr^{2+} ions would bond with preference to the silicate

network owing to their soft acid character.

As can be seen in Fig. 7.7, the slight shift to higher frequencies for B12.5-Mg5-Sr10 related to B12.5 (~ 0.4 ppm) may be addressed as a deshielding of the Q_p^0 resonance caused by a relative enrichment with Na^+ ions. This may be attributed to two effects. Firstly that Mg^{2+} and Ca^{2+} ions already in a relative minor quantity (Table 7.5), may associate also to the borate and silicate networks. Secondly as mentioned above, that the Sr^{2+} ions may bind with preference to the silicate network owing to their soft acid character. Hence the overall effect may be a deshielding caused by Na^+ rather than Sr^{2+} around the phosphate species in the B12.5-Mg5-Sr10 glass.

Chapter 8

Conclusions

Kinetics and mechanism of cation-catalyzed hydrolysis of $P_2O_5-CaO-Na_2O$ glasses: the effect of ligand competition and reactivity of intermediate complexes on ^{31}P NMR spectra

Structural changes in phosphate glasses tailor degradation, which is key for therapeutic applications such as drug delivery. ^{31}P MAS NMR of $45P_2O_5 - xCaO - (55 - x)Na_2O$ glasses was correlated with dissolution kinetics on the system $45P_2O_5 - xCaO - (55 - x)Na_2O$ (CNP45, $25 \leq x \leq 40$ mol%, O/P = 3.1), where the CaO/Na₂O ratio was varied while the phosphate content was maintained constant. The glasses consist of phosphate chains, with the experimental average chain length of 8 to 9 phosphate groups agreeing well with the theoretical one of 9. The chains are connected to one another through randomly distributed Ca²⁺ and Na⁺ ions. The glass system seemingly has a relatively high resistance to corrosion, since the nature of the water determined by 1H MAS NMR is related to adsorbed water exclusively.

These glasses dissolve congruently in aqueous solutions and their durability increase with increasing CaO/Na₂O ratio. Dissolution under static conditions was shown to be a diffusion-controlled process where the durability is associated with a decreasing diffusion coefficient with increasing CaO content. Protonation of the two end groups of hydrated chains released from the glass causes an initial pH rise. Over time, ring-formation from chains and accumulation of weak acidic species produced by hydrolysis caused a monotonic pH decrease.

^{31}P liquid NMR allowed for the identification of cyclic metaphosphates owing to their ^{31}P chemical shift remaining constant even when the pH changes. In Tris buffer solution or water, the delayed build-up of orthophosphate species suggests stable intermediary species, most likely rings. By contrast, the low intensity of Q¹ and Q² resonances throughout the experiment suggests a low hydrolytic stability of chains compared to rings.

The suggested mechanism of aqueous degradation corresponds to a reaction similar to S_N2.

Nucleophilic attack by water takes place on a P–O bond, which is polarised by cations, $(\text{P–O–M})^{n+}$, as an electrophilic centre. Metal cations thus seem to have a catalytic effect on P–O–P bond scission. The conjugated base of Tris is a stronger Lewis base than H_2O , thus forming stronger complexes and competing for cations. As a result, the relative intensity of resonances corresponding to chain Q^1 and Q^2 groups increases in the order $\text{H}_2\text{O} < \text{Tris pH 7.4} < \text{Tris pH 7.9}$. In EDTA, the high stability of $\text{Ca}(\text{EDTA})$ and the weak nature of Na^+ complexes lead to a pronounced decrease in degradation. However, phosphate species, as better Lewis bases, have the potential to replace H_2O as additional ligand, e.g., $\text{Ca}(\text{EDTA})(\text{P}_{3\text{m}})$, making hydrolysis still possible.

Structural role and coordination environment of cobalt in $45\text{P}_2\text{O}_5\text{–CaO–Na}_2\text{O}$ phosphate glasses: Thermal properties, Raman, UV–vis–NIR and EPR spectroscopy

Cobalt-doped phosphate glasses are attractive materials for several applications, e.g., to overcome the vascularization limitation in tissue engineering, semiconductors, optical devices and solid-state lasers among others. TGA-MS showed that the presence of both absorbed and structural water may be neglected in $45\text{P}_2\text{O}_5\text{–}(30 - x)\text{CaO–}25\text{Na}_2\text{O–}x\text{CoO}$ glasses (with $0 \leq x \leq 10$ mol%).

Raman spectra of the glasses do not show any appreciable change neither in the position nor in the intensity of the vibrations sensitive to the length of the phosphate chains, i.e., $\nu_s(\text{P–O–P})$, $\nu_s(\text{PO}_2)$ and $\nu_{as}(\text{PO}_2)$. This is in agreement with a constant polymerization obtained from ICP-OES analysis, O/P 3.1 – 3.2 and $\bar{n} \sim 9$ phosphate groups. The expected blue shifts of the cation-dependent bands, $\nu_s(\text{P–O–P})$ and $\nu_s(\text{PO}_2)$, may not be sensitive enough to be noticeable at the substitution range, $0 \leq x \leq 10$ mol% CaO for CoO.

According to the UV–vis–NIR spectroscopy, the d–d transitions corresponding to $^{[\text{VI}]}\text{Co}^{2+}$ symmetry were ascribed as $^4\text{T}_{1g}(^4\text{F}) \rightarrow ^4\text{T}_{1g}(^4\text{P})$ and $^4\text{T}_{1g}(^4\text{F}) \rightarrow ^4\text{A}_{2g}(^4\text{F})$ with maxima at 533 and 622 nm, respectively. While the d–d transition corresponding to $^{[\text{IV}]}\text{Co}^{2+}$ symmetry was assigned as $^4\text{A}_2(^4\text{F}) \rightarrow ^4\text{T}_1(^4\text{P})$ centred at 579 nm. Deconvolution in the visible range showed a relatively constant proportion between the tetrahedral and octahedral symmetries, independently of the CoO content. That is a consequence of the constant basicity consistent with invariant metal oxide content, 55 mol%, and accordingly constant polymerization of the glass network.

EPR spectra are typical of high-spin Co^{2+} ($S = 3/2$) with significant zero-field splitting. It is also obvious that the main fraction of cobalt ions in the glasses corresponds to Co^{2+} . Results are in agreement with a constant polymerization degree since Co^{3+} would lead to

depolymerization of the glass network.

A fairly levelling off of the thermal properties measured by DSC (T_g , $T_{c,o}$) and HSM (T_{si} , T_{xi}) occurs owing to the compensation between opposite effects, as a result of the constant $[IV]Co^{2+}$ and $[VI]Co^{2+}$ ratio over the glass series. Thus, T_g analogous to T_{si} may level off since $[VI]Co^{2+}$ in the glass would strengthen the glass network owing to the higher Z/r^2 , whereas $[IV]Co^{2+}$ would bind together less PO_4 tetrahedra, weakening the glass network. Likewise, the constant $T_{c,o}$ and T_{xi} values were addressed as a compensation between the increasing enthalpies of breaking and formation of Co–O bonds, at expenses of Ca–O bonds, in the glasses and crystal phases, respectively. Accordingly, the processing temperatures remained steady. Summarizing, the role of Co^{2+} on the structural properties, i.e. thermal properties, of phosphate glasses with constant basicity is dictated by the coordination environment of Co^{2+} .

Co^{2+} as an internal paramagnetic ^{31}P NMR probe for structural analysis of cobalt phosphate glasses in the solid-state and leachate solutions

A new approach based on the paramagnetic nature of Co^{2+} was used to investigate the mechanism of dissolution of $45P_2O_5-(30-x)CaO-25Na_2O-xCoO$ (x : 0 to 10 mol%) glasses for different applications, i.e. wound healing and bactericide. High spin, $S = 3/2$, Co^{2+} interacts with the ^{31}P nuclear spins causing the so called paramagnetic effects providing short an long-range structural information.

In the glass network, Co^{2+} causes severe broadening due to the combination of the BMS and the extended network of dipolar couplings. Thereby the transverse PRE does not contribute significantly to the linewidth. The non perfect cubic symmetry expected in the glass system is associated to large SO couplings and thus ZFS of the Co^{2+} ion. Hence, both the Fermi-contact and PCS contributions may be important in the overall paramagnetic shift of the glasses, being the shifts sufficiently large to lie outside the spectral window. Despite the rigid nature of the glasses, the vibration motion is still an efficient source of electronic relaxation related to the Co^{2+} ion, which subsequently induces PRE. The assessment of Co^{2+} ion distribution in the diamagnetic host glass suggested a cluster scenario at high Co^{2+} concentration.

In the leachate solutions, the broadening is proportional to the CoO content and it is given by a combination of PRE and the inhomogeneous broadening. It indicates that the ^{31}P nuclei are located in the immediate environment of the Co^{2+} ions. Hence, the Fermi-contact interactions should be important, even though the PCS contributions may be predominant

in Co^{2+} complexes. The paramagnetic shifts are expected to be sufficiently large to shift the peaks outside of the spectral window, rendering them non-observable. Owing to the presence of different potential ligands in solution (H_2O , Tris, EDTA), high-spin Co^{2+} ions are expected to undertake different distorted octahedral symmetries [319]. Thus rapid relaxation times are expected due to the low symmetry of Co^{2+} in the leachate solutions. The Solomon-Bloembergen-Morgan mechanism may apply for the system owing to the high external magnetic field and fast molecular dynamics of the relatively small phosphate fragments.

The aqua complexes of Na^+ , Ca^{2+} and Co^{2+} are labile, thus the cations are complexed to ligands with higher basicity than water, i.e. $\text{Tris} < \text{phosphate species} < \text{EDTA}$. Peak broadening as a function of the Co^{2+} concentration indicates a direct coordination between the phosphate fragments and Co^{2+} owing to the PRE and paramagnetic shift. That was observed for all the resonances in Tris buffer, namely Q^0 , Q^1 and Q^2 moieties. It confirms the direct binding of Co^{2+} to i.e. $\text{P}_{3\text{m}}$ ring, most likely in chair conformation. This supports a mechanism of hydrolysis is catalysed by metal cations such as Co^{2+} .

No broadening of the peaks was observed in EDTA, since owing to the chelate effects the equilibrium is not favoured towards the formation of Co^{2+} –phosphate complexes. Thereby, the only difference was the splitting of the $\text{P}_{3\text{m}}$ resonance, assigned as the $\text{Co}(\text{EDTA})(\text{P}_{3\text{m}})$. Despite the high stability of $\text{Co}(\text{EDTA})$, seemingly the coordination of the phosphate fragments to Co^{2+} occurs, potentially nearby the glass surface and at early time periods. Herein is suggested that in the $\text{Co}(\text{EDTA})(\text{P}_{3\text{m}})$ complex EDTA and $\text{P}_{3\text{m}}$ are initially coordinated to Co^{2+} in a tetra- and bidentate fashion, respectively. Even though low rates of hydrolysis in EDTA are expected, it still takes place as it is obvious from the appearance and evolution of the Q^0 peak.

Structural characterization of borate-based 45S5 bioactive glasses by solid-state NMR

Structural approaches concerning degradable borophosphosilicate glasses analogue to Bio-glass 45S5 are highly desirable to enable the design of new bioactive glasses with improved high-temperature processing. ^{31}P , ^{29}Si and ^{11}B MAS NMR were combined to investigate the system $24.4\text{Na}_2\text{O}-26.9\text{CaO}-x\text{B}_2\text{O}_3-(46.1-x)\text{SiO}_2-2.6\text{P}_2\text{O}_5$ with $0 \leq x \leq 6.1$ mol% in an attempt to get insights into the structure of such glasses. According to ^{31}P MAS NMR the system was composed mainly by orthophosphate Q^0 . The slight shift to higher frequencies with increasing boron content (~ 0.4 ppm) can be accounted for as a deshielding effect of sodium relative to calcium.

^{29}Si NMR spectra showed only one broad resonance ranging from -65 to -100 ppm which

corresponds to four-coordinated Si–O sites. The ^{29}Si line shape was fitted to three Gaussian peaks consisting of a dominant Q^2 merged with Q^1 and Q^3 groups. Only a weak but clear decrease in shielding (~ 1.2 ppm) from $x = 0$ to $x = 6.1$ mol% was observed, which can be explained by Si–O–B replacing Si–O–Si species. ^{11}B MAS NMR revealed that the boron-containing glasses are comprised of mostly BO_3 and some BO_4 moieties. The spectra exhibited a progressive decrease in the BO_3/BO_4 ratio with increasing boron-content with concomitant deshielding of both resonances.

Structural characterization of Mg/Zn-based 45S5 bioactive glasses by solid-state NMR

Another strategy to overcome the small processing window limitation of 45S5 Bioglass[®] is the incorporation of different ions into the 45S5 matrix, including Mg^{2+} and Zn^{2+} ions. These ions in turn may additionally play an active role in the human bone by stimulating osteoblast proliferation. ^{31}P and ^{29}Si solid-state MAS NMR were combined to get insights concerning the structural role of Mg^{2+} and Zn^{2+} ions substituting Ca^{2+} in the 45S5 glass network. Thus, $24.4\text{Na}_2\text{O} - (26.9 - x)\text{CaO} - x\text{XO} - 46.1\text{SiO}_2 - 2.6\text{P}_2\text{O}_5$ with $0 \leq x \leq 26.9$ mol% and X: Zn and Mg. According to ^{31}P MAS NMR, Mg/Zn-based 45S5 glasses are comprised mainly by orthophosphate Q_p^0 with a minor presence of pyrophosphate Q_p^1 tetrahedra, the latter corresponding most likely to P–O–Si species.

Regarding Zn-based 45S5 glasses, a steady shift of the Q_p^0 peak to higher frequencies with increasing zinc content occurs, ~ 3.1 ppm between the complete zinc-substituted (45S5-Zn100) and 45S5 glasses. This may be accounted as a deshielding effect of sodium relative to calcium owing to the higher field strength (Z/r^2) of the latter. The fwhm for the Q_p^0 peaks decreases with ZnO content, which translates into a narrower range of P environments. Hence, preferential bonding of Na^+ into the phosphate network may occur with increasing content of Zn^{2+} substituting Ca^{2+} ions.

Regarding Mg-based 45S5 glasses, a negligible change in the Q_p^0 shift (~ 0.2 ppm) and fwhm increase (~ 0.42 ppm) between 45S5 and 45S5-Mg100 was observed. By taking into account that PO_4^{3-} is a hard base, it is obvious that the orthophosphate species should coordinate as well with Mg^{2+} ions. Mg^{2+} in 4 and 5-fold coordination may be expected for pyrophosphate and orthophosphate species owing to the high basicity of short phosphates. Hence, the negligible shift of the Q_p^0 resonance even after complete substitution of Mg^{2+} for Ca^{2+} , may be owing to the compensation between the deshielding caused by enrichment of Q_p^0 with Na^+ ions and the shielding expected by Mg^{2+} coordinated to the phosphate species.

^{29}Si MAS NMR spectra of Mg/Zn-based 45S5 glasses showed only one broad resonance

ranging from -65 to -100 ppm which corresponds to four-coordinated Si–O sites. The ^{29}Si lineshape of 45S5 was fitted into three Gaussian peaks consisting of a dominant Q_{Si}^2 merged with Q_{Si}^1 and Q_{Si}^3 groups. The polymerization of the silicate network on Mg/Zn-based 45S5 glasses, is assumed to remain constant by substituting either Zn^{2+} ions or Mg^{2+} for Ca^{2+} ions. Hence, the basicity of such should remain invariant within the series. Negligible change in shielding (~ 0.6 ppm) from 45S5 to 45S5-Zn100 and (~ 0.7 ppm) from 45S5 to 45S5-Mg100 were observed.

Preferential bonding of Zn^{2+} into the silicate network was concluded from ^{31}P MAS NMR on Zn-based 45S5 glasses. The significant increase in the fwhm of the ^{29}Si lineshape (~ 3.2 ppm) between the same glasses is in agreement with the ^{31}P MAS NMR findings. The basicity of Zn^{2+} should remain invariant within the series and the ratio between the potential symmetries (4, 5 and 6-fold) around the silicate species may likewise remain constant. The coordination number of M is proportional to the basicity of the glass network. Thus, Q_{Si}^1 species may be coordinated to 4-fold coordinated Zn^{2+} ions. In contrast, highly covalent Si–O bonds such as Q_{Si}^3 species would force M–O bonds to be more ionic, increasing the symmetry into Zn^{2+} 6-fold coordinated. Regarding the Q_{Si}^2 species, the most likely symmetries may correspond to 5 and 6-fold coordinations.

By introducing Mg^{2+} into the glasses the Q_{Si}^n distribution should remain equal as for 45S5. Therefore, the potential symmetries of Mg^{2+} ions (4, 5 and 6-fold) around the silicate species may likewise remain constant. Highly covalent Si–O bonds would force M–O bonds to be more ionic, thus increasing the symmetry into Mg^{2+} 6-fold coordinated. This is in agreement with the slight ^{29}Si fwhm increase (~ 0.7 ppm) that displayed 45S5-Mg100 relative to 45S5. Likewise, in agreement with the ^{31}P MAS NMR findings which suggested that the phosphate species may preferably coordinate to Mg^{2+} in 4 and 5-fold coordination owing to the high basicity.

Structural characterization of Mg/Sr-based S53P4 bioactive glasses by solid-state NMR

BonAlive[®] S53P4 is a clinically used glass. An alternative to enhance its hot forming domain is the incorporation of ions such as Mg^{2+} and Sr^{2+} into the S53P4 matrix. ^{31}P solid-state MAS NMR was used to get insights concerning the structural role of Mg^{2+} and Zn^{2+} ions substituting Ca^{2+} in the S53P4 glass network. Thus, $47.12\text{SiO}_2 - 6.73\text{B}_2\text{O}_3 - (21.77 - x - y)\text{CaO} - 22.65\text{Na}_2\text{O} - 1.72\text{P}_2\text{O}_5 - x\text{MgO} - y\text{SrO}$ with $x, y = 0, 5, 10$ mol%. According to ^{31}P MAS NMR, Mg/Sr-based S53P4 glasses containing 1.72 mol% of P_2O_5 are comprised mainly by orthophosphate Q_{p}^0 with a minor presence of pyrophosphate Q_{p}^1 tetrahedra, the latter corresponding most likely to P–O–Si species. The polymerization of the glass network on

Mg/Sr-based S53P4 glasses was assumed to remain constant by substituting Mg^{2+} and Sr^{2+} for Ca^{2+} ions, which results from the unchanged number of NBOs.

By taking into account the Pearson's series, it is obvious that the orthophosphate species should coordinate as well with Mg^{2+} ions. Whereas, that may not be necessarily the case for Sr^{2+} ions. Thus, Sr^{2+} ions would bond with preference to the silicate network owing to their soft acid character. Hence, the preferential bonding of Na^+ and Ca^{2+} with phosphate species may explain the no shift related to B12.5 of the Q_p^0 resonance of the B12.5-Sr10 glass. The no shift of the Q_p^0 resonance of B12.5-Mg10 related to B12.5 may be addressed as the compensation between opposite effects. Thus, the deshielding caused by enrichment of Na^+ and the shielding expected by Mg^{2+} 5-fold to 4-fold coordinated to the phosphate species. The slight shift to higher frequencies for B12.5-Mg5-Sr10 related to B12.5 (~ 0.4 ppm) may be addressed as an overall caused by the deshielding of Na^+ rather than Sr^{2+} around the phosphate species in the B12.5-Mg5-Sr10 glass.

Acknowledgements

The present work would not have been possible without different tangible and intangible contributions during the journey. Therefore, it is my pleasure to acknowledge the following persons behind this endeavour. Likewise, I would like to thank funding by the German Research Foundation (grant BR 4608/4) which made possible my research adventure at the University of Jena. Thereby, Prof. Dr. Delia Brauer is acknowledged for acquiring the project's funding for this thesis work from September 2016 to August 2020. That gave me the opportunity to work in a really interesting interdisciplinary research topic. Yet, I was most passionate about trying to exploit NMR in new ways on the glass field.

I would like to thank Dr. Peter Bellstedt and Friederike Pielenz from the University of Jena for recording the ^{31}P liquid NMR spectra and for their kind support with the solid-state NMR spectrometer. I would like to express my sincere thanks to Prof. Leo van Wüllen from the University of Augsburg for the productive NMR discussions and giving me the opportunity to visit and work with his group. Thereby, thanks to Sabarinathan Venkatachalam and Alina Nizamutdinova for recording the ^{31}P and ^{11}B solid-state NMR spectra on the borate-based 45S5 glasses. I would like to express my gratitude to Prof. Jonathan Massera and Jenna Tainio from Tampere University, for giving me the chance to contribute on a common publication by performing the ^{31}P solid-state NMR. Special thanks to Dr. Leonid Grunin from Resonance Systems GmbH, for our inspiring and endless NMR discussions.

I would like to express my gratitude to Matvey Fedin from the International Tomography Center SB RAS and Novosibirsk State University, for undertaking the EPR spectroscopy on the cobalt phosphate glasses. Thereby, thanks to Dmitrii Bogdanov from Saint Petersburg State University, for making possible the EPR cooperation. I wish to thank Prof. Lothar Wondraczek and Omar Benzine from the University of Jena for the UV-vis-NIR and Raman measurements on the cobalt phosphate glasses.

I would like to acknowledge funding by the Johan Gadolin Scholarship, which financed my research stay at Åbo Akademi in Turku, Finland. Special thanks to Prof. Leena Hupa for giving me the unique opportunity to work with her supportive team and for her valuable

insights. Thereby, sincere thanks to Jaana Paananen for the HSM and Peter Backman for the DSC/TGA-MS measurements on the cobalt phosphate glasses; thanks also to Luis Bezerra for the ICP-OES, Linus Silvander for the SEM and Tor Laurén for his support on the optimization of the dissolution experiments.

Special thanks to Prof. Toshihiro Kasuga, Atsuhiko Miura and Yuki Oi from Nagoya Institute of Technology, for their diligent support on the preparation of the ICP-OES and ^{31}P liquid NMR samples. Likewise, thanks to Josephine Röhner from the University of Jena for her assistance in preparing liquid NMR samples. I would also like to thank all colleagues that provided me with glass samples to perform different studies, mainly NMR spectroscopy.

My sincere thanks to my colleague and friend Florian, you are always very supportive, I really appreciate your valuable advices and willingness to comment and correct my manuscripts. My gratitude is given to Dr. Hendrik Huthoff for proofreading my paper drafts, thank you for your kindness. I am particularly grateful with Jens, your engagement on proofreading my thesis and encouraging me on the "long" last stage, it was really meaningful.

I would also like to thank my friends around the world for listening to me and providing all kinds of support when things got tough. Thereby, special thanks to Sabine and Wolfgang, I appreciate your encouragement and positive energy.

"Far away, this ship took me far away, far away from the memories of the people who care if I live or die..."—Muse. Thus, last but not least, I would like to thank my family for their long-distance support during the course of my studies. Thanks to my brothers: Wilmar, Andrés and Jonathan, my sister Daniela and my aunt Martha, you have always believed in me. I would like to express my deepest gratitude to my inspiring mother Marlen.

References

- (1) Avila Salazar, D. A.; Bellstedt, P.; Miura, A.; Oi, Y.; Kasuga, T.; Brauer, D. S. *Dalton Transactions* **2021**, *50*, 3966–3978.
- (2) Tainio, J. M.; Avila Salazar, D. A.; Nommeots-Nomm, A.; Roiland, C.; Bureau, B.; Neuville, D. R.; Brauer, D. S.; Massera, J. *Journal of Non-Crystalline Solids* **2020**, *533*, 119893.
- (3) *Definitions in biomaterials*; Williams, D. F., European Society for Biomaterials, Eds.; Elsevier: New York, 1987.
- (4) Kokubo, T.; Takadama, H. *Biomaterials* **2006**, *27*, 2907–2915.
- (5) Bandyopadhyay, A.; Bernard, S.; Xue, W.; Bose, S. *Journal of the American Ceramic Society* **2006**, *89*, 2675–2688.
- (6) Bose, S.; Tarafder, S. *Acta Biomaterialia* **2012**, *8*, 1401–1421.
- (7) Pietrzak, W. S., *Musculoskeletal Tissue Regeneration: Biological Materials and Methods*; Springer Science & Business Media: 2008.
- (8) Hoppe, A.; Güldal, N. S.; Boccaccini, A. R. *Biomaterials* **2011**, *32*, 2757–2774.
- (9) Rahaman, M. N.; Day, D. E.; Sonny Bal, B.; Fu, Q.; Jung, S. B.; Bonewald, L. F.; Tomsia, A. P. *Acta Biomaterialia* **2011**, *7*, 2355–2373.
- (10) Kargozar, S.; Baino, F.; Hamzehlou, S.; Hill, R. G.; Mozafari, M. *Trends in Biotechnology* **2018**, *36*, 430–444.
- (11) Leyssens, L.; Vinck, B.; Van Der Straeten, C.; Wuyts, F.; Maes, L. *Toxicology* **2017**, *387*, 43–56.
- (12) Christian, W. V.; Oliver, L. D.; Paustenbach, D. J.; Kreider, M. L.; Finley, B. L. *Journal of Applied Toxicology* **2014**, *34*, 939–967.
- (13) Jones, J. R. *Acta Biomaterialia* **2013**, *9*, 4457–4486.
- (14) Hench, L. L.; Splinter, R. J.; Allen, W. C.; Greenlee, T. K. *Journal of Biomedical Materials Research* **1971**, *5*, 117–141.
- (15) Hench, L. L.; Polak, J. M. *Science* **2002**, *295*, 1014–1017.
- (16) Brink, M. *Journal of Biomedical Materials Research* **1997**, *36*, 109–117.
- (17) Lopez-Esteban, S.; Saiz, E.; Fujino, S.; Oku, T.; Suganuma, K.; Tomsia, A. P. *Journal of the European Ceramic Society* **2003**, *23*, 2921–2930.
- (18) Saravanapavan, P.; Jones, J. R.; Pryce, R. S.; Hench, L. L. *Journal of Biomedical Materials Research Part A* **2003**, *66A*, 110–119.
- (19) Saravanapavan, P.; Hench, L. L. *Journal of Biomedical Materials Research* **2001**, *54*, 608–618.

- (20) Yao, A.; Wang, D.; Huang, W.; Fu, Q.; Rahaman, M. N.; Day, D. E. *Journal of the American Ceramic Society* **2007**, *90*, 303–306.
- (21) Ahmed, I.; Lewis, M.; Olsen, I.; Knowles, J. C. *Biomaterials* **2004**, *25*, 501–507.
- (22) Brow, R. K. *Journal of Non-Crystalline Solids* **2000**, *263–264*, 1–28.
- (23) Muñoz, F.; Rocherullé, J.; Ahmed, I.; Hu, L. In *Springer Handbook of Glass*, Musgraves, J. D., Hu, J., Calvez, L., Eds.; Springer Handbooks; Springer International Publishing: Cham, 2019, pp 553–594.
- (24) Bunker, B. C.; Arnold, G. W.; Wilder, J. A. *Journal of Non-Crystalline Solids* **1984**, *64*, 291–316.
- (25) Van Wazer, J. R.; Callis, C. F. *Chemical Reviews* **1958**, *58*, 1011–1046.
- (26) Waclawska, I.; Szumera, M. *Journal of Alloys and Compounds* **2009**, *468*, 246–253.
- (27) Waclawska, I.; Szumera, M.; Stoch, P.; Sitarz, M. *Spectrochimica Acta Part A: Molecular and Biomolecular Spectroscopy* **2011**, *79*, 728–732.
- (28) Bergo, P.; Reis, S. T.; Pontuschka, W. M.; Prison, J. M.; Motta, C. C. *Journal of Non-Crystalline Solids* **2004**, *336*, 159–164.
- (29) Ma, L.; Brow, R. K. *Journal of Non-Crystalline Solids* **2014**, *387*, 16–20.
- (30) Ma, L.; Brow, R. K.; Schlesinger, M. E. *Journal of Non-Crystalline Solids* **2017**, *463*, 90–101.
- (31) Morena, R. *Journal of Non-Crystalline Solids* **2000**, *263–264*, 382–387.
- (32) Chakvetadze, D. K.; Zinina, É. M.; Spiridonov, Y. A.; Sigaev, V. N. *Glass and Ceramics* **2019**, *76*, 3–6.
- (33) Brow, R. K.; Alam, T. M.; Tallant, D. R.; Kirkpatrick, R. J. *MRS Bulletin* **1998**, *23*, 63–67.
- (34) Petrov, V.; Griebner, U.; Ehrhart, D.; Seeber, W. *Optics Letters* **1997**, *22*, 408–410.
- (35) Ebendorff-Heidepriem, H. *Phosphorus Research Bulletin* **2002**, *13*, 11–20.
- (36) Campbell, J. H.; Suratwala, T. I. *Journal of Non-Crystalline Solids* **2000**, *263–264*, 318–341.
- (37) Kartini, E.; Y. S. Panca Putra, T.; Kuntoro, I.; Sakuma, T.; Basar, K.; Kamishima, O.; Kawamura, J. *Journal of the Physical Society of Japan* **2010**, *79*, 54–58.
- (38) Sokolov, I. A.; Murin, I. V.; Kriy, V. E.; Pronkin, A. A. *Glass Physics and Chemistry* **2011**, *37*, 351.
- (39) Hogarth, C. A.; Basha, M. J. *Journal of Physics D: Applied Physics* **1983**, *16*, 869–878.
- (40) Tawati, D. M.; Jamel Basha Adlan, M.; Abdullah, M. J. *Journal of Non-Crystalline Solids* **2011**, *357*, 2152–2155.
- (41) Van Wazer, J. R., *Phosphorus and Its Compounds*; Interscience Publishers: New York, 1958; Vol. 1.
- (42) Van Wazer, J. R.; Holst, K. A. *Journal of the American Chemical Society* **1950**, *72*, 639–644.
- (43) Fugel, M.; Malaspina, L. A.; Pal, R.; Thomas, S. P.; Shi, M. W.; Spackman, M. A.; Sugimoto, K.; Grabowsky, S. *Chemistry – A European Journal* **2019**, *25*, 6523–6532.
- (44) Brow, R. K.; Kirkpatrick, R. J.; Turner, G. L. *Journal of Non-Crystalline Solids* **1990**, *116*, 39–45.

- (45) Brow, R. K.; Phifer, C. C.; Turner, G. L.; Kirkpatrick, R. J. *Journal of the American Ceramic Society* **1991**, *74*, 1287–1290.
- (46) Brow, R. K.; Kirkpatrick, R. J.; Turner, G. L. *Journal of the American Ceramic Society* **1993**, *76*, 919–928.
- (47) Brow, R. K.; Tallant, D. R.; Myers, S. T.; Phifer, C. C. *Journal of Non-Crystalline Solids* **1995**, *191*, 45–55.
- (48) Kirkpatrick, R. J.; Brow, R. K. *Solid State Nuclear Magnetic Resonance* **1995**, *5*, 9–21.
- (49) Alam, T. M.; Brow, R. K. *Journal of Non-Crystalline Solids* **1998**, *223*, 1–20.
- (50) Edén, M. *Annual Reports Section "C" (Physical Chemistry)* **2012**, *108*, 177–221.
- (51) Turner, G. L.; Smith, K. A.; Kirkpatrick, R. J.; Oldfieldt, E. *Journal of Magnetic Resonance* **1986**, *70*, 408–415.
- (52) Sato, R. K.; Kirkpatrick, R. J.; Brow, R. K. *Journal of Non-Crystalline Solids* **1992**, *143*, 257–264.
- (53) Jäger, C.; Hartmann, P.; Witter, R.; Braun, M. *Journal of Non-Crystalline Solids* **2000**, *263–264*, 61–72.
- (54) Sen, C. K.; Khanna, S.; Venojarvi, M.; Trikha, P.; Ellison, E. C.; Hunt, T. K.; Roy, S. *American Journal of Physiology-Heart and Circulatory Physiology* **2002**, *282*, H1821–H1827.
- (55) Lakhkar, N. J.; Lee, I.-H.; Kim, H.-W.; Salih, V.; Wall, I. B.; Knowles, J. C. *Advanced Drug Delivery Reviews* **2013**, *65*, 405–420.
- (56) Kim, K. S.; Rajagopal, V.; Gonsalves, C.; Johnson, C.; Kalra, V. K. *The Journal of Immunology* **2006**, *177*, 7211–7224.
- (57) Lee, I.-H.; Yu, H.-s.; Lakhkar, N. J.; Kim, H.-W.; Gong, M.-S.; Knowles, J. C.; Wall, I. B. *Materials Science and Engineering: C* **2013**, *33*, 2104–2112.
- (58) Peticone, C.; De Silva Thompson, D.; Owens, G. J.; Kim, H.-W.; Micheletti, M.; Knowles, J. C.; Wall, I. *Journal of Biomaterials Applications* **2017**, *32*, 295–310.
- (59) Chen, Y.; Whetstone, H. C.; Lin, A. C.; Nadesan, P.; Wei, Q.; Poon, R.; Alman, B. A. *PLOS Medicine* **2007**, *4*, e249.
- (60) Yamaguchi, M.; Weitzmann, M. N. *Molecular and Cellular Biochemistry* **2011**, *355*, 179.
- (61) Salih, V.; Patel, A.; Knowles, J. C. *Biomedical Materials* **2007**, *2*, 11–20.
- (62) Saidak, Z.; Marie, P. J. *Pharmacology & Therapeutics* **2012**, *136*, 216–226.
- (63) Bracci, B.; Torricelli, P.; Panzavolta, S.; Boanini, E.; Giardino, R.; Bigi, A. *Journal of Inorganic Biochemistry* **2009**, *103*, 1666–1674.
- (64) Dzondo-Gadet, M.; Mayap-Nzietchueng, R.; Hess, K.; Nabet, P.; Belleville, F.; Dousset, B. *Biological Trace Element Research* **2002**, *85*, 23–33.
- (65) Li, H.; Chang, J. *Acta Biomaterialia* **2013**, *9*, 6981–6991.
- (66) Pietak, A. M.; Reid, J. W.; Stott, M. J.; Sayer, M. *Biomaterials* **2007**, *28*, 4023–4032.
- (67) Julien, M.; Khoshniat, S.; Lacreusette, A.; Gatius, M.; Bozec, A.; Wagner, E. F.; Wittrant, Y.; Masson, M.; Weiss, P.; Beck, L.; Magne, D.; Guicheux, J. *Journal of Bone and Mineral Research* **2009**, *24*, 1856–1868.
- (68) Maier, J. A. M.; Bernardini, D.; Rayssiguier, Y.; Mazur, A. *Biochimica et Biophysica Acta (BBA) - Molecular Basis of Disease* **2004**, *1689*, 6–12.

- (69) Ahmed, I.; Ready, D.; Wilson, M.; Knowles, J. C. *Journal of Biomedical Materials Research Part A* **2006**, *79A*, 618–626.
- (70) Foroutan, F.; McGuire, J.; Gupta, P.; Nikolaou, A.; Kyffin, B. A.; Kelly, N. L.; Hanna, J. V.; Gutierrez-Merino, J.; Knowles, J. C.; Baek, S.-Y.; Velliou, E.; Carta, D. *ACS Biomaterials Science & Engineering* **2019**, *5*, 6054–6062.
- (71) Abou Neel, E. A.; Ahmed, I.; Pratten, J.; Nazhat, S. N.; Knowles, J. C. *Biomaterials* **2005**, *26*, 2247–2254.
- (72) Raja, F. N. S.; Worthington, T.; Isaacs, M. A.; Forto Chungong, L.; Burke, B.; Addison, O.; Martin, R. A. *ACS Biomaterials Science & Engineering* **2019**, *5*, 283–293.
- (73) Pessan, J. P.; Toumba, K. J.; Buzalaf, M. A. R. *Fluoride and the Oral Environment* **2011**, *22*, 115–132.
- (74) Yu, X.; Day, D. E.; Long, G. J.; Brow, R. K. *Journal of Non-Crystalline Solids* **1997**, *215*, 21–31.
- (75) Huffman, E. O.; Fleming, J. D. *The Journal of Physical Chemistry* **1960**, *64*, 240–244.
- (76) McCullough, J. F.; Van Wazer, J. R.; Griffith, E. J. *Journal of the American Chemical Society* **1956**, *78*, 4528–4533.
- (77) Strauss, U. P.; Treitler, T. L. *Journal of the American Chemical Society* **1956**, *78*, 3553–3557.
- (78) Van Wazer, J. R.; Campanella, D. A. *Journal of the American Chemical Society* **1950**, *72*, 655–663.
- (79) Watters, J. I.; Kalliney, S.; Machen, R. C. *Journal of Inorganic and Nuclear Chemistry* **1969**, *31*, 3817–3821.
- (80) Chakarawet, K.; Knopf, I.; Nava, M.; Jiang, Y.; Stauber, J. M.; Cummins, C. C. *Inorganic Chemistry* **2016**, *55*, 6178–6185.
- (81) Ma, L.; Brow, R. K.; Schlesinger, M. E. *Physics and Chemistry of Glasses - European Journal of Glass Science and Technology Part B* **2018**, *59*, 205–212.
- (82) Gao, H.; Tan, T.; Wang, D. *Journal of Controlled Release* **2004**, *96*, 29–36.
- (83) Tošić, M. B.; Nikolić, J. D.; Grujić, S. R.; Živanović, V. D.; Zildžović, S. N.; Matijašević, S. D.; Ždrale, S. V. *Journal of Non-Crystalline Solids* **2013**, *362*, 185–194.
- (84) Wang, J.; Flanagan, D. R. *Journal of Pharmaceutical Sciences* **1999**, *88*, 731–738.
- (85) Chen, Y.; Wang, J.; Flanagan, D. R. In *Developing Solid Oral Dosage Forms (Second Edition)*, Qiu, Y., Chen, Y., Zhang, G. G. Z., Yu, L., Mantri, R. V., Eds.; Academic Press: Boston, 2017, pp 253–270.
- (86) Oosterbeek, R. N.; Margaronis, K. I.; Zhang, X. C.; Best, S. M.; Cameron, R. E. *Journal of the European Ceramic Society* **2021**, *41*, 901–911.
- (87) Higuchi, T. *Journal of Pharmaceutical Sciences* **1961**, *50*, 874–875.
- (88) Higuchi, W. I.; Hiestand, E. N. *Journal of Pharmaceutical Sciences* **1963**, *52*, 67–71.
- (89) Ahmed, I.; Lewis, M. P.; Nazhat, S. N.; Knowles, J. C. *Journal of Biomaterials Applications* **2005**, *20*, 65–80.
- (90) Atkins, P.; Overton, T., *Shriver and Atkins' Inorganic Chemistry*; OUP Oxford: 2010.
- (91) Pearson, R. G. *Journal of the American Chemical Society* **1963**, *85*, 3533–3539.
- (92) Askalani, P.; Absi, T. *Journal of Inorganic and Nuclear Chemistry* **1979**, *41*, 31–35.

- (93) Christie, J. K.; Ainsworth, R. I.; Di Tommaso, D.; de Leeuw, N. H. *The Journal of Physical Chemistry B* **2013**, *117*, 10652–10657.
- (94) Van Wazer, J. R.; Griffith, E. J.; McCullough, J. F. *Journal of the American Chemical Society* **1955**, *77*, 287–291.
- (95) Griffith, E. J.; Buxton, R. L. *Journal of the American Chemical Society* **1967**, *89*, 2884–2890.
- (96) B. Gill, J.; A. Riaz, S. *Journal of the Chemical Society A: Inorganic, Physical, Theoretical* **1969**, *0*, 183–187.
- (97) Watanabe, M.; Sato, S.; Saito, H. *Bulletin of the Chemical Society of Japan* **1975**, *48*, 3593–3597.
- (98) Thilo, E.; Wieker, W. *Journal of Polymer Science* **1961**, *53*, 55–59.
- (99) Glonek, T.; Van Wazer, J. R.; Mudgett, M.; Myers, T. C. *Inorganic Chemistry* **1972**, *11*, 567–570.
- (100) De Jager, H.-J.; Heyns, A. M. *The Journal of Physical Chemistry A* **1998**, *102*, 2838–2841.
- (101) Bochove, M. A. v.; Swart, M.; Matthias Bickelhaupt, F. *Physical Chemistry Chemical Physics* **2009**, *11*, 259–267.
- (102) Friess, S. *Journal of the American Chemical Society* **1952**, *74*, 4027–4029.
- (103) Pauling, L., *The Nature of the Chemical Bond and the Structure of Molecules and Crystals: An Introduction to Modern Structural Chemistry*; Cornell University Press: 1945.
- (104) Samuelson, O. *Svensk Kem. Tid.* **1944**, *56*, 343–348.
- (105) Thilo, E. In *Advances in Inorganic Chemistry and Radiochemistry*, Emeléus, H. J., Sharpe, A. G., Eds.; Academic Press: 1962; Vol. 4, pp 1–75.
- (106) Kolthoff, I. M.; Bosch, W. *Recueil des Travaux Chimiques des Pays-Bas* **1928**, *47*, 826–833.
- (107) Hirokawa, T.; Kabayashi, S.; Kiso, Y. *Journal of Chromatography A* **1985**, *318*, 195–210.
- (108) Healy, R. M.; Kilpatrick, M. L. *Journal of the American Chemical Society* **1955**, *77*, 5258–5264.
- (109) Watanabe, M.; Matsuura, M.; Yamada, T. *Bulletin of the Chemical Society of Japan* **1981**, *54*, 738–741.
- (110) Watanabe, M. *Bulletin of the Chemical Society of Japan* **1982**, *55*, 3766–3769.
- (111) Barceloux, D. G.; Barceloux, D. D. *Journal of Toxicology: Clinical Toxicology* **1999**, *37*, 201–216.
- (112) Paustenbach, D. J.; Tvermoes, B. E.; Unice, K. M.; Finley, B. L.; Kerger, B. D. *Critical Reviews in Toxicology* **2013**, *43*, 316–362.
- (113) Lison, D. In *Handbook on the Toxicology of Metals (Fourth Edition)*, Nordberg, G. F., Fowler, B. A., Nordberg, M., Eds.; Academic Press: San Diego, 2015, pp 743–763.
- (114) Roto, P. *Scandinavian Journal of Work, Environment & Health* **1980**, *6*, 1–49.
- (115) Lison, D.; Carbonnelle, P.; Mollo, L.; Lauwerys, R.; Fubini, B. *Chemical Research in Toxicology* **1995**, *8*, 600–606.
- (116) De Boeck, M.; Hoet, P.; Lombaert, N.; Nemery, B.; Kirsch-Volders, M.; Lison, D. *Carcinogenesis* **2003**, *24*, 1793–1800.
- (117) Demedts, M.; Gheysens, B.; Nagels, J.; Verbeken, E.; Lauweryns, J.; Eeckhout, A. v. d.; Lahaye, D.; Gyselen, A. *American Review of Respiratory Disease* **2015**.

- (118) Léonard, A.; Lauwerys, R. *Mutation Research/Reviews in Genetic Toxicology* **1990**, *239*, 17–27.
- (119) Jensen, A. A.; Tuchsén, F. *Critical Reviews in Toxicology* **1990**, *20*, 427–439.
- (120) D’Adda, F.; Borleri, D.; Migliori, M.; Mosconi, G.; Medolago, G.; Virota, G.; Colombo, F.; Seghizzi, P. *Science of The Total Environment* **1994**, *150*, 179–186.
- (121) Fregert, S.; Gruvberger, B. *Contact Dermatitis* **1978**, *4*, 14–18.
- (122) Raffn, E.; Mikkelsen, S.; Altman, D. G.; Christensen, J. M.; Groth, S. *Scandinavian Journal of Work, Environment & Health* **1988**, *14*, 378–384.
- (123) Gál, J.; Hursthouse, A.; Tatner, P.; Stewart, F.; Welton, R. *Environment International* **2008**, *34*, 821–838.
- (124) Hindsén, M.; Persson, L.; Gruvberger, B. *Contact Dermatitis* **2005**, *53*, 350–351.
- (125) Fowler, J. F. *Dermatitis* **2016**, *27*, 3–8.
- (126) Thyssen, J. P.; Johansen, J. D.; Jellesen, M. S.; Møller, P.; Sloth, J. J.; Zachariae, C.; Menné, T. *Contact Dermatitis* **2013**, *69*, 276–279.
- (127) Alexander, C. S. *The American Journal of Medicine* **1972**, *53*, 395–417.
- (128) Barborik, M.; Dusek, J. *British Heart Journal* **1972**, *34*, 113–116.
- (129) Morin, Y.; Têtu, A.; Mercier, G. *British Heart Journal* **1971**, *33*, 175–178.
- (130) Coles, B. *Archives of Disease in Childhood* **1955**, *30*, 121–126.
- (131) Shuttleworth, V. S.; Cameron, R. S.; Alderman, G.; Davies, H. T. *Practitioner* **1961**, *186*, 760–764.
- (132) Duckham, J. M.; Lee, H. A. *QJM: An International Journal of Medicine* **1976**, *45*, 277–294.
- (133) Lippi, G.; Franchini, M.; Guidi, G. C. *Journal of Occupational Medicine and Toxicology* **2006**, *1*, 18.
- (134) Mabilieu, G.; Kwon, Y.-M.; Pandit, H.; Murray, D. W.; Sabokbar, A. *Acta Orthopaedica* **2008**, *79*, 734–747.
- (135) Hasegawa, M.; Yoshida, K.; Wakabayashi, H.; Sudo, A. *The Journal of Arthroplasty* **2012**, *27*, 990–996.
- (136) Lewis, A. C.; Heard, P. J. *Journal of Biomedical Materials Research Part A* **2005**, *75A*, 365–373.
- (137) Patntirapong, S.; Habibovic, P.; Hauschka, P. V. *Biomaterials* **2009**, *30*, 548–555.
- (138) Daou, S.; El Chemaly, A.; Christofilopoulos, P.; Bernard, L.; Hoffmeyer, P.; Demaurex, N. *Biomaterials* **2011**, *32*, 1769–1777.
- (139) E. Goode, A.; M. Perkins, J.; Sandison, A.; Karunakaran, C.; Cheng, H.; Wall, D.; A. Skinner, J.; J. Hart, A.; E. Porter, A.; W. McComb, D.; P. Ryan, M. *Chemical Communications* **2012**, *48*, 8335–8337.
- (140) Kriss, J. P.; Carnes, W. H.; Gross, R. T. *Journal of the American Medical Association* **1955**, *159*, 708–708.
- (141) Tribukait, B. *Acta Physiologica Scandinavica* **1963**, *58*, 101–&.
- (142) Davis, J.; Fields, J. *Proceedings of the Society for Experimental Biology and Medicine* **1958**, *99*, 493–495.

- (143) Bowie, E. A.; Hurley, P. J. *Australian and New Zealand Journal of Medicine* **1975**, *5*, 306–313.
- (144) Höck, A.; Demmel, U.; Schicha, H.; Kasperek, K.; Feinendegen, L. E. *Brain: A Journal of Neurology* **1975**, *98*, 49–64.
- (145) Paustenbach, D. J.; Galbraith, D. A.; Finley, B. L. *Clinical Toxicology* **2014**, *52*, 98–112.
- (146) Lee, S.-H.; Brennan, F. R.; Jacobs, J. J.; Urban, R. M.; Ragasa, D. R.; Glant, T. T. *Journal of Orthopaedic Research* **1997**, *15*, 40–49.
- (147) Morais, S.; Sousa, J. P.; Fernandes, M. H.; Carvalho, G. S. *Biomaterials* **1998**, *19*, 13–21.
- (148) Roy, P. E.; Bonenfant, J. L.; Turcot, L. *American Journal of Clinical Pathology* **1968**, *50*, 234–239.
- (149) Chave, T. A.; Warin, A. P. *Contact Dermatitis* **1999**, *41*, 236–236.
- (150) Veien, N. K.; Hattel, T.; Justesen, O.; Nørholm, A. *Acta Dermato-Venereologica* **1987**, *67*, 321–325.
- (151) Tower, S. S. *Journal of Bone and Joint Surgery-American Volume* **2010**, *92A*, 2847–2851.
- (152) Sunda, W. G.; Lewis, J. A. M. *Limnology and Oceanography* **1978**, *23*, 870–876.
- (153) CAMPBELL, P. G. C. *Metal Speciation and Bioavailability* **1994**, 45–102.
- (154) Mothes, E.; Faller, P. *Biochemistry* **2007**, *46*, 2267–2274.
- (155) Karovic, O.; Tonazzini, I.; Rebola, N.; Edström, E.; Lövdahl, C.; Fredholm, B. B.; Daré, E. *Biochemical Pharmacology* **2007**, *73*, 694–708.
- (156) Webb, M. *Biochimica et Biophysica Acta (BBA) - Specialized Section on Enzymological Subjects* **1964**, *89*, 431–446.
- (157) Seghizzi, P.; D’Adda, F.; Borleri, D.; Barbic, F.; Mosconi, G. *Science of The Total Environment* **1994**, *150*, 105–109.
- (158) Neilsen, J. L.; Abildtrup, A.; Christensen, J.; Watson, P.; Cox, A.; McLeod, C. W. *Spectrochimica Acta Part B: Atomic Spectroscopy* **1998**, *53*, 339–345.
- (159) Krantz, S.; Lober, M.; Fiedler, H. *Biochimica et Biophysica Acta (BBA) - General Subjects* **1971**, *230*, 630–633.
- (160) Sederholm, T.; Kouvalainen, K.; Lamberg, B.-A. *Acta Medica Scandinavica* **1968**, *184*, 301–306.
- (161) Simonsen, L. O.; Brown, A. M.; Harbak, H.; Kristensen, B. I.; Bennekou, P. *Blood Cells, Molecules, and Diseases* **2011**, *46*, 266–276.
- (162) Nandedkar, A. K. N.; Basu, P. K.; Friedberg, F. *Bioinorganic Chemistry* **1973**, *2*, 149–157.
- (163) Griffith, L. G.; Naughton, G. *Science* **2002**, *295*, 1009–1014.
- (164) Novosel, E. C.; Kleinhans, C.; Kluger, P. J. *Advanced Drug Delivery Reviews* **2011**, *63*, 300–311.
- (165) Kannan, R. Y.; Salacinski, H. J.; Sales, K.; Butler, P.; Seifalian, A. M. *Biomaterials* **2005**, *26*, 1857–1875.
- (166) Wan, C.; Gilbert, S. R.; Wang, Y.; Cao, X.; Shen, X.; Ramaswamy, G.; Jacobsen, K. A.; Alaql, Z. S.; Eberhardt, A. W.; Gerstenfeld, L. C.; Einhorn, T. A.; Deng, L.; Clemens, T. L. *Proceedings of the National Academy of Sciences* **2008**, *105*, 686–691.
- (167) M. Azevedo, M.; Jell, G.; D. O’Donnell, M.; V. Law, R.; G. Hill, R.; M. Stevens, M. *Journal of Materials Chemistry* **2010**, *20*, 8854–8864.

- (168) Steinbrech, D. S.; Mehrara, B. J.; Saadeh, P. B.; Greenwald, J. A.; Spector, J. A.; Gittes, G. K.; Longaker, M. T. *American Journal of Physiology-Cell Physiology* **2000**, *278*, C853–C860.
- (169) Jain, R. K. *Nature Medicine* **2003**, *9*, 685–693.
- (170) Pepper, M. S.; Ferrara, N.; Orci, L.; Montesano, R. *Biochemical and Biophysical Research Communications* **1992**, *189*, 824–831.
- (171) Ferrara, N.; Davis-Smyth, T. *Endocrine Reviews* **1997**, *18*, 4–25.
- (172) Zelzer, E.; Mamluk, R.; Ferrara, N.; Johnson, R. S.; Schipani, E.; Olsen, B. R. *Development* **2004**, *131*, 2161–2171.
- (173) Semenza, G. L. *Science* **2007**, *318*, 62–64.
- (174) Gleadle, J. M.; Ebert, B. L.; Firth, J. D.; Ratcliffe, P. J. *American Journal of Physiology-Cell Physiology* **1995**, *268*, C1362–C1368.
- (175) Hewitson, K. S.; McNeill, L. A.; Riordan, M. V.; Tian, Y.-M.; Bullock, A. N.; Welford, R. W.; Elkins, J. M.; Oldham, N. J.; Bhattacharya, S.; Gleadle, J. M.; Ratcliffe, P. J.; Pugh, C. W.; Schofield, C. J. *Journal of Biological Chemistry* **2002**, *277*, 26351–26355.
- (176) Yuan, Y.; Beitner-Johnson, D.; Millhorn, D. E. *Biochemical and Biophysical Research Communications* **2001**, *288*, 849–854.
- (177) Buttyan Ralph; Chichester Paul; Stisser Brian; Matsumoto Seiji; Ghafar Mohamed A.; Levin Robert M. *Journal of Urology* **2003**, *169*, 2402–2406.
- (178) Grasselli, F.; Basini, G.; Bussolati, S.; Bianco, F. *Reproduction, Fertility and Development* **2005**, *17*, 715–720.
- (179) Zheng, Y.; Yang, Y.; Deng, Y. *Materials Science and Engineering: C* **2019**, *99*, 770–782.
- (180) Chen, Z.; Yuen, J.; Crawford, R.; Chang, J.; Wu, C.; Xiao, Y. *Biomaterials* **2015**, *61*, 126–138.
- (181) Zhou, J.; Zhao, L. *Acta Biomaterialia* **2016**, *43*, 358–368.
- (182) Ignjatovic, N.; Ajdukovic, Z.; Rajkovic, J.; Najman, S.; Mihailovic, D.; Uskokovic, D. *Journal of Bionic Engineering* **2015**, *12*, 604–612.
- (183) Pell, A. J.; Pintacuda, G.; Grey, C. P. *Progress in Nuclear Magnetic Resonance Spectroscopy* **2019**, *111*, 1–271.
- (184) Bakhmutov, V. I., *Solid-State NMR in Materials Science: Principles and Applications*; CRC Press: 2011.
- (185) Softley, C. A.; Bostock, M. J.; Popowicz, G. M.; Sattler, M. *Journal of Biomolecular NMR* **2020**, *74*, 287–309.
- (186) Kowalewski, J.; Kruk, D. In *eMagRes*; American Cancer Society: 2011.
- (187) Bakhmutov, V. I.; Shpeizer, B. G.; Clearfield, A. *Magnetic Resonance in Chemistry* **2006**, *44*, 861–867.
- (188) Schmitt, K. D.; Haase, J.; Oldfield, E. *Zeolites* **1994**, *14*, 89–100.
- (189) Bloembergen, N.; Purcell, E. M.; Pound, R. V. *Physical Review* **1948**, *73*, 679–712.
- (190) Solomon, I. *Physical Review* **1955**, *99*, 559–565.
- (191) Clément, R. J.; Pell, A. J.; Middlemiss, D. S.; Strobridge, F. C.; Miller, J. K.; Whittingham, M. S.; Emsley, L.; Grey, C. P.; Pintacuda, G. *Journal of the American Chemical Society* **2012**, *134*, 17178–17185.

- (192) Mehrer, H., *Diffusion in Solids: Fundamentals, Methods, Materials, Diffusion-Controlled Processes*; Springer Science & Business Media: 2007.
- (193) Levitt, M. H., *Spin Dynamics: Basics of Nuclear Magnetic Resonance*; Wiley: 2008.
- (194) Harris, R. K., *Nuclear magnetic resonance spectroscopy: a physicochemical view*; Longman Scientific & Technical: 1986.
- (195) Slichter, C. P., *Principles of Magnetic Resonance*; Springer Science & Business Media: 2013.
- (196) Becker, E. D., *High Resolution NMR, Third Edition: Theory and Chemical Applications*, 3rd ed.; Academic Press: 1999.
- (197) MacKenzie, K. J. D.; Smith, M. E., *Multinuclear Solid-State Nuclear Magnetic Resonance of Inorganic Materials*; Elsevier: 2002.
- (198) Haeberlen, U., *High Resolution NMR in Solids: Selective Averaging*; Academic Press: 1976.
- (199) Mehring, M., *Principles of High Resolution NMR in Solids*; Springer Science & Business Media: 1983.
- (200) Spiess, H. W. In *Dynamic NMR Spectroscopy*; NMR Basic Principles and Progress 15; Springer Berlin Heidelberg: 1978, pp 55–214.
- (201) Bak, M.; Rasmussen, J.; Nielsen, N. *Journal of Magnetic Resonance* **2000**, *147*, 01256, 296–330.
- (202) Hennel, J. W.; Klinowski, J., *Fundamentals of nuclear magnetic resonance*; Longman Scientific & Technical: 1993.
- (203) Klinowski, J., *New Techniques in Solid-State NMR*; Springer Science & Business Media: 2005.
- (204) Pople, J. A., *High-resolution nuclear magnetic resonance*; McGraw-Hill: 1959.
- (205) De Groot, H. J. M.; Smith, S. O.; Kolbert, A. C.; Courtin, J. M. L.; Winkel, C.; Lugtenburg, J.; Herzfeld, J.; Griffin, R. G. *Journal of Magnetic Resonance* **1991**, *91*, 30–38.
- (206) Herzfeld, J.; Berger, A. E. *The Journal of Chemical Physics* **1980**, *73*, 6021–6030.
- (207) Li, W.; Celinski, V. R.; Weber, J.; Kunkel, N.; Kohlmann, H.; Schmedt auf der Günne, J. *Physical Chemistry Chemical Physics* **2016**.
- (208) Abragam, A., *The Principles of Nuclear Magnetism*; Clarendon Press: 1961.
- (209) Blumich, B., *NMR Imaging of Materials*; OUP Oxford: 2000.
- (210) Mandlule, A.; Döhler, F.; Van Wüllen, L.; Kasuga, T.; Brauer, D. S. *Journal of Non-Crystalline Solids* **2014**, *392–393*, 31–38.
- (211) *Master thesis*; tech. rep., Hartrampf, W.; Friedrich Schiller University, 2018.
- (212) Glonek, T.; Kleps, R.; Griffith, E.; Myers, T. *Phosphorus* **1975**, *5*, 157–164.
- (213) Topspin version 3.5 pl 5; Bruker NMR software, 2016.
- (214) Wetzels, R., Ph.D. Thesis, Friedrich Schiller University, 2019.
- (215) Brandt-Slowik, J., Ph.D. Thesis, Friedrich Schiller University, 2020.
- (216) Massiot, D.; Fayon, F.; Capron, M.; King, I.; Le Calvé, S.; Alonso, B.; Durand, J.-O.; Bujoli, B.; Gan, Z.; Hoatson, G. *Magnetic Resonance in Chemistry* **2002**, *40*, 70–76.

- (217) Stoll, S.; Schweiger, A. *Journal of Magnetic Resonance (San Diego, Calif.: 1997)* **2006**, *178*, 42–55.
- (218) Neuville, D. R.; Mysen, B. O. *Geochimica et Cosmochimica Acta* **1996**, *60*, 1727–1737.
- (219) Choueka, A.; Charvet, J.; Alexander, H.; Oh, Y.; Joseph, G.; Blumenthal, N.; Lacourse, W. *Journal of Biomedical Materials Research* **1995**, *29*, 1309–1315.
- (220) Salih, V.; Franks, K.; James, M.; Hastings, G. W.; Knowles, J. C.; Olsen, I. *Journal of Materials Science: Materials in Medicine* **2000**, *11*, 615–620.
- (221) Xu, H. H. K.; Eichmiller, F. C.; Giuseppetti, A. A. *Journal of Biomedical Materials Research* **2000**, *52*, 107–114.
- (222) Neel, E. A. A.; O'Dell, L. A.; Smith, M. E.; Knowles, J. C. *Journal of Materials Science: Materials in Medicine* **2008**, *19*, 1669–1679.
- (223) Stähli, C.; Muja, N.; Nazhat, S. N. *Tissue Engineering Part A* **2012**, *19*, 548–557.
- (224) Franks, K.; Abrahams, I.; Knowles, J. C. *Journal of Materials Science-Materials in Medicine* **2000**, *11*, 609–614.
- (225) Day, D. E.; Wu, Z.; Ray, C. S.; Hrma, P. *Journal of Non-Crystalline Solids* **1998**, *241*, 1–12.
- (226) Gao, H.; Tan, T.; Wang, D. *Journal of Controlled Release* **2004**, *96*, 21–28.
- (227) Ahmed, I.; Lewis, M.; Olsen, I.; Knowles, J. C. *Biomaterials* **2004**, *25*, 491–499.
- (228) Van Wazer, J. R.; Griffith, E. J.; McCullough, J. F. *Journal of the American Chemical Society* **1952**, *74*, 4977–4978.
- (229) Watanabe, M. *Bulletin of the Chemical Society of Japan* **1974**, *47*, 2048–2050.
- (230) Watanabe, M.; Sato, S.; Saito, H. *Bulletin of the Chemical Society of Japan* **1975**, *48*, 896–898.
- (231) Watanabe, M.; Sato, S.; Saito, H. *Bulletin of the Chemical Society of Japan* **1976**, *49*, 2474–2478.
- (232) Strauss, U. P.; Ross, P. D. *Journal of the American Chemical Society* **1959**, *81*, 5295–5298.
- (233) Huskens, J.; Lammers, H.; Bekkum, H. v.; Peters, J. A. *Magnetic Resonance in Chemistry* **1994**, *32*, 691–698.
- (234) Huskens, J.; Kennedy, A. D.; van Bekkum, H. v.; Peters, J. A. *Journal of the American Chemical Society* **1995**, *117*, 375–382.
- (235) Daniele, P. G.; Foti, C.; Gianguzza, A.; Prenesti, E.; Sammartano, S. *Coordination Chemistry Reviews* **2008**, *252*, 1093–1107.
- (236) Crutchfield, M. M.; Callis, C. V.; Irani, R. R.; Roth, G. C. *Inorganic Chemistry* **1962**, *1*, 813–817.
- (237) Mortlock, R. F.; Bell, A. T.; Radke, C. J. *The Journal of Physical Chemistry* **1993**, *97*, 775–782.
- (238) Van Wazer, J. R.; Kroupa, E. K. *Journal of the American Chemical Society* **1956**, *78*, 1772–1772.
- (239) Ahmed, I.; Lewis, M. P.; Knowles, J. C. *Physics and Chemistry of Glasses* **2005**, *46*, 547–552.
- (240) Glonek, T.; Costello, J. R.; Myers, T. C.; Van Wazer, J. R. *The Journal of Physical Chemistry* **1975**, *79*, 1214–1218.

- (241) Glonek, T. *Phosphorus* **1975**, *5*, 165–171.
- (242) Döhler, F.; Mandlule, A.; Van Wüllen, L.; Friedrich, M.; Brauer, D. S. *Journal of Materials Chemistry B* **2015**, *3*, 1125–1134.
- (243) Letcher, J. H.; Van Wazer, J. R. *The Journal of Chemical Physics* **1966**, *44*, 815–829.
- (244) Kohn, S. C.; Dupree, R.; Smith, M. E. *Nature* **1989**, *337*, 539–541.
- (245) Wenslow, R. M.; Mueller, K. T. *The Journal of Physical Chemistry B* **1998**, *102*, 9033–9038.
- (246) Alam, T. M.; Tischendorf, B. C.; Brow, R. K. *Solid State Nuclear Magnetic Resonance* **2005**, *27*, 99–111.
- (247) Knowles, J. C.; Franks, K.; Abrahams, I. *Biomaterials* **2001**, *22*, 3091–3096.
- (248) Ma, L.; Brow, R. K.; Schlesinger, M. E. *Journal of Non-Crystalline Solids* **2017**, *463*, 90–101.
- (249) Ruiz-Hernandez, S. E.; Ainsworth, R. I.; de Leeuw, N. H. *Journal of Non-Crystalline Solids* **2020**, *548*, 120332.
- (250) Cussler, E. L.; Cussler, E. L., *Diffusion: Mass Transfer in Fluid Systems*; Cambridge University Press: 1997.
- (251) Noyes, A. A.; Whitney, W. R. *Journal of the American Chemical Society* **1897**, *19*, 930–934.
- (252) Brunner, E. *Zeitschrift für Physikalische Chemie* **1904**, *47U*, 56–102.
- (253) Nernst, W. *Zeitschrift für Physikalische Chemie* **1904**, *47U*, 52–55.
- (254) Malini, R. I.; Freeman, C. L.; Harding, J. H. *CrystEngComm* **2019**, *21*, 6354–6364.
- (255) Garcia, N. A.; Malini, R. I.; Freeman, C. L.; Demichelis, R.; Raiteri, P.; Sommerdijk, N. A. J. M.; Harding, J. H.; Gale, J. D. *Crystal Growth and Design* **2019**, 6422–6430.
- (256) McGilvery, J. D.; Crowther, J. P. *Canadian Journal of Chemistry* **1954**, *32*, 174–185.
- (257) Crowther, J.; Westman, A. *Canadian Journal of Chemistry-Revue Canadienne De Chimie* **1956**, *34*, 969–981.
- (258) Griffith, E. J.; Buxton, R. L. *Inorganic Chemistry* **1965**, *4*, 549–551.
- (259) Davies, C.; Monk, C. *Journal of the Chemical Society* **1949**, 413–422.
- (260) Schülke, U. *Angewandte Chemie International Edition in English* **1968**, *7*, 71–71.
- (261) Glonek, T.; Myers, T. C.; Van Wazer, J. R. *Journal of the American Chemical Society* **1975**, *97*, 206–207.
- (262) Costello, A. J. R.; Glonek, T.; Van Wazer, J. R. *Inorganic Chemistry* **1976**, *15*, 972–974.
- (263) Crutchfield, M. M.; Irani, R. R. *Journal of the American Chemical Society* **1965**, *87*, 2815–2820.
- (264) Jones, H.; Monk, C.; Davies, C. *Journal of the Chemical Society* **1949**, 2693–2695.
- (265) Smith, R. M.; Alberty, R. A. *Journal of the American Chemical Society* **1956**, *78*, 2376–2380.
- (266) Smith, R.; Alberty, R. *Journal of Physical Chemistry* **1956**, *60*, 180–184.
- (267) Berto, S.; Chiavazza, E.; Canepa, P.; Prenesti, E.; Daniele, P. G. *Physical Chemistry Chemical Physics* **2016**, *18*, 13118–13125.
- (268) Bandura, A. V.; Lvov, S. N. *Journal of Physical and Chemical Reference Data* **2005**, *35*, 15–30.
- (269) Harris, D. C., *Quantitative Chemical Analysis*; W. H. Freeman: 2010.

- (270) Barnett, B. L.; Uchtman, V. A. *Inorganic Chemistry* **1979**, *18*, 2674–2678.
- (271) Einspahr, H.; Gartland, G.; Bugg, C. *Acta Crystallographica Section B-Structural Science* **1977**, *33*, 3385–3390.
- (272) Averbuch-Pouchot, M.; Durif, A.; Guitel, J. *Acta Crystallographica Section C-Crystal Structure Communications* **1989**, *45*, 1320–1322.
- (273) Vollhardt, K. P. C.; Schore, N. E., *Organic Chemistry*; W. H. Freeman: 2010.
- (274) Bobtelsky, M.; Kertes, S. *Journal of Applied Chemistry* **1954**, *4*, 419–429.
- (275) Duan, X.; Yuan, D.; Cheng, X.; Liu, Z.; Zhang, X. *Journal of Alloys and Compounds* **2008**, *453*, 379–381.
- (276) Abd El-Fattah, Z. M.; Ahmad, F.; Hassan, M. A. *Journal of Alloys and Compounds* **2017**, *728*, 773–779.
- (277) Ryba-Romanowski, W.; Golab, S.; Dominiak-Dzik, G.; Berkowski, M. *Journal of Alloys and Compounds* **1999**, *288*, 262–268.
- (278) Satyanarayana, T.; Kityk, I. V.; Piasecki, M.; Bragiel, P.; Brik, M. G.; Gandhi, Y.; Veeraiah, N. *Journal of Physics Condensed Matter* **2009**, *21*, 245104.
- (279) Suresh, B.; Reddy, M. S.; Ashok, J.; Reddy, A. S. S.; Rao, P. V.; Kumar, V. R.; Veeraiah, N. *Journal of Luminescence* **2016**, *172*, 47–52.
- (280) Naresh, P.; Naga Raju, G.; Srinivasa Rao, C.; Prasad, S. V. G. V. A.; Ravi Kumar, V.; Veeraiah, N. *Physica B: Condensed Matter* **2012**, *407*, 712–718.
- (281) Serment, B.; Corucho, L.; Demourgues, A.; Hadziioannou, G.; Brochon, C.; Cloutet, E.; Gaudon, M. *Inorganic Chemistry* **2019**, *58*, 7499–7510.
- (282) Robertson, L.; Gaudon, M.; Pechev, S.; Demourgues, A. *Journal of Materials Chemistry* **2012**, *22*, 3585–3590.
- (283) Low, W. *Physical Review* **1958**, *109*, 256–265.
- (284) Hunault, M.; Robert, J. .-.; Newville, M.; Galois, L.; Calas, G. *Spectrochimica Acta Part A: Molecular and Biomolecular Spectroscopy* **2014**, *117*, 406–412.
- (285) Duan, X.; Yuan, D.; Cheng, X.; Sun, Z.; Sun, H.; Xu, D.; Lv, M. *Journal of Physics and Chemistry of Solids* **2003**, *64*, 1021–1025.
- (286) Abdelghany, A. M.; ElBatal, H. A.; Ramadan, R. M. *Journal of King Saud University - Science* **2017**, *29*, 510–516.
- (287) Hunault, M. O. J. Y.; Galois, L.; Lelong, G.; Newville, M.; Calas, G. *Journal of Non-Crystalline Solids* **2016**, *451*, 101–110.
- (288) Möncke, D.; Ehrt, D. *Glass Science and Technology* **2002**, *75*, 243–253.
- (289) Abdelghany, A. M.; El-Damrawi, G.; Oraby, A. H.; Madshal, M. A. *Journal of Non-Crystalline Solids* **2018**, *499*, 153–158.
- (290) ElBatal, F. H.; Ouis, M. A.; Morsi, R. M. M.; Marzouk, S. Y. *Journal of Non-Crystalline Solids* **2010**, *356*, 46–55.
- (291) A. Duffy, J.; P. Glasser, F.; D. Ingram, M. *Journal of the Chemical Society A: Inorganic, Physical, Theoretical* **1968**, *0*, 551–554.
- (292) Duffy, J. A.; Ingram, M. D. *Journal of the American Ceramic Society* **1968**, *51*, 544–544.
- (293) Ingram, M. D.; Duffy, J. A. *J. Chem. Soc. A* **1968**, *0*, 2575–2578.

- (294) Paul, A., *Chemistry of Glasses*; Springer Science & Business Media: 1989.
- (295) Duffy, J. A. *Journal of Non-Crystalline Solids* **1989**, *109*, 35–39.
- (296) Griebenow, K.; Hoppe, U.; Möncke, D.; Kamitsos, E. I.; Wondraczek, L. *Journal of Non-Crystalline Solids* **2017**, *460*, 136–145.
- (297) Gray, P. E.; Klein, L. C. *Glass Technology* **1983**, *24*, Publisher: Society of Glass Technology, 202–206.
- (298) Bues, W.; Gehrke, H. *Zeitschrift für Anorganische und Allgemeine Chemie* **1956**, *288*, 307–323.
- (299) Bertoluzza, A.; Battaglia, M. A.; Simoni, R.; Long, D. A. *Journal of Raman Spectroscopy* **1983**, *14*, 178–183.
- (300) Hudgens, J. J.; Brow, R. K.; Tallant, D. R.; Martin, S. W. *Journal of Non-Crystalline Solids* **1998**, *223*, 21–31.
- (301) Nelson, B. N.; Exarhos, G. J. *The Journal of Chemical Physics* **1979**, *71*, 2739.
- (302) Pemberton, J. E.; Latifzadeh, L.; Fletcher, J. P.; Risbud, S. H. *Chemistry of Materials* **1991**, *3*, 195–200.
- (303) Almeida, R. M.; Mackenzie, J. D. *Journal of Non-Crystalline Solids* **1980**, *40*, 535–548.
- (304) Rouse, G. B.; Miller, P. J.; Risen, W. M. *Journal of Non-Crystalline Solids* **1978**, *28*, 193–207.
- (305) Griebenow, K.; Bragatto, C. B.; Kamitsos, E. I.; Wondraczek, L. *Journal of Non-Crystalline Solids* **2018**, *481*, 447–456.
- (306) Shannon, R. D. *Acta Crystallographica Section A* **1976**, *32*, 751–767.
- (307) Nelson, C.; White, W. B. *Journal of Materials Research* **1986**, *1*, 130–138.
- (308) Katz, A. K.; Glusker, J. P.; Beebe, S. A.; Bock, C. W. *Journal of the American Chemical Society* **1996**, *118*, 5752–5763.
- (309) Al Hasni, B.; Martin, R. A.; Storey, C.; Mountjoy, G.; Pickup, D. M.; Newport, R. J. *Physics and Chemistry of Glasses - European Journal of Glass Science and Technology Part B* **2016**, *57*, 245–253.
- (310) Tanabe, Y.; Sugano, S. *Journal of the Physical Society of Japan* **1954**, *9*, 766–779.
- (311) Tanabe, Y.; Sugano, S. *Journal of the Physical Society of Japan* **1954**, *9*, 753–766.
- (312) Brow, R. K. *Journal of the American Ceramic Society* **1993**, *76*, _eprint: <https://onlinelibrary.wiley.com/doi/10.1002/jac.2916>, 913–918.
- (313) Van Wüllen, L.; Gee, B.; Züchner, L.; Bertmer, M.; Eckert, H. *Berichte der Bunsengesellschaft für physikalische Chemie* **1996**, *100*, 1539–1549.
- (314) Massera, J.; Hupa, L.; Hupa, M. *Journal of Non-Crystalline Solids* **2012**, *358*, 2701–2707.
- (315) Ibrahim, A.; Sadeq, M. S. *Ceramics International* **2021**.
- (316) Colak, S. C.; Aral, E. *Journal of Alloys and Compounds* **2011**, *509*, 4935–4939.
- (317) Elbashar, Y. H.; Mohamed, M. A.; Rayan, D.; Badr, A. M.; Elshaikh, H. A. *Journal of Optics* **2020**, *49*, 270–276.
- (318) Reif, B.; Ashbrook, S. E.; Emsley, L.; Hong, M. *Nature Reviews Methods Primers* **2021**, *1*, 1–23.
- (319) Gochin, M. *Journal of Biomolecular NMR* **1998**, *12*, 243–257.

- (320) McCarty, R. J.; Stebbins, J. F. *The Journal of Physical Chemistry C* **2016**, *120*, Publisher: American Chemical Society, 11111–11120.
- (321) Pavlov, A. A. *INEOS OPEN* **2020**, *2*, 153–162.
- (322) Stebbins, J. F. *American Mineralogist* **2017**, *102*, 2406–2414.
- (323) Li, W.; F. Smet, P.; J. Martin, L. I. D.; Pritzel, C.; Schmedt auf der Günne, J. *Physical Chemistry Chemical Physics* **2020**, *22*, 818–825.
- (324) Bertmer, M. *Solid State Nuclear Magnetic Resonance* **2017**, *81*, 1–7.
- (325) Möncke, D.; Tricot, G.; Winterstein-Beckmann, A.; Wondraczek, L.; Kamitsos, E. I. **2015**, *56*, 203–211.
- (326) Bertini, I.; Luchinat, C.; Scozzafava, A. *FEBS letters* **1978**, *93*, 251–254.
- (327) Harris, M. N.; Bertolucci, C. M.; Ming, L.-J. *Inorganic Chemistry* **2002**, *41*, Publisher: American Chemical Society, 5582–5588.
- (328) Lockyer, M.; Holland, D.; Dupree, R. *Journal of Non-Crystalline Solids* **1995**, *188*, 207–219.
- (329) Eckert, H. *Journal of Sol-Gel Science and Technology* **2018**, *88*, 263–295.
- (330) Pedone, A.; Charpentier, T.; Malavasi, G.; Menziani, M. C. *Chemistry of Materials* **2010**, *22*, 5644–5652.
- (331) Fayon, F.; Duée, C.; Poumeyrol, T.; Allix, M.; Massiot, D. *The Journal of Physical Chemistry C* **2013**, *117*, 2283–2288.
- (332) Stevansson, B.; Mathew, R.; Edén, M. *The Journal of Physical Chemistry B* **2014**, *118*, 8863–8876.
- (333) Mathew, R.; Stevansson, B.; Edén, M. *The Journal of Physical Chemistry B* **2015**, *119*, 5701–5715.
- (334) Grussaute, H.; Montagne, L.; Palavit, G.; Bernard, J. L. *Journal of Non-Crystalline Solids* **2000**, *263-264*, 312–317.
- (335) Brown, R. F.; Rahaman, M. N.; Dwilewicz, A. B.; Huang, W.; Day, D. E.; Li, Y.; Bal, B. S. *Journal of Biomedical Materials Research Part A* **2009**, *88A*, 392–400.
- (336) Huang, W.; Day, D. E.; Kittiratanapiboon, K.; Rahaman, M. N. *Journal of Materials Science: Materials in Medicine* **2006**, *17*, 583–596.
- (337) Liu, X.; Rahaman, M. N.; Day, D. E. *Journal of Materials Science: Materials in Medicine* **2013**, *24*, 583–595.
- (338) Bi, L.; Rahaman, M. N.; Day, D. E.; Brown, Z.; Samujh, C.; Liu, X.; Mohammadkhah, A.; Dusevich, V.; Eick, J. D.; Bonewald, L. F. *Acta Biomaterialia* **2013**, *9*, 8015–8026.
- (339) Durand, L. A. H.; E. Vargas, G.; M. Romero, N.; Vera-Mesones, R.; M. Porto-López, J.; R. Boccaccini, A.; P. Zago, M.; Baldi, A.; Gorustovich, A. *Journal of Materials Chemistry B* **2015**, *3*, 1142–1148.
- (340) Yu, Y.; Eden, M. *Rsc Advances* **2016**, *6*, 101288–101303.
- (341) Yu, Y.; Stevansson, B.; Edén, M. *The Journal of Physical Chemistry B* **2017**, *121*, 9737–9752.
- (342) Mathew, R.; Stevansson, B.; Tilocca, A.; Edén, M. *The Journal of Physical Chemistry B* **2014**, *118*, 833–844.

-
- (343) Van Wüllen, L.; Schwering, G. *Solid State Nuclear Magnetic Resonance* **2002**, *21*, 134–144.
- (344) Souza, M. T.; Crovace, M. C.; Schröder, C.; Eckert, H.; Peitl, O.; Zanutto, E. D. *Journal of Non-Crystalline Solids* **2013**, *382*, 57–65.
- (345) Watts, S. J.; Hill, R. G.; O'Donnell, M. D.; Law, R. V. *Journal of Non-Crystalline Solids* **2010**, *356*, 517–524.
- (346) Tilocca, A.; Cormack, A. N. *The Journal of Physical Chemistry B* **2007**, *111*, 14256–14264.
- (347) Pedone, A.; Malavasi, G.; Menziani, M. C. *The Journal of Physical Chemistry C* **2009**, *113*, 15723–15730.